UNIVERSITÀ
DI TORINO

Università degli Studi di **TORINO**
Dipartimento di **FISICA**

Dottorato di ricerca in **FISICA**
XXXV ciclo

Titolo della tesi:

METEORITES RECOVERY AND ORBITAL ELEMENTS OF NEAR-EARTH OBJECTS FROM THE OBSERVATION OF BRIGHT METEORS – SCIENTIFIC EXPLOITATION OF THE PRISMA FIREBALL NETWORK DATA AND OF THE MISSIONS OF THE JEM-EUSO PROGRAM

Tesi presentata da: **DOTT. DARIO BARGHINI**
TUTORS: **PROF. MARIO EDOARDO BERTAINA, DOTT. DANIELE GARDIOL**
COORDINATORE DEL DOTTORATO: **PROF. PAOLO OLIVERO**

ANNI ACCADEMICI: **2019/2020, 2020/2021, 2021/2022**

Settore Scientifico-Disciplinare di afferenza:
FIS/05 ASTRONOMIA E ASTROFISICA

UNIVERSITÀ
DI TORINO

Scuola di Dottorato
PhD in Fisica

Meteorites recovery and orbital elements of Near-Earth Objects from the observation of bright meteors

Scientific exploitation of the PRISMA fireball network data and of the missions of the JEM-EUSO program

Candidate Dott. Dario Barghini

Supervisor Prof. Mario Edoardo Bertaina
Dipartimento di Fisica
Università degli Studi di Torino

Supervisor Dott. Daniele Gardiol
OATo - Osservatorio Astrofisico di Torino
INAF - Istituto Nazionale di Astrofisica

Academic year 2021/2022

Dott. Dario Barghini
Meteorites recovery and orbital elements of Near-Earth Objects from the observation of bright meteors: Scientific exploitation of the PRISMA fireball network data and of the missions of the JEM-EUSO program
Academic year 2021/2022
Supervisors: Prof. Mario Edoardo Bertaina and Dott. Daniele Gardiol

Università degli Studi di Torino
PhD in Fisica
Scuola di Dottorato
Via Pietro Giuria, 1
10125 , Torino

> *Il fatto stesso che l'inconoscibile è, appunto, inconoscibile dona - secondo quelle genti - virtù alla fede e la rende sacrosanta. Dopo tutto, che virtù ci sarebbe nella fede se gli oggetti di culto fossero noti? Una persona capace di conservare la fede assoluta anche in mancanza di qualsiasi tipo di prova deve possedere una profonda virtù. Di conseguenza, solo quelli che hanno la fede per compiere il balzo dalla sicurezza del tangibile nel vuoto dell'impercettibile sono giusti e degni di una ricompensa eterna [...] È come se ti chiedessero di balzare da una scogliera dicendoti di aver fede nella tua capacità di volare, ma non devi agitare le braccia perché altrimenti tradiresti una fondamentale mancanza di fede, e questo ti condannerebbe senz'altro a un tuffo verso il terreno sottostante, dimostrandoti così che il fallimento della fede è in realtà un fallimento personale e letale.*
>
> — **Terry Goodkind**
> Phantom

Abstract

Extra-terrestrial material is an important source of information about the history and evolution of the Solar System. Therefore, gathering data or even samples from asteroids and comets is a major driver of international space missions. The recovery of meteorites samples, surviving the atmospheric transit of a meteoroid through the Earth atmosphere (which light emission is named meteor), is a much cheaper way to obtain this kind of material. In this context, the conjunct observation of the atmospheric entry of the object, recovery and classification of the meteorite sample and identification of the parent body is the most desirable condition for the full scientific exploitation of gathered data. Many fireball networks are operating worldwide to this purpose, deploying autonomous stations for the detection of bright meteors through the systematic monitoring of the night sky. Among them, the recent born PRISMA (Prima Rete Italiana per la Sorveglianza sistematica di Meteore ed Atmosfera), partner of the international project FRIPON, implemented this kind of instrument on the Italian territory. To date, the observations of PRISMA allowed for the recovery of two freshly-fallen meteorites, Cavezzo in January 2020 and Matera in February 2023. On the other hand, a space-based observatory offers the unique opportunity to observe and constrain the flux of much smaller objects, providing an uniform coverage on the whole Earth and reaching large exposure values within a little observation time. This is the case of Mini-EUSO, a pathfinder mission of the JEM-EUSO (Joint Experiment Missions for Extreme Universe Space Observatory) space program. While having the primary scientific target of observing ultrahigh energy cosmic rays, the missions of the JEM-EUSO program can gather invaluable meteor data since systematically observing the Earth's atmosphere in the UV wavelength range. In particular, the Mini-EUSO telescope installed on the Zvezda module of the International Space Station detected 24 thousand meteors within the first year of operation, summing up to a total observation time of approximately 6 days. In this manuscript, I present the results of my research activity during the period of the PhD, that was mainly dedicated to the development, implementation and testing of reduction procedures to the data analysis of meteor observations from the PRISMA and Mini-EUSO projects.

Contents

1

Introduction

Tons of extraterrestrial material are delivered each year to the Earth, a fraction of which consisting of particles large-enough to produce detectable meteors. In the last decades, the study of meteoroids, meteors and meteorites has become a major driver in the advancement of our knowledge in planetary science. This is because meteoroids (minor bodies up to 1 m in size) preserve unprocessed and unmelted material, a record of the early stages of the Solar System which allows investigation of its formation and evolution. Therefore, the recovery of freshly-fallen meteorites provides the easiest and cheapest way to gather pristine and uncontaminated samples of meteoroids. Since 1960, significant efforts have been made towards this goal by deploying meteor and fireball networks. These distributed telescopes are able to observe the atmospheric transit of the meteoroid, estimate its physical parameters, compute its preatmospheric orbit and, finally, constrain the area over which meteorite fragments are expected to be found. In Italy, this kind of technology was implemented by PRISMA, a project born in 2017 and currently led by INAF, the Italian National Institute for Astrophysics. The PRISMA project is a partner of the FRIPON international collaboration and deployed its new technology on the Italian territory, building a network of about 70 stations equipped with a fish-eye camera able to image the whole observable sky in just one frame. Up to date, the observations of PRISMA allowed for the recovery of two freshly-fallen meteorites. The first one was recovered on 04/01/2020 in the municipality of Cavezzo in the province of Modena, Emilia Romagna, after a meteorite-dropping bolide was observed over North Italy on the evening of the New Year's Eve 2020, three days before the fall. A similar event was detected by PRISMA over Southern Italy on Saint's Valentine Day of 2023. Few meteorites landed north of the Matera municipality, the capital of the Basilicata region, and were recovered on 17/02/2023.

A second and important scientific objective linked to the observations of meteors is the monitoring of the flux of these objects to the Earth's position. This directly relates to the population of Near Earth Objects, that is poorly constrained below 100 m of size, since they are scarcely observed in orbit by telescopic observations. At the same time, these moderate-sized bodies represent a significant source of impactors in the medium-term horizon. The monitoring of smaller, cm- to μ-sized meteoroids is also crucial since they pose serious threats to human space operations. Despite the observational effort in the last century, the quantification of the flux of these objects and the link with possibly common parent bodies are still argument of debate.

Space-based observation of meteors can then complement ground-based surveys, enriching meteor databases especially in the lower mass range. This can come as a by-product of certain space-based instruments, as in the case of the JEM-EUSO space program, mainly dedicated to the detection of ultrahigh energy cosmic rays. To this purpose, the JEM-EUSO collaboration is currently deploying path-finder missions to prove its observational concept, and Mini-EUSO is the second mission of JEM-EUSO observing from space. It is a wide-field telescope installed on the Zvezda module of the International Space Station (ISS), which observes the Earth's atmosphere in the nadir direction from an UV-transparent window with a field of view of $44° \times 44°$, divided in 48×48 pixels with a resolution of about 6.3 km on the ground. During its first 44 data-taking sessions, corresponding to a total observation time of about 5.7 days, Mini-EUSO detected 24 thousand meteors.

My research activity during the period of the PhD was mainly dedicated to development of analysis methods for both PRISMA and Mini-EUSO. The methods and results of my work are reported in this manuscript, which is organized as follows.

Chapter 2 presents a general overview of the broad topic of the study of minor bodies in the Solar System, with a particular attention to asteroids, meteoroids and Near Earth Objects. It then addresses the historical background and physical description of the meteor phenomenon observed in the Earth's atmosphere, and gives a short review on the topic of meteorites, their analysis and classification, highlighting the key role of meteoritic science in modern planetology.

Then, I give a comprehensive review of the PRISMA and JEM-EUSO experiments in Chap. 3, with a particular attention to their scientific target, the technical specifications and the data format of their observations.

Chapter 4 presents the data reduction pipeline that I developed for the analysis of the observations of PRISMA. Given the extension of the network and the size of the data collected each day, the pipeline was designed to be fully automatic and to operate on the servers of PRISMA, located at the INAF - Osservatorio Astrofisico di Torino. The data of PRISMA are subdivided in two categories, that are calibration images and event videos. The astrometric and photometric calibration of each PRISMA sensor is carried out against the data of stars detected on the first dataset, consisting of 5 s exposure images taken each 10 minutes during the whole night. Then, these calibration results are used to reduce the detection of fireballs, independently triggered on each station and managed by the FRIPON central servers. For each event, that is a collection of detections of the same fireball by different cameras of the network, the pipeline performs the computation of its 3D trajectory, the estimation of the physical parameters of the meteoroid through the evaluation of a dynamic model and, finally, the computation of its preatmospheric orbit.

The data analysis pipeline presented in Chap. 4 allowed the recovery of the Cavezzo and Matera meteorites, described in Chap. 5. For both events, I describe the results of the data analysis of the related fireball and the circumstance of the finding. For Cavezzo, I also detail the analysis of the meteorite that led to its peculiar classification as an L5 anomalous chondrite, and the measurement of the γ-activity of the main mass with the spectrometers operating at the Monte dei Cappuccini underground laboratory in Torino.

Chapter 6 is then dedicated to the description of the analysis of Mini-EUSO observations of meteors. The data acquisition at 41 ms time resolution, suitable for the detection of meteors, is not independently triggered by the instrument. Therefore, the first part of the chapter describes the adopted trigger methods and the study of their performance. This work allowed to identify 24 thousands meteor events, and their analysis is detailed in the second part of the chapter. To deduce an unbiased estimation of the absolute flux of meteors observed by Mini-EUSO, I then present the simulation toolkit developed for the estimation of the total exposure of the instrument. The resulting flux density is finally compared with available estimations in the same meteoroid's mass range observed by Mini-EUSO.

Chapter 7 discusses the topic of interstellar meteoroids and their detection within the Earth's atmosphere as meteors observed beyond the parabolic limit. In particular, I focus on the analysis of the significance of their identification, based on the error estimation of the measured speed and radiant of observed meteors. This analysis was applied to both the observations of FRIPON (within which the ones of PRISMA are included) and Mini-EUSO. The last part of this chapter describes my work within DIMS, a novel experiment born in 2017 and designed to search for fast-moving particles such as interstellar meteors and nuclearites, a candidate of macroscopic dark matter.

Finally, I draw the conclusions of this work in Chap. 8.

Minor bodies of the Solar System

2

While we can find records of naked-eye observations of comets back at least one millennia, the first observations of an asteroid dates back just a couple of centuries ago. In 1772, the German astronomer Johann Elert Bode published a formulation of a semi-empirical procession, known today as the *Titius-Bode law*, which predicted the orbital semi-major axes (and therefore the approximate distance from the Sun) of planets in the Solar System. This law can be expressed as:

$$a_n = 0.4 + 0.3 \cdot 2^n \text{ AU} \text{ , for } n \in [-\infty, 0, 1, ..., 7] \text{ .} \tag{2.1}$$

The semi-major axis of Mercury is given by $n = -\infty$, Venus by $n = 0$, and so on. Up until Uranus, the Titius-Bode law gives small deviations confined within ±5% with respect to observed values. The interesting thing was that the distance of Mars corresponded to $n = 2$, while the one of Jupiter to $n = 4$. This evidence led to believe that a new planet, between Mars and Jupiter, was yet to be discovered. Observational efforts were therefore dedicated to find this "missing planet". On New Year's day of 1801, Italian astronomer Giuseppe Piazzi actually discovered a new body, which is known today as (1) Ceres, the biggest asteroid in the main belt, with a diameter of approximately 940 km. The problem was that, in succeeding years, other astronomers (mainly from Germany) discovered other big objects, such as (2) Pallas, (3) Juno and (4) Vesta, each smaller than Ceres. It soon became obvious that a population of these bodies existed between the orbits of Mars and Jupiter and, as a whole, they represented the "missing planet".

The importance of small bodies, namely asteroids, meteoroids and comets, in planetary science has been known for decades, but only in the last decades we developed the tools to actually understand their key role in the formation and evolution of the Solar System. The purpose of this chapter is to give a general overview of the current knowledge on the topic of minor bodies in the Solar System (excluding planetary satellites). Starting with an introduction to the various classes of bodies and a short discussion about their main characteristics, the focus is then shifted towards Near-Earth Objects, which represent the main source population for meteors to be observed in the Earth's atmosphere. After a general overview of the meteor phenomenon (which will be detailed in Chap. 4), I present the topic of meteorites and a summary of their study and classification.

This chapter then concludes with a broad discussion of the importance of minor bodies and meteorite studies in modern planetology. I detail some of the fundamental contributions that these studies can bring to the advancement of our knowledge about the formation and evolution of the Solar System. The recovery of meteorites, and the outstanding effort in the deployment of sample-return missions, give us the opportunity to study pristine samples which reflect the composition of planetesimals, *i.e.*, the building blocks upon which all major bodies formed. This consequently provides us with fundamental and unique insights into the status and processes that took place in the early stages of our planetary system. Furthermore, the discovery and monitoring of these minor bodies is of utmost importance due to the potential threat they represent in case of an impact on the Earth, which could potentially wipe out life as we know it. On the other hand, they could represent, in the future, an important source of raw materials that are rare on Earth and are extensively exploited for the production of advanced technological devices.

2.1 Asteroids and meteoroids

The term *asteroid* typically refers to rocky and/or metallic small bodies orbiting around the Sun between Mars and Jupiter. This region of the Solar System exhibits, in fact, the higher spatial density of this kind of bodies and it is called the *main asteroidal belt* (MAB). To date, more than 1 million asteroids are known, being observed remotely using Earth- or space-based telescopes by means of the Sun light they reflect towards the Earth. They are believed to be the remnants of planetesimals that formed the terrestrial and Jovian planets.

The International Astronomical Union (IAU) has not yet issued an official definition for the term "asteroid". As a matter of fact, they can be defined as "*[...] an irregularly shaped rocky body orbiting the Sun that does not qualify as a planet or a dwarf planet under the IAU definitions of those terms introduced in 2006*" (Gargaud et al., 2011). Their official nomenclature follows the one for *Minor Planets*[1]. Upon discovery, they are given a provisional alphanumeric code (based on the rules defined by the Minor Planet Center - MPC[2]) enclosing the date of first observation. Once they are observed long enough, such that their orbits are well determined and can be confidentially projected into the future, the MPC issues a permanent and progressive numerical code, which will accompany an official name usually suggested by the discoverer.

As already mentioned, the largest known asteroid is (1) Ceres, which has an average geometrical diameter of ~940 km and orbits in the MAB with a semi-major axis of about 2.77 AU and a low eccentricity (McCord and Sotin, 2005). Because of its considerably large dimensions, Ceres is also classified as a dwarf planet. Figure

---

[1] https://www.iau.org/public/themes/naming/#majorplanetsandmoon

[2] https://www.minorplanetcenter.net

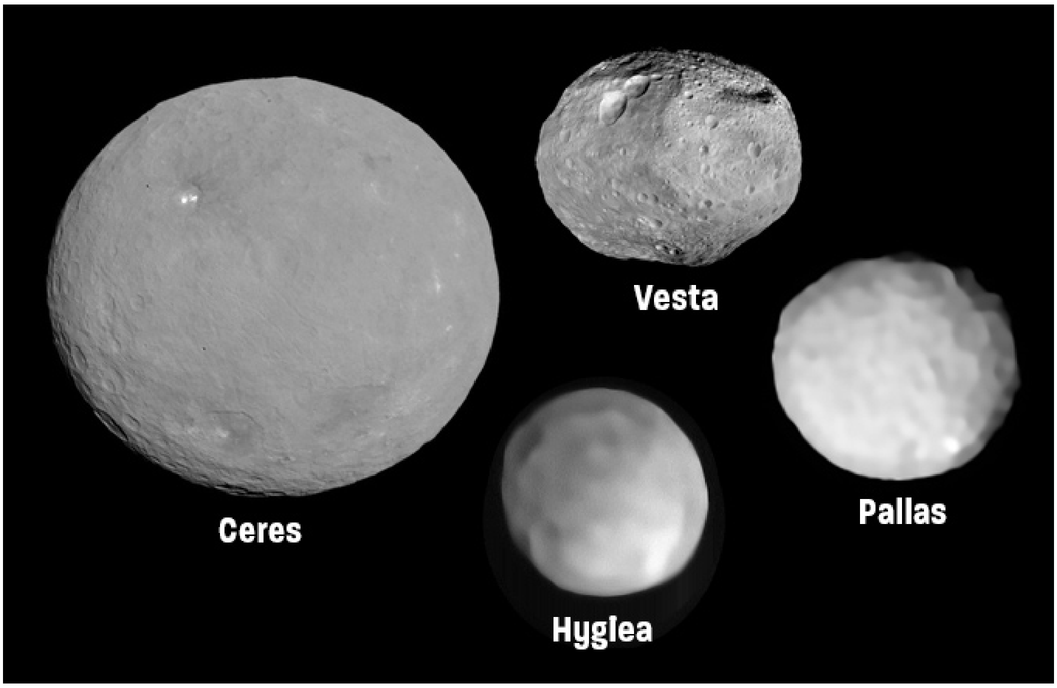

Fig. 2.1: A composite image of the four largest known asteroids, namely (1) Ceres, (4) Vesta, (2) Pallas and (10) Hygiea. The morphology of the surface of both Ceres and Vesta shows several impact features (credits: Greg Smye-Rumsby).

2.1 shows a composite image of the four largest known asteroids. They are (4) Vesta, (2) Pallas and (10) Hygiea and have a diameter of 525, 510 and 430 km respectively.

Meteoroids are smaller bodies compared to asteroids. Historically, the distinction between asteroids and meteoroids has not been strictly defined. However, in 2017 the IAU Commission F1 on Meteors, Meteorites and Interplanetary Dust[3] approved an explanatory text for the correct usage of these terms and defined a diameter range of ~30 µm to ~1 m for meteoroids (smaller objects are categorized as *interplanetary dust* or *micrometeoroids*).

A general dissertation able to cover all aspects of this wide class of minor bodies is indeed challenging. A query on the digital library portal of the SAO/NASA Astrophysics Data System[4] (ADS) for the keyword "asteroid" returns more than 45 thousand references, with an average of almost 1 thousand refereed publications per year in the last two decades. For a detailed review of many aspects in the topic of asteroid studies, the reader can refer for example to Burbine (2014) and Fernández et al. (2015). In the following sections, I will focus on four arguments that I believe are fundamental in getting an overall picture of this heterogeneous ensemble of bodies, *i.e.*, their physical properties, their size distribution, their classification based on the taxonomic grouping of their reflectance spectra and finally their clustering in orbital families.

---

[3] `http://iau.org/science/scientific_bodies/commissions/F1`

[4] `https://ui.adsabs.harvard.edu/`

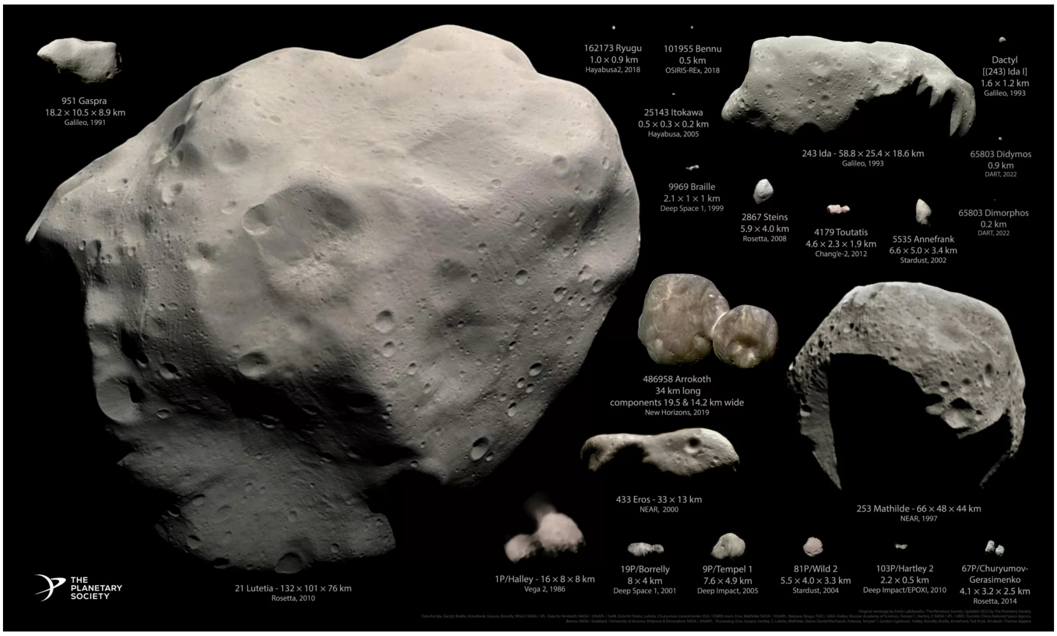

Fig. 2.2: Composite image of most of the minor bodies visited by spacecraft missions since 1990. Bodies are represented in a realistic relative scale, with the biggest one, (21) Lutetia, being about 100 km in size (original montage by Emily Lakdawalla / The Planetary Society. Updated in 2022 by The Planetary Society. Data from NASA / JPL / JHUAPL / SwRI / ESA / OSIRIS / ISAS / JAXA / Russian Academy of Sciences / UMD / China National Space Agency / Goddard / University of Arizona. Processed by Emily Lakdawalla, Daniel Machacek, Ted Stryk, Gordan Ugarkovic, Thomas Appéré - https://www.planetary.org/space-images/asteroids-and-comets-visited-by-spacecraft).

2.1.1 Morphology and physical properties of asteroids

A total of 20 minor planets (asteroids and comets) were visited by spacecraft missions since 1990 (see Fig. 2.2). These flybys allowed detailed and direct imaging of their surface and determination of their morphology features. Despite their small size, asteroids display a wide range of surface features, such as craters, boulders, lineaments, rough and smooth terrains, regolith and landslides. The dominant features are of course *impact craters*, which are subject to degradation processes right after their formation. From their geomorphological characteristic, size and spatial distributions various insights can be deduced, such as the age of last resurface and the size distribution of impactors. The *depth-to-diameter ratio* is an important parameter used as a proxy of the degradation state of craters. Associated with impacts as well, boulders represent the second most dominant surface feature and sometimes they are the most important ones. A large number of boulders in a particular surface region can indicate the young age of the relative craters.

An important physical property of asteroids is their bulk density, which directly relates to their porosity. As a matter of fact, asteroids often show a high porosity level, up to 50%, whereas this is not observed as often in meteorite specimens. As detailed in Sect. 2.1.2, the asteroid population we observe today originates from an intense collisional history and only the largest bodies (over 300 km of size) preserve their primordial mass and composition. Smaller bodies are thought to be the result of a process of a repetitive accretion-disruption equilibrium. Therefore, it is not surprising that most asteroids are lumps of loosely bound rubble with vast void inner portions resulting in a large porosity. This structural model is often referred to as *rubble pile*, in contrast with a whole solid body which is called a *monolith*.

Closely related to the internal structure is the topic of asteroid rotation or *spin*. This phenomenon is usually detected in optical light-curve observations as a modulation depending on the spin rate, orientation and shape of the body (Warner et al., 2009). In particular, it is observed that asteroids with absolute magnitude[5] $H < 20$ are bounded to rotate at a minimum period of about 2.4 hours. This limit is called *spin barrier* and corresponds to the fastest rate at which rubble pile bodies can rotate without disrupting (Pravec and Harris, 2000). Smaller asteroids, less than 300 m in size, are observed to break the spin barrier, most likely being monolithic.

2.1.2 Size-frequency distribution

An important aspect to characterize the population of asteroids in the MAB is their *size-frequency distribution* (SFD), which is in other words the numerical density of these objects as a function of their size. An accurate and precise determination of the SFD is crucial in the context of understanding the collisional equilibrium processes that led to the asteroid population we observe today (Bottke et al., 2005a). The SFD can be expressed in terms of the differential distribution (dSFD) according to the equivalent diameter $D = 2R$:

$$\rho_n(D) = \frac{\mathrm{d}n}{\mathrm{d}D} \,, \tag{2.2}$$

or by the cumulative one (cSFD):

$$N(>D) = \int_D^\infty \mathrm{d}D' \, \rho_n(D') \, . \tag{2.3}$$

Both observations (Bottke et al., 2005b; Gladman et al., 2009; Masiero et al., 2011) and theoretical/simulation works (O'Brien and Greenberg, 2003; Durda et al., 2007) suggest that the dSDF approximately follows a power law of the diameter with an exponent $a \simeq -7/2$ and, as a consequence, the cSFD also follows a power law with exponent $a + 1 \simeq -5/2$:

$$\rho_n(D) \propto D^a \quad \rightarrow \quad N(>D) \propto D^{a+1} \, . \tag{2.4}$$

---

[5] The absolute magnitude H for asteroids is defined at the reference distance of 1 AU and zero phase angle. Assuming a mean visual albedo of 0.2, $H = 20$ corresponds to a diameter of approximately 300 m (Harris and Harris, 1997).

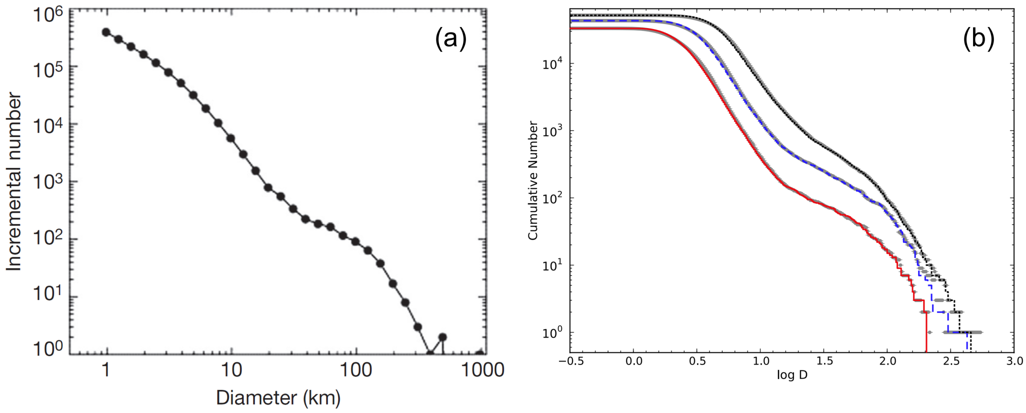

Fig. 2.3: Plots of the cumulative size-frequency distribution (cSFD) of asteroids in the MAB as derived by Bottke et al. (2005b) - panel a, and Masiero et al. (2011) - panel b. For the latter, the distribution is divided into inner (red), middle (blue) and outer MAB (black).

Figure 2.3 plots the results on cSFD curves derived from two observation surveys and displays additional other features such as "waviness" or bumps at certain size values. This could be interpreted as resulting from the strength-size relationship of asteroids (see Sect. 2.1.1). The first theoretical derivation of such power-law behaviour was presented by Dohnanyi (1969), based on an inelastic collisional model. Here is reported a summarized version[6] of this model proving that $a = -7/2$ under several simplifications.

Let us consider the mass density of asteroids $\rho(m)$, which relates to the dSFD $\rho_n(D)$ as:

$$\rho(m) = m\frac{\mathrm{d}n}{\mathrm{d}m} = m\frac{\mathrm{d}D}{\mathrm{d}m}\frac{\mathrm{d}n}{\mathrm{d}D} = m\frac{\mathrm{d}D}{\mathrm{d}m}\rho_n[D(m)] \ . \tag{2.5}$$

If we assume that the total mass within the MAB is constant, we can write a continuity equation:

$$\frac{\mathrm{d}}{\mathrm{d}t}\left(\int_{\mathrm{MAB}} \mathrm{d}m\,\rho\right) = 0 \quad \rightarrow \quad \frac{\partial \rho}{\partial t} + \frac{\partial}{\partial m}\left(\rho\frac{\partial m}{\partial t}\right) = 0 \ . \tag{2.6}$$

We are interested in the steady-state solution, meaning that $\frac{\partial \rho}{\partial t} = 0$ and:

$$\frac{\partial}{\partial m}\left(\rho\frac{\partial m}{\partial t}\right) = 0 \quad \rightarrow \quad m\frac{\mathrm{d}n}{\mathrm{d}m}\frac{\mathrm{d}m}{\mathrm{d}t} = \mathrm{const} \ , \tag{2.7}$$

having switched from partial to total derivates given the previous simplifications. Then, let us make the following assumptions:

1. a collision between two asteroids A1 (m_1) and A2 (m_2) at a relative speed v_{21} (of A2 w.r.t. A1) leads to the accretion of the larger one. Given a constant $f < 1$, A1 "incorporates" A2 if $m_2 < f m_1$, resulting in $m_1' = m_1 + m_2$;

---

[6] `https://www.reddit.com/r/Physics/comments/bno1q0/why_the_size_distribution_of_asteroids_follow_a/`

2. otherwise, if $m_2 \geq f m_1$, A1 is disrupted by the collision, resulting in $m_1' = 0$;
3. the collisional cross-section scales as $\sigma = \pi R^2 \propto m^{2/3}$;
4. the distribution of relative velocities v_{21} is independent of the asteroids' masses;
5. the numerical density of asteroids follows a power law with exponent γ to be determined, $\frac{\mathrm{d}n}{\mathrm{d}m} \propto m^\gamma$.

To solve Eq. 2.7 for γ we need to evaluate the term $\frac{\mathrm{d}m}{\mathrm{d}t}$, which is the net rate of variation of the mass of an asteroid and is given by the contributions of accretion [1] and disruption [2] terms as:

$$\frac{\mathrm{d}m}{\mathrm{d}t} = \left(\frac{\mathrm{d}m}{\mathrm{d}t}\right)_{\text{acc}} + \left(\frac{\mathrm{d}m}{\mathrm{d}t}\right)_{\text{dis}} . \tag{2.8}$$

The rate of accretion is given by the collisional integral as:

$$\left(\frac{\mathrm{d}m}{\mathrm{d}t}\right)_{\text{acc}} = \int_0^{f m_1} \mathrm{d}m_2 \, m_2 \frac{\mathrm{d}n}{\mathrm{d}m_2} \sigma_{21} v_{21} . \tag{2.9}$$

If we assume that $f << 1$, we can approximate $\sigma_{21} = \pi (R_1 + R_2)^2 \simeq \pi R_1^2 \propto m_1^{2/3}$ and, using assumptions [4,5], the accretion rate is proportional to:

$$\left(\frac{\mathrm{d}m}{\mathrm{d}t}\right)_{\text{acc}} \propto m_1^{2/3} \int_0^{f m_1} \mathrm{d}m_2 \, m_2^{\gamma+1} = m_1^{2/3} \left[m_2^{\gamma+2} \right]_0^{f m_1} \propto m_1^{\gamma+8/3} , \tag{2.10}$$

where we quietly assumed that $\gamma > -2$ to cancel the lower extreme of the integral. The same reasoning can be given for the disruption rate, with $\sigma_{21} \simeq \pi R_2^2 \propto m_2^{2/3}$ and M being the mass of the biggest asteroid in the population:

$$\begin{aligned} \left(\frac{\mathrm{d}m}{\mathrm{d}t}\right)_{\text{dis}} &= \int_{f m_1}^{M} \mathrm{d}m_2 \, m_1 \frac{\mathrm{d}n}{\mathrm{d}m_2} \sigma_{21} v_{21} \propto m_1 \int_{f m_1}^{M} \mathrm{d}m_2 \, m_2^{\gamma+2/3} = \\ &= m_1 \left[m_2^{\gamma+5/3} \right]_{f m_1}^{M} \propto m_1^{\gamma+8/3} \left[\left(\frac{M}{f m_1} \right)^{\gamma+5/3} - 1 \right] \propto m_1^{\gamma+8/3} . \end{aligned} \tag{2.11}$$

For the last simplification of Eq. 2.11 to be reasonable, we have to make additional assumptions on the values of M and γ. The exact value of M is not important to the discussion, but to close this integral we need $f m_1 << M$ and $\gamma < -5/3$. The first condition is already granted since we assumed $f << 1$ and, by definition, $m_1 \leq M$. Together with the limit given by Eq. 2.10, the validity domain of this model is $\gamma \in (-2, -5/3)$. Therefore, by evaluating Eq. 2.7 with Eqs. 2.10 and 2.11 (both scaling by the same power of m_1), we obtain:

$$m \frac{\mathrm{d}n}{\mathrm{d}m} \frac{\mathrm{d}m}{\mathrm{d}t} \propto m^{2\gamma+11/3} = \text{const} \quad \rightarrow \quad \gamma = -\frac{11}{6} , \tag{2.12}$$

that satisfies the aforementioned conditions on γ. Eq. 2.12, together with Eqs. 2.4, 2.5 and considering that $D \propto m^{1/3}$ and $\frac{\mathrm{d}D}{\mathrm{d}m} \propto m^{-2/3}$, finally gives the value of the exponent a for the dSFD:

$$m\frac{\mathrm{d}n}{\mathrm{d}m} = m\frac{\mathrm{d}D}{\mathrm{d}m}\rho_n[D(m)] \quad \rightarrow \quad m^{1+\gamma} \propto m^{(a+1)/3} \quad \rightarrow \quad a = -\frac{7}{2}\,. \tag{2.13}$$

2.1.3 Taxonomy of asteroids

The most viable and used way to remotely estimate the composition of asteroids is by means of reflectance spectroscopy (or spectrophotometry[7]) in the visible and near-infrared, *i.e.*, measurements of the relative fraction of light reflected as a function of the wavelength. The baseline of the reflectance measurement is of course the black-body spectrum of the Sun. Because this cannot be directly measured during the observation of the target asteroids, the reference spectra are built from Sun-like stars (G2 spectral type) observed simultaneously at comparable air mass. Since 1980, a significant number of spectrophotometry and spectroscopic surveys made substantial contributions to the study of the composition of asteroids (see, for example, references in Sect. 2.14.3.1 of Burbine, 2014). Reflectance spectroscopy observations are usually accompanied by measurements of the visual albedo, which also depends on the mineralogy and mean particle size of the asteroid's surface.

The first remarkable result was the discovery that many absorption bands observed in asteroids- spectra were attributable to crystal field electronic transitions and vibrational bands of minerals commonly found in meteorite samples, such as olivine, low-Ca and high-Ca pyroxene (see Sect. 2.6.2). However, the main limitation of this technique is that the reflectance spectra are a proxy of the surface composition of the asteroid only. This is also the portion of the body which is most subject to alteration, *i.e.*, space weathering (Moretti et al., 2007), in particular from solar wind irradiation and micrometeoroid impacts. Furthermore, the strength of the absorption band does not directly relate to the relative abundance of the mineral responsible for it, since most minerals are expected to be found as homogeneous mixtures on the surface. Therefore, the interpretation of such measurements relies on dedicated spectral mixing models that can be used to resolve into the single constituent bands (Sunshine and Pieters, 1993).

Reflectance spectroscopy allows classifying the observed asteroids in *taxonomic groups* according to the shape of the measured spectrum, often using the visual albedo to discern between similar shaped cases. The original classification scheme was proposed by Tholen (1984), which defined 14 asteroid classes by means of Principal Component Analysis: A, C-group (B, C, F and G), D, Q, R, S, T, V and X-group (E, M, P). For example, asteroids in the X-group can be distinguished in their E,

---

[7] Spectrophotometry observations use broadband filters to derive colour indices, whereas spectroscopy measures the actual wavelength spectrum of the asteroid.

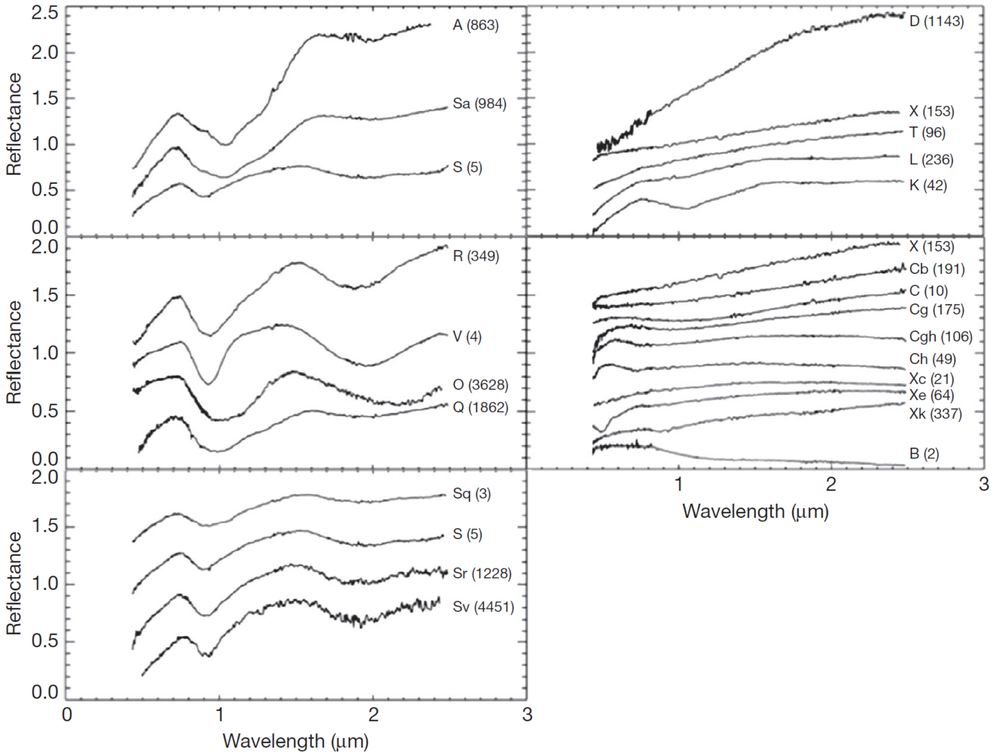

Fig. 2.4: Spectra of prototype asteroids in the Bus-DeMeo taxonomy (DeMeo et al., 2009). Spectra are shifted vertically for visualization purposes but they are defined at unit value for $\lambda = 0.55$ µm. The taxonomic type reported at the right edge of each spectrum, and the parentheses enclose the code of the prototype asteroid (Fernández et al., 2015, original plots from DeMeo et al., 2009).

M or P types only thanks to the albedo (high, moderate and low respectively). Many of the letters used to identify an asteroid type implicitly refer to the composition: C-types stands for carbonaceous, M for metal and O for ordinary chondrites (see Sect. 2.6.1). As already mentioned above, this link is often ambiguous and should be looked at with caution when inferring the composition of an asteroid from its class (Gaffey et al., 1993; Rivkin et al., 1995).

The classification scheme was therefore expanded to 24 classes by DeMeo et al. (2009), which are represented in Fig. 2.4 by the spectra of their prototype asteroids, *i.e.*, the asteroids chosen as a reference for the class[8]. Asteroids of the classes plotted on the left panels all show the classic two-band (I and II) absorption features due to olivine ($\lambda \sim 1$ µm) and pyroxene (~ 1 and 2 µm), while the ones on the right side lack such features, making their classification often problematic. The following section gives a short review of the main taxonomic types and their most important links with asteroidal families and/or meteorite classes.

---

[8] This classification scheme is usually referred as *Bus-DeMeo asteroids taxonomy*.

2.1.4 Taxonomic types and complexes

A-types asteroids show very strong UV features and deep bands near 1 μm similar to the spectra of olivine. Meteoritics analogs for A-types asteroids are pallasites, brachinites and R chondrites, all dominated by olivine content. From their composition, asteroids in this class are believed to be remnants of the disruption of mantle material from differentiated bodies. This interpretation is still problematic because it would suggest the presence of a significant number of members in this class (Chapman, 1986; Burbine et al., 1996). On the other hand, only ∼2% of asteroids were classified as A-types by DeMeo et al. (2009).

Asteroids in the C-complex are about 13% of the total according to DeMeo et al. (2009) and show flat-to-bluish and almost featureless spectra, together with a low albedo. In the Bus-DeMeo taxonomy, the C-complex includes the types B, C, Cb, Cg and Cgh. Approximately 60% of the objects in this complex show absorption bands at 3 μm, indicating the presence of hydrated silicates on their surface. Different carbonaceous chondrites are assumed to be samples of asteroids C-types asteroids. The two largest objects in the MAB, (1) Ceres and (2) Pallas, are of this complex. Also, the asteroid targets of the two most recent sample-return missions are classified in the C-complex, namely (162173) Ryugu for Hayabusa-2 (Watanabe et al., 2017) and (101955) Bennu for OSIRIS-Rex (Lauretta et al., 2017).

D-types asteroids are characterized by a strong red slope in their spectra, and their features are thought to originate from the presence of organics. They are commonly found in the Hilda group and among Jupiter Trojans, but also exist in the MAB. To date, the C2-ungrouped chondrite Tagish Lake is the only possible meteorite analog for D-types asteroids (Hiroi et al., 2001), even if the same analogy was found with T-types asteroids (Hiroi and Hasegawa, 2003).

The K-class is commonly associated with the Eos family and linked to carbonaceous CO, CV and CK chondrites. The classes of O- and R-types contain only one member each according to DeMeo et al. (2009).

L-types asteroids have pronounced UV features and absorption features consistent with calcium-aluminium inclusions (CAIs, see Sect. 2.6.2). They are particularly interesting objects since they should contain an extremely high portion of CAIs, about 30 vol%, therefore they may be more ancient than any meteorite ever collected on Earth (Sunshine et al., 2008; Hezel and Russell, 2008).

Q-types asteroids have spectral features associated to ordinary chondrites, and all Q-types identified by DeMeo et al. (2009) were actually Near-Earth Asteroids (NEAs, see Sect. 2.3). The first identified member of this class was (1862) Apollo, that is usually believed to be linked to LL chondrites.

Asteroids in the S-complex are the most studied and abundant in the inner MAB, being over 50% of the ones classified by DeMeo et al. (2009) and include the types S, Sa, Sq, Sr and Sv. They are believed to be primarily made of pyroxene and olivine,

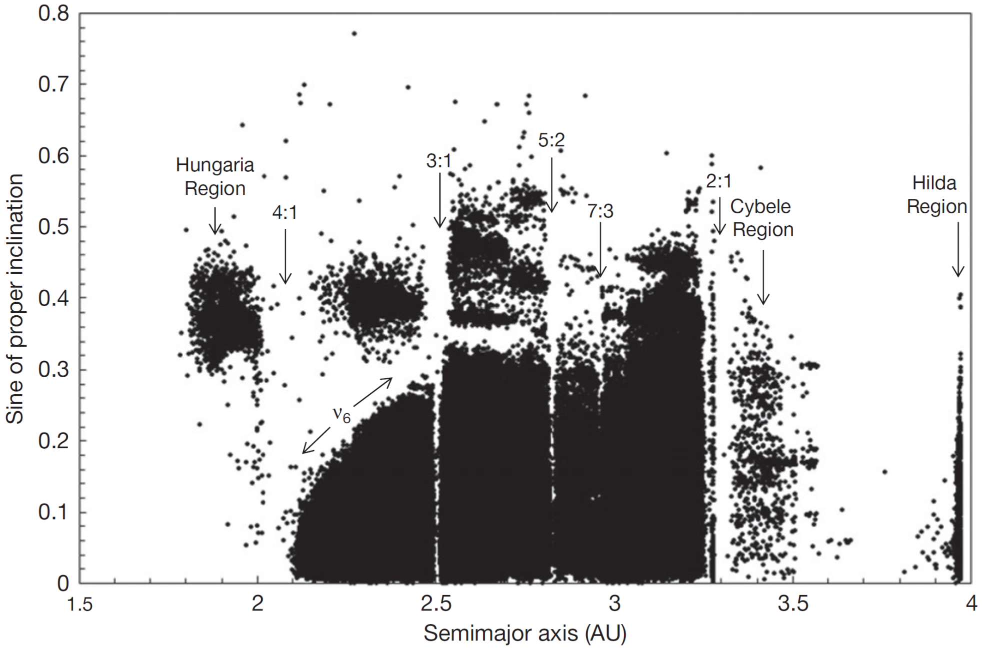

Fig. 2.5: Plot of the semi-major axis against the sine of the orbit inclination, referred as (a, i) in the text, for ∼300k asteroids. Arrows mark the position of MMRs, the secular ν_6 resonance and some asteroids regions (Burbine, 2014).

and in some cases metallic iron. Therefore, undifferentiated meteorites (mostly ordinary chondrites) are thought to be samples of this complex.

V-types asteroids have the most unusual spectral shape, characterized by strong UV features and a deep 1 µm band, which is quite similar to HED (howardites, eucrites and diogenites) meteorites spectra. The first observed asteroid in this class is (4) Vesta, assumed to be the parent body of HEDs, even if a general agreement on this link is yet to be reached (Consolmagno et al., 2011).

Finally, asteroids in the X-complex show little to no spectral features and a moderate red slope. This complex includes the types E, M and P, which are distinguished by their visual albedo. E-types are generally linked to aubrites, while M-types are thought to be related to iron meteorites.

2.1.5 Orbital distribution and asteroid families

The majority of the known asteroids orbit in the MAB, approximately between 2.1 and 3.3 AU of distance from the Sun. Figure 2.5 plots the semi-major axis and the sine on the proper[9] inclination, that is the (a, i) plot, for 300k asteroids in this region. Marked gaps in this distribution are evident at fixed values of the

---

[9] Proper elements are constants of motion that remain unchanged over astronomical timescales, in contrast with osculating Keplerian elements that vary with time for the effect of precession, among all. For the vast majority of asteroids, differences between proper and Keplerian elements are quite small (±1/100 AU for the semi-major axis, ±0.1 eccentricity and some degrees of inclination).

semi-major axis and are known as *Kirkwood gaps*. These features are due to *mean motion resonances* (MMRs), which arise from the periodic gravitational influence exerted by Jupiter on the much smaller bodies of the MAB, usually because their orbital periods are related by a ratio of small integers. For example, the 4:1 MMR occurring at ~2.06 AU corresponds to an asteroid with an orbital period 1/4 of the one of Jupiter ($T_J \simeq 11.86$ yr). Similar MMRs are present at 2.50 AU (3:1), 2.82 AU (5:2), 2.95 AU (7:3) and 3.27 AU (2:1). According to Kirkwood gaps, the MAB is divided into three regions: *inner* (from 4:1 to 3:1), *middle* (from 3:1 to 5:2) and *outer* (5:2 to 2:1). The repeated gravitational interactions due to MMRs gradually modify and destabilize the orbit of the asteroid and, in particular, they have the effect of increasing its eccentricity. The average distance with respect to the Sun does not vary, but the perihelion gets closer. This drives their orbit to become planet-crossing, increasing the impact probability and resulting in a depletion of bodies in correspondence with these resonances.

The inner boundary of the MAB arises from the *secular resonance* ν_6 with Saturn. This long-period resonance has the effect of modifying both the eccentricity and the inclination of the small body and causing it to enter an Earth-crossing orbit. The ν_6 resonance occurs if the perihelion of the asteroid precesses at the same rate as the one of Saturn. Therefore, the position of this resonance depends on both the position and orbital inclination of the asteroid; for example, it occurs at around 2.2 AU for asteroids orbiting in the ecliptic plane and farther from the Sun for more inclined orbits. This explains the peculiar shape of the inner boundary of the MAB in the (a, i) plot of Fig. 2.5. On the other hand, the outer region is thought to have been depleted by an inward migration of Jupiter in the early stages of the Solar System.

MMRs can also have the effect of stabilizing the orbit. This is the case for the Hungaria group, located between 1.8 and 2.0 AU at moderate inclination values, where about 10k asteroids are in 9:2 with Jupiter and 3:2 with Mars. Other examples of such effect are the groups of Cybele (7:4 with Jupiter) and Hilda (2:3 with Jupiter). Another special orbital case is the group of Jupiter *Trojans*. These asteroids orbit around the Sun at the same distance as Jupiter and are located in dynamically stable regions shifted of $\pm 60°$ anomaly, *i.e.*, Lagrangian points L_4 and L_5 that arise from the solution of three-body problem (Sun, Jupiter and the asteroid itself). Near-Earth Asteroids are a very important orbital class of bodies and are discussed in Sect. 2.3.

The evidence of clustering of objects in proper orbital elements defines the concept of *asteroid dynamical families*. The existence of orbital families was first suggested by Hirayama (1918), which identified 5 of them, and their number progressively increased in the next decades as more asteroids were observed and characterized (Cellino and Dell'Oro, 2010), up to 55 recognized families in most recent works (Nesvorny, 2015). Figure 2.6 plots orbital families identified and discussed in Nesvorny (2015), in the (a, i) plane. Families are named after their lowest-numbered asteroid member, and are thought to be due to the breakup of

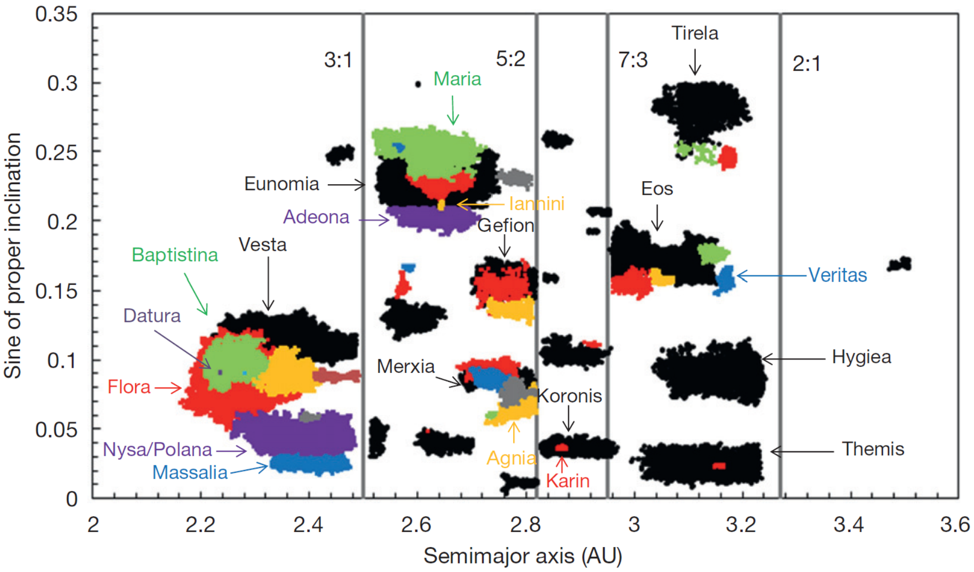

Fig. 2.6: Distribution of the asteroidal families identified by Nesvorny (2015) in the (a, i) plot (Burbine, 2014).

a larger object. Therefore, their study is of particular relevance since it gives the opportunity to observe the interior of asteroids, given that their surfaces are much younger and space weathering effects are supposed to be almost negligible.

The breakup of large and differentiated asteroids should produce a heterogeneous population of bodies, with a large metal core (M-types), a high number of mantle fragments (A-types) and some basaltic ones (V-types). This is in contrast with observational evidence, which suggests that most members of these families are instead similar in their composition, according to spectroscopic measurements (Cellino et al., 2002). It has been argued that families may originate from the disruption of pre-fragmented bodies and that larger members are formed by the gravitational re-accumulation of smaller fragments (Michel et al., 2003).

Problems in the interpretation of the link between asteroid families and taxonomic types also arise from the limited number of members that were spectroscopically observed. Nevertheless, abundances of taxonomic types are well-known to be varying according to the distance from the Sun. For instance, C-types are more common in the outer MAB, E-types are typically found in Hungaria, P-types in Hilda and D-types in the Trojans (Chapman et al., 1975; Gradie et al., 1989). Furthermore, Bell et al. (1989) distinguished three "superclasses" among the taxonomic types, being *primitive* (D, P, C, K, Q), *methamorphic* (T, B, G, F) and *igneous* (V, R, S, A, M, E), each one respectively with an increasing degree of metamorphic heating, presumably due to internal ^{26}Al decay and solar wind induced heating.

2.2 Comets

Similarly to asteroids, *comets* are also remnants of the process of planet formation. They are members of a wide distribution of minor bodies that formed in colder regions, at a higher distance from the Sun with respect to asteroids, and escaped both the aggregation into major bodies and ejection from the Solar System. Because of this, they are thought to be the best-preserved and most primitive samples of the solar nebula ice regions, beyond the *snow line*[10], which occupied ∼99% of the nebular disk. Nevertheless, they show a wide heterogeneity in composition and physical properties, suggesting that they originated from environments significantly different in temperature, pressure and accretion regimes. Most likely, comets were the building blocks upon which ice giants were formed. The most peculiar and famous feature of comets is the presence of a *coma* of gas and dust surrounding their nucleus and a *tail*, the expansion of the coma being dragged in opposition to the Sun's direction by the solar wind. This is due to the fact that comets have a large content of highly volatile ices that sublime when approaching the Sun closer than some AU. The provided heat and solar wind cause the sublimation of such components, causing the *cometary activity*. All comets are on unstable orbits that are easily perturbated by planets. At each perihelion passage, they lose volatiles and frequently fragment. For this reason, they are doomed to not retain such activity for long and eventually become inactive in time, if not totally disintegrate. For instance, the ones orbiting in a planet-crossing configuration are estimated to have a lifetime between 1 and 10 My.

The IAU defines the difference between comets and asteroids by the presence of cometary activity. However, differently from what has been the predominant opinion, during the last decades it has become more clear that asteroids and comets are not two entirely separate classes. Before 1990, asteroids were considered purely rocky and denser objects, whereas comets were believed to be relatively icy and more fragile. However, many objects were then observed to populate the whole region in between these two extrema. Active comets can be trapped in asteroid-like orbits, becoming inactive. On the other hand, asteroids can have highly eccentric elongated orbits similar to comets. Even asteroids in the MAB can show some sort of ejection activity, being named *active asteroids* or *main-belt comets*. The nomenclature for comets is similar to the one already discussed for asteroids (see Sect. 2.1). In addition to that, a letter prefix is used to distinguish the type of object: P/ for a periodic comet, C/ for non-periodic, X/ for a comet whose orbit has not yet be computed with sufficient precision, D/ for a periodic comet that no longer exists or is thought to have disappeared, and I/ for an interstellar object (see Chap. 7).

The comet 1P/Halley is the first comet whose nucleus was ever directly imaged in 1986 by the spacecraft Giotto (see Fig. 2.7). It takes its name from Edmond

---

[10] The snow line is the minimum distance at which water could have existed in ice form.

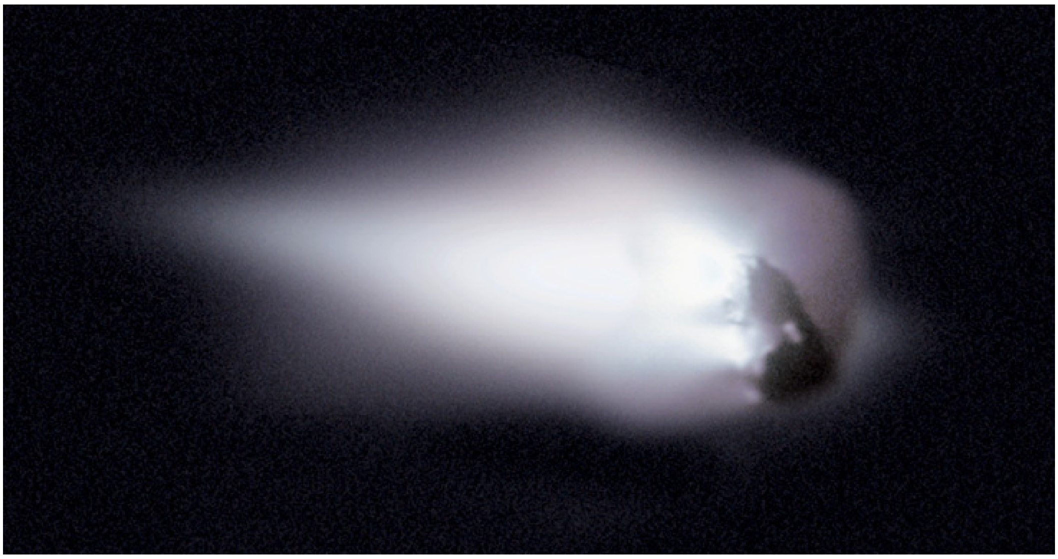

Fig. 2.7: First direct imaging of the comet 1P/Halley nucleus and coma, taken during its last perihelium in 1986 by the European spacecraft Giotto. As a scale for the image, the nucleus has an average diameter of ∼11 km (credits: Halley Multicolor Camera Team, Giotto Project, ESA - `https://solarsystem.nasa.gov/asteroids-comets-and-meteors/comets/1p-halley/in-depth/`).

Halley, who first predicted the periodic nature of its observations, dating back more than 2000 years. In 1705, Halley successfully predicted the perihelion for the year 1758 for this comet, later named after him. The next perihelium of 1P/Halley is predicted for the year 2061. At each perihelion passage, its nucleus releases debris along the orbit and this is responsible for two meteor showers, the Eta Aquarids in May and the Orionids in October (see Sect. 2.4.2).

Comets can be classified according to their orbital period. *Long-period* (LP) comets have a period greater than 200 years, otherwise they are called *short-period* (SP) comets. Within this last group, there is a further distinction. Comets with periods between 30 and 200 years are considered to be *Halley-like*, and those below 30 years are called *Jupiter family* comets (JFC). Comets are usually coming from two different major reservoirs, called *Oort cloud* and *Kuiper belt*, briefly discussed in the next sections. For a review about the topic, the reader can refer to Brownlee (2014), Fernández et al. (2015), and Dones et al. (2015), among all.

2.2.1 Oort Cloud

The term *Oort cloud* refers to a vast distribution of comets, orbiting as far as $5 \cdot 10^4$ AU of distance from the Sun and arranged with random inclinations (Weissman, 1996). A schematic representation of the Oort cloud is shown in Fig. 2.8. The inner boundary is given by gravitational perturbations that pull such objects into lower energy orbits. On the other hand, objects with a mean distance greater than $5 \cdot 10^4$ AU are likely to be stripped out from the Solar System due to encounters with

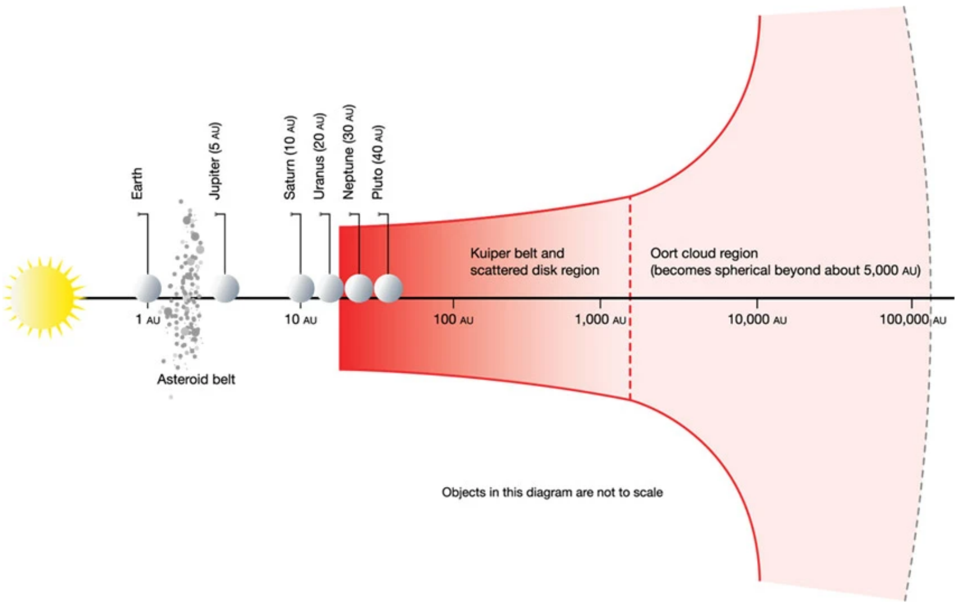

Fig. 2.8: Schematic true-scale representation of the Oort cloud and Kuiper Belt, the two main reservoirs for observable comets in the Solar System (Stern, 2003).

other stars when crossing the galaxy midplane. In fact, the nearest star is located just three times farther from what is thought to be the outer boundary of the Oort cloud.

Comets of the Oort cloud are too distant to be observed directly, and their existence was first proposed by Oort (1950) to explain the origin of LP comets. This region is believed to contain $\sim 10^{12}$ objects with a cumulative mass comparable to the Earth's one (Stern and Weissman, 2001). The bodies are thought to have been scattered outward as a result of the formation of giant planets, rather than having been formed in situ in this far distant region of the Solar System.

2.2.2 Kuiper Belt

Originally, also SP comets were thought to originate from the Oort cloud, being captured into SP orbits due to close encounters with Jupiter. This is indeed a possible mechanism that can explain the presence of SP comets and unveils the reason why they have smaller inclination values with respect to objects in the Oort cloud. However, Fernandez (1980) first demonstrated that such delivery was not strong enough to explain the vast population of SP comets. Later, Duncan et al. (1988) quantitatively proved that a population of objects beyond Neptune can actually provide a consistent flux of SP comets and their low orbital inclination. This region is today known as *Kuiper Belt*, and objects within it are called *Kuiper Belt objects* (KBOs), or *Trans-Neptunian objects* (TNOs). The name originates from Gerald Kuiper, who first discussed in 1951 the possible presence of such objects beyond Neptune.

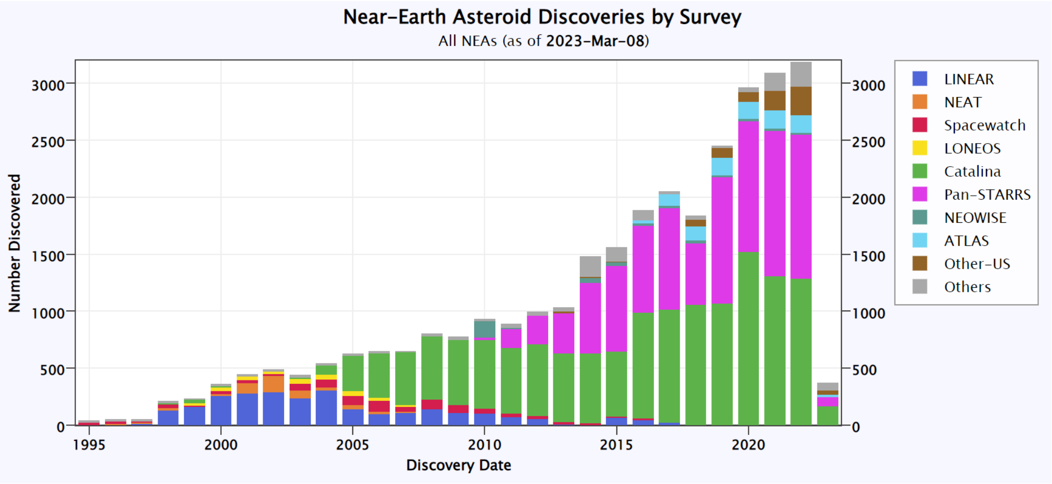

Fig. 2.9: Yearly number of discovered NEAs according to the various surveys dedicated to monitoring these objects since 1995 (credits: `https://cneos.jpl.nasa.gov/stats/`).

Being hypothesized as much closer to the Sun than Oort Cloud objects, KBOs can be observed from the Earth. Apart from (134340) Pluto and Caronte, the first object in this region was discovered in 1992 (Jewitt and Luu, 1993) and is now named (15760) Albion. Being the KBOs quite distant from the Sun (> 30 AU), they do not show any sign of cometary activity. They are all very faint objects and their discovery is heavily biased by these observation conditions. More than one thousand KBOs were discovered up to now, even if it is estimated that more than 10^5 objects with diameter > 50 km are thought to orbit in the Kuiper Belt. KBOs can be classified into three main groups. *Classical* KBOs have low-eccentricity, low-inclination orbits with a semi-major axis between 42 and 48 AU and are the most common in the Kuiper Belt, being about 2/3 of the total population. *Resonant* KBOs are in MMR with Neptune (3:2 or 2:1) and approximately represent the $\sim$20% of the total. Among all, Pluto is a resonant KBO in 3:2 with Neptune. Finally, *scattered* KBOs have highly-elliptical orbits, reaching beyond 400 AU.

2.3 Near-Earth Objects

The class of *Near-Earth Objects* (NEOs) is perhaps the most interesting and important among all minor bodies, from our perspective. An object is defined as a NEO if its perihelion distance q is lower than 1.3 AU, *i.e.*, its orbit penetrates well inside the inner Solar System and close enough to the Earth's orbit, if not crossing it. They usually have an aphelion distance $Q < 5.2$ AU, internal to Jupiter. These objects can be either asteroids (NEA) or SP comets (NEC). Among NEO, a narrow class of objects deserves the most attention. These are called *Potentially Hazardous Asteroids* (PHA) and, by definition, they are NEAs with absolute magnitude

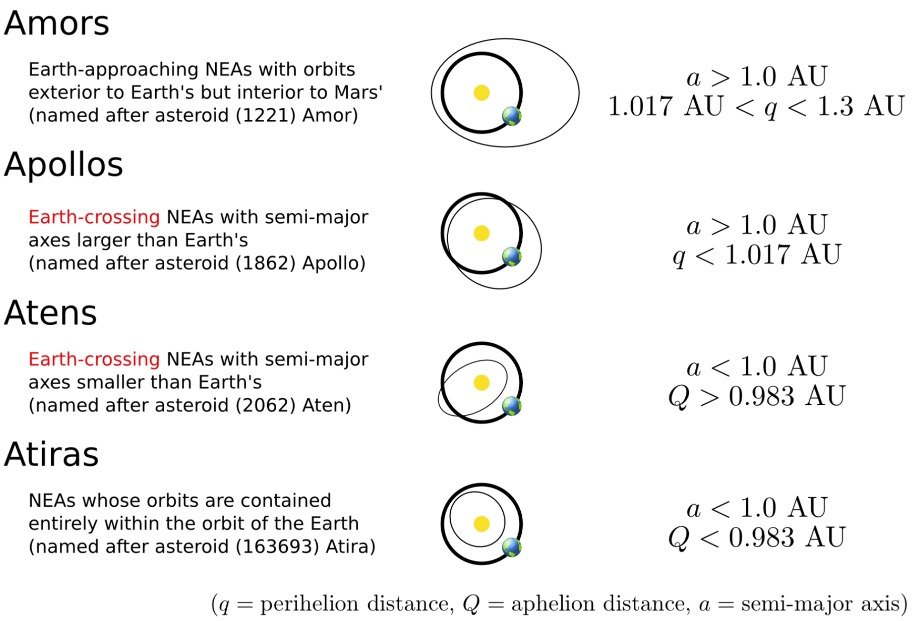

Fig. 2.10: Classification of NEOs based on their orbital configuration with respect to the Earth's one. The limits of 0.983 and 1.017 AU correspond to the minimum and maximum Sun-Earth distance values along the Earth's orbit (credits: https://cneos.jpl.nasa.gov).

$H < 22$, corresponding to a size greater than 140 m, and an Earth's Minimum Orbital Intersection Distance (MOID[11]) less than 0.05 AU. These limits are connected to the degree of threat that PHAs pose to the Earth. They are large enough to survive atmospheric transit without significant deceleration, striking the Earth's surface at orbital speed. In fact, an impact of a 140 m-sized object can have destructive effects on a regional scale, but even an asteroid of 30 m size can pose serious threats to the population of a city, considering that such object is likely to explode in the lower atmosphere prior to impact. The first discovered NEA is (433) Eros, a ~15 km sized asteroid observed in 1898 and with a MOID of 0.15 AU. To date, about 31.5k NEOs have been discovered[12], the majority of them being NEAs with only 119 known NECs. About 850 NEOs have a size greater than 1 km, while ~2.3k are classified as PHAs, 151 of them being greater than 1 km. Figure 2.9 plots the discovery statistics of NEAs, according to the various surveys dedicated to such monitoring.

According to their orbital configuration, NEOs are conventionally classified into four groups, presented in Fig. 2.10, which are:

- *Amors*, with orbits external to the Earth's one but internal to Mars;
- *Apollos*, with Earth-crossing orbits and semi-major axis greater than 1 AU;
- *Atens*, with Earth-crossing orbits and semi-major axis less than 1 AU;
- *Atiras*, whose orbits are confined within the Earth's one.

---

[11] The MOID is the distance between the closest points of the orbits of two bodies.

[12] https://cneos.jpl.nasa.gov/stats/

They are all named after a particular member of the group. The most populated group is the one of Apollos, counting about 56% of currently known NEOs, followed by Amors (36%) and Atens (8%). Only 29 Atiras asteroids are known to date.

2.3.1 Delivery of asteroids to the inner Solar System

The proximity of NEOs to planetary orbits makes them an evolving and short-lived population, limited to some million years of mean lifetime. They are doomed to be captured in Sun-grazing orbits and fall onto it, or to be ejected from the Solar System, while a small fraction of them impact with a terrestrial planet. Therefore, the NEO population has to be continuously replenished mainly from the MAB due to gravitational effects (MMRs) as discussed in Sect. 2.1.5. However, a purely gravitational and collisional replenishment mechanism fails to match observational evidence. For example, it has been proven that the NEO population is in a steady equilibrium for the last 3 Gy (Bottke et al., 2005b; Bottke et al., 2005a), and meteorites are found to have cosmic-ray exposure ages of the order of 100 My. On the other hand, an MMR-only driven delivery of asteroids into the NEO region would account for a perpetually-young population of bodies (Gladman et al., 1997). The strength of such scenario fails to match, by orders of magnitude, the observed flux of NEOs and meteorites. Furthermore, most of the potential parent bodies are observed far from powerful MMRs (Nesvorný et al., 2002), and the disruption of such large bodies should produce many asteroidal familied that are not observed (Nesvorný et al., 2003).

It was indeed found that non-gravitational effects are fundamental in explaining the population of NEO and the meteorite delivery rates to the Earth. The most important are the *Yarkovsky* and *YORP effects*. For a complete review of the topic, the reader can refer to Bottke et al. (2006) and references therein. Figure 2.11 shows a schematic representation of the Yarkovsky effect. In summary, due to the solar radiation heating and the lag (due to thermal inertia) between absorption and anisotropic re-emission of thermal photons on a spinning asteroid, a non-zero total recoil force acts on the body pushing outward its orbit (Opik, 1951). This is called *diurnal Yarkovsky effect*. On the other hand, the seasonal difference in heating between the northern and southern hemispheres of the asteroid causes a thermal force pushing the asteroid orbit inward (*seasonal Yarkovsky effect*). These effects are size-dependent and are relevant for small asteroids, below 10 km in diameter. Farinella et al. (1998) then proposed a delivery mechanism that could match observational evidence. It is assumed that, in a first stage, the Yarkovsky effect slowly acts on asteroids drifting them towards powerful MMRs (mainly 3:1 and ν_6), which therefore deliver these bodies in the NEO region, and eventually some of them (less then 1%) will impact the Earth. That being said, the orbital evolution of such bodies is quite complex, and this mechanism should be regarded as a "highway" for

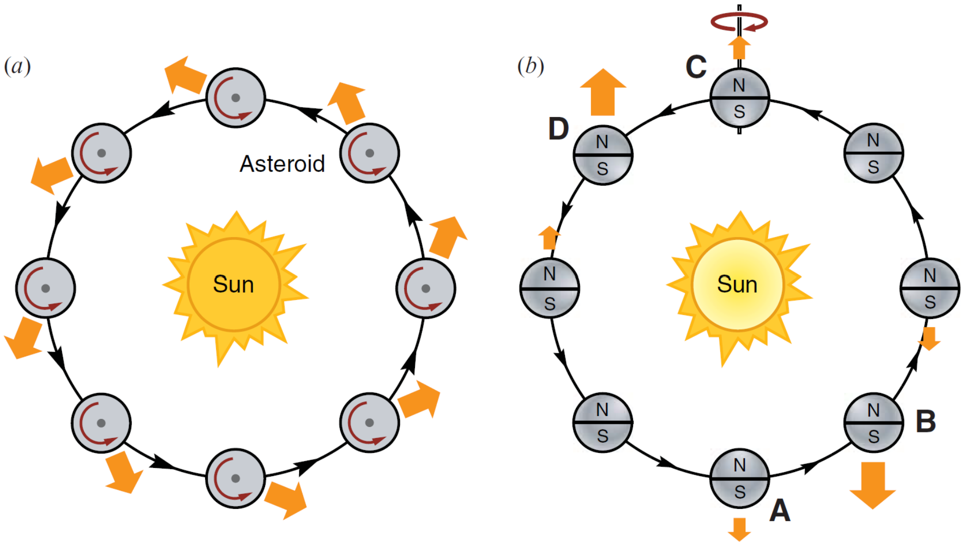

Fig. 2.11: Schematic representation of the diurnal (a) and seasonal (b) Yarkovsky effects (Bottke et al., 2006).

their delivery of NEOs from the MAB to the inner Solar System, while not being the only possible route. The YORP (Yarkovsky–O'Keefe–Radzievskii–Paddack) effect is also important in modelling the variation of spin rates and obliquity of non-spherical asteroids (Rubincam, 2000). This effect combines with the Yarkovsky effect, which drift rates are in fact dependent on the spin rate of the asteroid itself.

2.3.2 NEO impact hazard and mitigation

Major impact events marked the evolutional history of our planet. Evidence of ∼200 impact craters were found on the Earth's surface[13], with ages spanning from the order of 10 ky up to 1 Gy. It is thought that an intense period of asteroid collisions with terrestrial planets occurred between 3.8 and 4 Gy ago, called *Late Heavy Bombardment* (LHB). While representing a controversial topic among the scientific community, evidence of such a catastrophic event can be found on the highly cratered surface of the Moon and other planets such as Mars, while the Earth preserved no trace of those impacts (Gomes et al., 2005). The mass extinction event that occurred at the Cretaceous–Paleogene (K-Pg) boundary, around 66 My ago, is also thought to be linked to a major impact of an asteroid (Alvarez et al., 1980). The cause of this cataclysm is also an argument of debate. While being generally linked to the Chicxulub crater (Schulte et al., 2010), other scenarios were proposed involving, for example, a high volcanic activity during the K-Pg (Keller et al., 2008). However, recent studies seem to strongly support the impact origin of this mass extinction (Hull et al., 2020).

---

[13] `http://www.passc.net/EarthImpactDatabase`

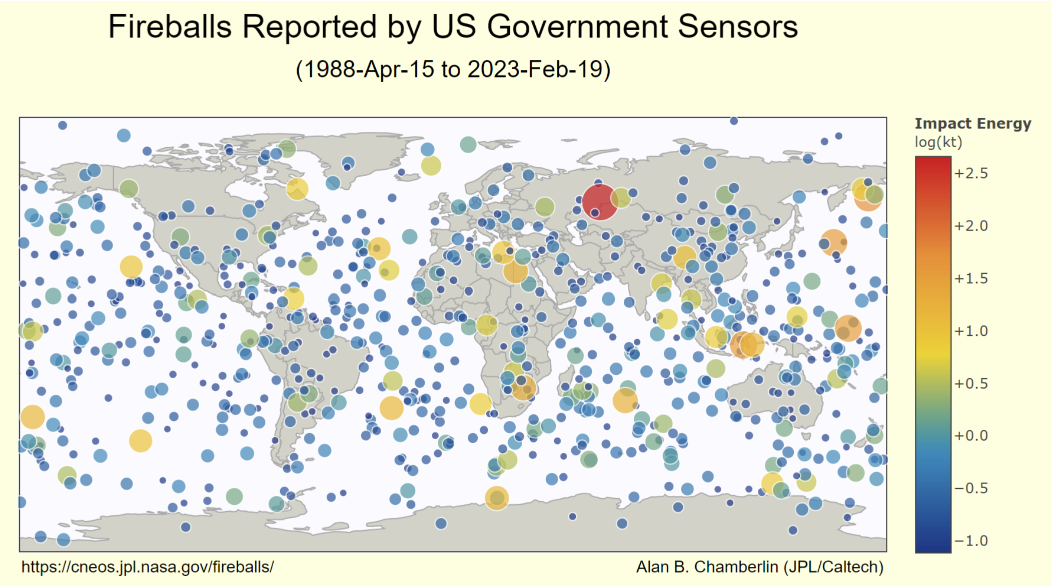

Fig. 2.12: Map of fireball events reported by US Government Sensors since 1998. The size and colour of the circles show the energy of the impact (credits: `https://cneos.jpl.nasa.gov/fireballs/`).

Shifting toward most recent times, the Tunguska (30 June 1908) and Chelyabinsk events (15 February 2013) are the biggest impacts that occurred in the last century. While no records of the Tunguska impact are available, it is strongly believed that this event was caused by an impact 50 m-sized asteroid, destroying an area of more than 2000 km^2 in the Eastern Siberian Taiga (Russia), even if no meteorite was ever found in the area (Carbognani et al., 2023). The Chelyabinsk asteroid was observed entering the Earth's atmosphere on the morning of 15 February 2013, over the southern Ural region in Russia, at a speed of ∼19 km/s (Borovička et al., 2013a). It was a small asteroid with a diameter of about 15 m and released 440 kilotons (TNT equivalent) into the atmosphere, damaging more than 7000 buildings in six nearby cities (Popova et al., 2013; Brown et al., 2013). More than 1000 kg of meteorites were recovered, with a main mass of about 550 kg. Figure 2.12 shows a map of energetic fireballs ($>$ 0.1 kt TNT) observed and reported by US government space-based sensors. Indeed, the biggest red circle represents the Chelyabinsk impact. These sensors detected ∼1000 impacts since 1988, summing up at an average of ∼30 events per year.

It is therefore clear that the study of the NEO population and its evolution is of utmost importance, even beyond the scientific interest. The surveillance of NEOs, together with the tracking of artificial objects (Space Surveillance and Tracking - SST) and space weather forecast, is included in the general framework of *Space Situational Awareness*[14], which is an initiative adopted by the European Space Agency (ESA) dedicated to monitoring hazards from space, determine their risk and mitigate the threat. Meteoroids impacts pose an hazard also for spacecraft operations, especially

---

[14] `https://www.euspa.europa.eu/european-space/space-situational-awareness`

in the long-term perspective (Foschini, 1999; Moorhead and Matney, 2021). As for the most recent example, the primary mirror of the James Webb Space Telescope experienced 19 micrometeoroid hits between February and May 2022, one of which inflicted significant and uncorrectable damage to the instrument (Rigby et al., 2022).

The characterization of the risk posed by asteroids and meteoroids impact is quite peculiar, since it can have a huge spread of possible consequences, from local small damages up to global catastrophic events (Perna et al., 2013). To the purpose of categorizing the impact hazard and enabling clear communication to the public, the *Torino scale* was established (Morrison et al., 2004). It is an integer scale, ranging from 0 to 10, based on collision probability and expected energy release[15]. It is divided into 5 colour zones: white (0 - zero impact probability), green (1 - close encounter with zero level of danger), yellow (2, 3, 4 - deserving attention from the scientific community), orange (5, 6, 7 - probable impact and danger of regional to global damages) and red (8, 9, 10 - almost certain impact, from regional damages to risk for the life on Earth). Other more technical scales were also developed, such as the *Palermo scale*, which is expressed as the 10-base logarithm of the impact probability of the particular NEO with respect to the background (sporadic) impact probability over the considered time interval (Chesley et al., 2002).

The highest value ever in the Torino Scale was reached by (99942) Apophis[16], a PHA initially classified as level 4. It is a 370 m asteroid observed for the first time in June 2004 and, upon discovery, it had a predicted impact probability of 2.7% for April 2029 (Sansaturio and Arratia, 2008). Fortunately enough, further investigations corrected this first estimation, and Apophis was recently removed from the risk table.

2.4 Meteors in the Earth's atmosphere

The term *meteor* refers to the wide range of phenomena occurring as a result of the collision and transit of an object into a planetary atmosphere. The official definition issued by the IAU for the term meteor is: "*[...] the light and associated physical phenomena (heat, shock, ionization), which results from the high-speed entry of a solid object from space into a gaseous atmosphere*"[17]. Meteors can be caused by meteoroids, asteroids or cometary fragments. By convention, a meteor with minimum absolute visual magnitude[18] less than -4 (the average apparent magnitude of the planet Venus) is called *bolide* or *fireball*, or a *superbolide* if less than -17. The following sections will give a short review of the history of meteors' observation, the

---

[15] `https://cneos.jpl.nasa.gov/sentry`

[16] The provisional designation of (99942) Apophis was 2004 MN4.

[17] `https://www.iau.org/static/science/scientific_bodies/commissions/f1/meteordefinitions_approved.pdf`

[18] For meteors, the absolute magnitude system is defined at a reference distance of 100 km and as observed at zenith.

Fig. 2.13: The first photograph of a meteor, taken on 27th November 1885 by the astronomer Ladislaus Weinek in Prague (credits: `https://www.amsmeteors.org/photos/?photo_id=1388`).

concept of meteor showers and the physics of meteor phenomenon. For a complete review on many aspects of meteor science, the reader can refer to Ryabova et al. (2019).

2.4.1 History of meteors' observation

As for the observations of comets' tails, we can find records of meteors' observations dating back at least three millennia ago (Astapovich, 1958). The connection between the meteor phenomena and asteroids, meteoroids and comets was first proposed by Schiaparelli (1867), whereas the link between meteors and the recovery of meteorite fragments is attributed to Chladni (1794). During the last century, meteor science witnessed great advances thanks to precise telescopic observations and systematic surveys carried out by distributed networks worldwide.

The first case of scientific meteor photography dates back almost 140 years, with the first image captured in Prague by the astronomer Ladislaus Weinek on 27th November 1885, reported in Fig. 2.13. The technological advances led to a major breakthrough in 1940, with the introduction of the *rotating disc shutter*[19], which allowed having a relative time reference in the image and therefore enabling the estimation of the meteor speed. The first multi-station systematic observation program was initiated in 1951 at the Ondřejov Observatory of Czechoslovakia,

---

[19] This technique consists in periodically occluding the lens with a rotating disc, which produces dark strikes along the meteor image. Knowing the rotation frequency of the disc and measuring the angular distance between subsequent dark strikes, it is possible to estimate the angular speed of the meteor.

consisting of 10 cameras in double-station observation mode. Observing the same meteor with two or more cameras, deployed at a certain distance (> 10 km) on the Earth's surface, allowed for the first time to reconstruct the three-dimensional path of the event in the atmosphere, thanks to the process of *triangulation*. In 1959, this new technology allowed the recovery of the first "pedigree" meteorite (see Sect. 2.7.1), named *Pribram* (Ceplecha, 1961). This was the first meteorite for which the atmospheric flight was observed by dedicated instruments, providing precise indications about the *preatmospheric orbit* of the meteoroid and the *strewn-field*[20] for meteorite fragments to be found on the ground.

Following the successful example of the Czechoslovakian Fireball Network, now European Fireball Network (Spurný et al., 2017b), many dedicated projects started to realize such observational networks. These projects are known today as *meteor* or *fireball networks*. Since 1980, technological advances allowed switching towards *video observations* at typical frame rates in the range 10–60 Hz, which is optimal for a proper angular sample of the meteor path. Usually, these networks deploy *all-sky cameras*, able to capture the whole observable sky in one frame. It is estimated nowadays that meteor networks cover $\sim$2% of the Earth's surface (Devillepoix et al., 2020).

2.4.2 Meteor showers

Meteor showers are recurring events characterized by a high number of meteoroids impacting the Earth's atmosphere, causing meteors which radiate from a particular region of the sky, called *radiant*, and moving within a narrow range of geocentric velocity at the Earth's position. An example of such events is shown in Fig. 2.14. An important observable of meteor showers is the Zenith Hourly Rate (ZHR), defined as the number of meteors visible by a human observed under perfect sky conditions (corresponding to a limiting visual magnitude of about $+6.5$) reported at the zenith direction. Meteor showers are due to the Earth crossing the orbit of a parent body, in most cases being a comet, which is filled with meteoroids ejected from it and dispersed along its orbit (see Sect. 2.2). This ensemble of meteoroids is called *meteoroid stream*, and the orbits of its members evolve after ejection on their own, driven by both gravitational and non-gravitation effects (see Sect. 2.1.5 and 2.3.1). The study of meteor showers is quite interesting since it provides a way to investigate the characteristics and probe the evolution of meteoroid streams (Ye and Jenniskens, 2022).

Even from historical records, there was already evidence that some periods along the year were characterized by an unusually high rate of meteors observed in the night sky. Hundreds of such records in the Asian literature can be found referring

---

[20] With the term *strewn-field* we refer to the area on the ground delimiting the region in which meteorite fragments are more likely to be found.

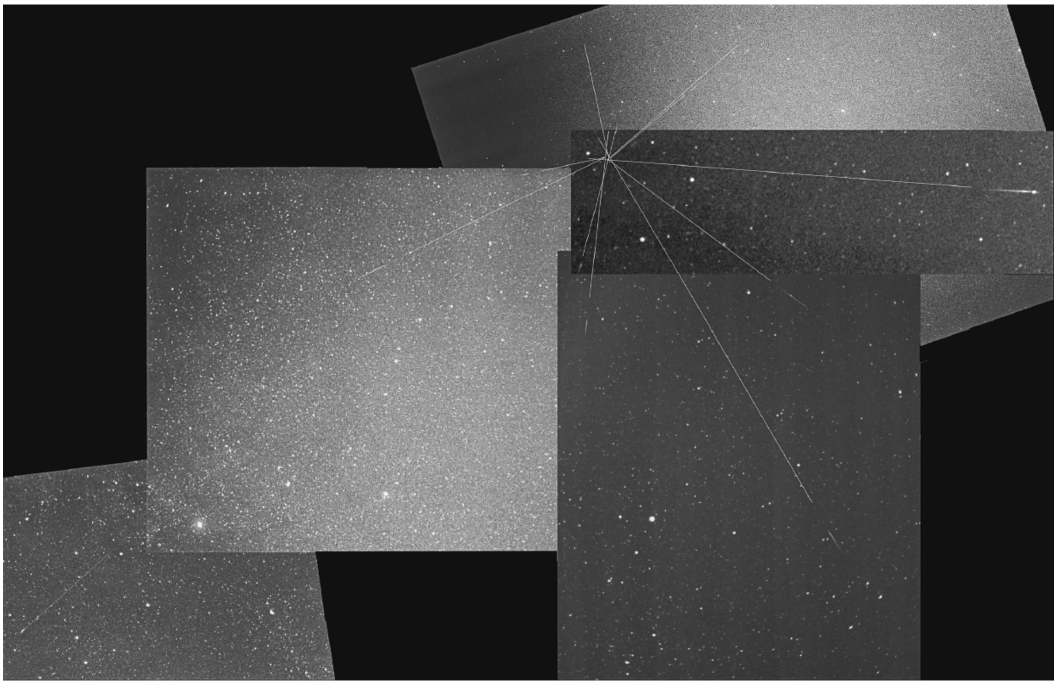

Fig. 2.14: Example of the radiant of a meteor shower: composite image of photographs of the 1985 Draconid outburst by members of the Nippon Meteor Society (Jenniskens, 2007).

to such a phenomenon. The definition of meteor shower is historically related to the concept of radiant. This discovery was made in 1833 by Denison Olmsted (Olmsted, 1834), who noticed that meteors that night were more likely to originate from the direction of the star γ-Leo. He hypothesized that such phenomenology was caused by bodies moving on parallel tracks and entering Earth's atmosphere. The definitive link between meteor showers and their parent bodies was deduced by Schiaparelli (1867), who noticed that the orbits of Perseids, perhaps the most intense meteor shower along the year, were nearly parabolic and very similar to the orbit for comet 109P/Swift-Tuttle, now acknowledged as the parent body for this shower.

The IAU defines meteoroid streams and meteor showers in one overall statement: "*A meteoroid stream is a group of meteoroids which have similar orbits and a common origin; a meteor shower is a group of meteors produced by meteoroids of the same meteoroid stream*". The Meteor Data Center (MDC[21]) is the organization responsible for the official cataloguing and designation of each new meteor shower, and it operates in conjunction with the Working Group of on Meteor Shower Nomenclature of the IAU Commission F1. The MDC operates and maintains the Shower Database (SD), counting to date 110 *established showers*. These are the meteor showers that were extensively observed through time allowing for a detailed characterization of their parameters, and which existence and statistical significance are undoubted. On the other hand, the SD counts 830 showers in its *Working List*. Most of these are *minor showers*, usually observed for a limited time span only and

---

[21] `https://www.ta3.sk/IAUC22DB/MDC2022/`

containing a restricted number of members. Their statistical significance is limited by these conditions, and the actual existence of most of them is to be confirmed by further observation campaigns. The nomenclature rules for meteor showers were changed very recently (Jopek et al., 2023). New meteor showers submitted to the MDC are given a provisional alphanumerical designation, very similar to the one of newly-discovered asteroids (see Sect. 2.1), enclosing the year and half-month of the submission. Once observations and analysis results allow for a new shower to become "established", it is given an official MDC progressive code and an official name[22], usually proposed by the discoverer and approved by the IAU.

For a complete review on the topic of meteor showers and meteoroid streams, the reader can refer to Jenniskens (2007) and Vaubaillon et al. (2019). A *meteor shower calendar* is issued every year by the International Meteor Organization (IMO[23]) and the American Meteor Society (AMS[24]), listing the observation periods and main features of major and minor showers.

2.5 Physics of the meteor phenomenon

This section gives a general overview of the physical processes and governing equations that characterize the hypersonic motion of a meteoroid when colliding and travelling through the Earth's atmosphere. Particular aspects of this phenomenon will be discussed in Sect. 4.2.4, while describing the analysis and interpretation of PRISMA data. For a detailed review of the observational and theoretical works on the subject, the reader can refer to Bronshten (1983), Ceplecha et al. (1998), and Popova et al. (2019).

2.5.1 Phenomenological description

While penetrating the atmosphere, the meteoroid goes through greatly varying environmental and dynamic conditions. The most important processes occurring during the meteor phenomenon are: deceleration due to atmospheric drag, *ablation* (loss of mass), emission of light, generation of electric charge (ionization) and sonic/shock waves. Their relative significance changes as a function of the meteoroid and atmospheric properties, governing its evolution. For example, not all bodies are large enough to produce visible light during their transit. If the size of the meteoroid is less than $\sim$10 μm (IDP - interplanetary dust), it is generally assumed that it is significantly slowed down in the upper atmosphere ($h > 200$ km) before triggering the ablation and consequently the light emission. The overall phenomenology of a

---

[22] Names of meteor showers usually refer to the nearest constellation to the radiant direction.

[23] `https://www.imo.net/resources/calendar/`

[24] `https://www.amsmeteors.org/meteor-showers/meteor-shower-calendar/`

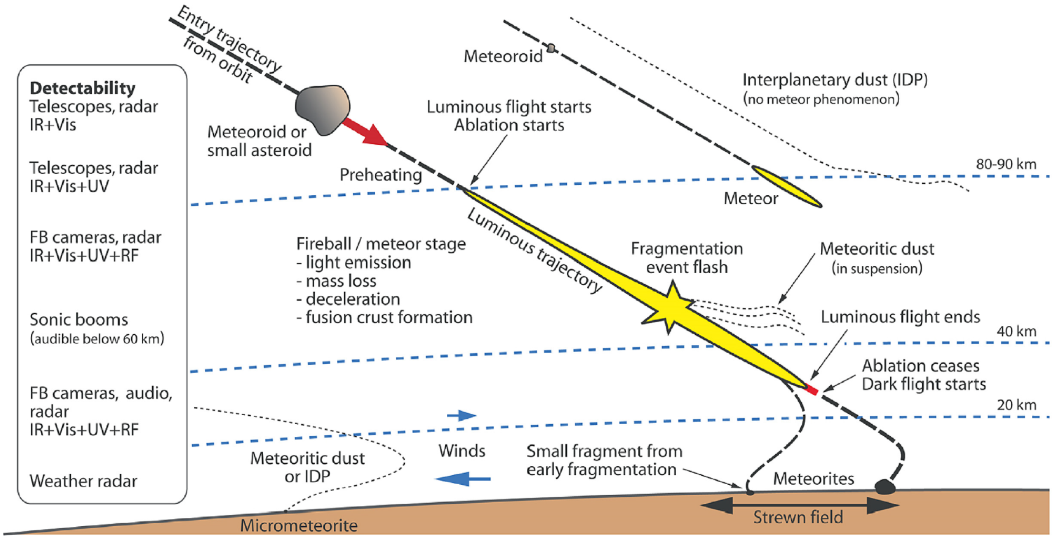

Fig. 2.15: Graphical representation of the several stages of meteor phenomenon due to a meteoroid entering the Earth's atmosphere (Moilanen et al., 2021).

meteor event is depicted in Fig. 2.15, and it can be summarized in the following stages (Ceplecha et al., 1998):

1. *Orbital motion*: due to collisional and/or gravitational perturbations (see Sect. 2.3.1), the meteoroid is delivered toward the inner Solar System and eventually collides with the Earth. With respect to an Earth-fixed reference frame, the range of impact speed for a meteoroid coming from the Solar System is approximately limited within 11.1 and 72.8 km/s. The lower limit V_m corresponds to the impact of a meteoroid in a prograde orbit, which approaches the Earth's orbit with a relative speed close to zero. The gravitation field of the Earth accelerates the body, which will have a speed module at 100 km altitude given by energy conservation as:

   $$\frac{1}{2}MV_m^2 = \frac{GM_0M}{R_0 + 100\ \text{km}} \quad \rightarrow \quad V_m = \sqrt{\frac{2GM_0}{R_0 + 100\ \text{km}}} \simeq 11.1\ \text{km/s}\,, \tag{2.14}$$

   where G is the gravitational constant, M is the meteoroid's mass, M_0 and R_0 are the mass and radius of the Earth, respectively. The upper limit of $V_M = 72.8$ km/s corresponds to a meteoroid impacting the Earth with a retrograde orbit at its perihelion ($V_0 \sim 30.3$ km/s) with a speed close to the parabolic limit of 42.5 km/s (see Chap. 7), in a head-to-head collision.
2. *Preheating*: for altitudes between 100 and 300 km from the ground, the atmosphere is still very rarefied and air molecule impacts causes the heating of the surface of the meteoroid only. The surface temperature rises quite rapidly, while the inside of the meteoroid remains practically unheated, due to the limited duration of this stage, usually $\lesssim 1$ s. As already mentioned,

smaller bodies can be significantly decelerated at these altitudes and may not enter the next phase. Otherwise, heat conductivity (for larger bodies) and radiation transfer (for smaller bodies) contribute to the heating of the meteoroid's interior.

3. *Ablation*: this is the most important stage of the atmospheric flight of the meteoroid. During the preheating, the temperature can rise as high as few thousand degrees, and the meteoroid material starts to melt. Then, evaporation starts when reaching ∼2500 K. Consequently, light emission is due to the ionization and electronic transitions of elements from both the surrounding air molecules and the meteoroid's material itself, together with black-body radiation. In this stage, the energy loss due to ablation (mass loss) competes with the one due to deceleration (velocity loss), and the fate of the meteoroid depends on the balance between these two processes (see Sect. 2.5.3).
4. *Dark Flight*: if the body is able to decelerate down to ∼4 km/s in the lower atmosphere ($H < 25$ km) preserving a significant mass from ablation, this residue will continue travelling towards the ground without emitting light. This is because there is no longer enough kinetic energy to either evaporate or melt the meteoroid's material. The body decelerates until completely loosing its cosmic speed, and free-fall begins due by Earth's gravity. In these conditions, the meteoroid's motion is quite sensitive to the state of the atmosphere, in particular to the wind's intensity and direction in the troposphere that modifies the free-fall trajectory of the residue. Impact velocities on the ground can vary in the order of 10–100 m/s, depending on the size of the fragments.

In this summary, we pictured the phenomenology often referred to as *single-body theory*, which does not account for *fragmentation* (Babadzhanov, 2002). On the other hand, it is quite common for the meteoroid to undergo different fragmentation mechanisms throughout the whole flight. Fragmentation can be triggered already in the preheating phase, when the surface tension reaches the internal strength of the material (named *spallation*). Major fragmentation events can occur in correspondence with a sudden brightening of the meteor (named *meteor flares*). This usually creates inconsistency between theoretical models and observational results, complicating the interpretation of the data of observed meteors and biasing the derived physical parameters. Dedicated fragmentation models can be applied to account for this phenomenon, but their actual usage is limited to a few selected cases to date (Popova et al., 2019).

Also, we have neglected the possibility of a fifth phase, *i.e.*, the formation of an *impact crater*. This happens when the body is massive enough to pierce the Earth's atmosphere without significant deceleration, impacting the ground at cosmic speed. The size of the impact crater can be as large as 20 times the size of the meteoroid itself (Flamini et al., 2019).

2.5.2 Flow regimes

In the range of meteor ablation (130 to 20 km), the atmospheric density varies by several orders of magnitude, affecting the energy and momentum input that the meteoroid receives and changing the conditions of the interaction. In other words, the flow regime of the hypersonic motion change mainly as a function of the altitude, the meteoroid speed and dimension, determining the dynamic of the fall, and in particular the heat transfer and ablation processes. The modern classification of hypersonic flow regimes was introduced by Tsien (1946), discussed and refined after by Bronshten (1983). This classification is based upon an adimensional parameter, named *Knudsen number* (Kn), which is defined as the ratio between the mean free path of the molecules in the medium λ and the characteristic dimensions of the body L:

$$Kn = \frac{\lambda}{L}\,, \tag{2.15}$$

where L is often assumed as the equivalent diameter D. The mean free path can be given as:

$$\lambda = \frac{2\mu}{\rho_a \bar{v}}\,, \tag{2.16}$$

where μ is the dynamic viscosity ($[\mu] = \mathrm{M\,L^{-1}\,T^{-1}}$), ρ_a is the density of the medium (air) and $\bar{v}$ is the average molecule speed, that is expressed for a Maxwell–Boltzmann distribution as:

$$\bar{v} = \sqrt{\frac{8RT_a}{\pi M}}\,, \tag{2.17}$$

being R the molar gas constant, M the average molar mass and T_a the absolute temperature of atmospheric air. That being said, the Knudsen number can be given as:

$$Kn = \frac{\mu}{\rho_a L}\sqrt{\frac{\pi M}{2RT_a}} = \frac{Ma}{Re}\sqrt{\frac{\gamma\pi}{2}} \sim \frac{Ma}{Re}\,, \tag{2.18}$$

where the term containing the heat capacity ratio γ is often neglected. Equation 2.18 tells us that the Knudsen number is a function of two other adimensional numbers, well known in fluid dynamics, being the *Reynolds* and *Mach numbers*:

$$Re = \frac{\rho_a V L}{\mu} \quad , \quad Ma = \frac{V}{c_s}\,, \tag{2.19}$$

being V the stream flow velocity, *i.e.*, the meteoroid speed and c_s the speed of sound in air:

$$c_s = \sqrt{\frac{\gamma R T_a}{M}}\,. \tag{2.20}$$

Depending on the value of the Knudsen number, there are four possible flow regimes according to Tsien (1946):

- *Free-molecular regime* ($Kn > 10$): the mean free path is substantially larger than the size of the body, and the flow can be considered as single molecules moving in straight lines, with negligible inter-particles interactions, impacting the meteoroid's surface and transferring energy and momentum. Several processes take place, such as *physical* or *chemical sputtering*, that is the removal of particles from the surface of the meteoroid due to the air molecules colliding with an energy greater than the bounding energy, or chemically reacting with the surface. This regime is typical of high-altitude meteors caused by small meteoroids. Single incident particles also heat the surface, and this flow regime is characteristic of the preheating phase (see Sect. 2.5.1).
- *Transition regime* ($Re^{-1/2} < Kn < 10$): the mean free path and the meteoroid's dimensions are comparable, and inter-particle interactions start to be significant. In this regime, the meteoroid becomes shielded from the incoming flow by a *vapour cap*, which forms as a result of sputtering and/or evaporation. This layer usually exceeds the air pressure and start expanding, and its outer layers attain hypersonic speed.
- *Slip-flow regime* ($10^{-2}Re^{-1/2} < Kn < Re^{-1/2}$): in these conditions, the tangential component of the flow near the body becomes small but finite, and there is no adhesion of the gas to the meteoroid's surface. A *shock layer* can be formed in this regime, due to the expansion and drag of the vapour cap previously formed.
- *Continuous-flow regime* ($Kn < 10^{-2}Re^{-1/2}$): the size of the body largely exceeds the mean free path of the air's molecules, that can be regarded as a continuous medium. These are the conditions for classical ablation, which is usually characterized by the formation of a strong shock-wave front preceding the meteoroid's motion towards lower layers of the atmosphere.

The boundary of these four regimes are semi-empirical, and different authors use different values. The classification reported here considers the effects of viscous forces, and the actual conditions for each event are taken into account thanks to the scaling with respect to the Reynolds number. Other boundary values often used are 10, 0.1 and 0.01 respectively, and sometimes the slip-flow regime is ignored and included within the transitional one. Also, these considerations can be modified due to the presence of the vapour cap, shielding the meteoroid from the flow and virtually increasing its cross-section and therefore the characteristic dimension L in the definition of Kn. Bronshten (1983) proposed a different expression for the Knudsen number, usually refereed as the *modified Knudsen number* (Kn_r), which accounts for the thermal velocity of reflected (evaporated) molecules from the meteoroid's surface, rather than the meteoroid speed itself:

$$\bar{v}_m = \sqrt{\frac{8RT_m}{\pi M}} \quad \rightarrow \quad Kn_r = \left(\frac{\bar{v}_m}{V}\right) Kn = \frac{1}{Re}\frac{\bar{v}_m}{c_s}\,, \tag{2.21}$$

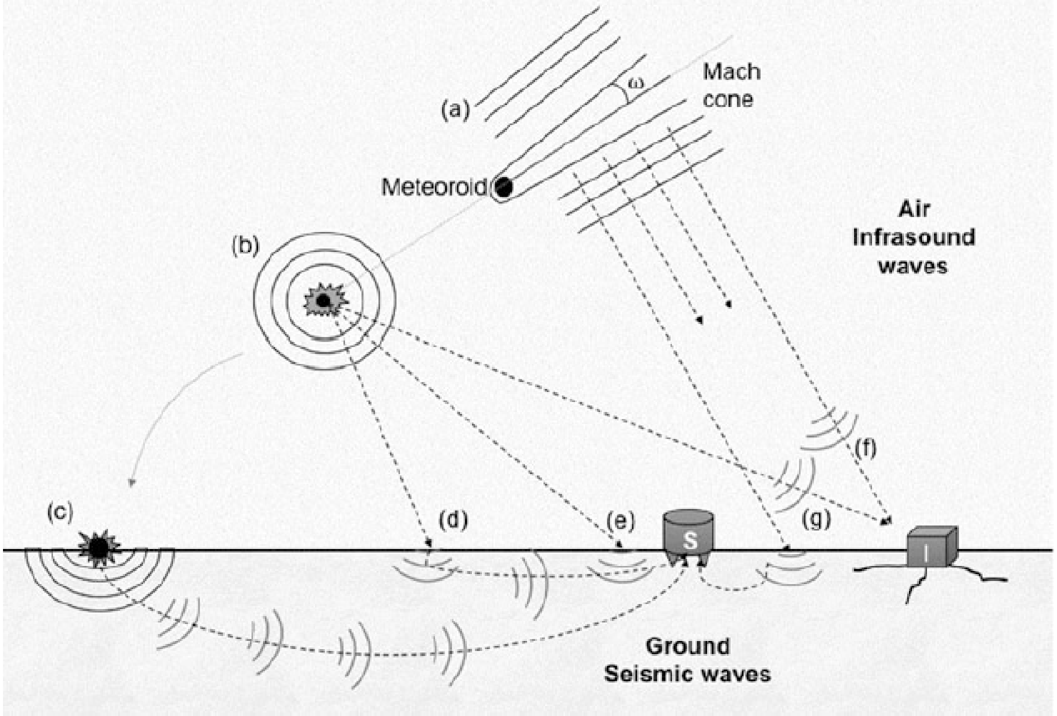

Fig. 2.16: Schematic diagram of meteor-generated waves. Shock waves are generated by the hypersonic motion of the meteoroid (a) or during meteoroid fragmentation (b). Seismic waves are generated during meteorite impact (c) or by the impact of shock waves and propagation in the ground (d,e). Due to the high Mach number values (35–270), the Mach cone aperture ω is very small and the shock wave is almost cylindrical (Trigo-Rodríguez et al., 2017).

where T_m is the temperature of the meteoroid's surface and is usually assumed to be in the range 3500–5000 K (Borovicka, 1993; Borovicka, 1994).

The usage of Kn versus Kn_r to evaluate the flow regime is questionable, since we cannot have prior and reliable information about the presence of such vapour cap from optical observations only. This is not the case if we can detect the shock wave. In particular, infrasound and seismic detectors can capture the low-frequency wave components generated by the shock, which are able to propagate for very long distances through the atmosphere (Edwards, 2009; Silber and Brown, 2014; Trigo-Rodríguez et al., 2017). The infrasound waves generated by the impact of Chelyabinsk (see Sect. 2.3.2) circled the globe twice and generated detections as far as 85000 km on 20 stations of the global International Monitoring System (Le Pichon et al., 2013). Infrasound signatures can be generated also by other meteor phenomena, such as abrupt fragmentation events (see Fig. 2.16). Moreno-Ibáñez et al. (2018) used optical and infrasound observations of the same bolides (24 cm-sized meteoroids) and concluded that the vapour cap and shock wave formation is indeed possible in slip-flow and continuous regime, supporting the flow regimes definition by Bronshten (1983).

2.5.3 Meteor's equations

Within the physical description of the meteor phenomenon, the first important effect to account for is the deceleration of the meteoroid due to atmospheric drag. The *deceleration equation* can be deduced from the momentum balance. The momentum lost by the meteoroid is given as $M\mathrm{d}V$ and it is proportional to the momentum of air impinging at speed V of the meteoroid on its section S, perpendicular to incoming flow:

$$M\mathrm{d}V = -\Gamma\,(S\rho_a V\mathrm{d}t)\,V\ , \tag{2.22}$$

where the term within parenthesis is the mass of impinging air with density ρ_a and Γ is the *drag coefficient* (also denoted as $C_D = 2\Gamma$). Equation 2.22 can also include the gravitational term, but this is often neglected compared to the range of entry velocity of meteoroids:

$$M\frac{\mathrm{d}V}{\mathrm{d}t} = -\Gamma S\rho_a V^2 + Mg\ . \tag{2.23}$$

This last term is important only when the meteoroid is significantly decelerated at the end of its trajectory in the atmosphere, so it is usually included during the computation of the dark flight. This also affects the inclination angle of the meteoroid[25] γ, which evolution through time can be given as:

$$MV\frac{\mathrm{d}\gamma}{\mathrm{d}t} = Mg\cos\gamma - \frac{MV^2}{R_0}\cos\gamma - \frac{1}{2}C_L S\rho_a V^2\ , \tag{2.24}$$

including also the terms due to Earth's curvature and lifting force, where C_L is the *lifting coefficient*. Alongside these two equations, the altitude of the meteor as a function of time is simply given as:

$$\frac{\mathrm{d}H}{\mathrm{d}t} = -V\sin\gamma\ . \tag{2.25}$$

The most relevant unknown in these equations is the value of Γ (apart from C_L). As discussed in Sect. 4.2.5, its value cannot be constrained directly from observations, forcing us to make some assumptions about it. The drag coefficient varies as a function of the flow conditions, mostly according to Re and Ma numbers, and is also dependent upon the shape of the body. This is the second most problematic aspect, *i.e.*, we have little to no evidence to infer the shape of the body and therefore to compute S as a function of M. From direct imaging of asteroids, we know that they can have greatly varying and non-spherical shapes. Also, the shape can be modified during atmospheric flight due to anisotropic ablation of the body. Section 4.2.5 will present a more detailed analysis of these problems.

---

[25] The inclination γ is defined as the angle between the meteoroid's trajectory and the local horizon.

The fourth equation is the *heat balance equation*, given as (Popova et al., 2019):

$$\Lambda\frac{S\rho_a V^3}{2} = A\epsilon\sigma_b(T_m^4 - T_a^4) + Mc\frac{\mathrm{d}T_m}{\mathrm{d}t} - Q\frac{\mathrm{d}M}{\mathrm{d}t}. \tag{2.26}$$

The left side of the equation represents the energy flux received by the meteoroid from impacting air molecules, where Λ is the *accommodation coefficient* (or *heat transfer coefficient*, also denoted as C_H) and it determines the fraction of incoming energy flux transferred to the meteoroid's section S. The first term of the right side is the radiative cooling given by the Stefan-Boltzmann law of black-body emission, where A is the meteoroid's outer surface, ϵ is the emissivity and σ_b is the Stefan-Boltzmann constant. The second term is the heat consumed for the heating of the meteoroid, where c is the bulk specific heat. Finally, the last term is the heat spent to melt or evaporate the meteoroid's material, and Q is the *latent heat of vaporization*. Depending on the particular application, Eq. 2.26 can be modified by adding terms, for example due to solar radiation absorption or sputtering, relevant for small particles, or removing them if negligible. For larger bodies, the received energy flux exceeds the heating and radiative cooling terms and contributes almost only to mass loss through ablation. This regime is called of *intensive evaporation* and it corresponds to altitudes of 110–130 km for cm-size meteoroids. For such regime, Eq. 2.26 is reduced to the *ablation equation*:

$$\frac{\mathrm{d}M}{\mathrm{d}t} = -\frac{\Lambda}{2Q}S\rho_a V^3\ . \tag{2.27}$$

If we divide Eq. 2.27 to Eq. 2.23 (neglecting the gravitational term) we obtain the following:

$$\frac{\mathrm{d}M}{M} = \frac{\Lambda}{2\Gamma Q}V\mathrm{d}V\ , \tag{2.28}$$

where we can define the *ablation coefficient* as a combination of the accommodation and drag coefficients and the latent heat of vaporization:

$$\sigma = \frac{\Lambda}{2\Gamma Q}\ . \tag{2.29}$$

Equation 2.28 provides a physical interpretation of the ablation coefficient as:

$$\sigma = \frac{\delta M}{MV\delta V} \propto \frac{\delta M/M}{\delta V^2}\ , \tag{2.30}$$

i.e., it represents the balance between the (relative) ablation to the deceleration term in the overall kinetic energy loss. Equation 2.28 can be easily integrated as:

$$\int_{M_\infty}^{M}\frac{\mathrm{d}M}{M} = \int_{V_\infty}^{V}\mathrm{d}V\sigma V \quad\rightarrow\quad M = M_\infty\exp\left\{\frac{1}{2}\sigma\left(V^2 - V_\infty^2\right)\right\}\ , \tag{2.31}$$

having assumed that the ablation coefficient is constant through the flight. This particular assumption will be used regarding all other parameters in solving the set of differential equations for the meteor's dynamic, and it is often referred to as *constant-parameters flight model*. In Eq. 2.31, M_∞ and V_∞ are the preatmospheric mass and velocity, respectively. This notation will be widely used in the text to indicate the unperturbed physical quantities, before the impact with the Earth's atmosphere.

Finally, a fifth equation is adopted to model the evolution of the meteor's brightness I as a function of the loss of kinetic energy $K = \frac{1}{2}MV^2$:

$$I = -\tau \frac{\mathrm{d}K}{\mathrm{d}t} = -\tau \left(\frac{V^2}{2} \frac{\mathrm{d}M}{\mathrm{d}t} + MV \frac{\mathrm{d}V}{\mathrm{d}t} \right) = -\tau MV \left(1 + \frac{\sigma V^2}{2} \right) \frac{\mathrm{d}V}{\mathrm{d}t} \,, \tag{2.32}$$

having introduced Eq. 2.28 and where τ is the *luminous* efficiency, *i.e.*, the fraction of kinetic energy converted to light in the wavelength band of our observations. Both values for σ and τ coefficients can be deduced from optical observations, if an independent measure of the deceleration and magnitude of the meteor is available, as discussed in Sect. 4.2.4.

2.6 Meteorites

The portions of meteoroids that survive the ablation phase of the atmospheric transit and eventually fall onto the ground are called *meteorites*. In case a meteorite is recovered after the meteoroid entry was appropriately observed and documented, it is called *fall*. On the other hand, a *find* is a meteorite specimen that cannot be definitively linked with an observed meteor and lacks basic and reliable data about it, such as the date of fall. Meteorites are usually named after their place of fall (or find), *i.e.*, cities or geographical features, except for meteorites collected in desert areas which are also given an incremental number or prefix, usually consisting of a 3–6 digit code, to the purpose of distinguishing different specimens recovered in the same area.

The Meteoritical Society[26] is the international organization in charge of the official cataloguing and nomenclature of meteorites, through its *Nomenclature Committee*. A rigorous and unique naming system for meteorites is needed to prevent confusion in the scientific literature and to link every specimen to a well-documented discovery, find or fall. New meteorites' names are periodically published in the *Meteoritical Bulletin* (Gattacceca et al., 2022) and online in the *Meteoritical Bulletin database*[27]. A specimen can be officially recognized as a meteorite only after approval from this organization, which certifies it when a name is submitted to the Nomenclature Committee including the following: the location of the fall or find, preferably as geographic coordinates; the circumstances of the recovery; the total

---

[26] `https://meteoritical.org/`

[27] `https://www.lpi.usra.edu/meteor/`

	Total	Find		Non-A/NWA		Fall	
Chondrites							
– Carbonaceous	3005	2953	(98.3%)	394	(13.1%)	52	(1.7%)
– Enstatite	666	649	(97.4%)	114	(17.1%)	17	(2.6%)
– Ordinary	60601	59640	(98.4%)	13271	(21.9%)	961	(1.6%)
— H	26992	26598	(98.5%)	6942	(25.7%)	394	(1.5%)
— L	25528	25074	(98.2%)	5417	(21.2%)	454	(1.8%)
— LL	8101	7994	(98.7%)	862	(10.6%)	107	(1.3%)
– Ungrouped	97	90	(92.8%)	41	(42.3%)	7	(7.2%)
Achondrites							
– Primitive	347	344	(99.1%)	43	(12.4%)	3	(0.9%)
– Differentiated	3699	3611	(97.6%)	471	(12.7%)	88	(2.4%)
— HED	2767	2697	(97.5%)	285	(10.3%)	70	(2.5%)
— Stony-Irons	485	474	(97.7%)	166	(34.2%)	11	(2.3%)
— Irons	1359	1310	(96.4%)	1021	(77.9%)	49	(3.6%)
— Lunar	613	613	(100%)	147	(24.0%)	0	(0%)
— Martian	349	344	(98.6%)	59	(16.9%)	5	(1.4%)
– Ungrouped	140	139	(99.3%)	20	(14.3%)	1	(0.7%)
Unclassified	6843	6800	(99.4%)	1356	(19.8%)	43	(0.6%)

Tab. 2.1: Number of meteorite specimens listed in the Meteoritical Bulletin Database updated to 19 March 2023. The columns give the total number and percentage of meteorites, find, non-desertic (Antarctica or North-West Africa) and fall specimens in each class (–) or group (—).

known mass (or weight, TKW) and the number of recovered pieces; an authoritative classification; the location of the main mass[28]. Moreover, a *type specimen* must be deposited in a official repository, that is an institution recognized and approved by The Meteoritical Society which is able to ensure its long-term preservation. The type specimen must be of at least 20% of the recovered mass, with a minimum of 20 g.

A complete review on the topic of meteorites analysis can be found in Lipschutz and Schultz (2007), Grady et al. (2014), and Krot et al. (2014), and reference therein. In the following, I give a short summary of meteorite classification and the main aspects of their analysis.

2.6.1 Meteorite classification

The work of classification of such a huge collection of meteorites is fundamental to understand the linkage between properties of collected meteorites and the population of NEOs and asteroidal families. The Meteoritical Bulletin database counts ~71k meteorites, as updated to 19 March 2023. Table 2.1 presents the overall statistics of catalogued meteorites, updated to 19 March 2023 and separated according to

---

[28] https://www.lpi.usra.edu/meteor/docs/nc-guidelines.pdf

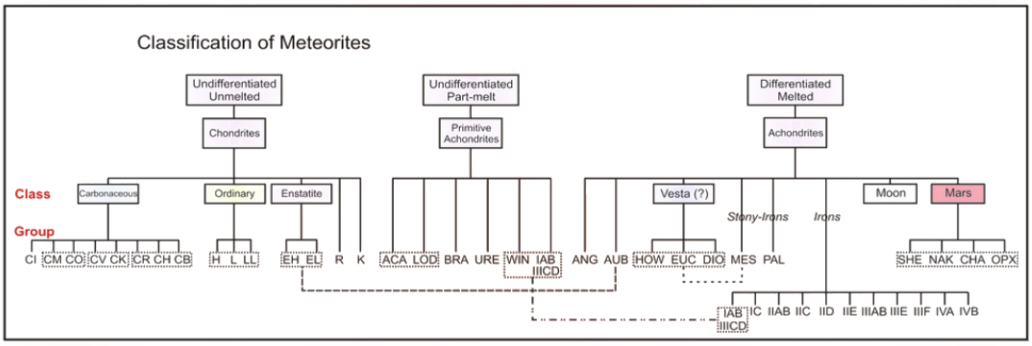

Fig. 2.17: Schematic classification of meteorites, highlighting the main groups of each class. Dashed boxes and lines indicate clans or supergroups of meteorites and their association within different groups (Grady et al., 2014).

the main classes and groups. From these data, it is evident that the vast majority of meteorite samples are indeed finds, with an average fraction of about 98%. Only ∼2% of the total are falls, for a total of about 1.2k specimens. This heavy unbalance is even worse if we consider that approximately 80% of finds were recovered in hot and cold deserts. In fact, the vast majority of meteorites in our collections comes from dedicated expeditions in the Antarctic continent and North-West Africa (NWA) deserts. The environment of such hostile places is indeed favourable for the recovery of meteorites. Deserts offer a predominantly flat morphology and high-contrast background over which spotting meteorites is particularly easy, and expeditions in these areas are quite fruitful in this regard. Moreover, the terrestrial weathering of meteorites in a desert environment is quite slow and accumulation processes can occur in the Antarctic continent, due to both the topography and dynamic of the ice sheet. Regions that are interested by a particularly high number of meteorites recovery are named *Dense Collection Areas* (DCAs) and are also monitored and listed by The Meteoritical Society[29].

Various classification schemes were proposed over time. Concerning the chemical composition, most of them agree with the distinction between *stony meteorites*, mainly composed of silicate minerals, and *iron meteorites*, largely or fully made of metallic iron and nickel. Some classification schemes also allow for the *stony-iron meteorites* class. Furthermore, meteorites can be divided into two main types: *unmelted* (undifferentiated) and *melted* (differentiated). Specimens fitting in the first class are addressed as *chondrites* and are stony meteorites, and those categorized into the melted class are called *achondrites*. The partially-melted class of *primitive achondrites* falls in-between chondrites and achondrites. These three big clusters are further divided into classes and groups, and a schematic classification scheme is presented in Fig 2.17. This scheme is not rigid, since new groups and sub-groups of meteorites are frequently discovered, neither fully comprehensive. To date, more than 200 meteorite specimens do not fit in any of the proposed classes.

---

[29] `https://www.lpi.usra.edu/meteor/DenseAreas.php`

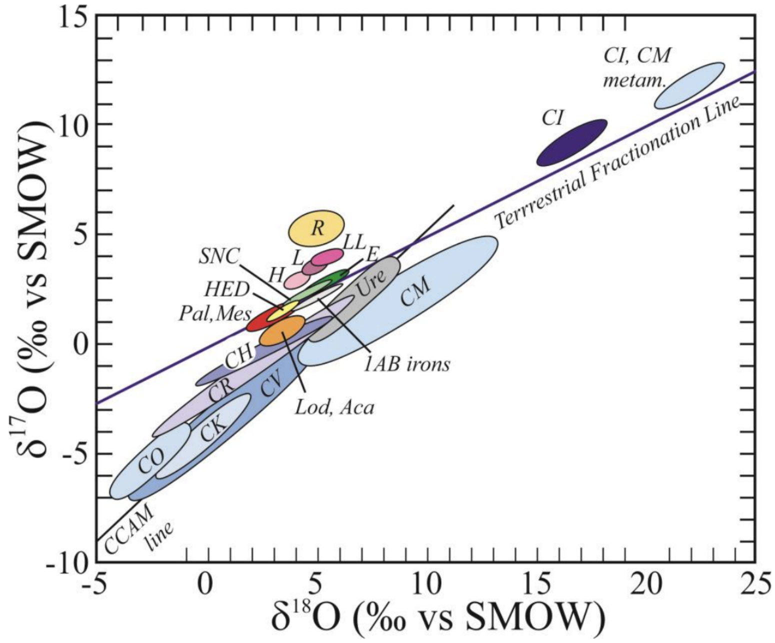

Fig. 2.18: Oxygen isotope fields in the δ^{17}O vs δ^{18}O plot for different meteorite types. It is worth noticing that almost all carbonaceous chondrite groups are distributed along a line with slope ~1 and named *Carbonaceous Chondrite Anhydrous Minerals* (CCAM) line, being evidence of preterrestrial aqueous alteration of hydrolysis of this class (Sharp, 2017).

Primary classification parameters of meteorites are based on the bulk composition. Each meteorite group has a specific compositional pattern, usually expressed as ratio between concentrations of various elements with different volatility. One of the most important discriminants is the *bulk oxygen isotopic composition*. The three stable isotopes of oxygen, being ^{16}O (99.756%), ^{17}O (0.039%) and ^{18}O (0.205%), are fractioned by any mass-dependent physical or chemical process, increasing or decreasing their concentration ratios. These are usually expressed as δ ratios normalized to ^{16}O concentration in Standard Mean Ocean Water (SMOW). Data from terrestrial samples defines the Terrestrial Fractioning Line (TFL), with a 0.5 slope on the δ^{17}O vs δ^{18}O plot. Figure 2.18 plots the distribution on this plane of meteorite groups, each one occupying different and distinct regions. This peculiar result is interpreted as due to different groups of meteorites having formed in different regions of a significantly inhomogeneous solar nebula.

Other classification parameters are, among all: the *oxidation state*, that is, the distribution of iron between Fe (+0, Fe-Ni metal and sulfides), Fe II (+2, silicates) and Fe III (+3, oxides); the *petrologic type* (see Sect. 2.6.2); the degree of *shock metamorphism* caused by asteroid impacts and observed in olivine and plagioclase, referred to as *shock stage* from S1 (unshocked) to S6 (fully shocked and melted); the degree of *terrestrial weathering*, especially for finds that experiences significant alterations during the terrestrial age and expressed as a letter from A, minor rustiness, to E, evaporite minerals visible to the naked-eye.

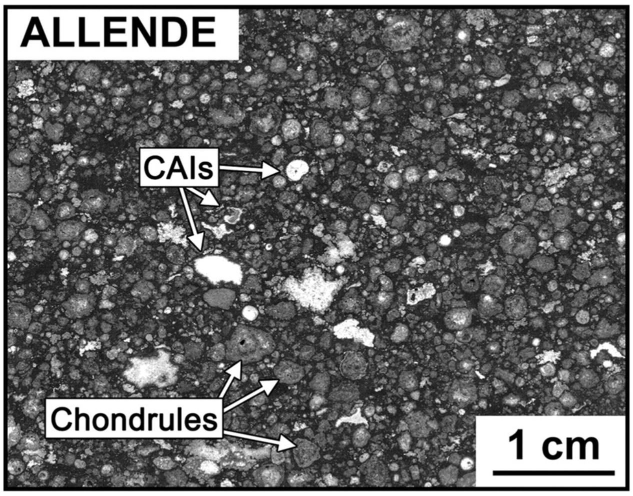

Fig. 2.19: A cut surface of the Allende meteorite (CV3) with highlighted three chondrules and CAIs included in the matrix (MacPherson and Boss, 2011).

2.6.2 Chondrites

Chondrites are mixtures of sub-μm to cm-sized dust, grains and particles of rock and metal. They are the oldest rocks in our collections, having formed approximately 4.5 billion years ago at the very birth of the Solar System. Concentration ratios of non-volatile elements in chondrites are similar to those remotely estimated in the Sun's photosphere. Therefore, chondrites have been thought to be representative of the composition of the protoplanetary disk from which the planets formed. Chondrites are very heterogeneous in their physical and chemical characteristics, and mainly consist of four major components, which are chondrules, refractory inclusions, metallic Fe and Ni and fine-grained matrix material. An example of chondrules and refractory inclusions is shown in Fig. 2.19 for the Allende meteorite.

Chondrules are the most abundant components of chondrites and also their dominant structural feature, usually accouting up to 80% of their volume. Chondrules are submillimeter-sized, igneous[30] spherules mostly made of ferromagnesian silicate minerals, olivine and pyroxene[31]. Therefore, it is believed that they represent the most abundant components of the early Solar System during planetesimal accretion, as free-floating molten droplets in the solar nebula (Jones, 2012). Links between asteroidal population and chondrites also suggest that chondrules are abundant in the inner MAB, so that terrestrial planets may have formed from chondritic material. Evidence on their compositions compared to laboratory experiments shows that chondrules experienced heating events up to peak temperatures of 1500–2500 °C and then rapidly cooled, for a very limited time of the order of minutes to hours (Connolly et al., 2006). For a complete review about the current knowledge on

---

[30] An igneous rock is one that was melted and subsequently cooled.

[31] Olivine is a magnesium iron silicate $(Mg,Fe)_2SiO_4$. Pyroxenes is a group of inosilicate minerals $XY(Si,Al)_2O_6$, where X can be Ca, Na, Fe II or Mg, and Y are ions of Cr, Al, Mg, Co, Mn, Sc, Ti or V.

chondrules and hypothesis on their link to formation, evolution and chronology of the protoplanetary disk, the reader can refer to Connolly and Jones (2016).

Refractory inclusions are a minor but important constituent of chondrites. As their name suggests, they are sub-mm to cm-sized clasts particularly rich in non-volatile (refractory) elements, such as Ca and Al, and their mineralogy is quite distinct to other chondritic components. As a matter of fact, the vast majority of them are called *Calcium-Aluminium rich Inclusions* (CAIs). They appear to be the oldest and more primitive component of chondrites (4.56 Gy) and show an unusual isotopic composition, suggesting an origin from presolar dust (MacPherson, 2014). Like chondrules, also refractory inclusions are thought to have undergone significant heating events, probably followed by more prolonged cooling periods.

Chondrules and refractory inclusions are submerged in a fine-grained matrix, cementing the chondritic components together. This matrix is richer in volatiles with respect to chondrules and inclusions, and therefore is supposed to have formed at lower temperatures. Organic matter is also found in many chondrites, up to 2% of weight, and this is especially true for carbonaceous chondrites (Botta and Bada, 2002; Sephton, 2002).

Tens of thousands of chondrites in our repositories can be classified into 15 groups. Except for R (Rumurutiites) and K (Kakangari) chondrites, which apparently have no relationship to other groups, the 13 remaining groups are included in 3 major classes:

- *Ordinary chondrites* (O): this class account for approximately 80% of all meteorite falls and for over 90% of all chondrites. Three groups are included in this class and are H, L and LL ordinary chondrites, different in their bulk iron concentration. H chondrites have a high iron content and represent 40% of collected chondrites, L have a low iron content (50%) and LL are low both in iron and metal content (10%).
- *Carbonaceous chondrites* (C): this class encloses 8 groups, which are CI, CM, CO, CV, CK, CR, CH and CB carbonaceous chondrites. The second letter in the group code refers to the name of a typical chondrite in it. For example, CI are Ivuna-like, and so on. The term "carbonaceous" is somehow a misnomer, because only CI, CM and CR have significantly higher carbon content with respect to other chondrite classes. Despite being classified as chondrites, CIs do not contain chondrules. Nevertheless, this group is particularly interesting because its members provide the best match to the composition of the solar photosphere, being the most primitive meteorites, and CI compositional pattern is often used as a reference for it.
- *Enstatite chondrites* (E): this is the least populated class of chondrites and comprises two groups, EH and EL. The mineralogy of these meteorites is dominated by *enstatite*, which is iron-free orthopyroxene. EH chondrites have a higher bulk iron content ($\sim$30%) than EL ones ($\sim$25%).

Within each group, chondrites are further subclassified according to their petrologic type, which appears as a number, from 3 to 7, usually inserted after the group code and originally proposed by Van Schmus and Wood (1967). A low petrologic type refers to meteorites showing a low degree of thermal metamorphism with abundant and distinct chondrules, whereas a high petrologic type is attributed to a severe degree of metamorphism and almost melted chondrules. Originally, numbers 1 and 2 were used to describe the degree of aqueous alteration.

2.6.3 Achondrites

Achondrites contain virtually no chondrules and lack other features found in chondrites, like CAIs. They are believed to originate from chondritic-like material that underwent significant melting and fractioning processing during planetary formation and evolution. As a general rule of thumb, stony achondrites originate from the outer shells of differentiated bodies, while stony-iron and iron meteorites come from the metallic core and the inner portion around it. Therefore, their analysis gives us the unique opportunity to hold and study samples of the core of planetary bodies, which is otherwise impossible. This connection is still debatable, since up to date we never directly observed an asteroid with an exposed core. Achondrites are usually divided into two broad classes, which are:

- *Primitive achondrites*, having a "near-chondritic" bulk composition but highly fractioned with respect to chondrites and exhibiting igneous features. This class encloses the *Acapulcoite-Lodranite* clan, containing meteorites with compositions varying from chondrite-like (in few cases displaying relict chondrules) to distinctly non-chondritic. The clan of *Winonaite-IAB-Iron* meteorites is the second major group of primitive achondrites. *Brachinites* and *Ureilites* are also commonly classified as primitive achondrites, but a clear consensus is not yet achieved and some authors acknowledge them as differentiated achondrites, as they have characteristics of both classes.
- *Differentiated achondrites*, on the other hand, experienced higher degrees of melting and large-scale differentiation and have features markedly far from chondritic ones. In this class we found the groups of *Angrites*, *Aubrites* and the *Howardite-Eucrite-Diogenite* (HED) clan. We also find stony-irons, in the two groups of *Mesosiderites* and *Pallasites*, and iron meteorites. Planetary meteorites, *e.g.*, lunar and martian meteorites, are also enclosed in this class.

A more in-depth description of achondrites and their groups and clans can be found in Mittlefehldt (2014) and Benedix et al. (2014).

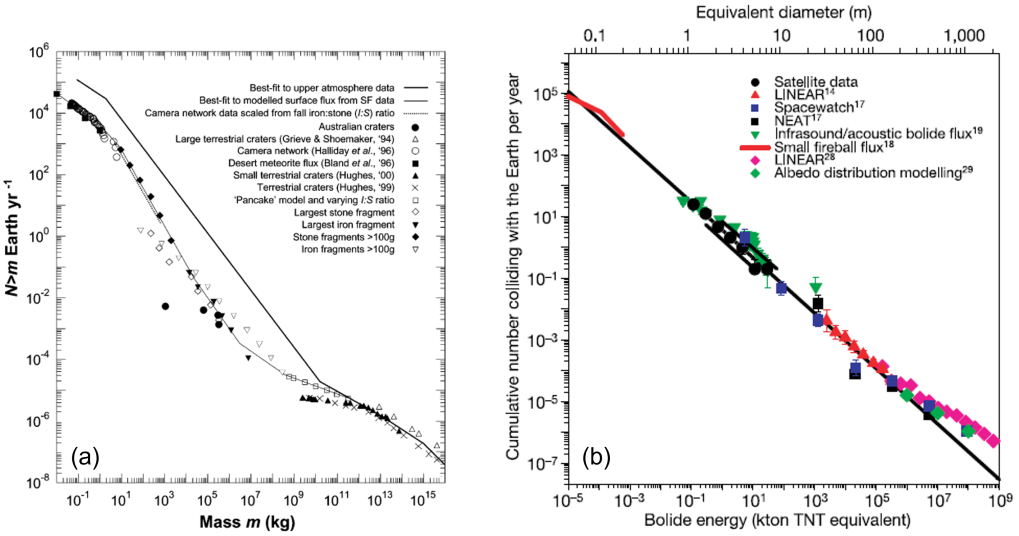

Fig. 2.20: Estimates of cumulative impact rate of small bodies to the Earth's surface as determined by several observations (see legends), ranging from meteor and fireballs observations to the statistics of terrestrial cratering rate and albedo distribution modelling of NEAs. Panel a - Bland and Artemieva (2006), panel b - Brown et al. (2002a).

2.7 The key role of meteoritic science

In this chapter, I reported a general overview on the study of minor bodies in our Solar System. The purpose of this final section is to give a summary of the key role that *meteoritic science* has played and still plays in the advancement of our knowledge in the field of planetary science.

As already detailed in Sect. 2.3.2, the first important driver for asteroid and meteoroid monitoring studies is due to the hazard they pose to the Earth and the survival of life on it. From the very beginning of the space era, great attention was always given to the monitoring of the asteroidal population and, in particular, to the class of NEOs. However, direct observation of such objects is limited by the current achievable performance of ground- and space-based telescopes. The smallest asteroid ever observed in space is 2015 TC25, with an estimated size of 2 m (Reddy et al., 2016; Farnocchia et al., 2017). However, this observation was possible only thanks to his unusually high albedo, of about 60%. Current estimations suggest that we observed >90% of the NEO population above 1 km of size. On the other hand, the population of small asteroids below 100 m is poorly constrained. Nevertheless, this population of NEO is source of significant impactors in the medium-term horizon (Brown et al., 2002a; Bland and Artemieva, 2006). Systematic observation of meteors to bright fireballs is therefore the only reliable tool to pinpoint the flux of such objects to date. An asteroid of 10 m dimensions is expected to collide with the Earth approximately once per year (see Fig. 2.20), and the case of the Chelyabinsk superbolide showed how dangerous these events can be. A 100 m sized object can cause a local-to-regional catastrophic event, and their flux to the Earth is such as one impact may occur every thousand years.

On the other hand, the recovery of meteorites allows analyzing samples originating directly from the early stages of the Solar System, providing unique insights into the processes of its formation and evolution (*e.g.*, Kleine et al., 2020, and references therein). Significant efforts have been made within the scientific community in the last decades to relate the welth of results on asteroids and meteorites studies. A recent and enlightening review on the subject is given by Greenwood et al. (2020) and references therein. The first remarkable result is the linkage between asteroidal taxonomy classes and orbital families to the wide but still limited variety of meteorite classes and groups present in our collection. Most of the meteorite's groups have been proposed to be linked to asteroidal taxonomical classes only (see Sect. 2.1.3), based on the similarity of their reflectance spectroscopy to the meteorite composition of that group (see Table 2 of Greenwood et al., 2020). This is due to the limitations of spectroscopical measurements and to the non-uniqueness of reflectance spectra among different complexes. Just a handful of meteorite groups have been associated with an asteroid orbital family, which therefore points towards a possible parent body. The most remarkable example is the quite likely link of the group of HED differentiated achondrites to the Vesta family and V-type asteroids (McCord et al., 1970; Binzel and Xu, 1993).

It is also worth noticing that, while our meteorite collection counts more than 70k specimens, among them we can identify only about 100 to 150 possible *parent bodies*. Greenwood et al. (2020) argue that the concept of parent body is vaguely defined and loosely interpreted, but most widely used in scientific literature. While it can be defined as "a body that supplies meteorites to the Earth", this definition is incomplete. We must distinguish between the concept of *primary parent body*, *i.e*, the ultimate source of meteoritic material and a member of the primordial asteroid population, and *secondary parent bodies*, derived by the primary and that finally delivered the meteorite to the Earth (see Fig. 2.21). Different causes are called into question when trying to understand this heavy unbalance between the large number of known asteroids compared to the little number of primary parent bodies of recovered meteorites. Possible explanations provided by Greenwood et al. (2020) for such evidence are: (1) unrepresentative sampling, since meteorites are delivered to the Earth from specific regions of the MAB, as detailed in Sect. 2.3.1; (2) the current asteroidal population may originate from a limited number of primordial bodies; (3) meteorites could be mainly derived by few asteroidal families; (4) the Earth's atmosphere acts as a very selective filter for meteoritic material, with a preference for low porosity and high strength bodies.

In this scenario, it is evident that achieving a higher recovery efficiency of meteorites is fundamental to increase and refine the meteorite classification scheme, allowing more detailed links between asteroids and meteorites. Furthermore, we must consider that the vast majority of meteorites we collected were found in deserts.

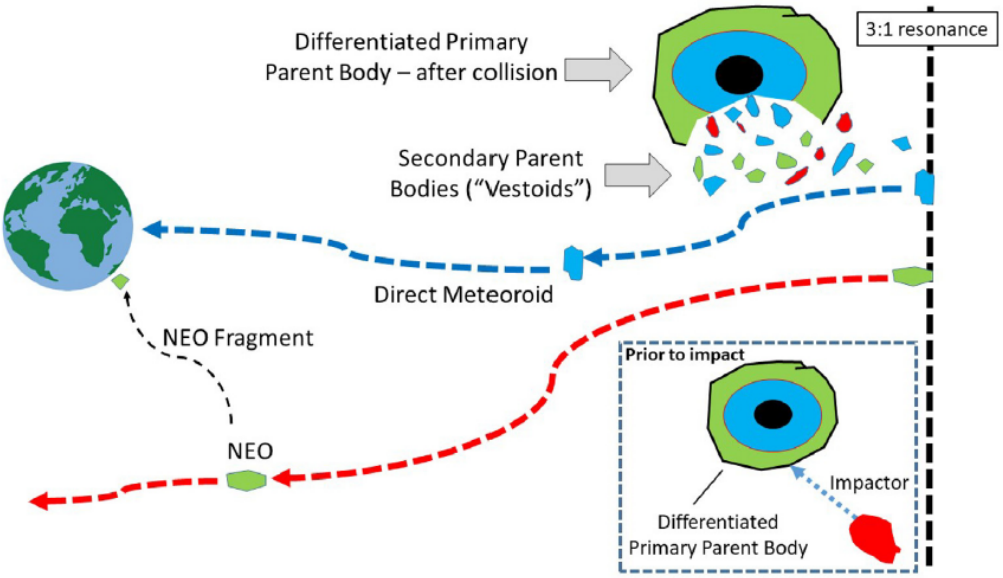

Fig. 2.21: Schematic representation of the possible delivery routes of meteorites, showing the difference between primary and secondary parent bodies. Meteorites can be delivered to the Earth either by secondary parent bodies after fragmentation of the primary, drifted towards resonance regions in the MAB (grey arrows), directly from a small meteoroid close to resonance (blue line) and from fragments of NEOs (red line). The picture presents the example of Vesta and Vestoids (Greenwood et al., 2020).

In many cases, huge numbers of samples found in neighbouring areas are probably originating from the same fall, and are therefore *paired*. Also, desertic meteorites are usually subject to heavy terrestrial weathering. Instead, freshly-fallen meteorites are pristine samples and almost untouched from their original state after the fall, and their recovery is much more valuable to our cause.

2.7.1 The case of "pedigree" fall meteorites

Among the class of fall meteorites, a restricted but most relevant group deserves particular attention. That is, the class of meteorites which recovery was accompanied by a sufficient set of observations enabling the three-dimensional reconstruction of the meteoroid path through the atmosphere. Such occurrence allows to deduce the dynamics of the body and, for example, it is possible to estimate the preatmospheric meteoroid mass (M_∞) by measuring the deceleration in the terminal part of the trajectory (see Sect. 2.5.3). The measurement of the light emitted by the meteor can also provide an independent estimation of the meteoroid mass (Ceplecha, 1966; Campbell-Brown et al., 2012). A wealth of additional physical quantities of the meteoroid can be deduced, such as the preatmospheric velocity (V_∞) and the terminal mass (M_{fin}), that is the residue of the meteoroid after ablation at the start of the dark flight. Furthermore, the detection of flares and/or fragmentation, and knowing the altitude of such events, can give hints about the strength of the meteoroid material (Foschini, 2001). These are the main parameters to be evaluated when trying to understand if meteorites are likely to be found on the ground. Precise measurements also allow to define a strewn-field, indicating the area of most probable fall and maximizing the outcome of on-field searches for meteorites. All these conditions highly increase the probability of recovering meteorites, as demonstrated by the case of the Pribram meteorite, the first of this kind (Ceplecha, 1961, see Sect. 2.4.1).

Even more relevant is the possibility to compute the preatmospheric orbit of the meteoroid for such events, thanks to the measurements of the meteoroid's geocentric velocity, position and time of impact (see Sect. 4.2.6). This represents the most favourable conditions to fully exploit the scientific outcome of the analysis of meteorite specimens. In fact, it is possible to correlate the meteorite classification to the region of origin of the meteoroid, and this is the "Holy Grail" of meteoritic science. The knowledge of the meteoroid's orbit prior to impact allows to integrate back its evolution, finally understanding how it was injected into the inner Solar System in the NEO region, usually from the MAB (Granvik and Brown, 2018). This kind of events also allowed to suggest or disprove candidates of parent bodies for different groups of meteorites (*e.g.*, Unsalan et al., 2019; Jenniskens et al., 2019).

Due to the outstanding importance of this particular group of meteorites, they were first addressed as "pedigree" meteorites by Gardiol et al. (2021). Up to date, 48 of these meteorites were recovered, plus at least 6 additional ones pending official publication and approval by The Meteoritical Society. Table 2.2 reports the most relevant data about published pedigree falls. While before the year 2000 only 5 pedigree meteorites were recovered (Pribram, Lost City, Innisfree, Benesov and Peekskill), the last 20 years witnessed a remarkable increase in the detection and recovery efficiency, also thanks to the global deployment of advanced fireball networks. Since 2018, we reached an outstanding average of 3 meteorites per year. It is worth noticing that only 27 of these were actually recorded by fireball networks while, for the remaining 21 events, the triangulation was possible thanks to ad-hoc efforts to calibrate sporadic and fortuitous observations from security cameras, dash cams, and visual reports.

Within the collection of pedigree meteorites, 44 are chondrites (92%) and only 4 are achondrites (8%). Among chondrites, 38 are ordinary (86%), 5 are carbonaceous (11%) and only 1 is enstatite (3%). Ordinary chondrites are further subdivided into H, L and LL in ratios of 37%, 47% and 16% respectively, similar to the average ratios of finds and falls outlined in Tab. 2.1 (44% H, 42% L and 10% LL). Slight deviations are evident, but they may not be statistically significant yet due to the limited sample of pedigree meteorites. Published preatmospheric orbital elements of pedigree meteorites are tracked and reported on the following website: `https://www.meteoriteorbits.info/`, curated by Dr. Matthias M. M. Meier.

Name	Date UT	Met. class.	V_∞ [km/s]	M_∞ [kg][a]	M_{fin} [kg][b]	TKW [kg]	$\mathcal{M}$[c]	E [T][d]	Fireball Network[e]	Ref.
Příbram	07/04/1959	H5	20.9	1300	80	5.6	-19	70	CFN	1,2
Lost City	04/01/1970	H5	14.1	165	25	17	-12	4	PMN	3,4,5
Innisfree	06/02/1977	L5	14.7	42	4.9	4.58	-12.1	1	MORP	5,6
Benešov	07/05/1991	LL3.5/H5	21.3	4100	300[f]	0.0116	-19.5	200	EFN	5,7,8,9
Peekskill	09/10/1992	H6	14.7	5000	-	12.4	-16	130	-	2,10
Tagish Lake	18/01/2000	C2-ung	15.8	56000	1300	10	-22	1700	-	11,12,13
Morávka	06/05/2000	H5	22.5	1500	100	1.4	-20	90	-	14,15,2
Neuschwanstein	06/04/2002	EL6	20.9	300	20	6.22	-17.2	16	EFN	16,17,18
Park Forest	27/03/2003	L5	19.5	11000	-	30	-21.7	500	-	19,20
Villalbeto de la Peña	04/01/2004	L6	16.9	600	13	5.2	-18	20	-	21,22,23
Bunburra Rockhole	20/07/2007	Eucrite	13.4	22	1.1	0.339	-9.6	0.5	DFN	24,25
Almahata Sitta	07/10/2008	Ureilite-an	12.4	40000	39	10.7	-19.7	730	-	26,27,28,29
Buzzard Coulee	21/11/2008	H4	18.0	10000	-	>200	-20	390	-	30,31,32
Maribo	17/01/2009	CM2	28.3	2000	<20	0.0258	-20	190	-	33,34
Jesenice	09/04/2009	L6	13.8	170	20	3.611	-15	4	SFN	35,36
Grimsby	26/09/2009	H5	20.9	30	5	0.215	-14.8	2	SOMN	37
Košice	28/02/2010	H5	15.0	3500	500	11.3	-18	100	-	38,39
Mason Gully	13/04/2010	H5	14.5	40	-	0.0245	-9.4	1	DFN	40,41
Križevci	04/02/2011	H6	18.2	50	<5[g]	0.291	-13.7	2	CMN	42
Sutter's Mill	22/04/2012	C[h]	28.6	40000	-	0.943	-19	4000	-	43
Novato	18/10/2012	L6	13.7	80	-	0.363	-13.8	3	CAMS	44
Chelyabinsk	15/02/2013	LL5	19.0	$1.2{\cdot}10^7$	10000	730	-27.3	$5{\cdot}10^5$	-	45,46,47
Annama	18/04/2014	H5	24.2	470	12.5	0.1679	-18.3	30	FFN	48,49,50
Žďár nad Sázavou	09/12/2014	L3	21.9	150	>1.3[i]	0.087	-15.3	9	EFN	51
Porangaba	09/01/2015	L4	-	-	-	0.970	-	-	-	52
Sariçiçek	02/09/2015	Howardite	17.3	1700	-	24.78	-16.8	60	-	53
Creston	23/10/2015	L6	16.0	50	-	0.8523	-12	2	CAMS, SACN	54
Murrili	27/11/2015	H5	13.7	38	2	1.68	-	0.9	DFN	55,56

... next page ...

Name	Date UT	Met. class.	V_∞ [km/s]	M_∞ [kg]^a	M_{fin} [kg]^b	TKW [kg]	$\mathcal{M}^c$	E [T]^d	Fireball Network^e	Ref.
Osceola	24/01/2016	L6	-	$>1800^j$	-	1.1	-	-	-	57
Ejby	06/02/2016	H5/6	14.5	120	-	8.982	-14.0	3	-	58,59
Stubenberg	06/03/2016	LL6	14	600	-	1.473	-15.5	14	EFN	60,61
Hradec Králové	17/05/2016	LL5	13.3	90	-	0.134	-11.5	2	EFN	62
Dishchii'bikoh	02/06/2016	LL7	16.6	1000^k	-	0.07957	-16	30	CAMS, SACN	63,64
Dingle Dell	31/10/2016	LL6	15.4	40	1.4	1.150	-	1	DFN	65
Hamburg	17/01/2018	H4	15.8	140	>1	~ 1	-16.3	5.5	-	66,67
Motopi Pan	02/06/2018	Howardite	17	5700	-	0.215	-23	200	-	68
Ozerki	21/06/2018	L6	15	98000	-	>10	-21	2500	-	69,70
Renchen	10/07/2018	L5-6	18.6	17	-	1.227	-13.4	2	EFN	62
Viñales	01/02/2019	L6	16.9	-	-	50–100	-	1400	-	71,72
Arpu Kuilpu	01/06/2019	H5	17.8	2.2	0.04	0.0422	-9.3	0.08	DFN	73
Flensburg	12/09/2019	C1-ung	19.4	10000	$\sim 10^l$	0.0245	-21	480	AS7	74
Cavezzo	01/01/2020	L5-an	12.8	3.5	1.5	0.0553	-9.5	0.07	PRISMA	75
Novo Mesto	28/02/2020	L5	22.1	470	10	0.720	-19	28	-	76
Madura Cave	19/06/2020	L5	14.0	60	2.5	1.072	-	1.4	DFN	77
Kindberg	19/11/2020	L6	14	270	-	0.233	-	6	AS7, FRIPON, EFN	78,79,80
Traspena	18/01/2021	L5	16.4	2600	2	0.527	-17	80	-	81
Winchcombe	28/02/2021	CM2	13.9	13	0.35^m	0.602	-11	0.3	UKFAll and others^n	82,83
Antonin	15/07/2021	L5	17.7	75^o	$\sim 10^p$	0.352	-15	3	EFN	84

Tab. 2.2: List and relevant data of "pedigree" meteorites, *i.e.*, for which recovery was accompanied by a sufficient set of systematic or sporadic observations (optical, radio, infrasound, seismic, satellite), allowing for pre-impact orbit reconstruction (updated to the end of the year 2021). From left to right: name of the meteorite (approved by The Meteoritical Society), date of fall, official meteorite classification (according to the Meteoritical Bulletin), preatmospheric velocity (V_∞) and mass (M_∞), estimated terminal mass (M_{fin}), meteorite total known weight (TKW) recovered on the ground, minimum absolute magnitude recorded, impact energy (equivalent tons of TNT, 1 T = $4.187 \cdot 10^9$ J), fireball network which provided the observations (if any, otherwise sporadic observations only) and references for table data. The uncertainties associated to the values of the table are not given here for the sake of simplicity but can be found in the respective references. While standard errors on the V_∞ are usually $\lesssim$ 0.1 km/s, uncertainties on M_∞ are often quite large and can be 50% or even higher. Notes and references are reported on the next page (Gardiol et al., 2021).

Notes and references for Table 2.2

[a] The preatmospheric mass of the meteoroid can be estimated through various techniques, mainly from: (1) dynamic, measuring the deceleration of the meteoroid; (2) photometry, measuring the emitted light intensity and assuming a luminous efficiency value; (3) cosmogenic radionuclides activity measurements. When multiple estimations of M_∞ are available, we preferred (1) > (2) > (3).

[b] Values for the final mass are very heterogeneous and should be considered only as a qualitative estimation of the survived mass after ablation (sometimes they refer just to the main mass or, in other cases, the authors account for fragmentation).

[c] Magnitude values are given in different passbands (e.g. visual, panchromatic) and might be not strictly comparable to one another.

[d] The impact energy was calculated by the authors, if not provided in the original work, or updated to more precise estimates of preatmospheric mass and/or velocity.

[e] CFN = Czechoslovakian Fireball Network (now EFN), PMN = Prairie Meteorite Network, MORP = Meteorite Observation and Recovery Project, EFN = European Fireball Network, DFN = Desert Fireball Network, SFN = Slovakian Fireball Network (part of EFN), SOMN = Southern Ontario Meteor Network, CMN = Croatian Meteor Network (part of EFN), CAMS = Cameras for All-sky Meteor Surveillance, FFN = Finnish Fireball Network, SACN = Spalding Allsky Camera Network, SkySentinel, AS7 = AllSky7 Fireball Network Europe, PRISMA = Prima Rete Italiana per la Sorveglianza sistematica di Meteore ed Atmosfera, FRIPON = Fireball Recovery and InterPlanetary Observation Network, UKFAll = UK Fireball Alliance.

[f] Most of the terminal mass in gram-sized meteorites.

[g] Apart from the main mass, just a few 10–100 g meteorites are expected and ~2000 meteorites with mass > 1 g.

[h] A carbonaceous chondrite that has not yet been classified.

[i] Main mass of 1.3 kg plus a second largest meteorite in the range 100–200 g (~250 meteorites in the range 10–200 g, 6 kg total, and ~3000 meteorites of 0–1 g, 7 kg total).

[j] Computed considering a preatmospheric radius > 50 cm deduced from cosmogenic radionuclide data and a mean bulk density of 3.4 g cm^{-3} for L chondrites, assuming a spherical shape.

[k] There is a disagreement between meteoroid size deduced from radiated energy from satellite observations (~15000 kg) and cosmogenic radionuclide data (400–1800 kg).

[l] The available data were not sufficient to rigorously determine the total fallen mass. Hundreds of meteorites of ~10 g and tens of thousands of ~1 g may exist.

[m] Only the main fragment (0.23–0.59 kg), consistent with the recovered main mass of 0.319 kg.

[n] Many meteor and fireball networks participated in the detection of the Winch-

combe bolide: UKFAll, SCAMP (System for Capture of Asteroid and Meteorite Paths), UKFN (UK Fireball Network of the Global Fireball Observatory), GMN (Global Meteor Network), UKMON (UK Meteor Network), NEMETODE (Network for Meteor Triangulation and Orbit Determination).

[o] The terminal part of the fireball was not instrumentally recorded due to clouds. The dynamical mass was estimated in the range 50–100 kg, while the photometric mass is 50–500 kg.

[p] It was not possible to determine a precise value of the terminal mass. In the last observed part of the trajectory, the mass is of the order of few tens of kilograms.

List of references: [1] Ceplecha (1961), [2] Borovička and Kalenda (2003), [3] McCrosky et al. (1971), [4] Ceplecha (1996), [5] Ceplecha and Revelle (2005), [6] Halliday et al. (1981), [7] Spurný (1994), [8] Borovička et al. (1998), [9] Spurný et al. (2014), [10] Brown et al. (1994), [11] Brown et al. (2000), [12] Brown et al. (2002b), [13] Hildebrand et al. (2006), [14] Borovička et al. (2003a), [15] Borovička et al. (2003b), [16] Spurný et al. (2002), [17] Spurný et al. (2003), [18] Revelle et al. (2004), [19] Simon et al. (2004), [20] Brown et al. (2004), [21] Llorca et al. (2005), [22] Trigo-Rodríguez et al. (2006), [23] Bischoff et al. (2013), [24] Bland et al. (2009), [25] Spurný et al. (2012), [26] Jenniskens et al. (2009), [27] Borovička and Charvát (2009), [28] Shaddad et al. (2010), [29] Welten et al. (2010), [30] Hildebrand et al. (2009), [31] Milley et al. (2010), [32] Wilson and McCausland (2012), [33] Haack et al. (2012), [34] Borovička et al. (2019), [35] Spurný et al. (2010), [36] Bischoff et al. (2011), [37] Brown et al. (2011), [38] Borovička et al. (2013c), [39] Tóth et al. (2015), [40] Spurný et al. (2011), [41] Dyl et al. (2016), [42] Borovička et al. (2015), [43] Jenniskens et al. (2012), [44] Jenniskens et al. (2014), [45] Popova et al. (2013), [46] Borovička et al. (2013b), [47] Brown et al. (2013), [48] Trigo-Rodríguez et al. (2015), [49] Kohout et al. (2017), [50] Bouvier et al. (2017), [51] Spurný et al. (2020), [52] Ferus et al. (2020), [53] Unsalan et al. (2019), [54] Jenniskens et al. (2019), [55] Bland et al. (2016), [56] Sansom et al. (2020), [57] Meier et al. (2020), [58] Spurný et al. (2017a), [59] Haack et al. (2019), [60] Spurný et al. (2016), [61] Bischoff et al. (2017), [62] Borovička et al. (2020), [63] Palotai et al. (2019), [64] Jenniskens et al. (2020), [65] Devillepoix et al. (2018), [66] Brown et al. (2019), [67] Gattacceca et al. (2020a), [68] Jenniskens et al. (2021), [69] Kartashova et al. (2020), [70] Korochantseva et al. (2019), [71] Zuluaga et al. (2019), [72] Gattacceca et al. (2020b), [73] Shober et al. (2022), [74] Borovička et al. (2021), [75] Gardiol et al. (2021), [76] Vida et al. (2021b), [76] Devillepoix et al. (2022), [78] Kővágó (2021), [79] Ferrière (2021), [80] Gattacceca et al. (2022), [81] Andrade et al. (2023), [82] King et al. (2022), [83] McMullan et al. (2023), [84] Shrbený et al. (2022)

3

Observation of meteors with PRISMA and Mini-EUSO

My work during the PhD period was mainly dedicated to the analysis of the meteor observations from two experiments, that are the PRISMA fireball network and the Mini-EUSO UV telescope onboard the International Space Station (ISS). These two experiments are quite diverse in their scientific and technical aspects. The PRISMA network was designed and implemented for the monitoring of bright meteors and the recovery of freshly-fallen meteorites over the Italian territory. On the other hand, the main scientific objective of Mini-EUSO is the monitoring of the UV background emission in the Earth's atmosphere, providing a tool to demonstrate the principle and probe the performance of a space-based observatory dedicated to the detection of Ultra-High Energy Cosmic Rays (UHECRs). Nevertheless, the unique design and implementation of the Mini-EUSO mission allows to pursue a wide range of secondary scientific objectives, among which is the observation of meteors.

In this chapter, I describe the two projects, reviewing their scientific context, their technical and operational details and the data used for the analysis presented in the next chapters of this manuscript.

3.1 The PRISMA fireball network

Before 2020, only 40 meteorites were recovered on the Italian soil, being 32 falls and 8 finds according to the Meteoritical Bulletin. The oldest one is Narni, an unclassified stony meteorite that fell in the year 921 in the Umbria region. The vast majority of these meteorites were recovered in the last two centuries, with 24 falls and 7 finds since the year 1800. Taking the 20th century as an example, only 11 falls are officially recognized. This sums up to a very disappointing average of approximately one meteorite recovery every 10 years. On the other hand, current estimates of meteorites' flux to the Earth suggest a number between 2 to 10 meteorites with mass greater than 100 g to be recovered every year over the Italian territory of $\sim 3 \cdot 10^5$ km^2 (see Sect. 2.7 and Fig. 2.20). Even if we take the lower estimate and also considering the particularly adverse geographical conditions of Italy[1], this is one order of magnitude less than the actual recovery rate. Such evidence suggests

---

[1] The prevalence of mountainous territory in Central and Southern Italy does not facilitate meteorites search campaigns.

a very low recovery efficiency of meteorites, and this is true not only for Italy. For example, similar considerations are reported by Colas et al. (2020) for the French territory, also underlining the drastic decrease of observed meteorite falls in this country between the 19th century, with 45 recovered falls, and the 20th century, with only 5 documented falls.

The idea of the realization of an Italian fireball network was first proposed by Dr. Mario di Martino and Dr. Daniele Gardiol in 2016 during the *XIII Congresso Nazionale di Scienze Planetarie*[2], held in Bormio (SO), and first reported to the international scientific community by Gardiol et al. (2016). This idea was inspired by the realization of a fully automated fireball network in France, named FRIPON (see Sect. 3.1.1), also with the scientific motivation of tracking cm-sized objects entering the Earth's atmosphere, accurately determining their orbit, and improving the recovery efficiency of meteorites over the French territory (Colas et al., 2012).

This Italian project was named PRISMA, an acronym for *Prima Rete Italiana per la Sorveglianza sistematica di Meteore ed Atmosfera*[3]. From its very beginning, PRISMA was developed with a strong sense of a participatory project, mainly because of the lack of substantial starting funding but also thanks to the interest of the Italian scientific and amateur community in its potential. To date PRISMA involves more than 70 institutions, both public and private, and is coordinated by INAF[4], the Italian National Institute for Astrophysics. The project counts more than 130 collaborators, mainly but not only among professional and amateur astronomers, academic researchers, school teachers and people working in museums and planetaria. Detailed information about PRISMA and its collaboration can be found at the following website: `http://www.prisma.inaf.it/`.

Thanks to the involvement of its participants, the PRISMA network counts today about 70 stations deployed over the Italian territory. Fig. 3.1 shows the location of PRISMA stations. While the coverage of the northern part is almost complete, some areas of Central and Southern Italy would benefit from the installation of additional PRISMA nodes to achieve sufficient detection efficiency. The optimal grid distance for a network of this kind is between 60 and 100 km, considering that meteors are usually observed at starting altitudes of ~100 km and at least two cameras are needed to trigger the same event to enable triangulating its trajectory. A certain degree of redundancy, *i.e.*, a higher density of cameras, is also not a bad thing and allows to prevent possible downtimes of single stations due to maintenance. Also, the achievable triangulation precision increases as more cameras are involved in the triangulation of the same meteor.

The systematic observation of the night sky carries a wealth of secondary scientific objectives beyond the observation of meteors, mainly in the atmospheric

---

[2] `https://web.archive.org/web/20180204000546/http://www.iaps.inaf.it/attivita/convegni/planetologia/bormio-2016/`

[3] (in English) First Italian Network for the systematic Surveillance of Meteors and the Atmosphere.

[4] `http://www.inaf.it/it`

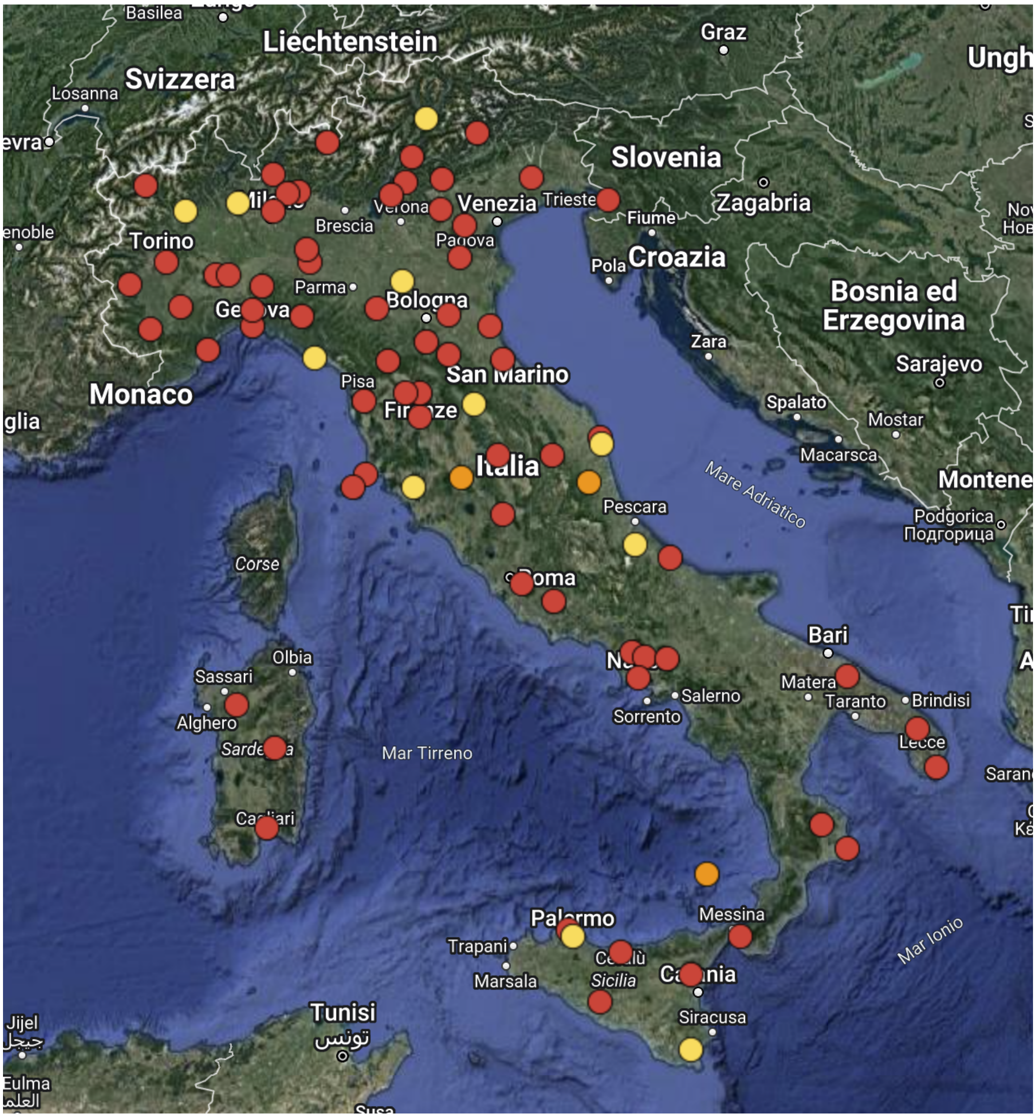

Fig. 3.1: Map of the stations of the PRISMA network. Red dots represent operational nodes, orange dots are nodes in installation phase and yellow dots are being purchased. An up-to-date version of the map is available on the PRISMA website: `http://www.prisma.inaf.it/` (map credits: Google Maps).

sciences. As an example, PRISMA data can be used for the monitoring of the sky brightness and light pollution (Walker et al., 2006; Rabaza et al., 2010; Zamorano et al., 2015), a topic of utmost importance in the modern era that is posing a serious threat to the operation of ground-based observatories (Green et al., 2022) and most importantly to biodiversity (Hölker et al., 2010). For example, data from all-sky cameras were already used for the monitoring of the phenomenon of ALAN (Artificial Lights At Night), a form of light pollution, and its impact on skyglow due to cloud reflection (Jechow et al., 2017). Further fields of application for PRISMA data are the monitoring of cloudiness and other atmospheric events, such as lightnings and TLEs (Transient Luminous Events).

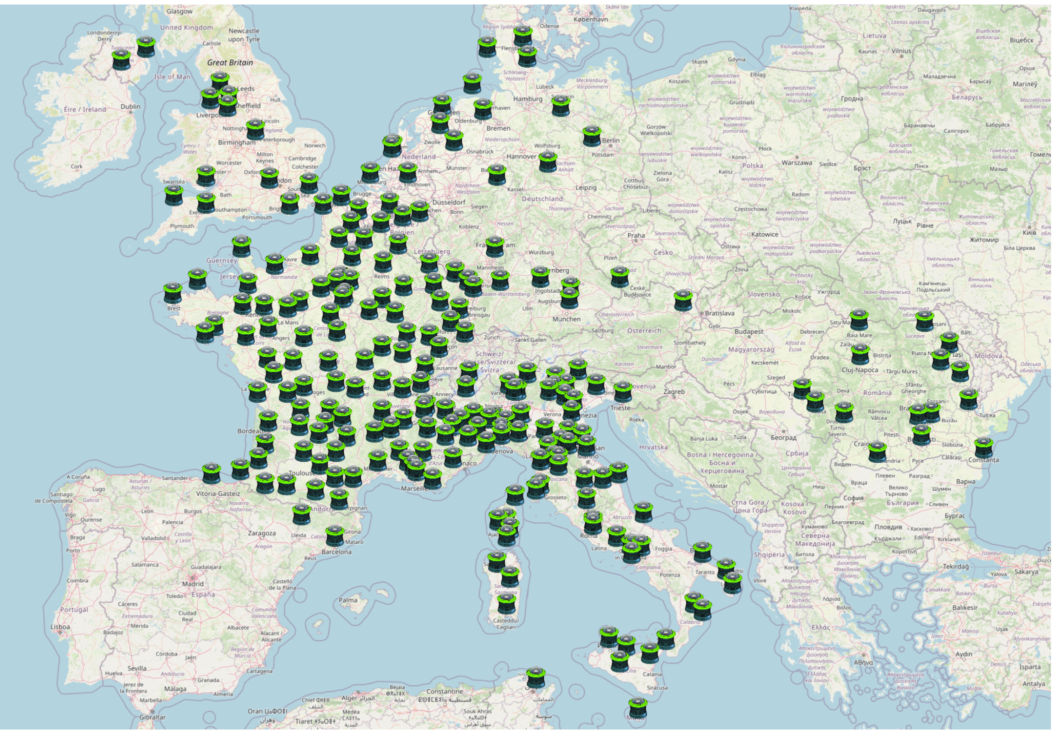

Fig. 3.2: Map of the stations of the FRIPON network installed in Europe. The network also counts 37 stations outside Europe in Canada, Morocco, Senegal, Burkina Faso, Chile and Australia. The full and updated map is available on the FRIPON website: `https://www.fripon.org/map/` (map credits: Leaflet, OpenStreetMap, FRIPON consortium team).

3.1.1 The FRIPON European collaboration

PRISMA was born in the framework of FRIPON[5], the Fireball Recovery and InterPlanetary Observation Network, a science project originally designed by a core team of six French scientists (Colas et al., 2020). FRIPON realized a network of over 100 cameras installed in France and officially launched its operation in 2016 (Colas, 2016). After this, scientists from many neighbouring countries manifested their interest in joining the project and implementing a FRIPON-like network. Italy was the first country to join the FRIPON collaboration, and PRISMA is the second biggest partner in the network to date. Figure 3.2 shows the map of the FRIPON network in Europe, which today counts ∼180 stations. Apart from FRIPON-France and PRISMA, other countries involved in the project are Romania (MOROI - Meteorite Orbits Reconstruction by Optical Imaging, Nedelcu et al., 2018), UK (SCAMP - System for Capture of Asteroid and Meteorite Paths), the Netherlands (DOERAK - Dutch Observers of Entries to Recover Asteroidal Krumbs), Germany, Austria, Switzerland, Belgium and Spain. FRIPON was also implemented in many countries outside Europe, that are Canada (DOMe - Détection et Observation de Météores), Morocco, Senegal, Burkina Faso, Chile and Australia.

---

[5] `https://www.fripon.org/`

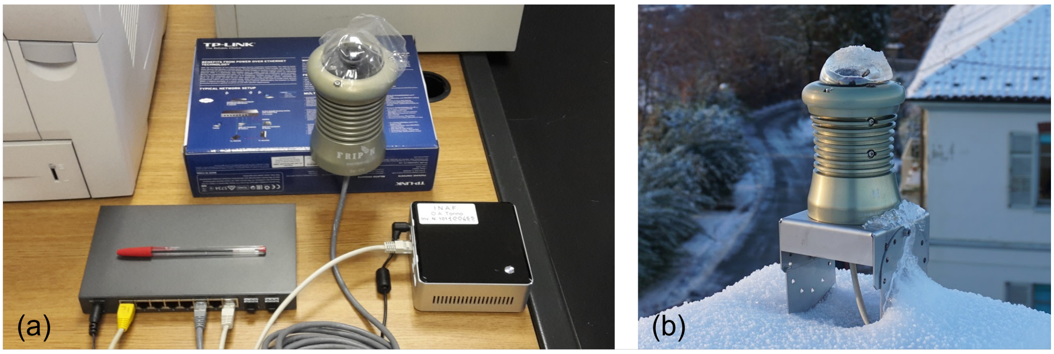

Fig. 3.3: The PRISMA/FRIPON station, composed of an all-sky camera module, a network switch and a mini-PC (panel a), usually installed on the roof of buildings or mounted on a pole. Panel b shows the first station of the PRISMA network, ITPI01 - Pino Torinese, installed at the INAF - Osservatorio Astrofisico di Torino.

3.1.2 The PRISMA/FRIPON station node

PRISMA implemented the technology developed by FRIPON for its station node. The setup of a FRIPON station in the lab is shown in Fig. 3.3a and it is composed of three main units: an all-sky camera module, a network switch and a mini-PC to operate and control the station itself (Colas et al., 2020). Each station within FRIPON is uniquely identified by a code, enclosing the nation, region and a sequential number, together with the name of the city that hosts the station. Fig. 3.3b shows the first camera of the PRISMA network, named ITPI01 - Pino Torinese, installed on the roof of the main building of the INAF - Osservatorio Astrofisico di Torino[6] and operational since 2016.

The PRISMA/FRIPON station implements a fish-eye camera module, able to image the whole visible hemisphere in just one frame. Most of the Italian stations operate with a camera module from Basler, model acA1300-30gm[7], equipped with a CCD sensor chip from Sony (model ICX445AL, 6 mm diagonal, 1296 x 966 px) and a short focal fish-eye lens objective (1.25 mm, F2.0). The camera is exposed through a transparent plastic dome and enclosed in a housing module, protecting it from weather conditions and designed also to act as a passive cooler, to release the heat produced by the electronics during the warm periods of the year and to minimize CCD dark current (Colas et al., 2014). The station is controlled by a mini-PC NUCi3 system connected via LAN to the camera through a network switch, which also provides the power supply to the module via a single PoE (Power Over Ethernet) cable. The continuous acquisition of images and the trigger of meteor events are controlled by a dedicated open-source software, designed and implemented by the FRIPON collaboration and named FREETURE[8] (Audureau et al., 2014).

---

[6] https://www.oato.inaf.it/

[7] https://www.baslerweb.com/en/downloads/document-downloads/basler-ace-aca1300-30gm-emva-data/

[8] https://github.com/fripon/freeture

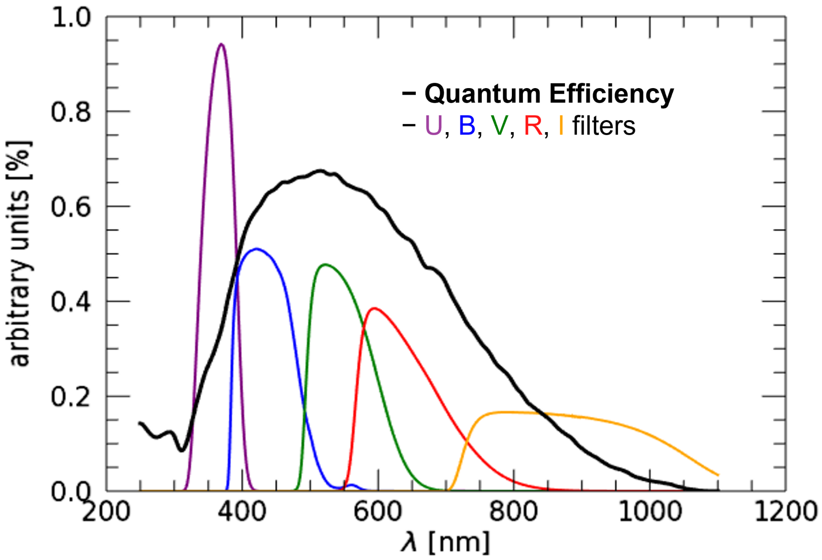

Fig. 3.4: Quantum Efficiency (QE, black thick line) of the Sony ICX445AL CCD sensor installed on the stations of the PRISMA and FRIPON networks, expressed in percentage over incoming photon flux. This plot also includes the contribution of the dome in the total QE, measured on one PRISMA camera. The coloured lines plot the Johnson-Cousins filters in the bands U (violet line), B (blue), V (green), R (red) and I (orange), normalized to unit integral.

3.1.3 Characterization of the PRISMA/FRIPON camera

The camera module implemented in the PRISMA/FRIPON station is not equipped with any bandpass filter. The spectral response of the system is therefore characterized by the wide and panchromatic bandpass of the CCD sensor. The black line of Fig. 3.4 plots the quantum efficiency (QE) of the Sony ICX445AL sensor, as provided by the manufacturer. Also, the protective dome was tested for its spectral sensitivity and did not show any significant spectral features, except for a slight decrease in sensitivity below 250 nm, included in the plot of Fig. 3.4. This minor effect is not particularly relevant, since the QE of the sensor is already quite low at this wavelength range. The coloured lines of the figure show the standard bandpass filters of the Johnson-Cousins system, which are U, B, V, R and I (Bessell and Murphy, 2012). While being centered on the V band, it is evident that the QE of PRISMA cameras covers the whole visible spectral range. B and R bands are included with high values of efficiency, with most of their area modulated with QE > 50%. On the other hand, the contribution from the U and I filters is small compared to the PRISMA bandpass, but still significant enough not to be totally ignored. This evidence poses some issues in the photometric calibration of PRISMA cameras based on the measured flux of stars with their catalogue magnitudes, usually given in the UBVRI system, and it is addressed in Sect. 4.1.6.

The PRISMA/FRIPON camera module was also tested to check the uniformity of its response in its focal plane. In particular, a known effect to be estimated for all-sky

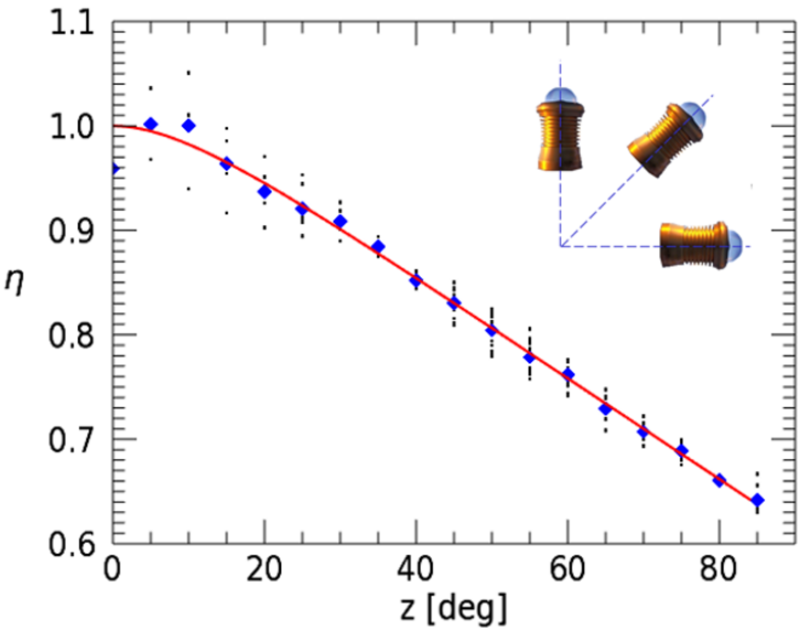

Fig. 3.5: Radial dependence of the optical system sensitivity (coming manly from the lens and the protective dome) obtained as described in Sect. 3.1.3. Small black dots are the values of single measurements corresponding to different datasets during the night of observation, normalized to the 1 at $z = 0°$, while blue dots are mean values. The red line is the plot of the fitting function of Eq. 3.1.

cameras is the sensitivity loss along the radial direction, *i.e.*, the zenith distance (z) dependency of measured fluxes not included in the atmospheric extinction, resulting from the whole optical system. To this purpose, we mounted one PRISMA camera in alt-azimuth configuration to be able to modify the pointing direction and observe different portions of the celestial dome at a varying apparent elevation, corresponding to different regions on the CCD. The pointing direction was modified at 5° steps and in each configuration a set of images was acquired (Barghini et al., 2019a). Each measurement set was done in a short time span, so that the observed portion of the sky was approximately unchanged in its conditions, during a cloudless and moonless night. Figure 3.5 shows the results of these measurements from $z = 0°$ to $z = 85°$ (blue points). The red curve plots a fitted function of this modulation, in the form of:

$$\eta(z) = 1 - B_1 z - B_2 \exp\left\{-\frac{B_1}{B_2} z\right\}, \tag{3.1}$$

that is specified to fulfill the requirement of null derivative for $z = 0°$, because specular symmetry is expected around the optical axis. Values obtained for parameters of Eq. 3.1 applied to the measurements of the PRISMA camera are $B_1 = (483 \pm 8) \cdot 10^{-5}$ deg^{-1} and $B_2 = (48 \pm 9) \cdot 10^{-3}$. For $z > 20°$, the decreasing slope is nearly constant (about -10% each 20°). The sensitivity decreases by about 40% from the centre to the edge of the focal plane.

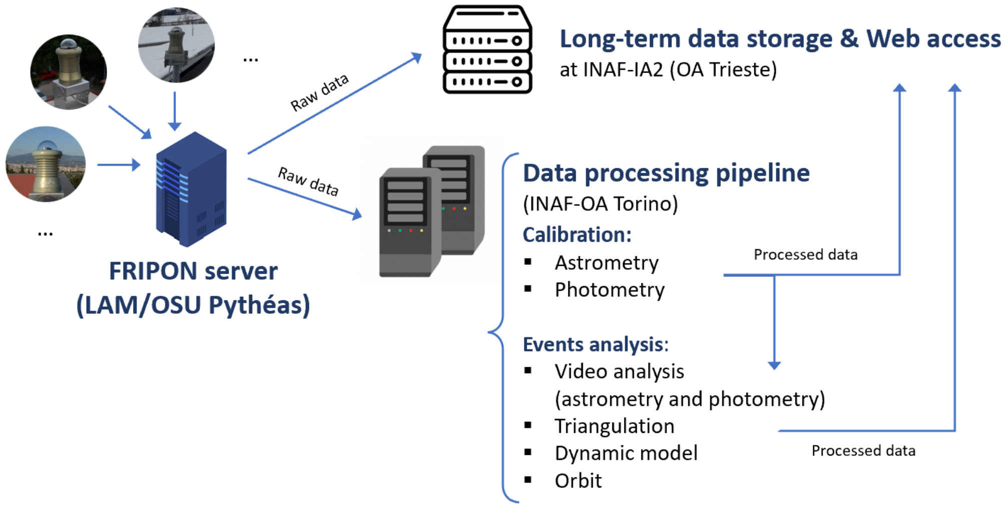

Fig. 3.6: Schematization of the flow of PRISMA data. Acquisitions from each station are collected by the central FRIPON server, located at the LAM/OSU Pythéas facilities in Marseille. A copy of the Italian raw data is synced to the servers of the INAF-IA2, in Trieste, for their long-term storage and preservation, and to provide access to the PRISMA collaboration. Raw data consist of events (video of meteors seen by two or more stations) and calibration data (long-exposure images). A second copy is transferred to be processed at the servers installed at the INAF - Osservatorio Astrofisico di Torino. The results of this processing are finally synced back to INAF-IA2.

3.2 Format and flow of PRISMA data

Data from each node of all the national networks are collected and processed by a central FRIPON server[9], operating at the Aix-Marseille University in France[10]. Italian data are synced to INAF facilities for storage and processing purposes. The flow of PRISMA data is summarized in Fig. 3.6. A copy of the Italian raw data is sent to the INAF-IA2[11] facility at the Astronomical Observatory of Trieste for its long-term storage, preservation and to provide a web access[12] to the PRISMA collaboration. A second copy of the data is transferred to the servers at the INAF - Osservatorio Astrofisico di Torino, for their processing. My activity in the framework of PRISMA during the PhD period was mainly dedicated to developing the analysis pipeline for these data, described in Chap. 4. This pipeline is now in its final testing phase and will run automatically on the data collected since 2016 by the network, to produce the first version of the PRISMA data release, most probably within the year 2023. The results of this processing are also transferred to the INAF-IA2 storage.

---

[9] `https://fireball.fripon.org/`

[10] SIP - Service Informatique Pythéas at the LAM/OSU - Laboratoire d'Astrophysique de Marseille of the Observatoire des Sciences de l'Univers (`https://www.osupytheas.fr/`).

[11] Italian center for Astronomical Archive (`https://www.ia2.inaf.it/`).

[12] `http://archives.ia2.inaf.it/prisma/`

3.2.1 Event data

To properly sample the apparent meteor path on the focal plane, the camera is continuously operated at 30 Hz during night-time, when the Sun is 12° below the local horizon (nautical dawn). This represents a trade-off between not having an excessively elongated shape of the Point Spread Function (PSF) and maximizing the Signal-to-Noise Ratio (SNR) of the acquired image, considering that the meteor is a fast-moving source in the field of view of the camera. With this exposure, the limiting magnitude for meteors is about 0, although being slightly variable (± 1 mag) depending on the illumination conditions and light pollution of the station site. The FREETURE software manages the image acquisition of each node, which independently triggers the detection of meteors in the field of view of the camera by a simple frame difference method. To tentatively filter non-meteor events, the implemented algorithm computes a rough estimation of the angular speed of the moving source and compares it to the expected range of meteors (11–72 km/s), discarding the trigger if not compatible with it. Even if the camera is all-sky, the last $\sim 5^\circ$ above the horizon are usually masked to the algorithm in order to avoid false triggers induced by the flickering of neighbouring lights. Once triggered, FREETURE saves the video of the meteor, usually spanning ±100–300 frames before and after the trigger, in the format of single FITS files, a widely used data format for astronomical images (Wells et al., 1981). This collection of FITS is therefore called *detection*. Figure 3.7a shows an example of a detection triggered by the PRISMA camera ITPI02 - Cuneo on 09/12/2018 at 20:08 UT. The meteor trail image represented here is reconstructed from the video of the detection, by selective image stacking. This meteor was detected by a total of 9 PRISMA cameras in North-West Italian regions, and by 3 FRIPON cameras in Southern France[13].

All cameras are monitored by the central FRIPON server, exchanging the basic metadata about each detection, like the trigger time and geographical coordinates. Two or more detections within ±3 s triggered from cameras closer than 190 km are considered an *event*, that is most probably generated by the signal of a meteor. If the central FRIPON server triggers one event, data of the corresponding detections are downloaded from the involved stations and synced to PRISMA servers in Italy. The cameras of the PRISMA network trigger an average of 1-2 events per night, except during major meteor showers when this rate can go as high as some tens to hundreds of events per night. Otherwise, data of detections that did not result into an event are erased every two months approximately, depending on the disk space locally available on the mini-PC of the station. More technical details about the functioning of the FRIPON network data exchange can be found in Colas et al. (2020).

---

[13] `https://fireball.fripon.org/displaymultiple.php?id=1321`

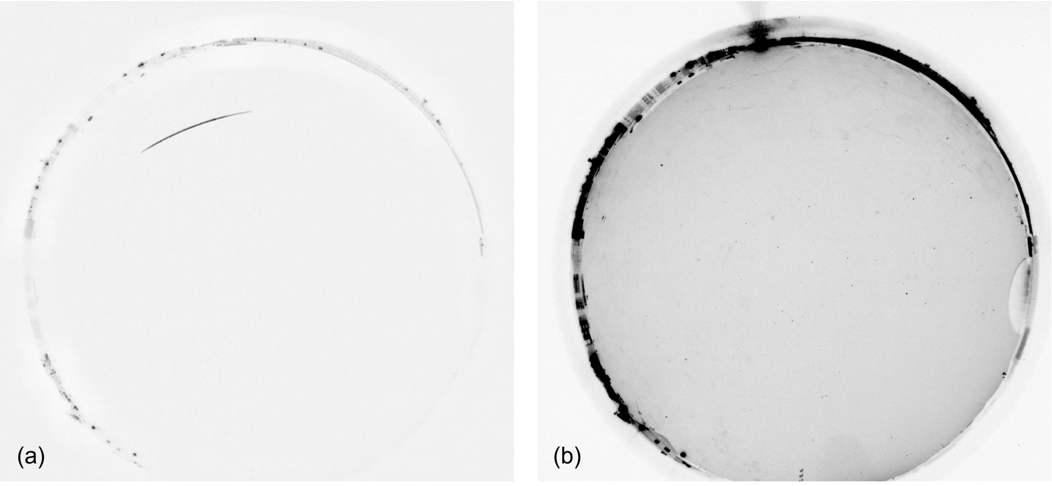

Fig. 3.7: Example of images taken by the PRISMA camera ITPI02 - Cuneo. (a) Detection of a meteor of -4 minimum absolute magnitude triggered on 09/12/2018 at 20:08:30 UT, seen by a total of 9 PRISMA cameras in North-West Italy. The meteor trail image is reconstructed from the video, through a selective image stacking. From PRISMA analysis, the object was estimated to be of 3 ± 0.4 cm size, with a mass of 50 ± 20 g and entered the atmosphere at 19.6 ± 0.1 km/s with an inclination of $\sim$25° with respect to the ground. (b) Capture from the same night at 20:11:13 UT, with $\sim$100 stars visible in the FoV. From this image, it is evident that the observation site is quite light-polluted. This camera is in fact installed on the roof of a high-school building in the city centre of Cuneo (Liceo Classico e Scientifico Statale "Pellico-Peano"). The two images are not in the same colour scale, which is reverted, and are cropped to the sides (original dimensions are 1296 x 966 px).

3.2.2 Calibration data

The detection stacked image shown in Fig. 3.7a does not display any star in the field of view (FoV) of the camera. As already mentioned, the limited performance of the camera and the CCD, together with the short exposure time of 1/30 s needed to properly sample the meteor track, put the limiting magnitude for astronomical sources at approximately 0 in the visual band. At this magnitude, only a handful of stars are potentially visible and most often not at the same time in the FoV. This poses an important limit since the position and intensity of catalogue stars are the main input to perform the astrometric and photometric calibration of the camera. To this purpose, FREETURE performs a 5 s exposure each 10 minutes during day- and night-time, resulting in a set of equally time-spaced images that are named *captures*, following FREETURE nomenclature. This dataset consists of a continuous flow of FITS files that is therefore used for the astrometric and photometric calibration of PRISMA cameras, as described in Sect. 4.1. An example of a capture image is presented in Fig. 3.7b for the ITPI02 - Cuneo station, taken just 3 minutes after the detection of panel a. While being only supplementary for meteor studies, captures are the main data to be used for secondary scientific objectives of PRISMA, such as the monitoring of light pollution (see Sect. 3.1).

3.3 The JEM-EUSO program

After lightnings, meteors are probably the most common light-emitting phenomena occurring in the Earth's atmosphere. Apart from dedicated experiments like meteor networks, their observation can come as a by-product of many other surveys. This is the case of the JEM-EUSO, an acronym for *Joint Experiment Missions for Extreme Universe Space Observatory*. It is a scientific program mainly dedicated to the space-based observation of ultrahigh-energy cosmic rays (UHECRs) which are cosmic rays with energy $E \geq 10^{19}$ eV. The detection principle of JEM-EUSO is represented in Fig. 3.8. The Earth's atmosphere represents the most extensive detector at our disposal for the study of these highly energetic cosmic particles. UHECRs produce Extensive Air Showers (EASs) due to the interaction and propagation into the Earth's atmosphere of the stream of secondary particles induced by the primary impact, and emit light mainly by fluorescence and Cherenkov radiation in the near-UV wavelength range, from 290 to 430 nm. The detection and imaging of EASs from a space observatory like JEM-EUSO allow the reconstruction of the energy and arrival direction of the primary particle. Due to their very high rigidity, UHECRs preserve their direction when propagating in space and are most likely to come from outside our Galaxy. Therefore, their observation provides unique insights into the most extreme processes occurring in the Universe. They also represent the sole tool to probe particle physics well beyond the energies reachable by human-made accelerators (Coleman et al., 2023). However, their flux is estimated to be very little, of the order of 1 particle/km^2/millenium for energies of $\sim$$10^{20}$ eV. To date, two ground-based observatories are dedicated to the study of UHECRs, which are the Pierre Auger Observatory (PAO, Abdul Halim et al., 2023) and the Telescope Array (TA, Abbasi et al., 2018).

The idea of a space-based cosmic ray observatory, looking nadir during the night to capture the fluorescence light produced by EASs, was first proposed by John Linsley in the late 70's (SOCRAS - Satellite Observatory of Cosmic Ray Showers, Benson and Linsley, 1981). Compared to a ground facility, a space-based observatory of UHECR provides an extremely large atmospheric volume that can be simultaneously monitored, reaching highly uniform exposures over the full sky, almost one order of magnitude greater than the ones of PAO and TA (Adams et al., 2015b). Moreover, a space-based instrument looking nadir in the UV range from space can detect may other atmospheric phenomena, and of course meteors among all. In the 90's, technological advancement started to make feasible such an ambitious project and the idea was rediscovered by Yoshiyuki Takahashi. The major breakthrough consisted in the development of a new imaging optic made of lightweight diffractive Fresnel lenses, which can implement a wide FoV while keeping a moderately compact size of the telescope (MASS - Maximum-energy Auger Air-Shower Satellite, Takahashi, 1995). Then, this idea evolved into a mission study proposal (OWL - Orbiting Wide

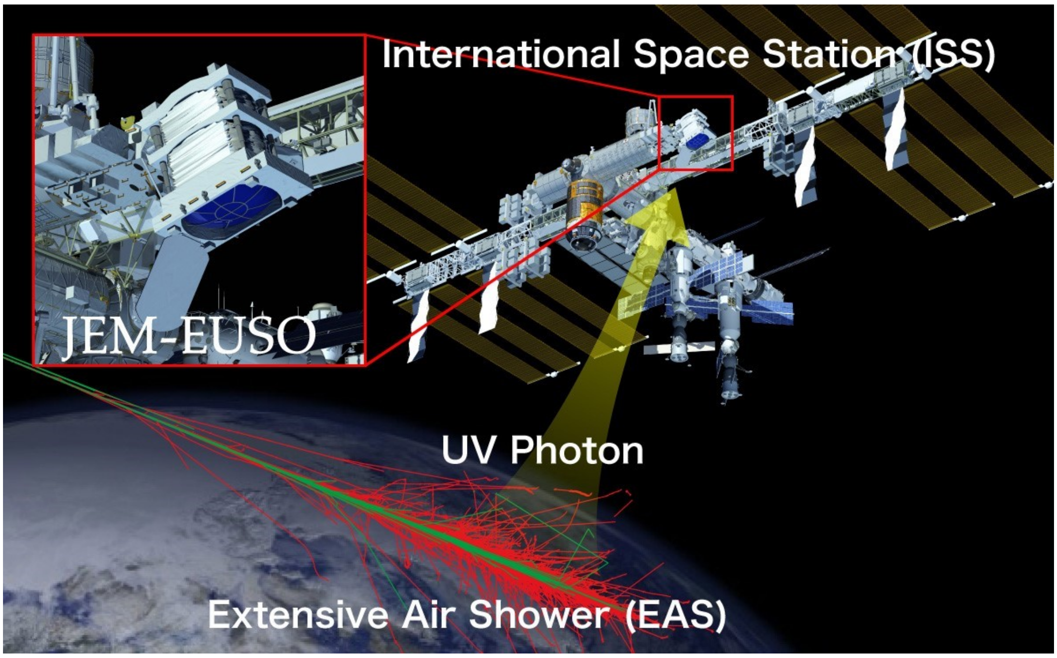

Fig. 3.8: Graphical representation of the principle of UHECR observation of JEM-EUSO from space (credits: `https://atlas.riken.jp/en/`).

Angle Light Concentrator) originally accepted by NASA in 1996 in its mid-term strategic plan for 2010, and consisted of two satellites orbiting and observing in a stereo configuration, with an aperture of 3 m and a total FoV of about 45°. This concept transformed in Europe into the mission EUSO, the Extreme Universe Space Observatory. This mission was first selected by ESA, then re-oriented it as a payload for the Columbus module of the ISS (Clavel et al., 2003; Gianiglio et al., 2003). After successfully completing its phase-A, ESA discontinued the EUSO mission, partially as a consequence of the Columbia Space Shuttle disaster of 2003. The mission concept was therefore repurposed by the Japanese and US teams to be developed on KIBO, the Japanese Experiment Module (JEM) of the ISS, and was renamed JEM-EUSO. The Japan Aerospace Exploration Agency (JAXA[14]) was the leading agency for the deployment of JEM-EUSO. Unfortunately, JAXA decided to discontinue the mission at the end of 2013, due to the size and cost of the instrument.

After 2013, the mission evolved into its current form. Today, the JEM-EUSO collaboration[15] consists of hundreds of researchers coming from 16 different countries, working to develop path-finder missions to prove the concept of a space-based UHECR observatory and aiming to deploy a larger mission, similar to the original JEM-EUSO proposal. More details about the JEM-EUSO program and its missions can be found in Adams et al. (2015e), Casolino et al. (2017), and Bertaina et al. (2022) and references therein. In the next sections, I give a short overview of the missions of the JEM-EUSO program and its main scientific objectives.

---

[14] `https://global.jaxa.jp/`

[15] `https://www.jemeuso.org/`

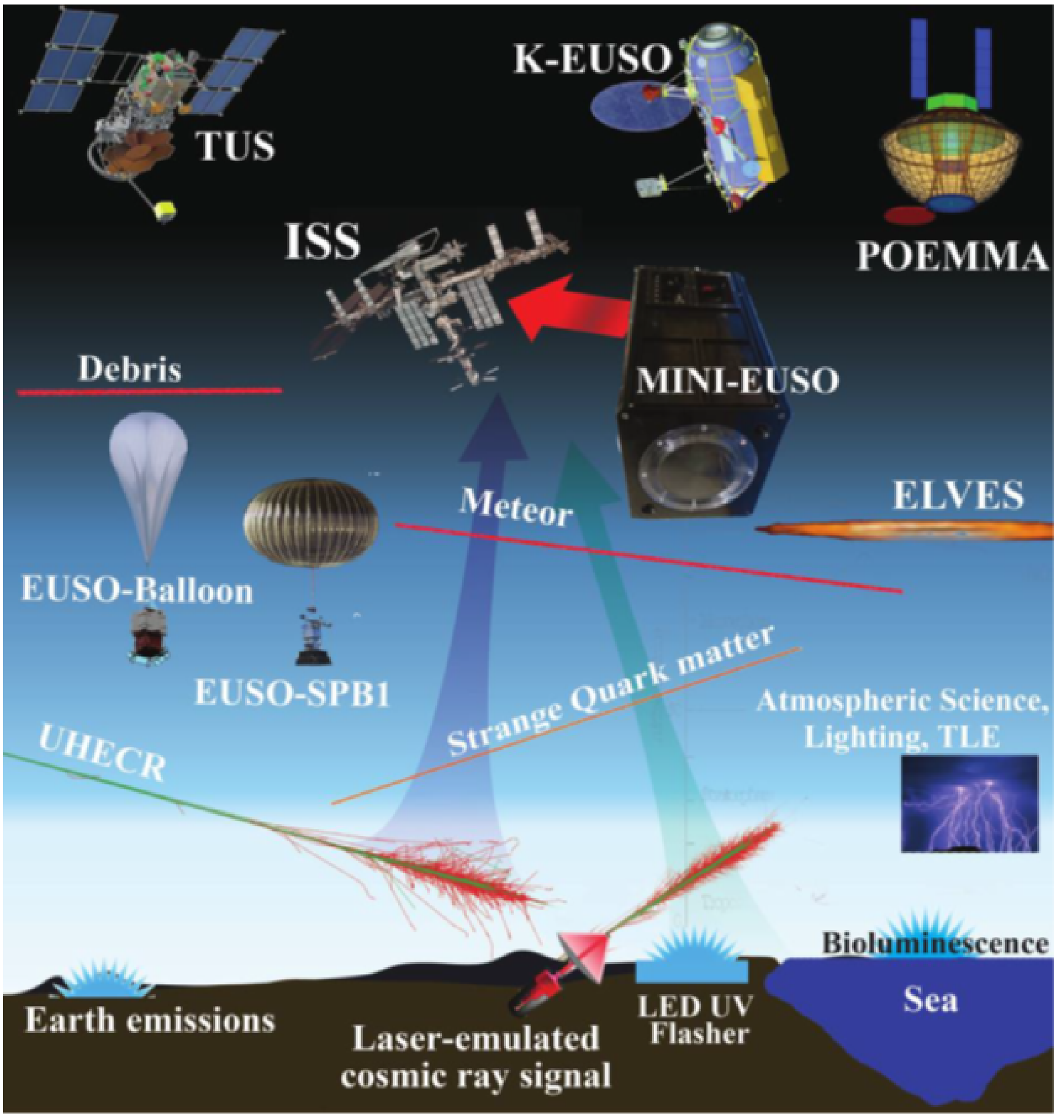

Fig. 3.9: The missions and main scientific objectives of the JEM-EUSO program.

3.3.1 Missions of JEM-EUSO

Figure 3.9 shows a graphical representation of most of the past, current and future missions developed in the framework of JEM-EUSO (Bertaina, 2019; Bertaina et al., 2022), together with the main scientific objective of the program (see Sect. 3.3.3). All these missions implement the EUSO technology and, in particular, the peculiar design of its focal surface and optics, which details are given in Sect. 3.4.1.

The first experiment to implement the EUSO technology was EUSO-TA, a ground telescope installed at the TA site in Black Rock Mesa, Utah, USA. This telescope is located in front of one of the TA fluorescence detectors and was first operated in 2015 with a few observation campaigns (Abdellaoui et al., 2018). EUSO-TA took about 120 hours of data and observed 9 UHECRs, imaging a FoV of $\sim 11^\circ \times 11^\circ$ with a focal surface of 48×48 px. These data allowed first estimations of the performance of the EUSO technology in observing UHECR events, and its optimization in view of space-based missions. EUSO-TA also detected few meteors during its operation. Since observing from the ground, it was also possible to perform an on-field absolute calibration using stars imaged in the FoV (Plebaniak et al., 2022).

Progressively going towards space, JEM-EUSO implemented a series of stratospheric balloon experiments with increasing complexity and an updated design. They were thought to demonstrate the EUSO capabilities in detecting UHECRs from the edge of space, providing at the same time key data about the UV natural and artificial emission from the Earth's surface as a tool to optimize space-based operations of future missions. The first experiment of this kind was EUSO-Balloon (Adams et al., 2015d), launched by CNES[16] from the Timmins base in Ontario, Canada on the night of 25 August 2014. It measured the UV intensity for 5 hours from an altitude of ∼38 km with a spatial and temporal resolution of 130 m and 2.5 μs, respectively, and a FoV of $\sim 11^\circ \times 11^\circ$ (Abdellaoui et al., 2019; Adams et al., 2022). Together with the data of EUSO-TA, the observations of EUSO-Balloon were used to define the EUSO internal trigger for UHECR and fast events in the atmosphere (Abdellaoui et al., 2017a).

A second balloon flight named EUSO-SPB1 (Super Pressure Balloon 1) was launched on 25 April 2017 from Wanaka, New Zealand, as a mission from NASA to test SPB flights to circle the southern hemisphere (Wiencke et al., 2017; Eser, 2019). This was the first EUSO mission to implement an automatic trigger to detect UHECR (Battisti et al., 2019; Osteria et al., 2019). Unfortunately, the flight was terminated early than expected due to a leak in the carrying balloon, after only 12 days. About 30 hours of data were collected but no EAS tracks were detected, because of this limited duration (Díaz Damian, 2019; Shinozaki et al., 2019). A new super-pressure balloon flight has been developed in the past three years, named EUSO-SPB2 (Eser, 2019; Scotti et al., 2020), and it is expected to be launched in the forthcoming weeks by NASA for a long-duration flight, up to 100 days, also from Wanaka. This instrument is equipped with two telescopes, one implementing the standard EUSO technology (Filippatos et al., 2022a; Filippatos et al., 2022b; Battisti et al., 2023) and a second one designed for the detection of the Cherenkov emission of UHECR (Bagheri et al., 2022), looking at the limb of the atmosphere.

The first space-based mission of the JEM-EUSO program was TUS – Track Ultraviolet Setup (Adams et al., 2015c; Klimov et al., 2017). It was launched on 28 April 2016 as a part of the scientific payload of the Lomonosov satellite (Sadovnichii et al., 2017) of the Moscow State University[17], orbiting in a Sun-synchronous configuration with a period of ∼94 min at an height of 470–500 km. The instrument was active until November 2017 and operated in different modes dedicated to various scientific targets, which are cosmic rays, lightnings and meteors (Barghini et al., 2022b). While not specifically designed for the observation of meteors, TUS detected 13

---

[16] Centre national d'études spatiales - `https://cnes.fr/en`.

[17] `http://lomonosov.sinp.msu.ru/en/`

meteors during its operations (Ruiz-Hernandez et al., 2022). TUS observed with a focal surface of 16 × 16 px, with a square footprint on the ground of about 5 km for a total area of 80 km × 80 km. The telescope detected about $8{\cdot}10^5$ events and their analysis allowed to understand how to recognize UHECR-like events generated by anthropogenic ones (Khrenov et al., 2020).

The second space-based experiment of the JEM-EUSO program is Mini-EUSO, presented in Sect. 3.4 and currently operating onboard the ISS. The future planned missions within JEM-EUSO are K-EUSO and POEMMA. K-EUSO is the first EUSO-like telescope that will have real capabilities of detecting UHECRs, to be equipped with two lenses and a $\sim 40^\circ$ FoV (Kalashev et al., 2019; Klimov et al., 2022). It represents the evolution of the concept of the KLYPVE mission, updated with the technology developed by the JEM-EUSO collaboration (Khrenov, 2002). It is planned to be installed outside the ISS, attached to the Russian MRM-I module, and will provide a large exposure and homogeneous coverage of the full celestial sky with an operational lifetime of 2 years, potentially up to 6 years. Finally, POEMMA (Probe Of Extreme Multi-Messenger Astrophysics) is being designed to provide an unprecedented contribution to astroparticle physics, targeting cosmic neutrinos above $2{\cdot}10^{16}$ eV and UHECR above $2{\cdot}10^{19}$ eV, observing high volumes of the Earth's atmosphere in nadir to limb orientation (Poemma Collaboration et al., 2021). This project is the combination of the original OWL mission integrated with the new JEM-EUSO technology. POEMMA will consist of two twin free-flyer orbiting in formation at 525 km altitude and observing overlapping regions, having therefore stereoscopic capabilities for the reconstruction of EAS events.

3.3.2 Space-based meteor observations with JEM-EUSO

As already introduced in the previous section, EUSO experiments already had the chance to detect meteors, in particular with EUSO-TA (from ground) and TUS (from space). The trigger system of the TUS detector was designed to record cosmic ray atmospheric showers and was not optimized to image the signal of meteors, much slower with respect to EAS-like events. Despite these limitations, 13 meteors were registered and it was possible to determine their arrival directions and brightness profile (Ruiz-Hernandez et al., 2022). Figure 3.10 shows two examples of meteors detected by TUS, plotting the lightcurve and pixel map of one of the meteors detected by TUS, both with an estimated magnitude in the U band of +0.5.

Space-based instruments have several advantages over ground-based meteor networks. First of all, their efficiency for the detection of meteors is much less dependent on the sky and weather conditions with respect to ground observatories, since they observes well above the typical altitude of clouds. While meteor networks are limited to the continental surface of the globe, space observatories can observe the whole Earth's surface and provide highly uniform coverage of the whole Earth

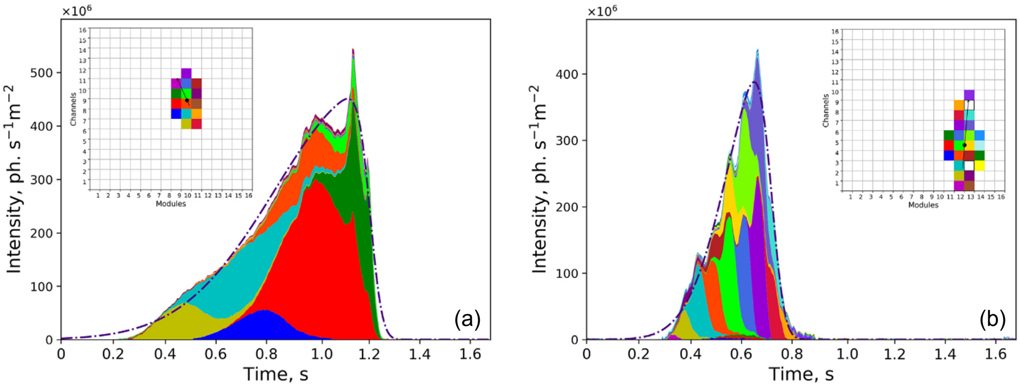

Fig. 3.10: Examples of lightcurves of two meteors detected by the TUS experiment onboard the Lomonosov satellite. The colour code of each pixel is represented in the map of the inset plot. (a) TUS171111b event, of +0.5 U magnitude, detected on 11/11/2017, 11:47:16 UT at 0.22° S latitude and 166.89° E longitude, over the Central Pacific Ocean north of the Nauru Island; (b) TUS170318b event, of +0.4 U magnitude, detected on 18/03/2017, 10:56:39 at 14.14° N latitude and 176.25° W longitude, over the Northern Pacific Ocean (Ruiz-Hernandez et al., 2022).

in both space and time. Moreover, they can monitor at the same time a huge volume of atmosphere compared to a ground telescope and reach huge exposure values. Of course, they also come with some limitations. Their spatial resolution can be limited in comparison, for example, to the performance achievable by a typical and much cheaper station of a meteor network. Also, they usually lack the capabilities to reconstruct the three-dimensional trajectory of the event, apart from stereo experiments such as POEMMA. Due to these features, space experiments may not be the best candidates to precisely track the trajectory of incoming meteoroids, compute their orbit and help in the recovery of new meteorites. For this purpose, fireball networks operating on the ground are still the best option. Nevertheless, a space telescope has the potential to detect a number of events in order of magnitudes greater than meteor networks and can provide an exceptional tool to pinpoint the flux of meteoroids over a large interval of masses. As a comparison, a precise evaluation of the absolute meteor flux from the data collected by meteor networks is non-trivial. This is because the computation of the total exposure for such distributed and heterogeneous facilities can be quite complicated, having to account for weather and cloud coverage variations and the wide range of observing conditions of their nodes (Koschny and Zender, 1998; Vida et al., 2022).

In spite of these advantages, meteor and fireball detection from space have not been routinely reported in the past for a long time. The reason for a general lack of detection reports in past years was mainly due to the fact that many satellites are equipped to monitor phenomena occurring over much longer time scales than the few seconds which generally characterize meteor phenomena. Consequently, in many cases meteor events were not detected or recorded. There are two noticeable exceptions. The NASA-JPL Center for NEOs Studies (CNEOS) monitors very bright bolides with space sensors (see Sect. 2.3.2 and Fig. 2.12). These data are collected by US Government (USG) sensors, in the framework of the Nuclear Test Ban Treaty monitoring satellites (Tagliaferri et al., 1994). Such instruments have a quite high energy threshold (total energy $E > 0.073$ kT TNT) and they detected only 853 events since 1988. CNEOS publishes regularly data about these events, including position, velocity and computed total energy of the event. Since 2020, they also release the measured lightcurve of detected events. Similarly, in 2019 it was determined that the Geostationary Lightning Mapper (GLM) instruments on GOES[18] weather satellites can detect fireballs and bolides (Jenniskens et al., 2018a; Smith et al., 2021) and their detections are routinely reported online[19], available to the scientific community. To date, GOES satellites detected about 5000 events in the range from -25° to -180° longitude and ±55° latitude.

Starting from the early stages of the program, it was clear that the JEM-EUSO program had the chance to significantly contribute to the field of meteor science. Its potentiality in meteor studies is described in Adams et al. (2015a) and Abdellaoui et al. (2017b). JEM-EUSO experiments also have the peculiarity of observing in the UV range. Observation of meteors from the ground in this wavelength range is difficult due to atmospheric ozone absorption and it is almost unprecedented, with only a few recorded events in this wavelength range (Jenniskens et al., 2002; Carbary et al., 2003; Kasuga et al., 2005). This is not the case for space-based observations which allow for an extinction-free spectral domain. By considering a UV detector covering the interval of wavelengths of JEM-EUSO instruments, and assuming a typical V band centred at 550 nm, we can expect that the flux in the two bands should be comparable for the light emitted by a meteor, as a first approximation. This is because both UV and V are dominated by Mg, Fe, and Na emission from the warm component (∼4500 K) of ablation products in the meteor wake, rich in low excitation lines by metal atoms. This prediction looks reasonable even taking into account that (1) Na sometimes shows differential ablation and can vary among different meteors, and (2) the V-band can also exhibit some air plasma emission from the first positive band of N_2, which can cause some variations.

Table 3.1 gives the estimated flux of meteors that could be observed by the original JEM-EUSO telescope, also rescaled for the observations of Mini-EUSO, as reported by Abdellaoui et al. (2017b). According to these results, both JEM-EUSO and Mini-EUSO should be sensitive to meteors down to absolute magnitude +7, corresponding to signals of 4 and 0.04 photo-electrons per GTU[20] respectively. Such faint events should be detectable only in the most favourable background conditions, considering that the typical UV background flux, on a moonless light,

---

[18] `https://www.goes.noaa.gov/`

[19] `https://neo-bolide.ndc.nasa.gov/`

[20] GTU (Gate Time Unit) is the temporal unit used for JEM-EUSO experiments, and in this case corresponds to ∼41 ms.

Abs. mag.	U-band flux [erg/s/cm^2/Å]	Mass	Event rate (JEM-EUSO)	Event rate (Mini-EUSO)
+7	$6.7{\cdot}10^{-12}$	2 mg	1/s	0.4/s
+5	$4.2{\cdot}10^{-11}$	10 mg	6/min	2.4/min
0	$4.2{\cdot}10^{-9}$	1 g	0.27/orbit	0.11/orbit
-5	$4.2{\cdot}10^{-7}$	0.1 kg	6.3/year	2.5/orbit

Tab. 3.1: Expected event rates for meteors from +7 to -5 of absolute magnitude, as observed by the original JEM-EUSO experiment and scaled for the Mini-EUSO telescope, assuming a duty cycle of 20% (Abdellaoui et al., 2017b). The relationship between mass and magnitude is to be considered only as a qualitative indication and was obtained following Robertson and Ayers (1968).

is of about 500 photons/m^2/ns/sr. This flux corresponds to a measured value of 1 count/px/GTU for both JEM-EUSO and Mini-EUSO (see Sect. 6.2.1). Considering a reasonable operational lifetime of a few years, JEM-EUSO and Mini-EUSO have the potential to observe meteors down to -5/-2 with statistically significant rates, therefore probing a range of ~10 magnitudes which corresponds to ~6 orders of magnitude for the meteoroid's mass, from milligrams up to kilograms.

3.3.3 Other scientific objectives of JEM-EUSO

Beyond the science of high-energy cosmic rays and the observation of meteors, the systematic monitoring of the Earth's atmosphere in the UV range can provide useful data in many other research fields. Therefore, the JEM-EUSO program pursues a wide range of secondary scientific objectives, which are:

- *Night UV emission*: while representing the background for EAS detection, the monitoring of the UV intensity from the Earth provides useful data to constraints emissivity of different surface types, also in relation to seasonal variations and human activities. Measurement of UV emission from land areas allows monitoring the light pollution from highly populated areas, while on the ocean UV light can be emitted by algae and plankton and it can provide information about marine pollution (Miller et al., 2005; Miller et al., 2021a; Miller et al., 2021b). Also, the atmospheric phenomenon of *airglow* can be detected in the UV and EUSO experiments can provide data to study its geographical and temporal variation.
- *Space debris*: with a population of 10k man-made satellites orbiting around the Earth, which account for a total mass of more than 10 kT, the problem of space debris is becoming of utmost importance for the future of space operations. Dismissed satellites also go through collisions and fragmentation, generating a population of cm- to mm-sized debris that still poses a significant hazard if

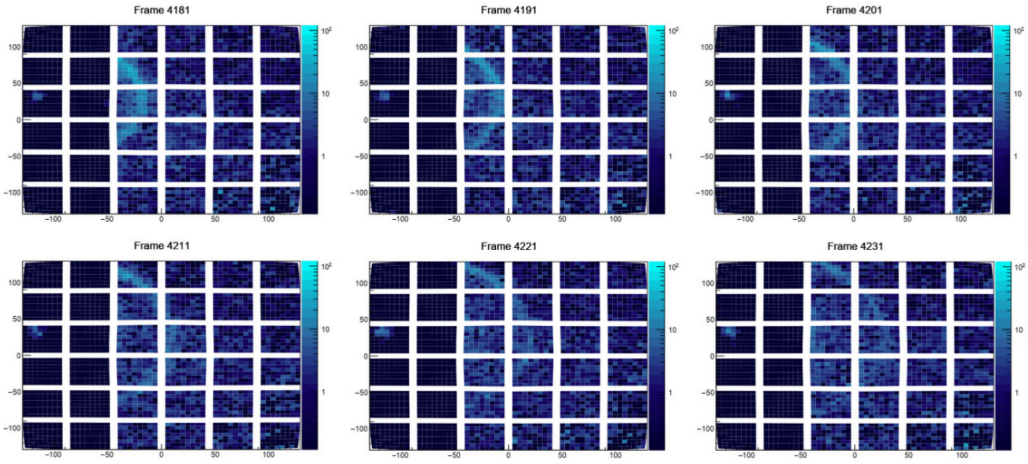

Fig. 3.11: A sample of frames of an ELVES observed on the focal surface of Mini-EUSO. Pictures are 25 µs apart and chronologically sorted, from top to bottom and from left to right (Marcelli et al., 2022).

impacting on space instruments that are still operational. It is estimated[21] that this population counts 36.5k objects greater than 10 cm, 1 million from 10 to 1 cm, and 130 million from 1 cm to 1 mm. Monitoring of space debris is another target of JEM-EUSO experiments. Their observation is possible during the local twilight period. If considering the ISS motion, this corresponds to a window of 5 min over the orbital period of 90 min. For example, Mini-EUSO could be able to observe debris of 0.1 m in size from a maximum distance from the ISS of 100 km. A precise tracking of such objects would also allow their remediation and removal by laser ablation (Ebisuzaki et al., 2015).

- *Transient Luminous Events* (TLEs): these are upper-atmospheric optical phenomena of electromagnetic nature, connected to thunderstorms, occurring at the timescales of micro to milliseconds, and therefore observable with instrumentation designed for EAS detection. The TLE class encloses a wide range of phenomena, such as sprites, jets, halo and ELVES - Emission of Light and Very low-frequency perturbations due to Electromagnetic pulse Sources (Füllekrug et al., 2006), and many others. Mini-EUSO can observe far-from-thunderstorm TLEs and, in the first year of data-taking, it detected 17 ELVES (Marcelli et al., 2022), which consist of glow rings concentrically expanding at speed of light and lasting a few hundred of µs. An example of ELVES detected by Mini-EUSO is presented in Fig. 3.11.
- *Strange Quark Matter* (SQM): possible candidates for Dark Matter are in the class of *macros* (macroscopic dark matter, see Sect. 7.4.1). The original idea was proposed by Witten (1984) who suggested that SQM, in the form of macroscopic aggregates of up, down and strange quarks, might be more stable than ordinary matter. Later, De Rujula and Glashow (1984) developed

---

[21] `https://www.esa.int/Space_Safety/Space_Debris/Space_debris_by_the_numbers`

a theoretical description of the interaction with the Earth's atmosphere of such compact objects, that were named *nuclearites*. They should exhibit a phenomenology similar to meteors but with significantly different signatures, mostly with respect to their typical speed of the order of 250 km/s. They should appear as high-speed moving tracks emitting a constant flux of photons, only modulated by the varying distance of observation, and should be clearly distinguishable from meteors. Therefore, experiments dedicated to meteors can pose limits on their observation and existence (Sidhu and Starkman, 2019; Piotrowski et al., 2020; Barghini et al., 2022a). EUSO experiments will be also able to provide similar constraints down to masses of 10^{24} GeV/c (Adams et al., 2015a; Abdellaoui et al., 2017b; Piotrowski et al., 2022).

3.4 The Mini-EUSO telescope onboard the ISS

After the TUS experiment, Mini-EUSO is the second mission observing from space within the JEM-EUSO program and the first one to operate on the ISS. Its name stands for *Multiwavelength Imaging New Instrument for the Extreme Universe Space Observatory*, known also as *UV atmosphere* in the Russian Space Program. It is a small-size telescope operating in the near UV range, predominantly between 290–430 nm, with a square focal surface corresponding to a field of view of $\sim 44^\circ$. Its spatial resolution at ground level is approximately 6.3×6.3 km^2, corresponding to 4.7×4.7 km^2 at the typical meteor altitude of 100 km, varying slightly with the altitude of the ISS and the pointing direction of the pixel. Mini-EUSO was launched and brought to the ISS with the uncrewed Soyuz MS-14, on 22/08/2019. The first observations took place on 07/10/2019 from the nadir-facing UV transparent window in the Russian Zvezda module of the ISS. Since then, Mini-EUSO is operated periodically by the ISS crew, being installed every couple of weeks during dedicated observation sessions. Figure 3.12 shows a picture of the instrument installed in this configuration. Until early 2023, Mini-EUSO performed 81 of such sessions. An overview of the mission and its first results can be found in Capel et al. (2018), Bacholle et al. (2021), and Casolino et al. (2023), and references therein. In the next sections, I will detail the instrument's technical specifications and the data acquisition and format of Mini-EUSO observations.

3.4.1 Mini-EUSO instrument overview

Mini-EUSO has been designed to operate from the interior of the ISS on the UV-transparent window located in the Zvezda module. The small size of the detector ($37 \times 37 \times 62$ cm^3) was thus constrained by the dimension of the window and the Soyuz spacecraft. Like all instruments operating on the ISS, the design is

Fig. 3.12: Picture of the Mini-EUSO telescope installed for observations from the ISS, mounted on the UV transparent window of the Zvezda module. The velocity vector of the ISS is usually oriented towards the bottom of the picture, on the side marked as '1' (Bacholle et al., 2021).

consistent with the safety requirements (no sharp edges, low surface temperature, robustness...) associated with manned spaceflight. Installation to the window is done via a mechanical adapter flange, and the only connection to the ISS is via a 28 V power supply and a grounding cable (power consumption ∼60 W). The weight of the instrument is about 35 kg, including the 5 kg flange. Being located in the middle of the Zvezda module, the detector is usually installed during onboard night-time, approximately at 18:30 UT with operations lasting about 12 hours until the following local morning (see Fig. 3.12). Since it only operates during night time, when not directly illuminated by the Sun, this usually accounts for 4–6 hours of effective data taking. If necessary and before each session, specific working parameters and patches in software and firmware are uplinked to the ISS and then copied on the SSD disk to fine-tune the acquisition of the telescope.

The Mini-EUSO telescope can be described by its three main components, which are the optics, the focal surface and the data acquisition module. The Engineering Model (EM) of the instrument is shown in Fig. 3.13a, during assembly and with its interior components exposed. The optics of the telescope consists of two Fresnel lenses[22] of 25 cm diameter. They are made of PMMA - Poly(methyl methacrylate), used to reduce the total weight of the lenses without sacrificing their robustness, being well suited for space applications. Each lens has a thickness of 11 mm and weighs 0.87 kg only, providing a FoV of about ±22°. They have good transmittance and uniformity of response, with a measured photon collection energy that varies

---

[22] Fresnel lenses are a particular type of refractive composite lenses able to achieve a large aperture and a short focal length with a smaller amount of material and a reduced thickness compared to standard optics. This is possible by dividing the lens into a set of concentric annular sections.

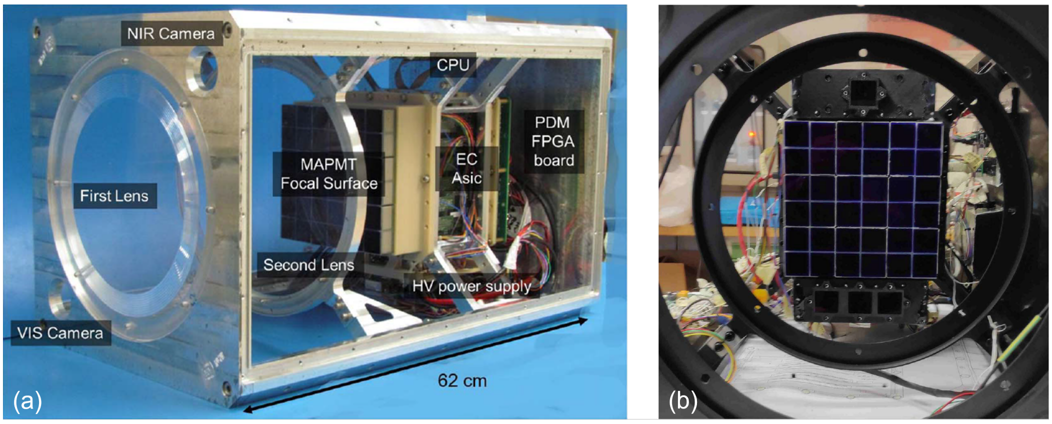

Fig. 3.13: (a) Mini-EUSO Engineering Model during its assembly, with the main elements visible and highlighted in the figure. (b) A picture of the focal surface (PDM) of Mini-EUSO, composed of 36 MAPMTs in 6 × 6 configuration, each one with 8 × 8 independent channels and for a total of 2304 px. The focal plane also houses two light sensors and a single-pixel SiPM used for day/night information.

from ∼57% down to ∼45% for large incident angles >20°, corresponding to the very edge of the focal surface (see Fig. 5 of Bacholle et al., 2021)

The Mini-EUSO focal surface (Fig. 3.13b) is also named *Photon Detector Module* (PDM) and consists of a matrix of 36 Multi-Anode Photomultiplier Tubes (MAPMTs, Hamamatsu Photonics R11265-M64), arranged in an array of 6 × 6 elements. Each MAPMT consists of 8 × 8 pixels, resulting in a total of 2304 channels. The MAPMTs are grouped in Elementary Cells (ECs) of 2 × 2 MAPMTs. Each EC has an independent high-voltage power supply (HVPS) and board connecting the dynodes and anodes of the four photomultipliers. The HVPS system is based on a Cockroft-Walton circuit. The system has an internal safety mechanism which removes the electric potential difference between the photocathode and the first dynode in case of a particularly bright signal (more than 3 pixels of an EC with more than 100 counts in a given GTU). This reduces the collection efficiency of the four MAPMTs. A second analogue safety system limits the current flowing from the Cockroft-Walton circuit to the EC, reducing the gain of the MAPMTs and eventually turning off the HV. This second mechanism protects the MAPMTs from bright and diffuse signals that would not reach 100 counts but invest many pixels. More details can be found in (Plebaniak et al., 2017). These statuses of reduced efficiency are called *cathode-2* mode (Cat2). The nominal working condition is instead called *cathode-3* mode (Cat3), which is the one assumed in the rest of the text unless differently reported. The switching from Cat3 to Cat2 is usually due to lightning strikes or to very bright light sources like large cities. The recovery to Cat3 takes place only few ms after the light level has decreased to a sufficiently low value, to avoid continuous oscillation between Cat2 and Cat3 when the light level is close to the switching value. The whole system (weighting 250 g per EC) is potted with Arathane and located in the back of the photosensor array.

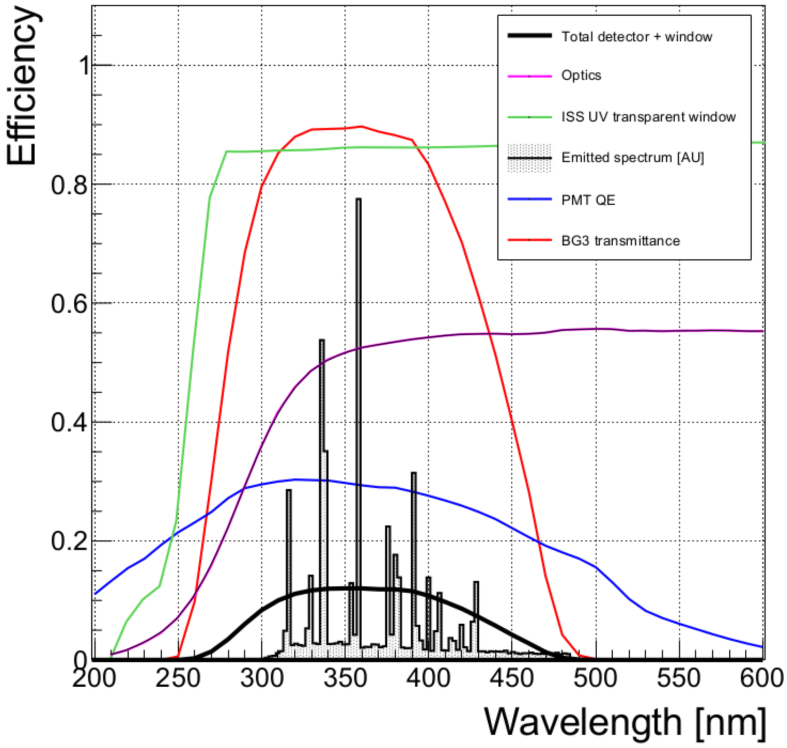

Fig. 3.14: Plot of the overall detection efficiency of the Mini-EUSO detector (black curve) as a function of wavelength. This is the result of the transmittance of the UV transparent window of the ISS (green curve), the optics (purple curve), the BG3 bandpass filter (red curve) and the MAPMT photon detection efficiency (blue curve). The detection efficiency of the MAPMTs has been obtained by rescaling the quantum efficiency curve provided by Hamamatsu by a typical collection efficiency of 80%. As a comparison, the grey histogram represents the typical emission spectrum of EASs (Bacholle et al., 2021).

The effective focal length of the system is 30 cm, with a PSF size of 1.2 px. UV bandpass filters (2 mm of BG3 material) with anti-reflective coating are glued in front of the MAPMTs to predominantly select wavelengths between 290 nm and 430 nm. Figure 3.14 plots the various contributions (coloured curves) to the overall detector efficiency of Mini-EUSO (black curve). The system has been designed to maximize observations of the fluorescence light emitted by nitrogen atoms excited by the EAS of cosmic rays (grey histogram). As shown in the figure, Mini-EUSO has a maximum total efficiency of about 12% at ∼350 nm, with values higher than 50% of the maximum in the wavelength range 290–430 nm. Complementary to this theoretical result, a series of UV flasher campaigns were deployed in the last two years to perform an end-to-end in-flight calibration of Mini-EUSO (Battisti et al., 2022b). To perform such calibration, a near-UV flasher emitting at 398 nm was designed and tested in the laboratory. During some Mini-EUSO data-taking sessions, this system was then transported to low light-polluted regions (mainly in Europe) over which the ISS was going to fly and switched on accordingly to the forecasted passage time. Analysis of the data taken during such campaigns pointed out an efficiency value of 8.0 ± 1.5%, slightly lower than the value evident from Fig. 3.14 at 398 nm of 10.6% (accounting also for the photon collection efficiency). Even if these results are still preliminary, values from the plot of Fig. 3.14 might be rescaled to account for this mismatch. Also, future flasher campaigns will confirm or correct these estimations.

The instrument is also equipped with two cameras, one in the near-infrared (1500–1600 nm) and one in the visible (400–780 nm) band, to provide additional information in different wavelength ranges. They are located in the corners of the plane, as shown in Fig. 3.13a for the Mini-EUSO EM. The instrumentation of Mini-EUSO also includes a 64-channel multipixel photon counter SiPM (Hamamatsu C14047-3050EA08) array, a single-pixel SiPM (Hamamatsu C13365), and two UV sensors (Analog Devices AD8304ARUZ, Lapis Semiconductor ML8511) used to retrieve day/night information. These sensors are located in the focal plane of the PDM (see Fig. 3.13b).

3.4.2 Data acquisition and format of Mini-EUSO

Acquisition, preamplification and digitalization of the signal from MAPMTs of Mini-EUSO are handled by the front-end electronics implemented in Spaciroc-3 ASICs (Blin et al., 2018). The instrument is operated in single photon-counting mode with a double pulse resolution of ~5 ns, to minimize the contribution of integrated noise. Photon counts are summed in Gate Time Units (GTUs) of 2.5 μs. The PDM Data Processor (PDM-DP) stores these 2.5 μs GTU data stream, named D1, in a running buffer over which the trigger code operates. The PDM-DP is based on a Zynq board containing a Xilinx FPGA and an embedded dual-core ARM9 CPU processing system (Bacholle et al., 2021). The trigger algorithm searches for a signal above 16 standard deviations from the average in any pixel of the focal surface. Both the average and root mean square are calculated in real-time to account for the continuous variation of the illumination conditions observed by the detector. In case of a trigger, a 128 frame buffer (64 frames before the trigger and 64 after it) is stored in memory. Independently from the trigger, sums of 128 frames (320 μs, D2) are calculated and stored in another buffer where a similar trigger algorithm, at this time scale, is continuously run. Similarly, sums on 128 D2 frames (40.96 ms, D3) are calculated and stored in real-time. Therefore, D3 frames represent a continuous data flow, since the acquisition of this timescale is not triggered. Every 5.24 s, 128 packets of D3 data, up to 4 D2 packets and up to 4 D1 packets (if triggers were present) are sent to the CPU for storage. The reader can refer to Belov et al. (2018), Capel et al. (2019), and Battisti et al. (2022a) for a more detailed description of the data acquisition and the trigger algorithm.

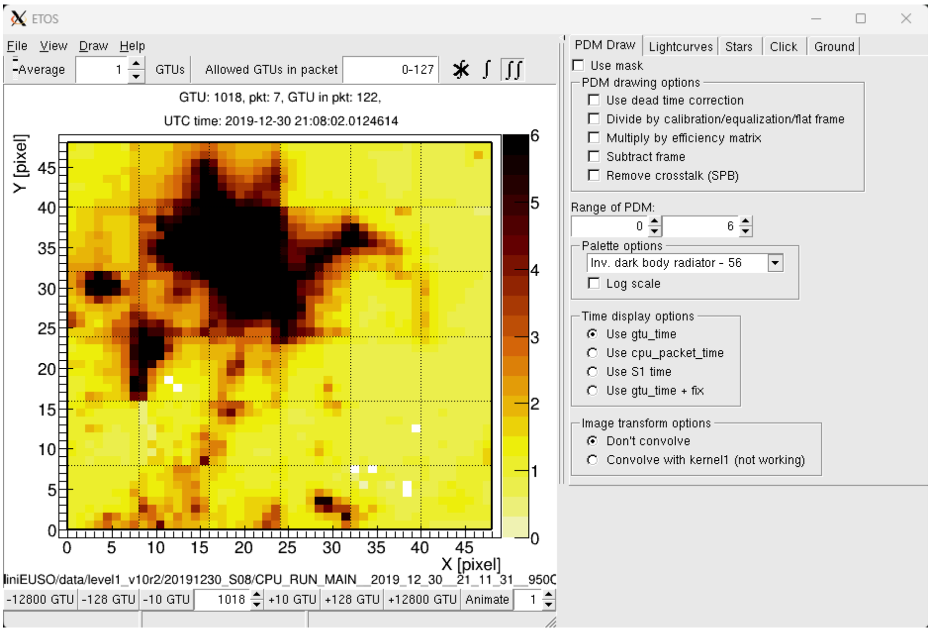

Average: 1 GTUs
Allowed GTUs in packet: 0-127

GTU: 1018, pkt: 7, GTU in pkt: 122,

UTC time: 2019-12-30 21:08:02.0124614

liniEUSO/data/level1_v10r2/20191230_S08/CPU_RUN_MAIN__2019_12_30__21_11_31__950C

GTU: 1018; Animate: 1

☐ Use mask

PDM drawing options
- ☐ Use dead time correction
- ☐ Divide by calibration/equalization/flat frame
- ☐ Multiply by efficiency matrix
- ☐ Subtract frame
- ☐ Remove crosstalk (SPB)

Range of PDM: 0 6

Palette options
- Inv. dark body radiator - 56
- ☐ Log scale

Time display options
- ● Use gtu_time
- ○ Use cpu_packet_time
- ○ Use S1 time
- ○ Use gtu_time + fix

Image transform options
- ● Don't convolve
- ○ Convolve with kernel1 (not working)

Fig. 3.15: The main windows of the ETOS (EUSO To Screen) visualization tool for Mini-EUSO data. In this capture, the count map of D3 data for a particular GTU of the 8th Mini-EUSO session is plotted, imaged on 30/12/2019 at 21:08:02 UT. At that time, the ISS was flying over South Africa, and the big dark spot visible on the map is the city of Pretoria, the administrative capital of the country, together with neighbouring cities. ETOS also allows visualization of D1 and D2 data, together with lightcurve plots and quick analysis of the data.

To overcome the bottleneck of the limited telemetry flow from the station, data sent to CPU are stored locally on 512 GB USB Solid State Disks (SSD) inserted in the side of the telescope by the cosmonauts at the start of each session. Although no direct telecommunication with the ground is present, samples of data (about 10% of stored data, usually corresponding to the beginning and the end of each session) are copied after each data-taking session and transmitted to the ground to verify the correct functioning of the instrument and subsequently optimize its working parameters. The pouches, containing 25 SSDs, are then returned to Earth every ∼12 months by Soyuz spacecraft. Raw data are therefore processed by the Mini-EUSO team and made available to the collaboration in the form of ROOT[23] files. Each of these files contains 3200 GTU D3 (∼131 s of acquisition) together with triggers from D1 and D2, if any. Conversion from CPU-format binary data to ROOT format and their visualization is made with ETOT (EUSO To Tree) and ETOS[24] (EUSO To Screen), an open-source software developed by the JEM-EUSO collaboration (Capel et al., 2019). Also, a wealth of useful metadata is added to the ROOT files, such as information about the time and the ISS position, speed and orientation, among all. An example of the ETOS visualization tool window for Mini-EUSO D3 data is shown in Fig. 3.15.

---

[23] This is a widely used format in high-energy particle physics, developed in the framework of the ROOT-CERN collaboration (`https://root.cern/`).

[24] `https://minieuso-software.readthedocs.io/en/latest/`

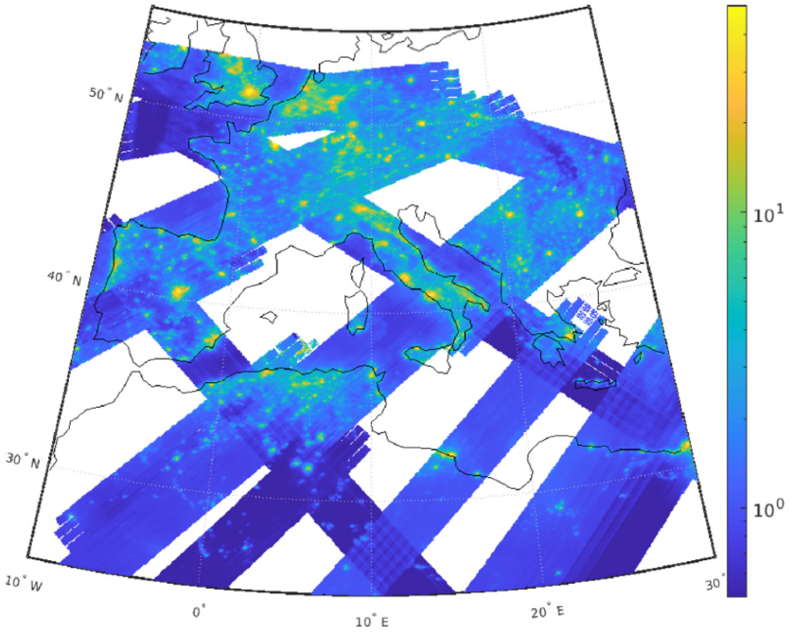

Fig. 3.16: Map of counts/GTU (plotted in logarithmic scale) in moonless conditions over parts of Europe and North Africa imaged by the Mini-EUSO telescope onboard the ISS. Note the relative darkness in areas over sparsely populated areas like the Sahara desert and the Carpathian and Apennine mountains (Casolino et al., 2023).

One of the peculiarities of Mini-EUSO observations is its multiple time resolutions, which allow the study of a wide range of atmospheric phenomena (see Sect. 3.3.3). D1 data at 2.5 µs are suitable to search for UHECRs, as they typically last hundreds of µs, or fast TLEs such as ELVEs, while the 320 µs of D2 data is appropriate for slower lightnings. The 41 ms time resolution of D3 data is well suited to capture much slower phenomena such as meteors, but also for bioluminescence studies, search for SQM, space debris, among others. Moreover, anthropogenic emissions such as towns, fishing boats, and flashers can be studied as well with Mini-EUSO. Fig. 3.16 shows the reconstruction of the UV emission map over parts of Europe and North Africa from available data of Mini-EUSO passages to date in these regions (Casolino et al., 2023). The map is given in D3 counts per GTU units on a logarithmic scale. If not stated otherwise, both D3 and D2 counts are normalized to the scale of D1 counts, accounting for the different integration times, so that the average counts per pixel per GTU are the same in all three timescales.

3.4.3 Test of the Mini-EUSO EM with PRISMA

Prior to the launch, the instrument underwent a series of integration and acceptance tests (Cambiè and Marcelli, 2019) in Rome, Moscow, and Baikonur cosmodrome, where it was integrated into the uncrewed Soyuz capsule. A systematic

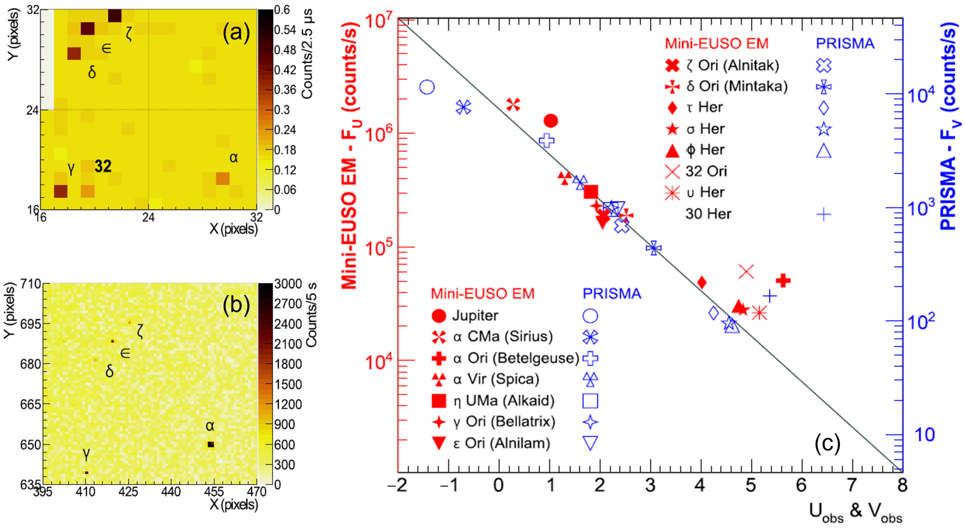

Fig. 3.17: Results of the test of the Mini-EUSO EM in open-sky conditions at the Osservatorio Astrofisico di Torino, with the PRISMA camera ITPI01. (a) Counts map of stars of the Orion constellation and Jupiter taken by the Mini-EUSO EM, integrated over a D3 frame of 41 ms. (b) Detail of the capture in the same FoV acquired by ITPI01 of 13/03/2018 at 20:09:16 UT, the closest in time in the PRISMA calibration dataset (5 s exposure) with respect to the time of Mini-EUSO EM observations. (c) Plot of comparison between experimental fluxes recorded by the two instruments (red for Mini-EUSO EM and blue for ITPI01) as a function of the U and V catalogue star magnitudes (Bisconti et al., 2022).

test of the acquisition logic was performed at the TurLab[25] facility of the University of Turin, where the Mini-EUSO Engineering Model (EM) was operated with a rotating tank of 5 m diameter designed for fluid-dynamics studies (Bisconti et al., 2022). The EM was mounted on the ceiling of the lab in a dark environment, pointing down and exposed to light sources and materials placed on the floor of the tank, to reproduce various phenomena that Mini-EUSO is able to observe from space. The rotation of the tank is able to simulate the apparent movement of ground sources, such as the ones visible from the ISS by the Mini-EUSO telescope. These tests allowed checking the general performance, the data acquisition and control software and the trigger system of D1 and D2 data.

The Mini-EUSO EM was also tested in open-sky conditions at the Osservatorio Astrofisico di Torino. During these observations, made on 13/03/2018, it was possible to detect stars, meteors, planets, and artificial light sources such as airplanes, satellites reflecting the sunlight, and city lights. The four meteors detected by the Mini-EUSO EM had an estimated magnitude of +4, being too faint to be triggered by the PRISMA camera ITPI01 installed on the roof of the observatory. However, it was possible to compare the data of stars imaged by the EM with the calibration captures of ITPI01. The simultaneous observations of stars, with the same atmospheric condition, allow a direct comparison of the observations made with the two detectors,

---

[25] `http://www.turlab.ph.unito.it/`

also in view of possible future simultaneous stereo detections of the same meteors by both Mini-EUSO from the ISS and PRISMA from the ground. In its FoV of $\sim 10^\circ \times 10^\circ$, the Mini-EUSO EM was able to detect 13 stars down to magnitude +5 in the U band, plus the planet Jupiter. Almost all these stars were also detected in the PRISMA capture from ITPI01. In fact, the limiting magnitude of the Mini-EUSO EM is similar to the one of PRISMA cameras, of about +4.5 in the V band. However, the EM is mode of only 1 EC and its lens size is 1/10 of that of Mini-EUSO, accounting for a light-collection efficiency ratio of about 1/100 between the EM and the actual instrument on the ISS. A detail of the Orion constellation seen by the Mini-EUSO EM and the PRISMA camera ITPI01 is pictured in Fig. 3.17a,b, while panel c plots the comparison of fluxes recorded by the two instruments as a function of the U and V magnitudes. The overall agreement is good, with few deviations that can be attributed to the differences in the bandwidth of the two instruments (see Sect. 3.1.3 and Sect. 3.4.1) combined with the specific colour index of each star, *e.g.*, for Betelgeuse (alf-Ori). For more details about these test campaigns, the reader can refer to Bisconti et al. (2022).

Analysis pipeline of PRISMA data

4

The analysis of data collected by a distributed network like PRISMA required significant efforts in developing an automatic and comprehensive data reduction pipeline. The network collects several tens of GBs of data on a daily basis, consisting of calibration captures and videos of detected events. During the PhD period, my work was indeed dedicated to developing reduction strategies and analysis procedures for the PRISMA data and implementing them in a fully functioning analysis pipeline, which is now operating on the servers installed at the INAF - Osservatorio Astrofisico di Torino. It consists of two main parts, dedicated to the two datasets of PRISMA. The first part handles the analysis of the dataset of calibration captures and returns a daily- and monthly-based astrometric and photometric calibration for each camera of the PRISMA network. These calibrations are therefore used to perform the analysis of the event data, consisting of four main steps: (1) astrometry and photometry reduction of each detection video, (2) triangulation of the detection results to compute the three-dimensional trajectory of the meteor, (3) application of a dynamic model to estimate the main physical parameters of the events and (4) computation of the heliocentric preatmospheric orbit of the meteoroid.

In this chapter, I will detail each step of this pipeline, giving the needed theoretical background and explaining how these methods were implemented and improved for the analysis of PRISMA data. The whole pipeline is written in IDL[1] v8.8 and makes extensive use of the IDL Astronomy User's Library[2] (Landsman, 1993), which contains very many routines for the analysis of astronomical data, and of the non-linear fitting routines (MPFIT) included in the Markwardt-IDL Library[3] (Markwardt, 2009), which implements the Levenberg–Marquardt (LM) optimisation algorithm (Levenberg, 1944; Marquardt, 1963; Moré, 1978) applied to chi-square minimisation. Together with the computation of the strewn-field for possible meteorite fragments, this pipeline allowed for the recovery of two meteorites on the Italian soil, which are Cavezzo on January 2020 and Matera on February 2023, presented in the next chapter of this manuscript.

---

[1] IDL - Interactive Data Language, Harris Geospatial Solutions, `https://www.l3harrisgeospatial.com/Software-Technology/IDL`

[2] `https://idlastro.gsfc.nasa.gov/`

[3] `https://cow.physics.wisc.edu/~craigm/idl/`

4.1 Calibration of PRISMA cameras

The astrometric (positional) and photometric (intensity) calibration of each PRISMA camera is essential to process the detection videos of meteors triggered by the network and triangulate their entry trajectory in the atmosphere. Laboratory calibration of each instrument would be highly impractical and require a disproportionate experimental effort, given the network extension. Also, the controlled laboratory environment is quite far from the actual open-air operative condition of PRISMA stations, which are continuously exposed to the greatly varying temperature and bad weather, such as wind, rain and ice in the winter season. Therefore, an on-field calibration of PRISMA cameras is made by comparing the measured position and flux of stars detected in the FoV with their catalogues coordinates and magnitude. As already introduced in Sect. 3.2.2, videos of detection acquired at a frame rate of 30 Hz do not show any stars, due to the limited exposure and performance of the camera module. Therefore, a set of 5 s exposure *captures* is acquired during the night, where stars are visible with a limiting magnitude of +4.5 approximately in the V band. Since the calibration sources are not visible in the same frame of the meteor, the approach of *differential* astrometry and photometry is not an option. Also, this approach is usually not preferable with the very large FoV of all-sky cameras, which astrometric solution must account for the heavy distortions that come with fish-eye lenses. On the other hand, we need to define an *absolute* calibration of the instrument, *i.e.*, a set of mathematical relationships enabling the conversion of measured pixel position on the CCD (x, y) and flux (counts/s) of identified sources to their catalogue position, usually expressed in angle coordinates (celestial - right ascension α and declination δ; or horizontal - azimuth a and zenith distance z) and apparent magnitude. The developed astrometric and photometric calibration methods for PRISMA cameras were published in two papers, Barghini et al. (2019b) and Barghini et al. (2019a).

4.1.1 Astrometry of all-sky cameras

The definition of an absolute astrometric model for an all-sky camera was first addressed by Ceplecha (1987) for the cameras of the CFN network at the Ondřejov observatory. He empirically deduced a parametric description that takes into account the heavy optical distortion in the zenith distance direction when progressively approaching the horizon:

$$z = U + Vr + Se^{Dr} , \tag{4.1}$$

where $r = \sqrt{(x - x_C)^2 + (y - y_C)^2}$ is the distance of the source from the centre of the camera $C = (x_C, y_C)$, V is the linear plate scale and U, S, D are the distortion parameters, modelled as an exponential function of the radius. For PRISMA cameras,

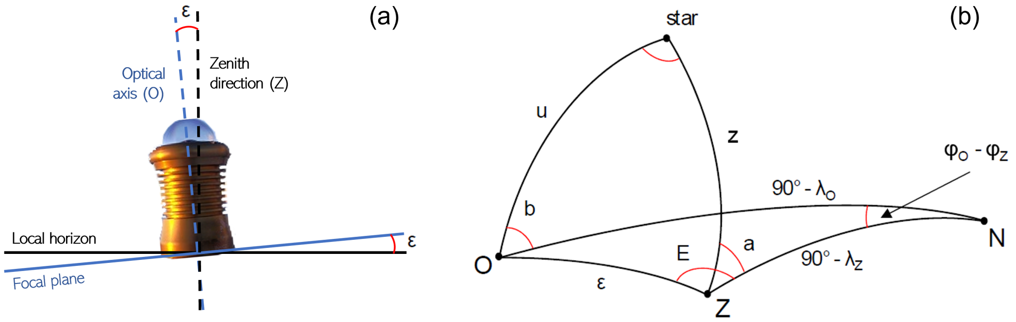

Fig. 4.1: (a) Graphical representation of the possible misalignment of the optical axis with respect to the zenith direction by a small angle ϵ. (b) Geometrical illustration of the optical centre (O), the zenith direction (Z) on the CCD, and corresponding projection coordinates (b, u) and horizontal coordinates (a, z) (Barghini et al., 2019b).

the typical plate scale $V \sim 10$ arcmin/px, so that one degree is covered by approximately 6 adjacent pixels. The projection in the azimuth direction is instead spherical, in a first approximation:

$$a = a_0 + \text{atan}\left(\frac{y - y_C}{x - x_C}\right) . \tag{4.2}$$

where a_0 is the local direction of the North. At first sight, the definition of the centre C is ambiguous and its physical interpretation is not straightforward. It could be interpreted as either the projection of the optical axis onto the focal plane $O = (x_O, y_O)$ or the direction of the local zenith $Z = (x_Z, y_Z)$. In Eq. 4.2 we are assuming that $C \equiv O \equiv Z$, while this is not given a priori. On the contrary, it is highly probable that the focal plane of the camera is not exactly aligned with the local horizon and therefore $O \not\equiv Z$. The geometry of this problem is presented in Fig. 4.1. This effect can result directly from the building over which the camera is installed, if not due to the camera mount itself. Even if this misalignment is usually small, of the order of fractions of a degree, it can lead to a significant bias on the final astrometric solution of the camera if not taken into account.

To this regard, refinements of the original astrometric model of Ceplecha (1987) have been proposed mainly by Borovička (1992) and Borovička et al. (1995). When the optical axis is not perfectly aligned with the local zenith direction, Eqs. 4.1 and 4.2 refer to projections coordinates (b, u) instead of to the horizontal celestial coordinates (a, z), as represented in Fig. 4.1b. If (E, ϵ) are the azimuth and zenith distance, respectively, of the optical centre O with respect to the zenith direction Z, then (b, u) and (a, z) are related through a translation in spherical coordinates as:

$$\begin{cases} \sin(a - E) = \frac{\sin b \sin u}{\sin z} \\ \cos z = \cos u \cos \epsilon - \cos b \sin u \sin \epsilon \ , \end{cases} \tag{4.3}$$

to be paired with the expression for the azimuth cosine:

$$\cos(a - E) = \frac{\cos u - \cos z \cos \epsilon}{\sin z \sin \epsilon} \; . \tag{4.4}$$

The explicit form of the transformation for the projection coordinates (b, u) can be given as:

$$\begin{cases} b = a_0 - E + \mathrm{atan}\left(\frac{y - y_O}{x - x_O}\right) \\ u = Vr + S(e^{Dr} - 1) \; , \end{cases} \tag{4.5}$$

where now r is computed with respect to the optical centre. Moreover, Borovička (1992) theoretically deduced that $U = -S$. Therefore, the explicit transformations to compute (a, z) from (b, u) are:

$$\begin{cases} a = E + \mathrm{atan}\left(\frac{\sin b \sin u}{\cos u \sin \epsilon + \cos b \sin u \cos \epsilon}\right) \\ z = \arccos(\cos u \cos \epsilon - \cos b \sin u \sin \epsilon) \; . \end{cases} \tag{4.6}$$

Considering Eqs. 4.5 and 4.6, the resulting astrometric model consists of $M = 8$ parameters $(a_0, x_O, y_O, E, \epsilon, V, S, D)$ to be estimated. Borovička (1992) reported some issues and advice to manage the convergence of the estimation algorithm. Other authors reported similar issues in the determination of the parameters of this model. For example, Bannister et al. (2013) proposed a polynomial representation for u rather than the exponential of Eq. 4.1, for the NMSU SkySentinel[4] cameras. Equations 4.5 and 4.6 are strongly non-linear, and some parameters are not independent from each other (see Sect. 4.1.3).

4.1.2 Source identification and catalogue correlation

Captures are analysed on a daily basis, considering Julian days (from 12 AM to 12 AM of the next day) to include the whole night in the same set of images. The goal is therefore to compute an astrometric solution for each night of observation of each camera, if the weather and cloud coverage allows for the identification of any star. The first task to be performed is the identification of the bright sources in each frame during the night and the correlation of these sources with a reference catalogue, that is, the definition of the list of associations $(x, y) \leftrightarrow (a_{cat}, z_{cat})$. The reference astrometric catalogue is built through a query to the SIMBAD[5] astronomical database (Wenger et al., 2000). The Hipparcos (Perryman et al., 1997) and Tycho catalogues (Høg et al., 1997) are the main sources of stellar positions in SIMBAD; in particular, the Tycho-2 catalogue (Høg et al., 2000) provides equatorial coordinates of stars with $V_T < +9$ with standard errors of about 7 mas. The much higher precision achievable nowadays by GAIA, of the order of tens of μas (Gaia Collaboration et al.,

---

[4] skysentinel.nmsu.edu/allsky

[5] http://simbad.cds.unistra.fr/simbad/

2016), is not necessary for our purposes. In any case, GAIA performances on bright stars are poorer, and GAIA DR3 does not include stars with magnitude $G < 1.7$ (Gaia Collaboration et al., 2021). The catalogue built in this way provides celestial equatorial coordinates (α, δ) of stars up to magnitude +6 in the V band in FK5 reference frame at J2000 epoch, which are therefore projected into local horizontal coordinates (a, z) at the epoch of observation. For this purpose, we use the EQ2HOR[6] procedure provided by the IDLAstro library of NASA, which performs precession, nutation, aberration and refraction corrections and it is typically accurate to about 1 arcsecond or better.

At most a few hundred stars are detectable with optimal conditions of sky brightness (corresponding to a limiting magnitude of about +4.5), therefore the definition of the complete astrometric solution cannot be performed at this level because the sky vault is poorly sampled. For this same reason, we do not need an accurate astrometric solution to build the list of associations because the sky vault is not too crowded with stars. We therefore use the following simplified astrometric model:

$$\begin{cases} a = a_0 + \text{atan}\left(\frac{y-y_C}{x-x_C}\right) \\ z = F\,\text{arcsin}\left(\frac{r}{R}\right) \ , \end{cases} \tag{4.7}$$

which only depends upon five parameters and takes into account only one centre of symmetry C, providing residuals in $|a - a_{cat}|\sin(a_{cat})$ and $|z - z_{cat}|$ as large as 2°. The five parameters (a_0, x_C, y_C, F, R) can be easily estimated starting from the frame size and the known approximate radial plate scale of about 10 arcmin/pix. Thus, convergence can easily be achieved even with a small number of stars per frame. For the station ITPI01 - Pino Torinese, and similarly in all the other cameras of the network, the residual minimisation algorithm returns values of $F = 1.9 \pm 0.1$ and $R = 650 \pm 20$ px. These values are consistent with an *equisolid* projection, for which nominal values are $F = 2$ and $R = 2f/d_{px} = 667$ px, being $f = 1.25$ mm the focal length of PRISMA cameras and $d_{px} = 3.75$ µm the pixel size of the CCD. Furthermore, it is easily shown that $F = V \cdot R$. This implies that PRISMA cameras adhere to equisolid projection within the tolerance of 2°. Because the agreement is not exact, F and R are not fixed to their nominal values in order to provide the minimum residuals for stars associations. We prefer this description for z over the one proposed by (Bannister et al., 2013) because it allows star associations up to the local horizon with only two parameters, while a second-order polynomial barely reaches $z \simeq 70^\circ$and required higher orders to achieve the same performance.

Identification of stars and their association with catalogue positions are therefore performed through a pipeline designed to be fully automatic, after a first initialization where the basic parameters of each camera are inputted by the user on a configuration file. Such parameters are the approximate orientation of the camera with respect to the local North direction, *i.e.*, an approximate value for a_0, a rough

---

[6] `https://idlastro.gsfc.nasa.gov/ftp/pro/astro/eq2hor.pro`

estimation of the centre of the frame $C = (x_C, y_C)$ and the geographical coordinates of the station. The details of this procedure are presented in Barghini et al. (2019b). In summary, a median flat frame is computed in order to normalise each frame with respect to the mean brightness spatial distribution, which is substantially varying within the all-sky FoV of the camera because of bright sources near the horizon due to neighbouring lights and cities. This allows scaling all the pixels in the FoV to an average value of unity, and the threshold limits can be set independently of the mean sky brightness of the single frame. This artificial flat normalization is also performed to remove stationary sources of noise, while non-stationary ones are cancelled through the application of a mask usually covering the last 5° above the horizon. Even if the camera specifications provided by the manufacturer report negligible spatial noise, this operation provides a partial correction for differential pixel gain and offset because no flat-fielding calibration is available during operations. The search for stars in the FoV is made through the FIND[7] procedure of the NASA IDLAstro library, which implements marginal distribution fitting for the centring algorithm of bright sources. To account for different conditions of sky noise, we also compute an estimation of the standard deviation σ_b of sky background fluctuations by means of 100 × 100 px moving 2D median absolute deviation over each image. Detection limits can be therefore set as a function of the normalized positive excess $\delta = (h - b)/\sigma_b$, where h is the height of the PSF of the star (on the flat-fielded image) and $b \simeq 1$ is the local sky background. This last normalization enables to automatically discard most of the false positives due for example to the passage of clouds at a particular time during the night, which otherwise would enter into the astrometric processing and negatively impact its performance with an increased fraction of outliers. An empirical limit of $\delta = 4$ was found to be appropriate for all the cameras of the PRISMA network, regardless of the particular sky brightness conditions of each station's site.

Once the list of bright sources positions (x, y) is obtained, we consider the reference star catalogue and compute the expected position of each star onto the frame, by means of the inverse astrometric projection of catalogue coordinates from Eq. 4.7 as:

$$\begin{cases} x_{cat} = x_C + r_{cat}\cos(a_{cat} - a_0) \\ y_{cat} = y_C + r_{cat}\sin(a_{cat} - a_0)\ , \end{cases} \tag{4.8}$$

where $r_{cat} = R\sin(z_{cat}/F)$. This allows to spatially match the two lists of (x, y) positions registered on the frame to the catalogue (a_{cat}, z_{cat}) coordinates by means of the expected position (x_{cat}, y_{cat}) by a simple proximity criterion. This algorithm is implemented in an iterative way. Starting from very bright stars identified with $\delta > 16$, the magnitude limit in the catalogue is progressively increased from +2 to +5 as the indeterminacy on the model parameters becomes smaller. The correlation radius for the association $(x, y) \leftrightarrow (x_{cat}, y_{cat})$ is also reduced, from 15 to 5 px. At

---

[7] `https://idlastro.gsfc.nasa.gov/ftp/pro/idlphot/find.pro`

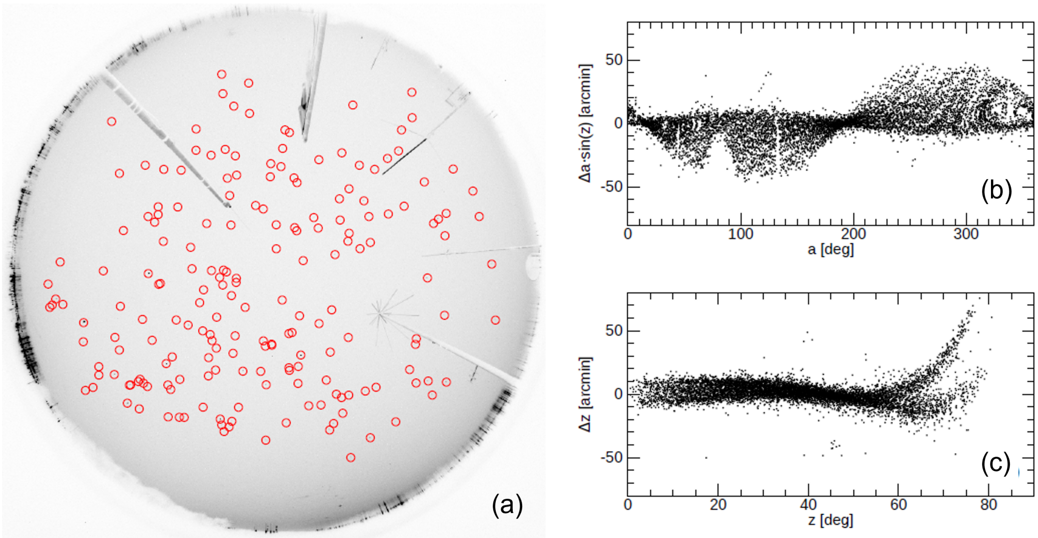

Fig. 4.2: Results of the stars identification and their catalogue association for one night (05/01/2017) of captures of the ITPI01 camera of PRISMA. (a) Image of one capture, acquired at 00:16:12 UT (5 s exposure), where red circles enclose the sources associated with catalogue positions ($N_* = 191$). The image is oriented with N direction approximately corresponding to the positive abscissa axis and E direction to the positive ordinate axis. (b) Azimuth residuals for the whole night, with respect to the simplified model of Eq. 4.7. (c) Same as (b), but for zenith distance residuals (Barghini et al., 2019b).

each step, the catalogue projection is implemented with the updated projection parameters of the step before. Iterations stop when the number of identified stars and the projection parameters values become stable with respect to the imposed tolerance limits, of 1% relative variation between two subsequent steps, or if the number of iterations exceeds 20. Also, captures with less than 20 identified and correlated stars are discarded.

Figure 4.2 shows the final results of this correlation algorithm, where panel a plots the identified stars in one capture of the night of 05/01/2017 of the ITPI01 night, and panels b and c plot the astrometric residuals for the whole night. Significant systematic deviations in the residuals are evident even if confined to $\pm 1°$, as it could be expected due to usage of a the simplified model for the sources identification process. As discussed in Barghini et al. (2019b), the shape of these systematics is primarily due to the fact that $O \not\equiv Z$ while, in this first step, we assumed only one projection centre as C. Also, an evident bias is present in the zenith distance residuals for $z > 60°$, pointing out that the model of the equisolid projection is not sufficient to precisely account for the radial distortion of PRISMA cameras. It has also to be noted that no stars are visible in the first 10° above the horizon, for $z > 80°$. This is mainly due to light pollution, together with the radial counting efficiency loss of the optical system (see Sect. 3.1.3). This limit is generally valid for PRISMA cameras located nearby populated cities, for which the horizon is polluted by incoming artificial lights. In a few cases, for cameras located in darker places, stars are detected down to $z \sim 85°$.

4.1.3 Determination of the astrometric solution

The next step is the derivation of the complete astrometric solution of Eqs. 4.5 and 4.6, that is, the determination of the value of their 8 projection parameters. Any optimisation algorithm requires a proper estimate of the starting point to ensure convergence of the output parameters, especially for complex and non-linear mathematical relations such as those we are dealing with here. In this case, some estimates come easily from the parameters computed during the star association procedure. The parameter a_0 is the local direction of the North and its meaning is the same in both models, so that a good estimate is already provided. Similarly, an estimate of V is given by F/R. This value can be used to compute estimates for (S, D) assuming that $z \simeq u$ and performing an exponential regression with respect to the residuals $\Delta z = z - Vr = S(e^{Dr} - 1)$. The main complication comes with the remaining 4 parameters, which are (x_O, y_O, E, ϵ). The first problem is that the simplified model provides an estimation for an "artificial" centre of projection C, but two centres exist, the optical centre O that (b, u) refers to, and the zenith direction Z that (a, z) refers to. Because C does not have a direct physical meaning, we expect that it will lie somewhere between O and Z. The distribution of computed positions of C for the 2017-2018 calibration statistics of the ITPI01 camera is presented in Fig. 4.3a, showing that x_C and y_C are correlated. In Barghini et al. (2019b), we showed that the inclination of such 2D distribution is a good estimate for the parameter E, that is the azimuth of the O with respect to Z. Nevertheless, we cannot derive an estimate for the value of ϵ from this evidence, which also relies on a yearly statistics and it is not feasible on the calibration data of one day only.

We solved this impasse by adopting a different approach. It must be noticed that the 4 parameters (x_O, y_O, E, ϵ) are clearly mutually dependent, since they express the position of two centres on the focal plane by giving the coordinates of the first (O) and its polar distance from the second one (Z). This heavy correlation is also a problem in the framework of any optimization algorithm, where all the parameters are required to be independent of one another to ensure convergence. Therefore, we adopted a new parametrization of the model of Eqs. 4.5 and 4.6, where the coordinates (x_Z, y_Z) of Z are explicitly given instead of (E, ϵ). This requires adding a new set of equations, coming from the definition of:

$$\begin{cases} E = a_0 + \text{atan}\left(\frac{x_O - x_Z}{y_O - y_Z}\right) \\ \epsilon = Vr_\epsilon + S(e^{Dr_\epsilon} - 1) \ , \end{cases} \tag{4.9}$$

where $r_\epsilon = \sqrt{(x_O - x_Z)^2 + (y_O - y_Z)^2}$. A direct benefit of this new parametrization is the possibility of independently determining an estimate of the coordinates (x_Z, y_Z). This can be done, for example, by analysing meridian crossings of stars identified on the considered night of acquisitions. From the catalogue associations

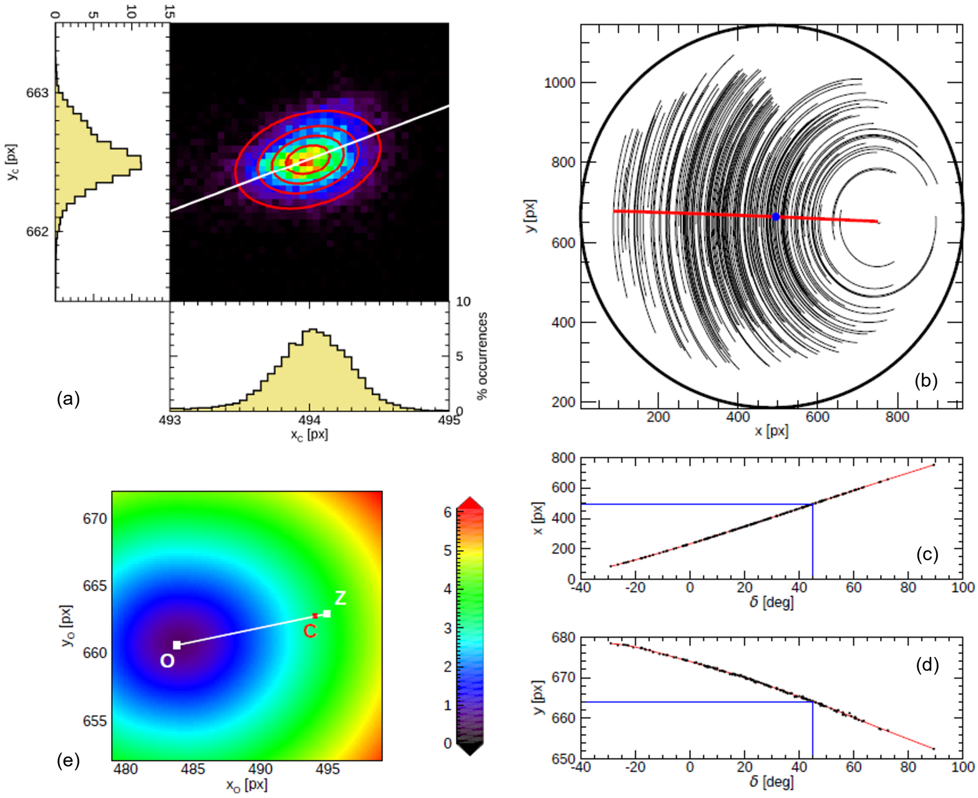

Fig. 4.3: Estimation of the centres of projection for the ITPI01 all-sky camera of the PRISMA network. (a) Distribution of computed positions of the projection centre $C = (x_C, y_C)$ of the simplified model of Eq. 4.7 derived from the 2017–2018 statistics of calibration data. Contours lines are plotted in red and the tilt direction of the distribution (white line) corresponds to the azimuth E. (b) Local meridian (red line) and zenith position (blue dot) on the CCD, identified by the interpolation of the trajectories of stars (black lines) for the night of 05/01/2017. (c) Declination vs. x pixel position of the observed crossings of the local meridian (black dots), spline interpolation (red line) and evaluation of x_Z value (blue); (d) Same as (c), but for y_Z determination. (e) Map of the sum of the residuals χ_{LAV} (Eq. 4.10) for the night of 05/01/2017, showing an evident minimum ($\chi_{LAV} \sim 1$) at about 12 px distance from Z and indicating the initial guess for the coordinates of the optical centre O (Barghini et al., 2019b).

list, the path of each star during the night can be extracted, sampled every 10 min, that is, each 2.5° of hour angle. The meridian crossings can be evaluated when the local sideral time is equal to the right ascension α of the star. The result is a set of coordinates (x_m, y_m) that describes the local meridian projected onto the CCD plate as a function of declination δ. An example is given in Fig. 4.3b for data of the ITPI01 camera of the night of 05/01/2017; the interpolation of (δ, x_m) and (δ, y_m) allows to retrieve the zenith direction (x_Z, y_Z) evaluated for δ equal to the geographic latitude λ_z of the observational site, as shown in Figs. 4.3c,d. At this point, it is also possible to determine an initial estimate for (x_O, y_O) by varying the position of O around Z and requiring the minimisation of residuals $\Delta a \sin z$ and Δz. An example of the results of this processing is shown in Fig. 4.3e.

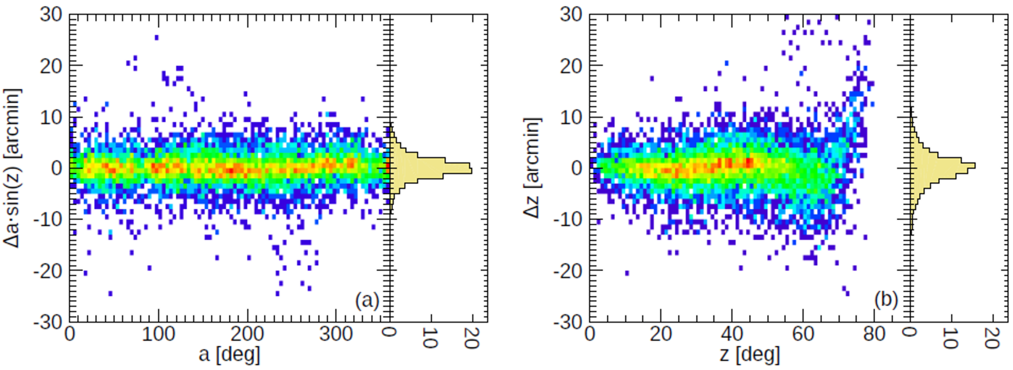

Fig. 4.4: Bi- and mono-dimensional residuals distribution of the full astrometric model of Eqs. 4.5, 4.6 and 4.9 fitted on the data of the night on 05/01/2017 for the ITPI01 station of PRISMA ($N_* = 8300$), for azimuth (a) and zenith distance (b). The colour scale of 2D histograms is log-stretched to ease the visualization of the distribution (Barghini et al., 2019b).

This procedure is therefore used to automatically compute a first estimation for each parameter of the full astrometric model, which is fitted over the list of associations by a LM optimisation algorithm (see the introduction of this chapter). The residual histograms for azimuth and zenith distance obtained with the fitting of this new parametrisation are shown in Fig. 4.4. Both histograms show residuals well distributed around zero, with a standard deviation of about 2 and 3 arcmin for $a \sin(z)$ and z respectively, and are characterized by a small excess kurtosis of $\sim$3. Also, a small fraction (<1%) of outliers is evident resulting from incorrect associations of the correlation procedure described in Sect. 4.1.2, typically coming from false positives of the source search algorithm. This is an expected drawback of any automatic procedure and problems of this kind will be common during the definition of the entire pipeline. To treat the presence of these outliers, and also because of the non-Gaussianity of the residuals, we implement a weight-reduction scheme. We choose to modify the L^2-norm of the ordinary least-squares (OLS) by adopting the L^1-norm of the least absolute value (LAV) regression (Narula and Wellington, 1982; Dielman, 2005). In the case of the astrometry fitting the ordinary chi-square is transformed into the following expression:

$$\chi_{LAV} = \sum_{i=0}^{N_*-1} \frac{|a(x_i, y_i, \vec{p}) - a_{cat,i}| \sin(z_{cat,i})}{\sigma_{a,i}} + \sum_{i=0}^{N_*-1} \frac{|z(x_i, y_i, \vec{p}) - z_{cat,i}|}{\sigma_{z,i}} , \quad (4.10)$$

where $\vec{p}$ is the vector of projection parameters. If not stated otherwise, we will always use the LAV regression when fitting models over data for the whole PRISMA pipeline. LAV is an efficient estimator like OLS, has low variance in the case of heavy-tailed residual distributions and is provided with control bias in the case of large samples. Because of these features, LAV is preferable over OLS minimisation to reduce the bias induced by vertical outliers.

4.1.4 Random and systematic error analysis

Error quantification is a very important aspect to be discussed in the framework of astrometric calibration. In fact, the uncertainty in the horizontal celestial coordinates measured for the bolide's positions through time (see Sect. 4.2.1) is the first and main driver for the determination of the confidence range for all the physical parameters of the observed event, such as the pre-atmospheric mass, velocity and radiant, among all. As for an example, the relative extension of these ranges will affect the precision with which one can determine the final mass of the meteoroid after ablation, a crucial information when deciding if it is worth searching for meteorite fragments on the ground, and the extension on the ground of the strewn-field area. Finally, the computation of the pre-atmospheric orbit of the meteoroid is highly sensitive to small variations of the radiant coordinates and geocentric velocity, so a precise and unbiased determination of those is desirable. Granvik and Brown (2018) recommended a precision in the measured speed of order 0.1 km/s to be able to infer significant links between meteorites and their pre-impact heliocentric orbits, ultimately pointing towards their source regions in the Solar System. The importance of an appropriate uncertainty quantification is also discussed in Chap. 7, when dealing with the identification of candidates of interstellar meteoroids in currently available databases of meteors observations.

The indeterminacy introduced by the astrometric calibration has two main contributions: (1) the random component, driven by the measurement error on calibration sources, and (2) the systematic component due to possible model inadequacy, for example, related to the parametrization of radial distortion. An in-depth analysis of the astrometric uncertainty for PRISMA cameras is given in Barghini et al. (2019b).

The astrometric performance of PRISMA are constrained by the limited resolution of the equipped CCD. Given the specification of the optics (see Sec. 3.1.2), the full-width at half-maximum (FWHM) of star's PSF on the focal plane is of the order of 0.5 to 2 arcmin, taking into account the 5 s integration time that introduces a variable smearing due to their apparent movement on the celestial dome. Since the pixel size is of about 10 arcmin, we are operating in a heavy undersampling regime. This is confirmed by a visual inspection of the imaged PSF of stars on captures, which usually display all the signal confined in just one pixel and, in some cases, up to a maximum of 4 adjacent pixels depending on the relative position of the star with respect to the CCD lattice. The main drawback of these operative conditions affects the achievable precision of centroiding algorithms. Since the vast majority of the light from a star is focused on one pixel only, the positional precision is of the order of the pixel size, being nominally 0.5 px. To verify this intuitive conclusion, we designed simulations to test the performance of the most

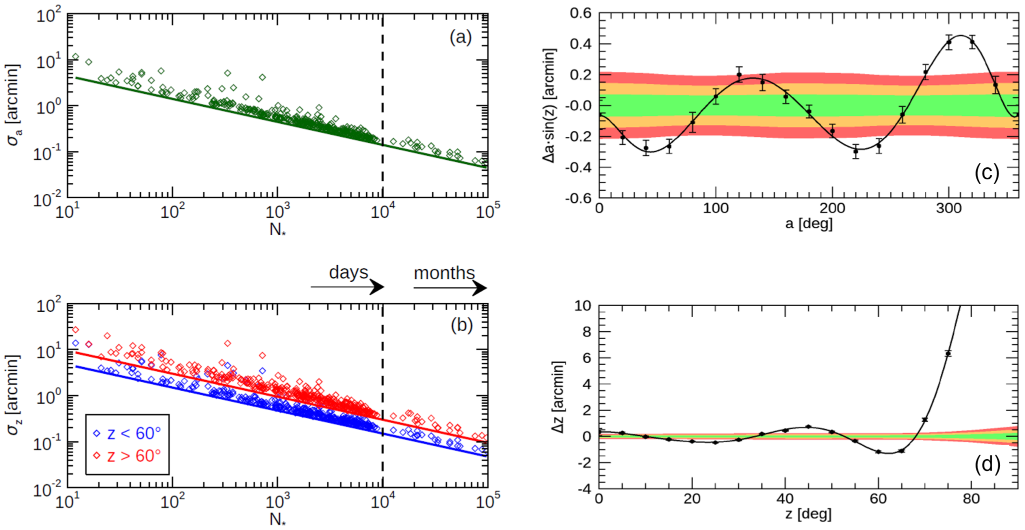

Fig. 4.5: Analysis of random projection error (RPE) and systematic projection error (SPE) for the 2017-2018 statistics of calibrations of the ITPI01 camera of the PRISMA network. (a) RPE values for the azimuth component plotted as a function of the calibration sample size (N_*), for daily and monthly statistics. (b) Same as (a), but for the zenith distance component. In this case, the data are presented for $z < 60^\circ$ (blue) and $z > 60^\circ$ (red) separately to outline the plate scale degradation close to the horizon. (c) Azimuth SPE values computed for the month of January 2017 (black) compared with RPE confidence intervals (green: 1σ, orange: 2σ, and red: 3σ). (d) Same as (c), but for zenith distance systematic residuals (Barghini et al., 2019b).

used centroiding algorithms[8] in this peculiar undersampling condition, which are detailed in Barghini et al. (2019b). These simulations confirmed our initial thoughts and showed residuals, for the measured position of the PSF's centre with respect to the simulated signal, with a standard deviation between 0.2 to 0.4 px. From these results, we always attribute an uncertainty of 0.3 px to the measurement of (x, y) positions of stars imaged on captures and identified as detailed in Sect. 4.1.2.

These uncertainties are therefore fed to the LM optimisation algorithm, modified for LAV estimates, for the fitting of the complete astrometric solution as described in Sect. 4.1.3. The covariance matrix of the fitted parameters' space is given as an output of this fitting procedure and allows us to evaluate the *random projection error* (RPE). This represents the uncertainty on the computed astrometric positions due to the model parameter indeterminacy resulting from the optimization algorithm itself. The magnitude of RPE is driven by the single measurement error, discussed in the paragraph above, and the size of the calibration sample N_*. Figure 4.5a,b plots RPE values averaged on the FoV in the $a \sin(z)$ and z components respectively, as a function of N_*, derived from the 2017-2018 statistics of calibrations of the ITPI01 camera. For the zenith distance component, the average was subdivided for

---

[8] We tested four centroiding algorithms: (1) simple barycentre; (2) filtered barycentre, computed by preserving only pixels with values 3σ over the sky median; (3) derivative search; and (4) marginal distribution fitting, implemented in the FIND procedure we adopted to identify bright sources on PRISMA captures.

$z < 60^\circ$ (blue points) and $z > 60^\circ$ (red points), given the significant change of the pixel scale close to the horizon. Values on these plots are mildly scattered above the expected square root dependence, plotted as solid lines in both panels. The RPE for $N_* = M + 1$ is of the order of few arcmin and is comparable to the single measurement precision of 0.3 px $\simeq$ 3 arcmin estimated from simulations. This is also fully compatible with the standard deviation of residuals' distribution plotted in Fig. 4.4. These two evidences strongly denote and confirm the self-consistency of the implemented procedure and the pertinence of the error treatment within the pipeline. Dashed lines on the plots mark the regions of daily and monthly statistics. A daily-based calibration for the ITPI01 camera has a maximum of 10k stars and provides an RPE as lower as $\sim$0.2 arcmin in the best case, while a monthly-based one contains 10k–100k stars and allows to reach an RPE of the order of tens of arcsec.

The magnitude of the RPE achievable with different calibration statistics is to be compared with the astrometric uncertainties on event data. In particular, the main requirement on the astrometric model is that the introduced RPE has to be negligible with respect to the single measurement error of the bolide position. In Barghini et al. (2019b), we discussed this aspect based on results from simulations and real meteors data from the PRISMA network. Because the extension of the PSF of meteors is usually of few pixels, undersampling is not an issue in this case. On the other hand, we now have to deal with additional problems such as strong PSF asymmetries and saturation of the bolide's images (see Sect. 4.2.1). Due to these limitations, we can achieve a precision of 1/20 px in the best observative conditions for the centroiding of bolide's PSF, corresponding approximately to 0.5 arcmin. Therefore, this requires a calibration sample of the order of 10^4 star associations, according to the results of Fig. 4.5a,b. In general, a monthly statistics is sufficient to provide quality astrometry.

Finally, addressing the systematic projection error (SPE), one may have already noticed that some significant deviations are evident for the residuals plotted in Fig. 4.4. An example of SPE values as a function of a and z for a monthly calibration statistics of ITPI01 is shown in Fig. 4.5c,d compared to the RPE (coloured bands). These are computed as the average of $\Delta a \sin z$ and Δz within fixed intervals. In addition to the model presented in Sect. 4.1.1, this result is already corrected for the minor but still significant effect of optical plate misalignment that causes the azimuth projection to be elliptical rather than spherical, requiring two more parameters to be added to the model. These are the amplitude K and phase ϕ of the sinusoidal correction of the computed distance of the source with respect to O, as proposed by Borovička et al. (1995):

$$r = [1 + K \sin(b + E - \phi)] \sqrt{(x - x_O)^2 + (y - y_O)^2}\,, \tag{4.11}$$

that is therefore used in Eq. 4.5 to compute the intermediate projection coordinate u. Even with this additional correction, a residual SPE is still evident. One systematic in azimuth is clearly visible in Fig. 4.5c with a period of 180° and modulated in amplitude. This could be related to optical aberrations affecting the fish-eye lens and/or mechanical stresses due to the holding system, which is not given to be symmetrical in azimuth. A much more significant SPE is evident in the zenith direction, plotted in Fig. 4.5d. As a matter of fact, Borovička et al. (1995) introduced an additional correction term also for this kind of systematics, adding to the radial distortion model of Eq. 4.5 an exponential term of argument r^2 and requiring two more parameters for the complete astrometric model:

$$u = Vr + S(e^{Dr} - 1) + P(e^{Qr^2} - 1)\ . \tag{4.12}$$

By adopting this correction, Borovička et al. (1995) was able to improve the accuracy of the projection for $z > 75°$ for the astrometric reduction of the cameras of the European Fireball Network. It is to be noted that, while being significant with respect to the RPE, the residual SPE plotted in Fig. 4.5c,d for the PRISMA case is always within the pixel size, given the plate scale degradation from 10 arcmin/px at the zenith to almost 20 arcmin/px at the horizon. Also, our cameras are not able to detect stars in the last 10° above the horizon. Because of these reasons, we prefer a numerical correction to account for these residual systematics, rather than adding a new complexity level to the mathematical expression of the astrometric solution, like the one of Eq. 4.12. This is implemented for both a and z by tabulating SPE values, as from Fig. 4.5c,d and adding them over the analytical projection results of the analytical astrometric model of Eqs. 4.5, 4.6 and 4.9. This is also done having in mind the possible future implementation in the network of different types of all-sky cameras, with different optics from the currently deployed model, which may show a different SPE with respect to the radial distortion model. For example, Hughes et al. (2010) considered several analytical lens models and highlighted that an ad hoc correction is always required regardless of the nominal distortion model that is applied, mostly due to manufacturing tolerances.

4.1.5 Variation of astrometric parameters with time

The error analysis presented in the previous section suggests that we should use a monthly astrometric calibration at least, to be able to reach a negligible RPE with respect to single measurement error on the bolide's PSF position on event data. Then, we may ask ourselves if the projection parameters of the complete astrometric solution can be considered constant during this time interval. On the other hand, we also have to understand whether they vary on a longer timescale, to know how often one needs to update such calibration in order to avoid the introduction of systematics in the event analysis.

Figure 4.6 shows the plots of the 10 parameters of Eqs. 4.5, 4.6, 4.9 and 4.11 as a function of time for the astrometric calibration of the ITVA01 - Lignan camera of PRISMA, from 2017 to 2021. This is one of the earliest cameras installed in the network in 2017, after ITPI01 in Pino Torinese. ITVA01 is located in the Aosta Valley near the Astronomical Observatory of Saint Barthélemy, one of the best observative sites of PRISMA in terms of sky brightness and light pollution. In each plot, the black dots represent parameter values from the daily calibration whereas the red ones come from the monthly calibrations. A significant trend is visible from the first five parameters, being the North direction a_0 and the (x, y) coordinates of the two centres O and Z. For example, the value of x_O varied from 512.2 px at the beginning of 2017 down to 511.2 px at the end of 2021, with an overall variation of $\sim$1 px. Even if being a very small variation, we have to consider that 1 px corresponds to an angle in the sky of approximately 10 arcmin. Such difference, projected at a 100 km distance (the typical altitude of meteors) corresponds to $\sim$300 m, which is surely not negligible when dealing with the triangulation of the meteor's trajectory. The observed trend may be due to the progressive adjustment of the camera mount system on the support surface of the building where it is installed, or by the slow movement and settling of the building itself on the ground, but these hypotheses are merely speculative. Also, a seasonal variation with a period of about 1 y is evident for the parameters (x_O, y_O, x_Z, y_Z). These oscillations may be induced by thermal expansion effects during the year. A similar explanation may hold also for the slight oscillation, less than 0.2% in amplitude, of the linear plate scale V which has a phase similar to the variations of the projection centres' coordinates. On the other hand, the variations of the parameters S and D of the fish-eye distortion are strongly correlated and also anti-correlated with V, as evident from the respective plots of Fig. 4.6. From daily astrometric results, S and D are usually determined with a correlation coefficient $|\rho_{SD}| > 0.9$, and this is also true for ρ_{VS} and ρ_{VD}. Therefore, their oscillations may be purely artificial and related to the variations of V. These strong correlations, originating from the mathematical model of the distortion, are also another reason that led us to prefer not implementing the additional exponential term of Eq. 4.12, since this would have introduced an even larger correlation degree into the model. Finally, the parameters K and ϕ of the elliptical projection of Eq. 4.11 do not show significant variations at first sight. This is probably because they are related to the least significant correction in the complete astrometric model and are determined with the largest uncertainties.

From this evidence, we understand that we need to update the calibration parameters every few months, at least. Systematic trends and seasonal oscillations were observed for the vast majority of PRISMA cameras. For the sake of simplicity, the pipeline implements an automatic updating of the calibration parameters at the end of each month for each camera, after the monthly astrometric solution is computed.

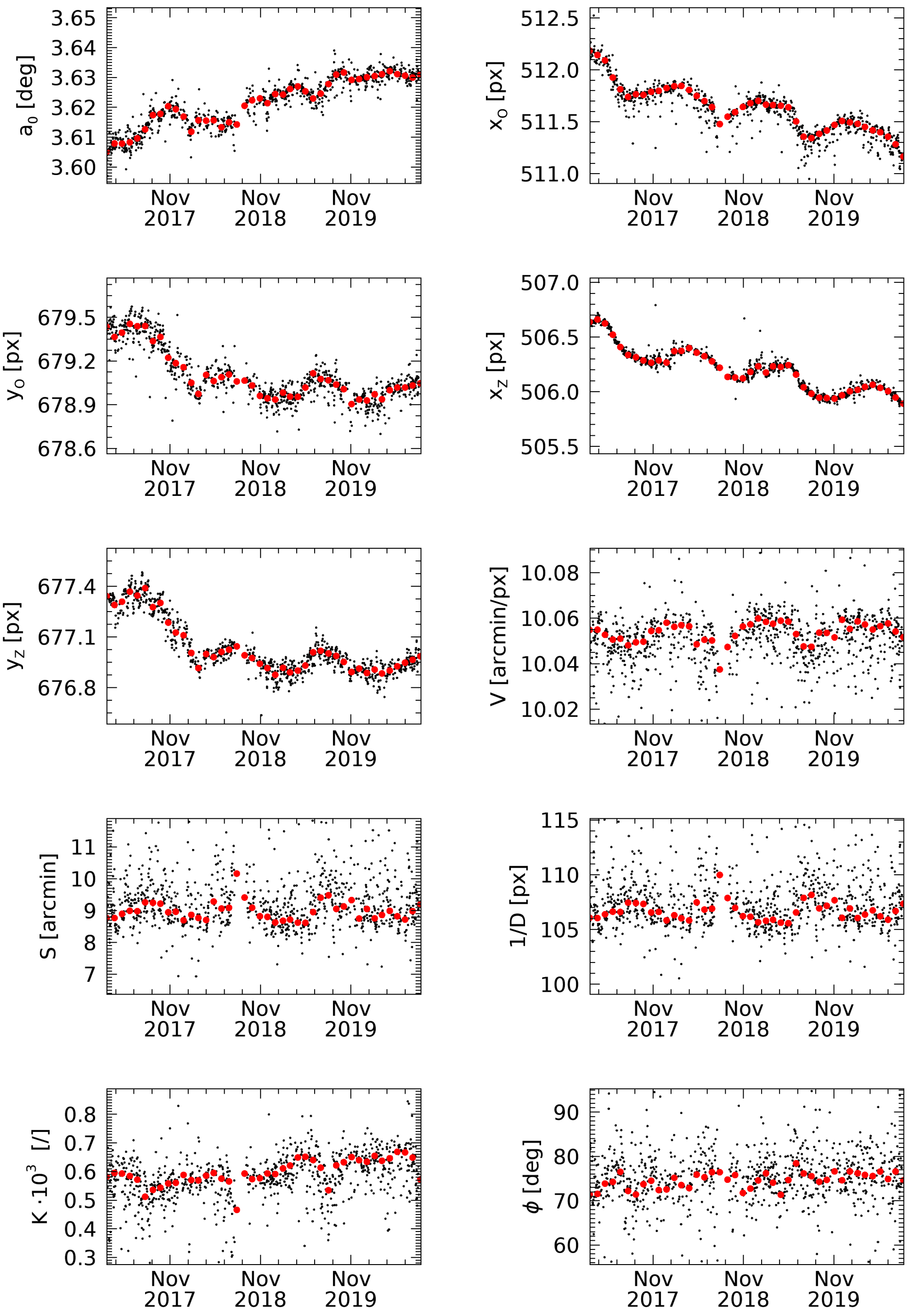

Fig. 4.6: Plots of the values of the astrometric parameters of Eqs. 4.5, 4.6, 4.9 and 4.11 as a function of time for the astrometric calibration of the ITVA01 - Lignan camera of PRISMA, from 2017 to 2021. Small black dots are resulting from daily calibrations, whereas the bigger red dots refer to monthly-based astrometry. From left to right, top to bottom: direction of the North (a_0), x and y coordinates on the CCD of the optical centre O and zenith direction Z, linear plate scale V and distortion parameters S and D, amplitude K and phase ϕ of the elliptical projection. Days with less than 1000 identified stars were excluded from the plot.

4.1.6 Photometric calibration

The identification of stars and their correlation with the catalogue allows also to perform the photometric calibration of PRISMA cameras. The conversion between measured flux on the CCD to apparent magnitude is needed to reconstruct the total emitted energy by the observed meteor and it can be used to compute a photometric estimation of the preatmospheric mass of the meteoroid.

The flux F of identified stars in the FoV on captures is measured by standard aperture photometry, implemented in IDL in the APER[9] procedure of the IDLAstro library from NASA. Given the size of PSF of stars onto the focal plane (see Sect. 4.1.4), we use an aperture radius of 2 px. APER automatically performs background subtraction by estimating the average sky value on a surrounding annular region defined by an inner and outer radius, which are set to 5 px and 10 px respectively. The procedure automatically identifies and excludes bright sources within this annular region, and performs a polygonal approximation of its subtended area to account for its ratio compared to the star's aperture radius when performing background subtraction. Therefore, the instrumental magnitude m_s is computed for each identified star as the following:

$$m_s = -2.5 \log_{10} \left[\frac{F}{\eta(z)\ \Delta t} \right] \ , \tag{4.13}$$

where F is given in ADU (Analog-to-Digital Units), $\eta(z)$ is the radial efficiency factor from Eq. 3.1 expressed as a function of the zenith distance z of the star (see Sect. 3.1.3) and Δt is the exposure time of the image (5 s for captures and 1/30 s for events). The instrumental magnitude measured in this way is to be compared with the apparent magnitude m of that star from the catalogue:

$$\Delta m = m - m_s = C - kX \ , \tag{4.14}$$

where C is the photometric zero-point of the magnitude system of the PRISMA camera, being approximately the instrumental magnitude of Vega[10], k is the atmospheric extinction coefficient and X is the airmass, which is the measure of the amount of air traversed by the light of the star before reaching the observer. The airmass is estimated by the empirical formulation of Rozenberg (1966):

$$X = \left(\cos z + \frac{1}{40} e^{-11 \cos z} \right)^{-1} \ , \tag{4.15}$$

---

[9] `https://idlastro.gsfc.nasa.gov/ftp/pro/idlphot/aper.pro`

[10] Vega (alf-Lyr) was originally used as the reference for the definition of magnitude systems, so that it had a magnitude of 0 in all bands. Today, a VEGAMAG system (like UBV) is defined as having Vega's colors (magnitude differences), such as U-B and B-V that are identically zero. The magnitudes of Vega in UBV bands are not exactly zero in most recent catalogues, since the (synthetic) zero-point is taken as a standard radiance value integrated on a reference spectrum (Bessell and Murphy, 2012).

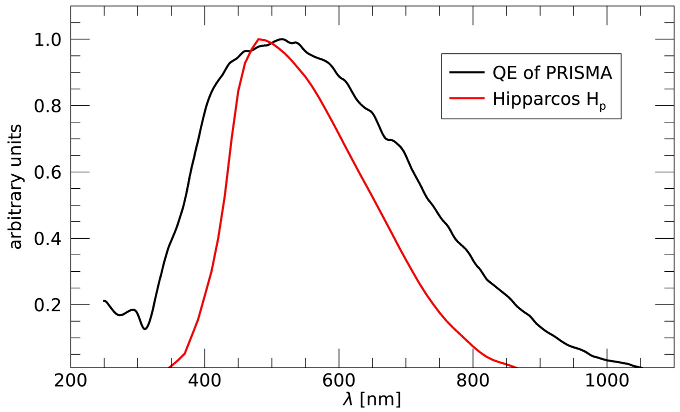

Fig. 4.7: Comparison between the QE curve of PRISMA (black line) with the H_p bandpass (red) of the photometric Hipparcos survey as reported in Bessell and Murphy (2012).

varying from the reference value of 1 at the zenith up to a maximum of 40 at the very horizon. At the usual detection limit of stars for PRISMA cameras at $z = 80°$ the expression for the airmass of Eq. 4.15 gives $X \sim 5.6$. Up to this zenith distance, various models for the estimation of X do not differ significantly, while diverging for $z > 85°$. This is not a problem for the case of PRISMA since no stars are ever detected on the first 5° above the horizon.

The goal of the photometric calibration is to estimate the values of the parameters C and k from the measure of instrumental magnitudes of stars and their comparison with catalogue values by fitting the magnitude residuals with Eq. 4.14. Therefore, we must choose the appropriate magnitude system for this task. As detailed in Sect. 3.1.3, PRISMA cameras are characterized by a wide bandpass, extending in the whole visible range of wavelengths. Therefore, the standard UBVRI magnitude system provided in the catalogue from SIMBAD astronomical database is not suitable. We opted instead for the H_p magnitude of the Hippacos catalogue (Perryman et al., 1997). The H_p bandpass is plotted in Fig. 4.7 as the red line, compared to the QE of PRISMA, plotted in black. The two bands are similarly shaped and their maxima are quite close (515 nm for PRISMA and 480 nm for Hipparcos). However, the H_p bandpass is narrower, with an FWHM of 230 nm compared to the one of PRISMA of approximately 370 nm. While not being a perfect match, we believe that this is the best option among photometric catalogues to date. A future improvement in this regard will be the implementation of a synthetic magnitude system, by integrating available stars' spectra over the bandpass of PRISMA.

Figure 4.8 shows the results of the photometric calibration of the ITVA01 camera for the data of 24/12/2017, with 28k identified stars. Panel a plots the density map of magnitude residuals Δm for the whole night and the red line is the result of a linear fit for Eq. 4.14. In this case, the photometric parameters were estimated to be $C = 8.65 \pm 0.01$ and $k = 0.19 \pm 0.01$. Panel b and c plot the values of C and k along

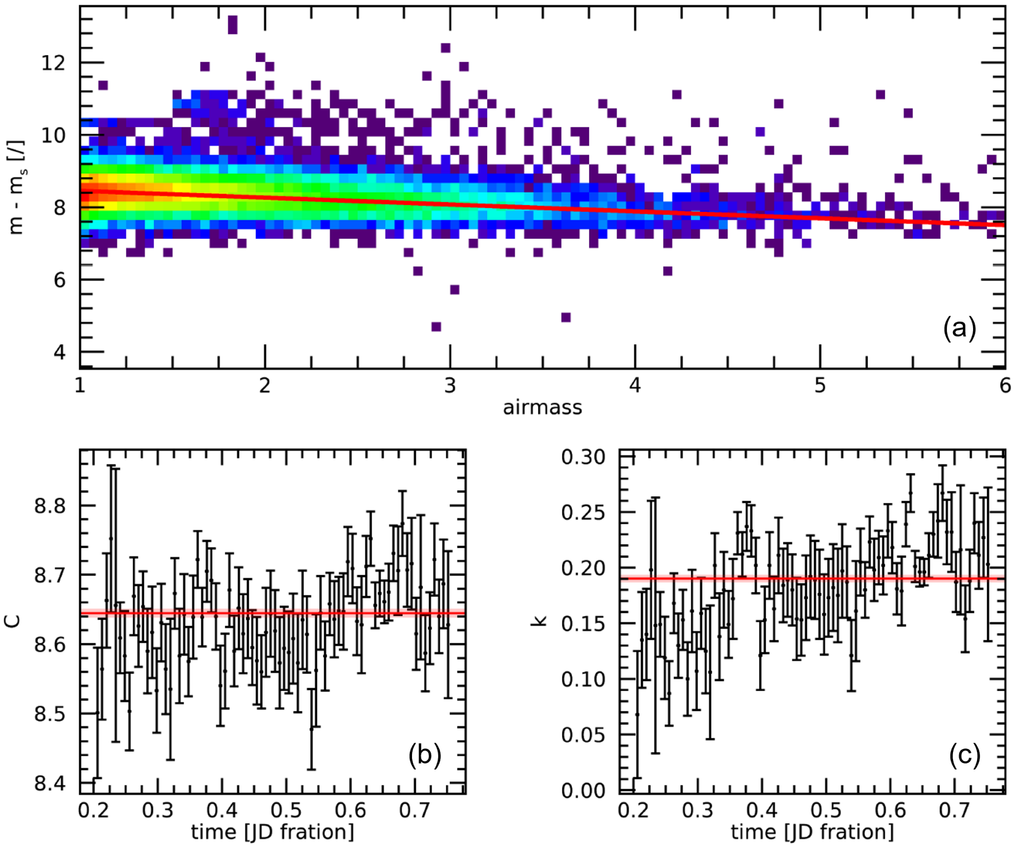

Fig. 4.8: Results of the photometric calibration of the ITVA01 camera of PRISMA for the night of 24/12/2017, with ∼28k identified stars. (a) Density plot of magnitude residuals $\Delta m = m - m_s$, in logarithmic color scale, as a function of the airmass of observed stars in the FoV. The red line plots the fit of Eq. 4.14 for the determination of the photometric parameters C and k. (b) Values of the photometric zero-point C as a function of the time during the night (fraction of day since 12 AM of the day before) computed on single capture images. (c) same as (b), but for the atmospheric extinction coefficient k. The red horizontal lines in panel b and c indicate the values of C and k from panel a.

the night, as estimated from the magnitude residuals of stars identified on single captures (300–400 per image). A slight variation of k during the night is visible in Fig. 4.8c, increasing from about 0.10 just after sunset to 0.20 in the early morning. The atmospheric extinction coefficient is indeed expected to vary during the night because of variable weather, for example. Nevertheless, the photometric results on single captures are usually not very reliable as a consequence of the limited statistics of stars (see also Sect. 4.1.7), showing also a high degree of correlation in the determination of C and k due to a non-uniform coverage at varying airmass values. We therefore rely on daily photometric results, like the ones of Fig. 4.8a, for the calibration used to estimate the apparent magnitude of bolides on event data.

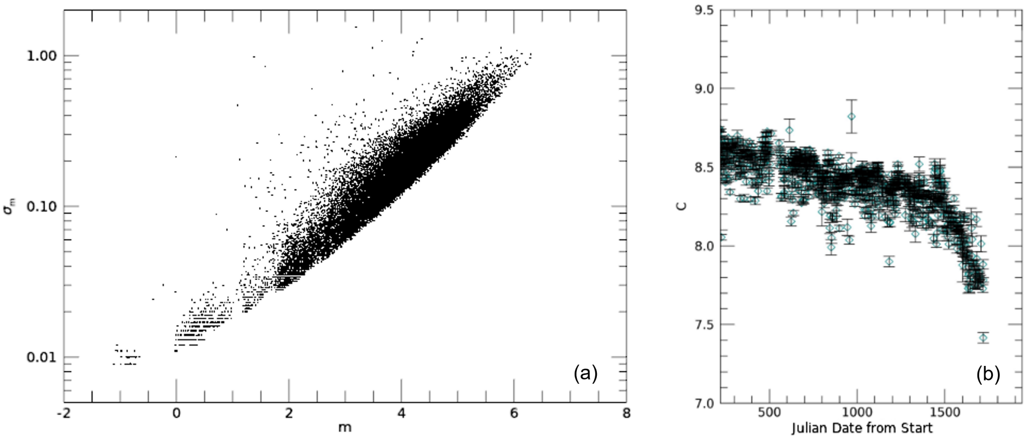

Fig. 4.9: Photometric performance of the PRISMA camera ITVA01. (a) Standard error in the determination of the magnitude from standard aperture photometry on stars detected in the captures of the ITVA01 camera on 24/12/2017. Apparent magnitude values m are computed from instrumental magnitudes m_s with Eq. 4.14, with C and k values as reported in Sect. 4.1.6. (b) Variability of the photometric zero-point C along the available calibration dataset (as for Fig. 4.6, from 2017 to 2021), denoting a drastic decrease of the detector efficiency of > 0.5 mag, most likely due to the degradation of the protective plastic dome that is progressively losing its transparency after years of usage and exposure to atmospheric agents.

4.1.7 Analysis of the photometric performance of PRISMA

The overall photometric performance of PRISMA cameras were found to be poorer with respect to what could be expected a priori and in comparison to the achieved astrometric precision level on the same data, and are affected by the operative conditions of PSF undersampling as well. Figure 4.9a plots the values of the standard error in the determination of stars' apparent magnitude as reconstructed through standard aperture photometry, for the statistics of the night of 24/12/2017 of the ITVA01 calibration data. Nominal uncertainties of the order of 0.01 mag are achievable only for very bright stars of magnitude 0 or below. For the vast majority of stars detected by the camera, that are in between magnitude +3 to +5, a nominal uncertainty in the range of 0.1 to 0.5 is evident from the plot. This is consistent with the standard deviation of magnitude residuals Δm from the plot of Fig. 4.8a of about 0.3 mag. Furthermore, we discovered a progressive decrease with time of the photometric zero-point C value, as plotted in Fig. 4.9b. This decrease is quite remarkable and accounts for >0.5 mag within 4 years, corresponding to a $\sim$60% loss in the amount of light detected by the sensor. Such a drastic reduction of the detector performance may be due to the degradation of the protective dome of the camera, being continuously exposed to atmospheric agents and resulting in a decrease in its transparency. Because of this evidence, we plan to replace the plastic domes of all the PRISMA cameras within the next year.

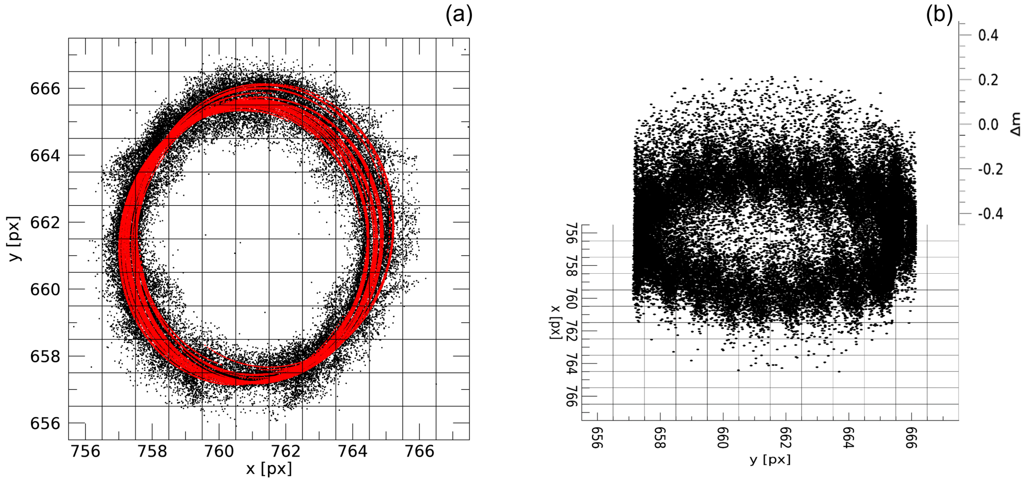

Fig. 4.10: Analysis of the spatial variability of the measured flux of Polaris on the calibration data of the ITVA01 camera of PRISMA, from 2017 to 2021. (a) Comparison of measured positions (black dots) and projected positions (red) from catalogue coordinates through the inverse astrometric formulas of Eqs. 4.5, 4.6, 4.9 and 4.11. (b) Apparent magnitude residuals of Polaris plotted as a function of its projected positions from panel a, showing a significant oscillation at the pixel scale, with minima located near the centre of the pixels and maxima at their border.

We therefore investigated if any systematic effects were evident in the data which were not yet considered within the pipeline, as already done for the case of the astrometric calibration (see Sect. 4.1.4). The lack of a dedicated magnitude system in our analysis poses a limitation in the comparison of the photometric results for different stars, which may be significantly different in their colour indices and therefore show systematics in this regard. To exclude this effect, we analyzed the measurement series of the instrumental magnitude of single stars with the available statistics of selected cameras within the PRISMA network. For this purpose, Polaris (alf-UMi) is one of the best candidates, given that its apparent motion on the focal plane is confined within a few pixels and we can neglect the effect of radial efficiency modulation and the differential atmospheric extinction at varying airmass values. Polaris is a classical Cepheid variable star but nowadays it shows a variability of a few hundredths of magnitude (Turner et al., 2010), not significant for our analysis. Having an apparent magnitude of $\sim$2 in the V band, it is quite bright with respect to the sky background, with a PSF height of $\sim$1000 ADU over $\sim$100 ADU of background on captures, it never saturates to the maximum of $2^{12} = 4096$ ADU (PRISMA data are saved in 12-bit format) and it is visible in every frame if the weather conditions are favourable.

Figure 4.10 presents the results of the study of the variations of measured flux of Polaris on the focal plane as observed by the ITVA01 camera of PRISMA. We found that the magnitude of Polaris shows a significant oscillation inside the pixel scale. The detection of these sub-pixel variations is not possible when considering the measured position of Polaris provided by the FIND algorithm (Fig. 4.10a), since we already discussed that this measure has an intrinsic precision of about 0.3 px (see Sect. 4.1.4) due to the condition of heavy PSF undersampling. On the other side, a much more precise estimation of the sub-pixel position of the PSF centre is available by considering its catalogue coordinates, *i.e.*, equatorial α and δ converted to local horizontal coordinates a and z as a function of the time, and projecting them on the focal plane by means of the inverses of Eqs. 4.5, 4.6, 4.9 and 4.11 using the monthly astrometric parameters. These computed positions are plotted as the red points in Fig. 4.10a and show concentric circles progressively shifting through time mainly due to the temporal variation of the projection centres (see Sect. 4.1.5). Figure 4.10b plots the magnitude residuals Δm as a function of these positions. With respect to Eq. 4.14, these residuals are further subtracted by the term $C - kX$ (given by the daily photometric calibration) to remove the long-term change in the detector efficiency response (see Fig. 4.9b) and the effect of variable atmospheric optical thickness. A remarkable oscillation pattern is visible, with a period corresponding to the pixel size, reported as the grid on the (x, y) plane for reference. The peak-to-valley amplitude of this modulation is about 0.25 mag, *i.e*, a ~25% relative modulation of the flux. The minima of Δm on this plot correspond to the maximum flux value recorded and it is usually located near the centre of the pixel. On the other hand, the maxima of Δm are located at the pixel borders and correspond to lower flux values.

To understand if this peculiar sub-pixel behaviour was present in the whole focal plane, we extended this analysis to all stars imaged by the camera. The magnitude residuals Δm were centred on their mean value for each star, to account for the difference in their colour indices. To explore the sub-pixel variability, the pixel area was divided into 0.1 px × 0.1 px regions. Then, we computed the average of the normalized Δm residuals of stars detected within each of these sub-pixel areas. In order to gain sufficient statistics at this level, we divided the focal plane into 100 px × 100 px blocks and averaged the response of each pixel in each block respectively. The results of this processing are presented in Fig. 4.11, where panel a plots the sub-pixels maps of Δm for each block defined above as a function of its positioning on the CCD. An example of the 3D surface representation of the magnitude residuals distribution at the sub-pixel is plotted in 4.11b for the block $[4, 6]$ that corresponds to $x \in [400 - 500]$ px and $y \in [600 - 700]$ px. The general behaviour outlined for the case of Polaris is confirmed on a vast portion of the focal plane. We can also observe that the sub-pixel modulation of the detector response is not homogeneous on the focal plane. Such effect is most significant in the central part of the CCD, with an amplitude of ~0.3 mag. This gradually declines towards the borders of the focal plane, down to < 0.1 mag for $r = 300$ px from the optical centre of the camera, and the modulation appears to break down for the outer blocks. This may be also due to the lack of statistics at low elevation values, since only a little number of stars are detected in the last 20° close to the horizon. Some blocks at the very edge of the

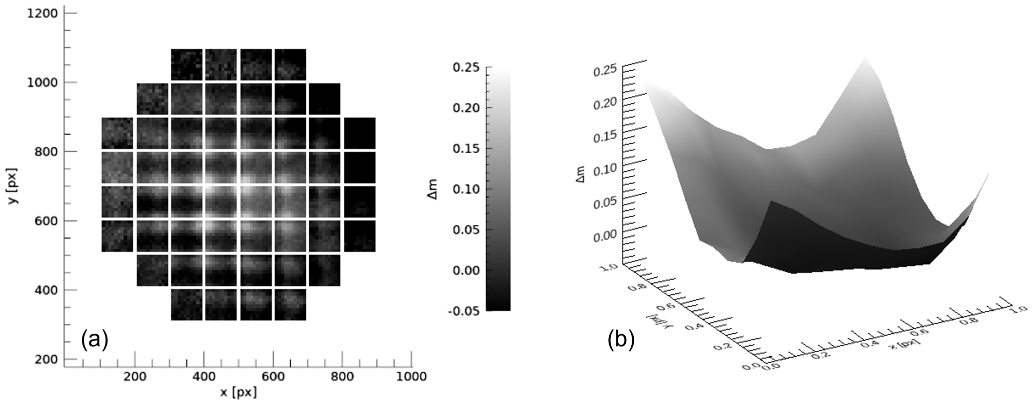

Fig. 4.11: Sub-pixel variability of the measured apparent magnitude of stars on the calibration data of the ITVA01 camera. (a) Image of the distribution of Δm residuals averaged on 100 px × 100 px blocks on the focal plane, where each square virtually represents the sub-pixel response on the corresponding block. (b) Surface representation of the magnitude residuals distribution of the block $[4,6]$, *i.e*, for $x \in [400-500]$ px and $y \in [600-700]$ px. An evident minimum is present near the centre of the pixel, corresponding to the maximum of the detector response. On the contrary, maxima are located near the corners of the pixel, with a difference of about 0.3 mag with respect to the value at the centre.

CCD were not reported because of this issue. Also, the centre of such modulation within the sub-pixel seems to shift when approaching the border of the focal plane.

We infer that this peculiar behaviour is again caused by the condition of PSF undersampling of stars. To be able to acquire and store images at a 30 fps rate, the cameras of the network are equipped with an interline CCD sensor (Sony ICX445AL), as outlined in Fig. 4.12a. This type of sensor deploys individually separated photodiodes, representing the area sensitive to light of the focal plane. Each photodiodes column is flanked by a vertical shift register, acting as a charge storage and physically masked to incoming light. After each exposure, charges are shifted to these memory cells and progressively read out via the horizontal shift register, where they are finally converted to voltage and amplified. This architecture allows operating the CCD at high frame rates, at the same time avoiding smearing effects due to fast and subsequent acquisitions. The main drawback of this technology is the presence of a considerable portion of the focal plane actually insensitive to incoming light. This effect is usually quantified as the *fill-factor*, being the ratio of the light-sensitive area of a pixel to the total pixel area. In this sense, a pixel can be thought as a virtual unitary cell made of one photoactive sensor and the neighbouring memory cell of the vertical shift register. Therefore, interline CCDs usually have quite low fill-factor values, down to 30%. Combining the low fill-factor of the CCD sensor with the small angular size of the PSF of stars results in a peculiar phenomenology, presented in Fig. 4.12b. Since the stars imaged by the all-sky optics of PRISMA have a small FWHM of ~0.2 px, the relative positioning of the PSF itself with respect to the pixel grid greatly affects the amount of light registered at the

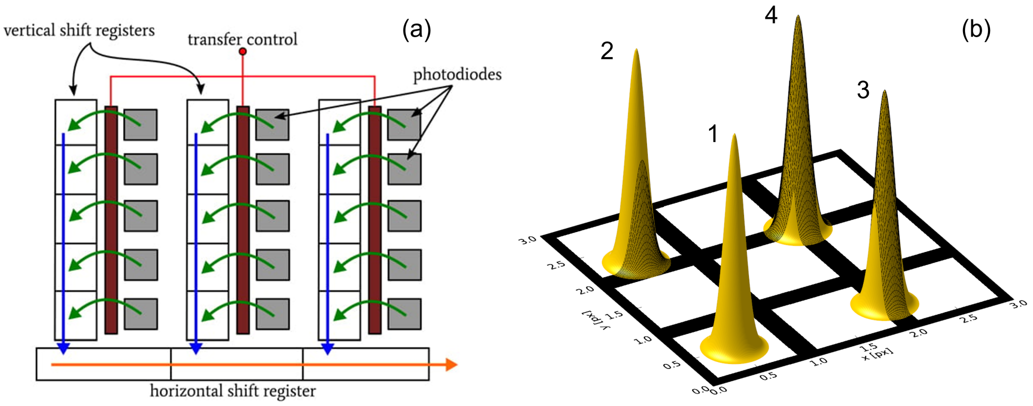

Fig. 4.12: (a) Schematization of the technology of interline CCDs, deploying singularly separated photodiodes organized in columns, each one being separated by a vertical shift register. After each exposure, the signal acquired by each photodiode is transferred to the vertical register and progressively read out by the horizontal shift register (credits: `https://www.allaboutcircuits.com/`). (b) The effect of PSF undersampling on an interline CCD. Active photodiodes are represented in white, while the borders and corners of each pixel are highlighted in black and are the insensitive portion of the focal plane. The PSFs plotted in yellow represent four cases of progressive signal loss (highlighted by a black shading) due to the relative positioning of the PSF on the pixel matrix, from negligible (1 - the PSF is located in the centre of the photodiode) to maximum (4 - the PSF is located in the corner between 4 neighbouring pixels).

photodiode, as pictured in Fig. 4.12b. When the star is centred on the active portion of the CCD, the amount of registered light is maximum and only the PSF tails are affected by the dead zone of the CCD. On the other hand, when the image of the star is located with its centre on the inactive portion, the output signal is minimum. Therefore, the intensity of this effect is a function of the relative ratio between the PSF size and the width of the inactive layer Δx. If the PSF can be approximated by a gaussian function centred on the position x_0 and with standard deviation σ, the relative intensity $I(x_0, \Delta x)$ registered on an interline CCD normalized to the theoretical flux I_0 of that star can be modelled, in the unidimensional case, as:

$$I_1(x_0, \Delta x) = \frac{1}{2} \sum_{i \in \text{CCD}} \left[\text{erf}\left(\frac{i + 1 - \Delta x - x_0}{\sqrt{2}\sigma} \right) - \text{erf}\left(\frac{i + \Delta x - x_0}{\sqrt{2}\sigma} \right) \right] , \qquad (4.16)$$

which is trivially deduced from a pixel-wise integral of the gaussian PSF with periodic masking on the borders within two consecutive pixels of $\pm\Delta x$. In this expression, i is the pixel index which virtually extends the whole CCD region, but the sum of Eq. 4.16 needs to be computed only in the neighbouring of the PSF on the focal plane. In the two-dimensional case of our interest, Eq. 4.16 can be easily generalized to $I_2(x_0, y_0, \Delta x, \Delta y) = I_1(x_0, \Delta x) I_1(y_0, \Delta y)$.

From the results of ITVA01 calibration data, we also noted that the sub-pixel modulation is not always symmetrical with the minimum Δm on the centre of the pixel. Within our hypothesis, this is easily explained if the active photodiode is not exactly centred on the area of the virtual digital pixel. The shift of the position of this minimum within the focal plane may be due to optical aberrations affecting the PSF's shape of stars approaching the border of the FoV. Also, the interline CCD of PRISMA cameras is equipped with on-chip microlenses (Sony EXview HAD CCD$^{\mathrm{TM}}$), which are installed on top of each individual pixel to focus the light onto the active photodiode, virtually increasing the fill-factor of the sensor. The coupling of this technology with an heavily distorted all-sky optics may also introduce further aberrations at low elevation angles in the FoV.

Similar results on the sub-pixel response of PRISMA cameras were found on the photometric data of two other stations of the network (ITPI01 - PinoTorinese and ITER03 - Medicina) and were presented in a recent contribution to the last International Meteor Conference[11] on September 2022. A preliminary application of the model of Eq. 4.16 to the data of ITPI01 pointed out a fill-factor of ∼80%, which is indeed compatible with the response of an interline CCD equipped with microlenses. However, implementing a dedicated correction of the photometric calibration in this respect requires a substantial effort in the analysis of yearly statistics of all PRISMA cameras and will be the argument of a future improvement of the PRISMA pipeline. Also, this sub-pixel modulation affects only marginally the photometry of bolides, since their PSFs usually extend over a few pixels. This analysis will be the subject of a forthcoming publication on the photometric performance of PRISMA cameras.

4.2 Analysis of PRISMA events

In the following sections, I describe the analysis of the meteor events recorded by the PRISMA network, which consist of four main steps: (1) astrometric and photometric analysis of the videos from each detection, using the results of the calibration process; (2) triangulation of the three-dimensional trajectory of the meteor in the atmosphere; (3) computation of a dynamic model to estimate the parameters of the meteor and the meteoroid and; (4) computation of the preatmospheric orbit of the meteoroid from the results of the triangulation and dynamic model.

4.2.1 Astrometric and photometric processing

Data of the detection of each camera of the network are collected by the FRIPON central server and merged into events according to their position and relative timing. Therefore, each event represents the same meteor as detected by different cameras of the network. Detections are acquired as a stream of single-frame FITS files. Moreover, FREETURE performs a first and rough estimation of the position of the meteor in

---

[11] `https://imc2022.imo.net/program`

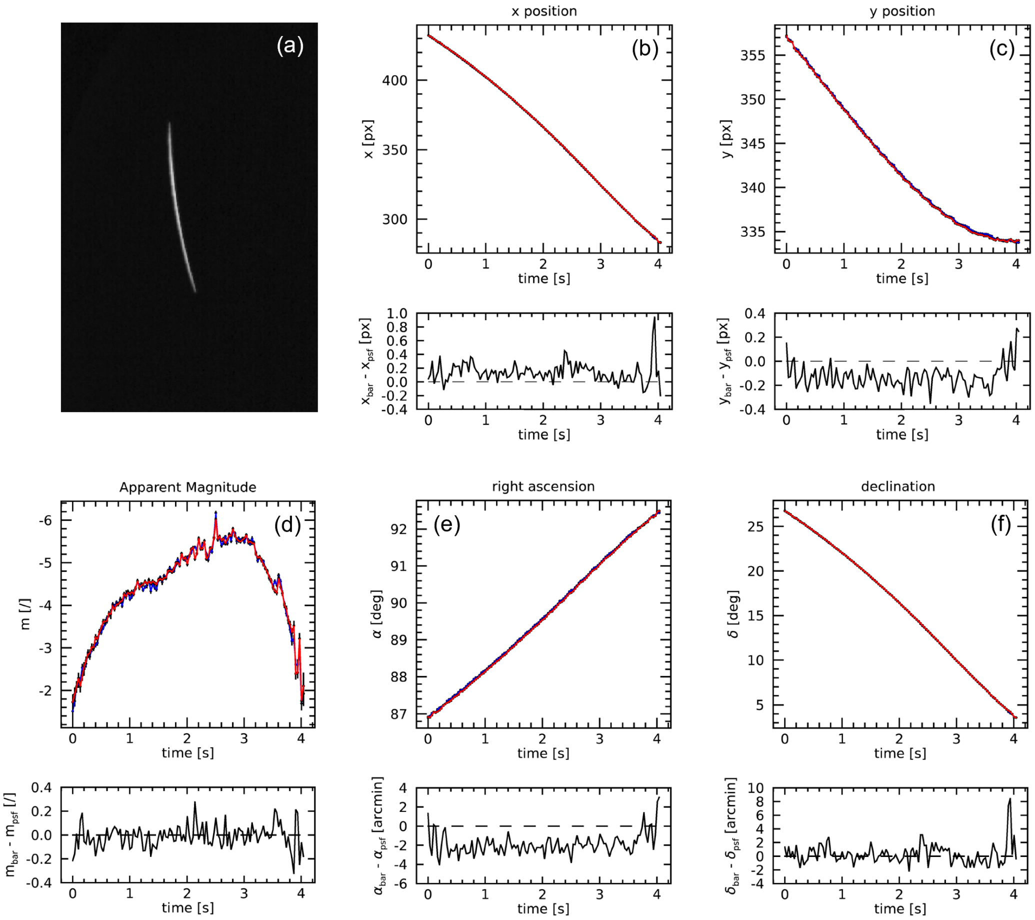

Fig. 4.13: Results of the astrometric and photometric processing of the detection from the ITPI06 - Barolo camera of the 20190415T194950_UT event, detected by 4 other PRISMA stations. These are plots automatically produced by the PRISMA pipeline to have a visual report of the results, exported in PDF format. (a) Visual reconstruction of the meteor track from the integration of the video acquisition; (b-c) x and y position of the meteor on the focal plane computed by the PSF fitting (blue curve) and FBC barycentre algorithm (red curve); (d) apparent magnitude evaluated from Eq. 4.14 with the monthly photometric calibration parameters ($C = 8.30 \pm 0.02$, $k = 0.28 \pm 0.01$) where F was computed from the fitted PSF integral (blue) and aperture photometry (red); (e-f) right ascension and declination at the J2000 epoch in the FK5 reference frame, computed from the (x, y) coordinated plotted on panels (b,c) through the monthly astrometric calibration. The bottom sub-panels of (b-f) show the difference between values computed from PSF and FBC algorithms.

(x, y) coordinates on the focal plane for each triggered frame. This information is stored on a TXT file for each detection and it is the basis for the astrometric and photometric analysis of the video, allowing to select the region of the focal plane interested by the passage of the meteor. Similar to what was already presented for the search of stars on the calibration data, we apply a centring algorithm to refine the estimation of the position onto each frame. In this case, we perform the filtered barycentre computation (FBC, see Sect. 4.1.4) together with a 2D Gaussian PSF fitting. Both methods were tested on synthetic meteors data and were found to be unbiased for non-undersampled PSF (Barghini et al., 2019b). For the FBC algorithm, the intensity of the meteor is computed through standard aperture photometry, while for the PSF fitting the intensity is automatically given as the mathematical integral of the 2D function. Then, the astrometric and photometric calibration parameters of the corresponding month are used to compute the equatorial positions (α, δ) and the apparent magnitude m of the meteor from the measured coordinates (x, y) and the instrumental flux F. An example of the results of this processing is given in Fig. 4.13 for the detection of the PRISMA camera ITPI06 - Barolo of the event 20190415T194950_UT[12]. Each plot reports the values computed by FBC (red) and PSF fitting (blue) and the sub-panel plots the difference between the two. For example, the differences in (x, y) coordinates are between ±0.2 px, comparable with the standard errors of both algorithms of ~0.1 px (which are plotted but not visible in scale).

We found that FBC results are usually more robust, particularly for low SNR values, *i.e.*, for faint meteors and/or for the very start and end of the meteor track. Therefore, we use FBC for the automatic processing within the pipeline. However, comparing the two methods is particularly useful in the case of saturation of the meteor image. For bolides of apparent magnitude $m \lesssim -8$, the intensity of the meteor registered by the camera results in a signal greater than $2^{12} = 4096$ ADU and the PSF is truncated around its maximum. To account for this instrumental effect, we apply a fitting of the PSF over the non-saturated portion of the image. This analysis aims to estimate the original PSF shape, with particular attention to the fraction of lost signal due to saturation. An example of the results of this procedure is presented in Fig. 4.14. The 3D black histogram of panel a plots the PSF of the meteor signal measured on a frame of the 20220305T185552_UT[13] event (at 5.6 s from the starting time) as captured by the ITUM01 - Perugia camera. This bolide reached an absolute magnitude of about -11 and was captured by 10 other stations of PRISMA, being one of the brightest bolides ever recorded by the network. The effect of saturation is clearly evident on the measured signal, and the fitted PSF (blue surface) accounts for a counts loss of ~15%. Panel b plots the comparison between the flux before (black curve) and after this correction (blue) for the whole lightcurve of this event, accounting up to a 35% of lost signal due to saturation. It is to be

---

[12] `https://fireball.fripon.org/displaymultiple.php?id=1949`

[13] `https://fireball.fripon.org/displaymultiple.php?id=17288`

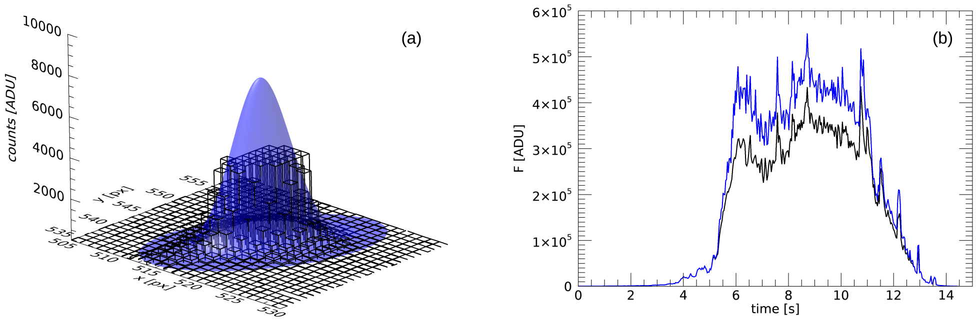

Fig. 4.14: Correction of the PSF saturation on images of very bright bolides, with apparent magnitude $m \lesssim -8$. (a) Distribution of the meteor signal on the focal plane on a frame of the 20220305T185552_UT event, at 5.6 s from the starting time, captured by the ITUM01 - Perugia camera. The black histogram plots the measured PSF, while the shaded blue surface is the reconstructed PSF shape by a 2D gaussian fit. (b) Comparison between saturated (black curve) and corrected (blue) flux F along the whole flight of the bolide recorded by the ITUM01 camera.

noted that this analysis is heavily dependent on the shape of the PSF, which may significantly differ from the assumption of a 2D gaussian distribution, for example because of strong asymmetries in the bolide images due to either fragmentation, flares, and PSF elongation caused by the high angular speed of its image on the CCD. For this reason, the correction we adopted can be regarded only as tentative and can provide a qualitative estimation of the fraction of the saturated meteor's signal. Beyond this caveat, results on simulated data showed that such reconstruction is reliable at least up to a relative flux loss of 40% (corresponding to a PSF height of $\sim 2^{14}$ ADU), and that the centring precision of the saturated image is also not significantly affected (Barghini et al., 2019b).

4.2.2 Triangulation

The astrometric reduction of video data presented in the previous section allows to perform the triangulation of the three-dimensional trajectory of the meteor in the Earth's atmosphere. Merging the data from N stations that detected the same event, we now have a series of measurements of time t_{ik} and equatorial coordinates $(\alpha_{ik}, \delta_{ik})$, where $i \in [0, N-1]$ is the index of the camera and $k \in [0, M_i - 1]$ is the index of the frame within each detection. This task was first addressed by Ceplecha (1987), who proposed the triangulation strategy presented in Fig. 4.15a. Let us consider that each (α, δ) defines a direction versor in the 3D space $\overline{v} = (\xi, \eta, \zeta)$ as:

$$\xi = \cos\delta\cos\alpha \quad , \quad \eta = \cos\delta\sin\alpha \quad , \quad \zeta = \sin\delta \, , \tag{4.17}$$

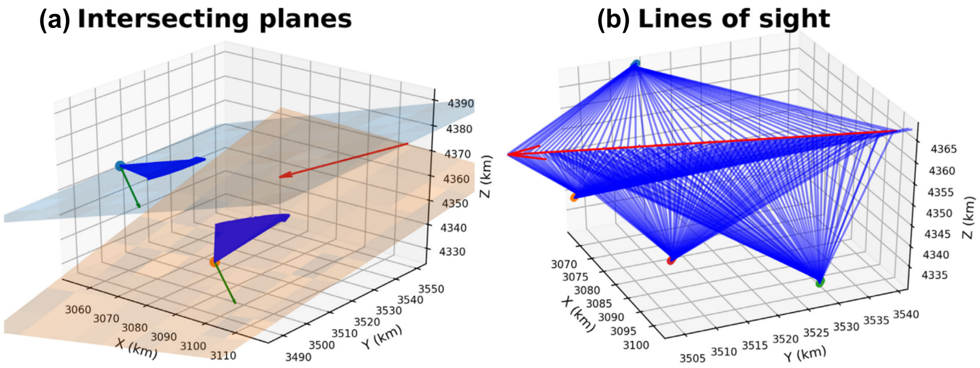

Fig. 4.15: Schematization of the two methods for the triangulation of the meteor's trajectory from optical observations that were considered for the PRISMA pipeline: (a) the original method of intersecting planes by Ceplecha (1987); (b) the method of Lines of Sight proposed by Borovička (1990). The detailed description on the two methods can be found in the text (Vida et al., 2020).

where (α, δ) are precessed to the epoch of observation. If we suppose that the meteor's trajectory can be described as a straight line, then the set of observed directions from the one camera will align on one 3D plane Π_i:

$$\Pi_i : a_i\xi + b_i\eta + c_i\zeta + d_i = 0 \, . \tag{4.18}$$

Therefore, we need to derive the coefficients (a_i, b_i, c_i, d_i) describing Π_i from the observations $(\xi_{ik}, \eta_{ik}, \zeta_{ik})$. Of course, the alignment on the plane will not be perfect due to measurement errors. Ceplecha (1987) used the analytical solution of the following χ^2 problem:

$$\chi^2 = \sum_{k=0}^{M_i-1} \Delta^2_{ik} = \sum_{k=0}^{M_i-1} (a_i\xi_{ik} + b_i\eta_{ik} + c_i\zeta_{ik})^2 = \text{ minimum} \tag{4.19}$$

to derive the least-square estimation of (a_i, b_i, c_i) as:

$$\begin{cases} a'_i = (\xi_{ik}\eta_{ik})(\eta_{ij}\zeta_{ik}) - (\eta_{ik}\eta_{ik})(\xi_{ik}\zeta_{ik}) \\ b'_i = (\xi_{ik}\eta_{ik})(\xi_{ik}\zeta_{ik}) - (\xi_{ik}\xi_{ik})(\eta_{ik}\zeta_{ik}) \\ c'_i = (\xi_{ik}\xi_{ik})(\eta_{ik}\eta_{ik}) - (\xi^2_{ik}\eta^2_{ik}) \end{cases} \xrightarrow{D_i^2 = a_i'^2 + b_i'^2 + c_i'^2} \begin{cases} a_i = a'_i / D_i \\ b_i = b'_i / D_i \\ c_i = c'_i / D_i \, , \end{cases} \tag{4.20}$$

having used the Einstein notation for the summation of repeated indices k. Then, we can compute the distance of the plane from the Earth's centre as:

$$d_i = -(a_iX_i + b_iY_i + c_iZ_i) \, , \tag{4.21}$$

where (X_i, Y_i, Z_i) are the rectangular coordinates of the i-th station in the Earth-Centred Earth-Fixed (ECEF) reference frame, computed from the geographic coordinates (λ_i, ϕ_i, h_i). If not parallels, each couple of planes (Π_i, Π_j) intersects into one straight line R_{ij}, that is the meteor's trajectory estimated from the i-th and j-th camera's data. Considering that $\overline{v}_i = (a_i, b_i, c_i)$ is the versor perpendicular to the i-th plane, the line R_{ij} is defined by the direction versor $\overline{w}_{ij}$ as:

$$\overline{w}_{ij} = \frac{\overline{v_i} \times \overline{v_j}}{|\overline{v_i} \times \overline{v_j}|} \; , \tag{4.22}$$

which is the vectorial representation of the original formulation of Eq. 14 of Ceplecha (1987). The application point $\overline{X}_{ij} = (x_{ij}, y_{ij}, z_{ij})$ of R_{ij} can be given by fixing $z_{ij} = Z_i$[14] and solving the following set of linear equations:

$$\begin{cases} a_i x_{ij} + B_i y_{ij} = -(c_i Z_i + d_i) \\ a_j x_{ij} + B_j y_{ij} = -(c_j Z_i + d_j) \; , \end{cases} \tag{4.23}$$

for example using Cramer's rule. Therefore, this procedure is run for all the couples of cameras, summing up to a number of $N_{ij} = \binom{N}{2} = \frac{N!}{(N-2)!2!}$ combinations. Ceplecha (1987) already noted that the statistical significance of each of these combinations varies accordingly to the angle Q_{ij} between the two planes (Π_i, Π_j), which can be computed as:

$$Q_{ij} = \text{acos}\left(\frac{|\overline{v}_i \cdot \overline{v}_j|}{|\overline{v}_i||\overline{v}_j|}\right) \; , \tag{4.24}$$

being null when Π_i and Π_j are parallel ($Q_{ij} = 0°$) and maximum when they are perpendicular ($Q_{ij} = 90°$). Therefore, we give a mean trajectory R, with direction $\overline{w}_R = (\xi_R, \eta_R, \zeta_R)$, of these combinations by a weighted average of $\overline{w}_{ij}$ components, by the following weights:

$$W_{ij} = (M_i + M_j) \sin^2 Q_{ij} \quad \rightarrow \quad \overline{w}_R = \frac{1}{\sum_{ij} W_{ij}} \sum_{ij} W_{ij} \overline{w}_{ij} \; . \tag{4.25}$$

With respect to the original formulation of Ceplecha (1987), we added the term $(M_i + M_j)$ to the definition of W_{ij} to have a weight that accounts for the different number of observations used to derive each trajectory R_{ij}.

Shortly after, Borovička (1990) proposed a different method for the triangulation of optical observations, presented in Fig. 4.15b. In this case, each observed direction $(\alpha_{ik}, \delta_{ik})$ is considered singularly as a Line of Sight (LoS) $\overline{v}_{ik} = (\xi_{ik}, \eta_{ik}, \zeta_{ik})$ with its application point in the rectangular coordinates of the i-th station $\overline{X}_i = (X_i, Y_i, Z_i)$. From a theoretical point of view, each LoS should exactly intersect the meteor's trajectory at some distance. In practice, a small distance δ_{ik} is expected between each LoS and the trajectory itself, due to measurement errors. Therefore, the method aims to minimize the distances δ_{ik} between the line of sights and the meteor trajectory $R : \overline{w}_R = (\xi_R, \eta_R, \omega_R)$ with its application point $\overline{X}_R = (X_R, Y_R, Z_R)$. We present

---

[14] This choice is arbitrary. For example, in the PRISMA pipeline we choose the z ECEF coordinate of the ITPI01 - Pino Torinese camera ($\lambda = 7.76494°$E, $\phi = 45.04124°$N, $h = 620$ m). If $(\overline{w_{ij}})_z = 0$, one can choose to fix the x or y coordinates as well, modifying Eq. 4.23 accordingly.

here the vectorial expression of the original problem illustrated by Borovička (1990). Let us consider the parametric representation of each LoS and the meteor trajectory as:

$$\begin{cases} \mathrm{LoS}_{ik} & : \overline{X} = \overline{X}_{ik} + \overline{v}_{ik}t \ , \ t \in \mathbb{R} \\ R & : \overline{X} = \overline{X}_R + \overline{w}_R s \ , \ s \in \mathbb{R} \end{cases} \tag{4.26}$$

where we now consider the Earth's rotation and pose ourselves in the Earth-Centred Inertial (ECI) reference frame, so that the rectangular coordinates X_i of the i-th station are also a function of the time (k). Then, the distance between these two lines can be given as:

$$\begin{cases} \overline{p}_{ik} = \overline{X}_{ik} + \overline{v}_{ik}t_{ik} \\ \overline{q}_{ik} = \overline{X}_R + \overline{w}_R s_{ik} \end{cases} \quad \rightarrow \quad \delta_{ik} = |\overline{p}_{ik} - \overline{q}_{ik}| \ , \tag{4.27}$$

where t_{ik} and s_{ik} define the points $\overline{p}_{ik}$ along LoS_{ik} and $\overline{q}_{ik}$ along R that satisfy the minimum distance requirement of the two 3D straight-lines:

$$\begin{cases} t_{ik} = [\overline{w}_R \times (\overline{X}_R - \overline{X}_{ik})] \cdot \frac{\overline{w}_R \times \overline{v}_{ik}}{|\overline{w}_R \times \overline{v}_{ik}|^2} \\ s_{ik} = [\overline{v}_{ik} \times (\overline{X}_R - \overline{X}_{ik})] \cdot \frac{\overline{w}_R \times \overline{v}_{ik}}{|\overline{w}_R \times \overline{v}_{ik}|^2} \ . \end{cases} \tag{4.28}$$

In this sense, $\overline{p}_{ik}$ represent the observed points along the LoS and $\overline{q}_{ik}$ are the fitted points along the trajectory R. Then, the problem is reduced to the standard χ^2 minimization as:

$$\chi^2 = \sum_{ik} \delta_{ik}^2 = \ \text{minimum} \tag{4.29}$$

that can be now solved numerically rather than analytically. We reviewed here the vectorial notation for both methods since this was the approach we chose in the implementation of these algorithms in the PRISMA pipeline, through the definition of an object-oriented framework in IDL that includes the classes of 3D lines, planes and points and the related geometrical operations (intersection, distance, etc...).

In his work, Borovička (1990) compared these two methods (IP - Intersecting Planes and LoS - Lines of Sight) and concluded that both were appropriate for the triangulation of meteors, even though the LoS method resulted in smaller residuals. Also, the LoS method allows for the station to move during the meteor's flight, according to the Earth's rotation. On the other hand, the IP method has an analytical solution and always gives a result, whereas the LoS distance minimization relies on a numerical solution of the χ^2 problem and may not converge appropriately if the measurements are of poor quality. In light of these features, we implemented the triangulation using and combining both these methods in the PRISMA pipeline. First, we perform the IP computation over all the available detections. Being analytically solvable, the major strength of this method is that it does not need any prior knowledge of the trajectory's direction $\overline{w}_R$. On the other hand, it can provide a starting point value for the numerical solution of the χ^2 problem of Eq. 4.29 for the LoS method, which is again modified with the LAV approach as already detailed for the astrometric solution fitting (see Sect. 4.1.3).

Figure 4.16 plots the results for the triangulation of the 20190415T194950_UT event, the same as the detection presented in Fig. 4.13. Panel a plots the height H above sea level as a function of the time, reconstructed from the triangulated rectangular ECI components projected onto geographical coordinates. The event lasted for 4.11 s and was first detected by the PRISMA network at an altitude of 80.3 km and ended at 40.8 km. The fit residuals of Eq. 4.27 are plotted in panel b. To represent the dispersion around the fitted trajectory (dotted line), we attribute to δ_{ik} the sign of the Z component of the difference $\overline{p}_{ik} - \overline{q}_{ik}$. The standard deviation of these residuals is 55 m, which is to be compared with the average astrometric precision level of about 1 arcmin for the results of all 5 detections (see Sect. 4.2.1 and Fig. 4.13 for the details of the detection of ITPI06 - Barolo). Considering an average distance of the meteor from the PRISMA stations of 140 km, plotted in panel c, this sums up to a nominal uncertainty of about 40 m, comparable to the width of the distribution of the residuals. Figure 4.17 shows the map of the reconstructed trajectory. The event occurred near the border between France and Italy. Projected on the ground, the trajectory started SE of Guillestre, in the region of High Alps in France, and travelled along the SSE direction (arrival azimuth $a = 325.5 \pm 0.1°$N) with an inclination $\gamma = 42.0 \pm 0.2°$, to end in Piedmont SW of Pietraporzio, a small village in the Stura Valley.

From the results of the triangulation, it is also possible to compute the speed profile of the meteor, plotted in Fig. 4.16d. To do this, we use a moving-window linear fitting procedure. We separate the time series of ECI coordinates between different cameras and perform a weighted linear fit over a window of 7 consecutive frames (0.23 s) for each (X, Y, Z) component. The slope of the fitted line is therefore assigned as the speed value of the central frame of the window for that camera, and the three rectangular components of the speed vector are therefore combined to retrieve the speed module. In comparison with the standard single- or double-sided numerical derivative, we found this procedure to be more robust with respect to points with higher dispersion, as for example the ones at the beginning or end of the flight. The speed values computed with this method have a standard error of the order of 0.1 km/s. We also perform an exponential fit on speed profile (Ceplecha, 1961) to derive a first estimation of the pre-atmospheric V_∞ of the meteor, in the form of:

$$V(H) = V_\infty - Ae^{-BH} \, . \tag{4.30}$$

The result of this fit is plotted as the red thick line of Fig. 4.16. This is done to retrieve a preliminary estimation of V_∞ in the case the dynamic model fitting (Sect. 4.2.4) fails to converge. In this case, we use this value of V_∞ for the computation

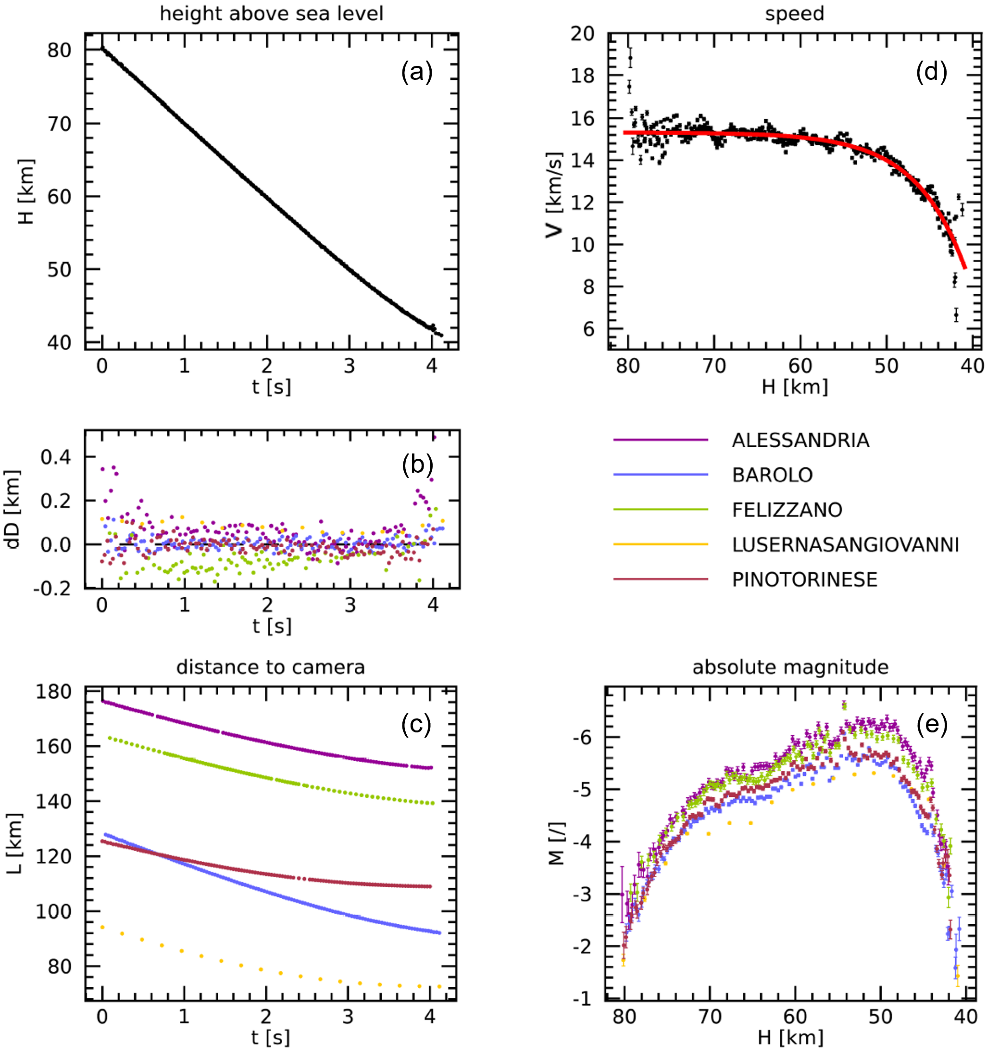

Fig. 4.16: Results of the triangulation processing for the 20190415T194950_UT event. These are plots automatically produced by the PRISMA pipeline to have a visual report of the results, exported in PDF format. (a) Height above sea level; (b) distance residuals of the LoS fitting procedure from Eq. 4.27; (c) distance of the trajectory from the various stations that detected the event; (d) speed profile reconstructed from the triangulated positions (dots with error bars) together with the result of the exponential fit of Eq. 4.30 (red thick line); (e) absolute magnitude lightcurve from Eq. 4.31.

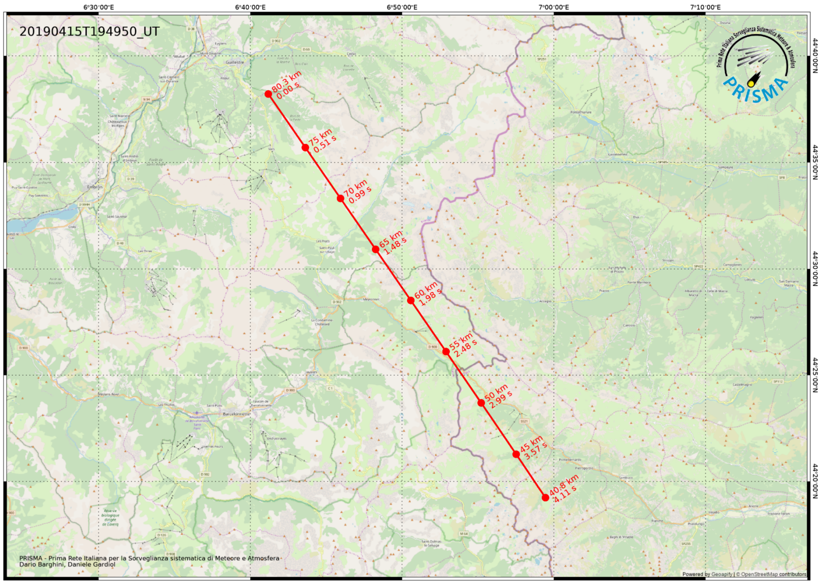

Fig. 4.17: Map of the triangulated trajectory projected on the ground for the 20190415T194950_UT event, that crossed the border between France and Italy. Markers are positioned at fixed intervals of height H together with their relative timing from the start of the event. This map is automatically produced by the PRISMA pipeline, and the background map is retrieved by an API of the Geoapify Location Platform (`https://www.geoapify.com/`) from the data provided by OpenStreetMap (`https://www.openstreetmap.org/`).

of the pre-atmospheric orbit of the meteoroid (see Sect. 4.2.6). For this event, the pre-atmospheric speed was estimated to be 15.32 ± 0.07 km/s, while the visible flight ended at 9.0 ± 0.3 km/s.

Finally, we can evaluate the absolute magnitude $\mathcal{M}$ of the meteor from the apparent magnitude m knowing the distance L of the meteor along its trajectory from the different cameras (see Fig. 4.16c), as:

$$\mathcal{M} = m - 5\log_{10}\left(\frac{L}{100\ \mathrm{km}}\right) , \tag{4.31}$$

being 100 km the reference distance for the definition of the absolute magnitude of meteors detected in the Earth's atmosphere. This event reached a peak magnitude of about -6. On the plot of Fig. 4.16e, we can observe a systematic dispersion in the magnitude values computed from the different stations of ± 0.5 mag. While this event is not affected by saturation effects, this evidence may be explained by the fact that we use a daily-averaged extinction coefficient for the photometric processing, which may be unrepresentative of the atmospheric conditions at the time of observations. To date, this is actually the major limitation on the accuracy of meteor's photometric data for the PRISMA network with the current analysis pipeline.

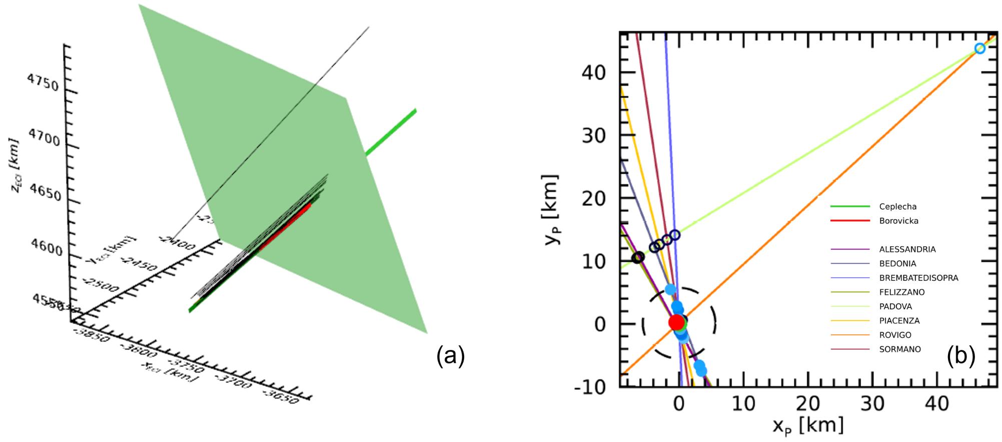

Fig. 4.18: Example of the outliers detection procedure for the triangulation of the 20180601T205147_UT event, detected by 8 PRISMA stations. (a) 3D representation of the ensemble of IP trajectories (black) together with the average IP and LoS trajectories (green and red thick lines). The green surface represents the plane Π_R perpendicular to the average IP trajectory. (b) Plot of the intersections on Π_R of the IP lines (dots) and planes Π_i (coloured lines), in projected coordinates onto Π_R. The colours of the lines indicate the i-th camera, and points laying over each line originate from that particular camera. All the points from the ITVE01 - Padova stations are outside the confidence region (dashed circle) and are therefore excluded from the computation of the LoS trajectory.

4.2.3 Error treatment in the triangulation processing

We also use the IP method to check for the presence of systematics of the data from the involved cameras in the event. This may be due to the usage of an astrometric solution not yet updated, for example after maintenance work on the camera. Another possibility is the presence of water or ice on the protective dome of the camera, which can significantly affect the astrometric accuracy of the instrument. An example of the procedure developed for the detection of systematics is presented in Fig. 4.18 for the 20180601T205147_UT event[15]. We consider the plane Π_R (green surface of panel a) perpendicular to the average IP trajectory R from Eq. 4.25 (green thick line) located in the middle point of the trajectory. Then, we evaluate the intersection points of all the IP lines R_{ij} (black thin lines) from all the couples of cameras (i, j). These are plotted as the dots in Fig. 4.18b, which represents the perpendicular back view of Π_R. The green and red dots in this plot are the intersections of the trajectory R with Π_R, respectively for the average IP and the LoS trajectories. On the other hand, the lines of different colours are the intersection of the camera planes Π_i with the average perpendicular plane Π_R. It is therefore evident that all the dots laying on one of these coloured lines are originating from the data of that particular camera, as indicated in the legend. Most of the points are accumulated in the near proximity of the average IP and LoS trajectory, within a distance of a few kilometres. However, the intersections originating from the

---

[15] https://fireball.fripon.org/displaymultiple.php?id=10271

ITVE01 - Padova camera (light green line) are significantly far from the others. The dashed circle represent the threshold level set to automatically detect such outliers, computed as three times the median distance of the intersections R_{ij} on Π_R from the average IP trajectory R. If more than one half of the intersecting points of one camera lie outside this confidence interval, we consider that the camera may be affected by a significant bias and exclude its data from the computation of the final LoS trajectory. In the example presented in Fig. 4.18, all the intersections of ITVE01 are outside this interval and this station is therefore excluded from the analysis of this event.

A particular attention is also to be paid to the estimated errors on the meteor's direction $\overline{w}_R = (\xi_R, \eta_R, \zeta_R)$. In fact, the polar coordinates of $\overline{w}_R$ represent the apparent radiant of the meteor. As already introduced in Sect. 4.1.4, this topic is of utmost importance since the relative width of the confidence intervals of $\overline{w}_R$ components will determine the uncertainties's magnitude on the deduced orbital parameters for the observed meteoroid (see Sect. 4.2.6), together with the indetermination on the pre-atmospheric speed V_∞. Then, a realistic estimation of these standard errors is required, that actually represents the quality of both our data and the results of the analysis pipeline. The problem of χ^2 minimization of Eq. 4.29, approached with a LM optimisation algorithm, will return the 3×3 covariance matrix $\overline{\Sigma}_R$ for the rectangular components of $\overline{w}_R$. First, we must notice that not all these three components are independently varied in the minimization process. One of them is automatically given by the normalization conditions $|\overline{w}_R| = 1$, Therefore, we fix $\xi_R = 1$ (the x component of $\overline{w}_R$) in the fitting procedure and normalize $\overline{w}_R$ to a unitary norm at the end of the computation. This will result in the first row and column of $\overline{\Sigma}_R$ being identically zero ($\Sigma_R[\xi,\xi] = \Sigma_R[\xi,\eta] = \Sigma_R[\xi,\zeta] = 0$).

Then, we also have to understand what is the actual number N_{DOF} of degrees of freedom (DOF) of the problem. This problem was first outlined by Jeanne et al. (2019) for the analysis of FRIPON data. On one hand, we can think that each point of each detection represents one DOF so that $N_{DOF} = N_p = \sum_{i=0}^{N-1} M_i$. This is the most optimistic scenario and it considers that each measurement $(\alpha_{ik}, \delta_{ik})$ from each camera i is independent of one another. Therefore, the uncertainties of the problem would be dominated by the random error on each (i,k). On the opposite side, we may think that each detection represents just one DOF, so that $N_{DOF} = N$. In this scenario, each measurement (i,k) from one detection i is perfectly correlated with all the other measurements of that detection. This would mean that the systematic error on each detection i is dominant over the random errors of each measurement k within that detection. The actual conditions of the problem will be in between these two extrema. In fact, it is reasonable to assume that a certain degree of correlation will always exist in the astrometric data of one detection, which are deduced from the same monthly astrometric solution of that camera. This is the same problem discussed for the photometric data of meteors at the end of the previous section, but at a lower order of magnitude. While we concluded that the astrometric parameters can be usually considered constant within a time interval of one month (see Sect. 4.1.5), smaller variations may be due for example to local temperature- or wind-driven effects at the specific time of observation. In the framework of a fully automatic processing pipeline, we have little to no evidence to check for these issues, which will require an ad-hoc inspection for each detection of each event registered by the network. Looking at the problem from a different perspective, the hypothesis of $N_{DOF} = N$ is implicitly assumed when triangulating the meteor trajectory with the IP method of Ceplecha (1987), where the whole detection is assumed as a single measurement represented by the plane Π_i. Similarly, the LoS method that we use to give the final value of $\overline{w}_R$ assumes each $(\alpha_{ik}, \delta_{ik})$ as a single measurement, corresponding to $N_{DOF} = N_p$. This hypothesis directly affects the computed covariance matrix $\overline{\Sigma}_R$ from the χ^2 minimization, which elements' magnitude scale as $N_{DOF}^{-1/2}$.

To estimate the actual value for N_{DOF}, Jeanne et al. (2019) developed an empirical method to evaluate the relative dominance of random and systematic errors based on the results of the astrometric calibration. For the PRISMA data processing, we implemented a different approach but with the same final goal. In the analysis described above concerning the LoS method, we never considered the measured positions $\overline{p}_{ik}$ in detail. As a matter of fact, the trajectory is determined from the fitted positions $\overline{q}_{ik}$, which are mathematically confined over the trajectory R determined through the optimization algorithm. While we already checked that the distances $\delta_{ik} = |\overline{p}_{ik} - \overline{q}_{ik}|$ are comparable with the overall astrometric precision level, we can also give an estimation of the direction versor from the measured $\overline{p}_{ik}$. These points will not exactly align on a straight-line, since they are bound to vary along the corresponding LoS (Eq. 4.26). From the data of each camera, we can therefore derive an estimation of $\eta_{R,i}$ and $\zeta_{R,i}$ by means of a weighted linear fit of the Y and Z coordinates series of $\overline{p}_{ik}$, while $\xi_{R,i}$ is given by the normalization condition. We now have N estimates of the direction versor, as $\overline{w}_{R,i} = (\xi_{R,i}, \eta_{R,i}, \zeta_{R,i})$. In this way, a second estimation of the trajectory direction $\overline{w}_R$ can be given as the weighted average of the components. For the example of the η component, that is:

$$\langle \eta_{R,i} \rangle = \frac{1}{\sum_i W_i} \sum_i W_i \eta_{R,i} \ , \tag{4.32}$$

where $W_{R,i} = \sigma_{\eta,i}^{-2}$ are the normal weights as derived from the linear fit. We prefer a weighted scheme because data from different cameras may have very different precision and accuracy, for example due to the apparent altitude at which the meteor was detected by each station that affects the plate scale of the image. Systematic effects on each camera will show at this point as values of $\eta_{R,i}$ significantly different from η_R. We are then interested to deduce a measure of the dispersion of $\eta_{R,i}$, that can be given as the weighted variance of the mean[16], as:

$$s_\eta^2 = \frac{1}{\left(\sum_i W_i\right)^2 / \sum_i W_i^2 - 1} \frac{\sum_i W_i \left[\eta_{R,i} - \langle \eta_{R,i} \rangle\right]^2}{\sum_i W_i} \,. \tag{4.33}$$

Therefore, an estimation of the effective number of DOF can be derived by comparing s_η^2 with the nominal variance deduced from the χ^2 minimization of the LoS problem:

$$N_{DOF} = \frac{\Sigma_R[\eta, \eta]}{s_\eta^2} N_p \tag{4.34}$$

If the dispersion of $\eta_{R,i}$ values is comparable with the nominal uncertainty of η_R, we can deduce that random errors are dominant in the problem and $N_{DOF} = N_p$. In this case, we consider that the nominal variance $\Sigma[\eta, \eta]$ is an appropriate estimation of the uncertainty of η_R derived from the LoS method. Otherwise, if $s_\eta^2 > \Sigma[\eta, \eta]$, the effective number of DOF is being overestimated and we are not acknowledging some systematics within the problem. Therefore, we correct the nominal LoS error accounting for this evidence. The same reasoning can be done for the ζ component of $\overline{w}_R$. In any case, we require that the estimated numbers of DOF is bounded within the two limit scenario, so that $N_{DOF} \in [N, N_p]$. If we take the example presented in Sect. 4.2.2 for the 20190415T194950_UT event, this method returns $N_{DOF} = 67$ for both the η_R and ζ_R components of $\overline{w}_R$, against the total number of observations $N_p = 460$. According to our method, this means that we need to correct the nominal uncertainties for a factor of 2.6, resulting in $\eta_R = 0.4020 \pm 0.0008$ and $\zeta_R = 0.8970 \pm 0.0007$ (determined with a correlation coefficient of 0.066). Some clues for this outcome may have been already evident from Fig. 4.16b to a critical observer. In fact, the residuals δ_{ik} of different cameras are not randomly distributed around zero. For example, the residuals of the ITPI03 - Felizzano camera are systematically below the trajectory, while the ones of ITPI04 - Luserna San Giovanni are above it.

A final note can be given about the goodness of the straight-line hypothesis of the meteor's trajectory in the atmosphere, which is assumed in both the IP and LoS methods. The movement of the meteoroid is indeed affected by the Earth's gravitation which may significantly curve its trajectory. In the worst possible case of a slow meteor ($V_\infty = 11.1$ km/s) travelling for 100 km with a trajectory parallel to the ground, the expected deviation from a straight-line is of about 50 m (Jeanne et al., 2019). This is comparable to the astrometric precision achievable with the FRIPON/PRISMA hardware, so we should not be able to detect such small curvature in our data, with the rare exception of outstandingly long and grazing fireballs.

---

[16] `http://seismo.berkeley.edu/~kirchner/Toolkits/Toolkit_12.pdf`

4.2.4 Dynamic model

Having determined from the triangulation the key quantities $(H_k, V_k, \mathcal{M}_k)$[17] as a function of the time t_k for the observed meteor, we can now evaluate a dynamical model to estimate the physical parameters of the meteoroid. Let us resume here the discussion about the physics of the meteor phenomenon, introduced in Sect. 2.5, and consider the set of equations derived in Sect. 2.5.3:

$$\begin{cases} \frac{\mathrm{d}H}{\mathrm{d}t} = -V \sin\gamma \\ M\frac{\mathrm{d}V}{\mathrm{d}t} = -\Gamma S \rho_a V^2 \\ M = M_\infty \exp\left\{\frac{1}{2}\sigma\left(V^2 - V_\infty^2\right)\right\} \\ I = -\tau M V \left(1 + \frac{\sigma V^2}{2}\right)\frac{\mathrm{d}V}{\mathrm{d}t} \ . \end{cases} \tag{4.35}$$

To be able to apply this set of equations to the observational data of altitude, speed and magnitude, we still need to make a few considerations. The main issue to be addressed is how to infer the meteoroid's section S from its mass without any prior knowledge of the shape of the body itself. A common assumption can be the one of a spherical shape that preserves its proportion during the flight with an isotropic ablation. A more general hypothesis is the one first proposed by Levin (1956), which assumes that S scales as a function of M as the following:

$$\frac{S}{S_\infty} = \left(\frac{M}{M_\infty}\right)^\mu \tag{4.36}$$

where μ can be addressed as the *shape-change parameter*. Assuming the variables $s = S/S_\infty$ and $m = M/M_\infty$ normalized with respect to their preatmospheric values, Eq. 4.36 can be given in the form of $s = m^\mu$. To understand the physical meaning of μ, let us consider that:

$$\mathrm{d}s = \mu m^{\mu-1}\mathrm{d}m \quad \rightarrow \quad \mu = \left[\frac{\mathrm{d}s}{\mathrm{d}m}\right]_{m=1} \ . \tag{4.37}$$

Then, μ is the rate of relative variation of the section s per unit mass loss m at the very beginning of the flight, when $m = 1$ (that is, $M = M_\infty$). Some illustrative examples can be given to better understand this assumption:

- $\mu < 0 \rightarrow \mathrm{d}s > 0$. This means that the meteoroid gains section as it loses mass. While this scenario may look quite unrealistic, we also have to consider that the evaporation and sublimation of material from the meteoroid's surface creates a vapour cap surrounding the body (see Sect. 2.5.2), which can virtually increase the section exposed to the flow at least in the first phase of the flight.

---

[17] From here on out, $k \in [0, N_p - 1]$ will represent the index of observations, regardless of which is the involved camera for each point.

- $\mu = 0 \rightarrow \mathrm{d}s = 0$. The meteoroid does not lose section as it ablates. This phenomenology corresponds to the case of frontal ablation, for which the meteoroid does not rotate during the flight, always exposing the same side to the flow and losing mass without significantly modifying its section.
- $\mu = 2/3$. The section scales as a function of $m^{2/3}$, which is the case of a spherical body ablating isotropically. In general, we can interpret this phenomenology as if the body is rotating fast enough to expose all its faces within a small interval of time so that the ablation can be considered isotropic.
- $\mu = 1 \rightarrow \mathrm{d}s = \mathrm{d}m$. This means that the relative variations of mass and section are equal. This phenomenology is quite peculiar. One example adhering to this condition is the case of the ablation of a body resembling a thin sheet, with a negligible thickness.
- $\mu >> 1$. Developing the analysis of Eq. 4.37, one can conclude that this regime is quite unusual too. In fact, it turns out that the loss of section occurs mostly at the very beginning of the flight (near $m = 1$), while after this transient the meteoroid loses mass without a significant section loss. This may be the case of a body with a high degree of density inhomogeneity, for example with most of the mass being concentrated in its centre and surrounded by an extended and thin "umbrella" (accounting for most of its preatmospheric section S_∞) that instantly ablates as the body enters the atmosphere.

From this analysis, we can deduce that $\mu \in [0, 1]$ is appropriate to describe the phenomenology of the vast majority of the cases, since all values outside this range represent a quite unrealistic dynamic. We can therefore rewrite the deceleration equation as a factor of the *mass-to-section ratio* (MSR or D), as:

$$D = \frac{M}{S} \quad \rightarrow \quad \begin{cases} D\frac{\mathrm{d}V}{\mathrm{d}t} = -\Gamma \rho_a V^2 \\ D = D_\infty \exp\left\{\frac{1}{2}\sigma(1-\mu)\left(V^2 - V_\infty^2\right)\right\} \end{cases} \tag{4.38}$$

A first approach to solve the problem of Eqs. 4.35 and 4.38 is to look for an analytical solution for it. This is summarized in the work of Gritsevich (2007), Gritsevich (2009), and Gritsevich and Koschny (2011). As a first step, we have to make the further assumption of an isothermal atmosphere, so that:

$$\rho_a = \rho_0 e^{-\frac{H}{H_0}} , \tag{4.39}$$

where ρ_0 is the atmospheric density at the sea level and H_0 is the scale height. We use again the normalized variables $v = V/V_\infty$, $h = H/H_0$ and $d = D/D_\infty$ and write the deceleration equation replacing dt with dh from the altitude equation as the following:

$$\frac{\Gamma \rho_0 H_0}{D_\infty \sin\gamma} e^{-h} \mathrm{d}h = \exp\left\{\frac{\sigma(1-\mu)}{2} V_\infty^2 (v^2 - 1)\right\} \frac{\mathrm{d}v}{v} . \tag{4.40}$$

In this expression, we can notice the presence of two adimensional parameters, that are:

$$\alpha = \frac{\Gamma \rho_0 H_0}{D_\infty \sin\gamma} \quad , \quad \beta = \frac{\sigma(1-\mu)}{2} V_\infty^2 \ . \tag{4.41}$$

and Eq. 4.40 can be written as:

$$\alpha e^{-h} \mathrm{d}h = e^{\beta(v^2-1)} \frac{\mathrm{d}v}{v} \ . \tag{4.42}$$

The parameter α is linked to the preatmospheric MSR value and is called the *ballistic coefficient*. On the other hand, β was originally named as the mass-loss parameter by Gritsevich (2007). As it is clear from Eq. 4.38, β is rather linked to the MSR loss, so we prefer the name of *MSR-loss parameter* for it. At the same time, we name Ω as the *mass-loss parameter* according to the following:

$$\Omega = \frac{\sigma V_\infty^2}{2} \quad \rightarrow \quad \beta = \Omega(1-\mu) \quad \rightarrow \quad \begin{cases} m = \exp\{\Omega(v^2-1)\} \\ d = \exp\{\beta(v^2-1)\} \ . \end{cases} \tag{4.43}$$

Then, we can integrate Eq. 4.42 as:

$$\int_\infty^h \mathrm{d}h' \alpha e^{-h'} = \int_1^v \frac{\mathrm{d}v'}{v'} e^{\beta(v'^2-1)} \ . \tag{4.44}$$

To solve this, we must make the hypothesis of a *constant-parameters flight*, that is α and β do not vary with H and V. With this assumption, we can bring α and β outside of the integral sign, resulting in the following:

$$-\alpha e^{-h} = e^{-\beta} \int_1^v \frac{\mathrm{d}v'}{v'} e^{\beta v'^2} \xrightarrow{u=\beta v'^2} -2\alpha e^{-h} = e^{-\beta} \int_\beta^{\beta v^2} \frac{\mathrm{d}u}{u} e^u \ . \tag{4.45}$$

Therefore, let us introduce the *exponential integral function*:

$$\mathrm{Ei}(u) = \int_{-\infty}^u \frac{\mathrm{d}t}{t} e^t \ . \tag{4.46}$$

A numerical approximation of this function is available in most programming languages. We can then solve the last integral on $\mathrm{d}u$ of Eq. 4.45, obtaining the following:

$$2\alpha e^{-h} = e^{-\beta} \left[\mathrm{Ei}(\beta) - \mathrm{Ei}(\beta v^2) \right] \ , \tag{4.47}$$

that can be written in the form of $h = h(v)$ as:

$$h = \ln(2\alpha) + \beta - \ln\left[\mathrm{Ei}(\beta) - \mathrm{Ei}(\beta v^2) \right] \ . \tag{4.48}$$

For particular cases, Eq. 4.48 has a simpler expression. If $\beta = 0$ (meaning either $\sigma = 0$ or $\mu = 1$), it can be written as:

$$h = \ln\alpha + \beta - \ln(-\ln v) \ . \tag{4.49}$$

For $\beta >> 1$, one can use the divergence expansion of the exponential integral function truncated at the first order, resulting in:

$$h = \ln(2\alpha\beta) + \ln\left[1 - \frac{e^{\beta(v^2-1)}}{v^2}\right] . \tag{4.50}$$

This last expression is particularly useful for the practical implementation of Eq. 4.48, since for $\beta \geq 710$ the result of the Ei function will exceed the machine's double-precision limit.

From this approach, we can fit Eq. 4.48 to the speed profile $V = V(H)$ from the triangulation results and derive an estimation of the flight parameters (α, β). The starting points for this fit can be provided by the analytical approach of the χ^2 problem, as developed by Gritsevich (2007). In summary, the MSR-loss parameter β can be estimated by the numerical solution of the following equation:

$$f(\beta) = \sum_k \left\{\left[\Delta_k \left(\sum_l e^{-2h_l}\right) - \left(\sum_l \Delta_l e^{-h_l}\right) e^{-h_k}\right] (\Delta_k - \Delta_k')\right\} = 0 \,, \tag{4.51}$$

where:

$$\begin{cases} \Delta_k = -2\ln v_k + \sum_{n=1}^{\infty} \frac{\beta^n}{n n!}(1 - 2v_k^{2n}) \\ \Delta_k' = \frac{\mathrm{d}\Delta_k}{\mathrm{d}\beta} = \sum_{n=1}^{\infty} \frac{\beta^{n-1}}{n!}(1 - 2v_k^{2n}) \,. \end{cases} \tag{4.52}$$

The solution for Eq. 4.51 can be found with the Newton–Raphson method, for example. If multiple positive solutions are found for β, we consider the smallest one. Then, a value for α can be estimated as:

$$\alpha = \frac{\sum_k e^{-\beta-h_k}\Delta_k}{2\sum_k e^{-2h_k}} \,. \tag{4.53}$$

These values of (α, β) are therefore fed as starting points to the LAV-modified LM optimisation algorithm to provide a final estimation for them. While it may look that (α, β) are the only two parameters involved in the problem, we must consider that the definition of the normalized speed $v = V/V_\infty$ requires the prior knowledge of V_∞. A possible approximation may be done by considering the result of the exponential fitting of Eq. 4.30 from the triangulation results. Instead, we prefer to consider V_∞ as a third parameter of the problem to be determined by the χ^2 minimization, indeed using the estimate from Eq. 4.30 as its starting point.

A further problem consists in the interpretation of the deduced value for β. As a matter of fact, β encloses both the ablation coefficient σ, in the Ω term, and the shape-change coefficient μ. From the analysis presented up to this point, there is no way to deduce σ and μ independently since they come multiplied in the expression of β (Eq. 4.41). This impasse can be solved by considering the luminosity equation (Gritsevich and Koschny, 2011). A closed form for it can be given by considering the deceleration and ablation equations (second and third ones of Eq. 4.35) and this results in the form of:

$$I = \left(\frac{\tau M_\infty \Gamma}{D_\infty}\right) \rho_a V^3 \left(1 + \frac{\sigma V^2}{2}\right) \exp\left\{\frac{\sigma\mu}{2}(V^2 - V_\infty^2)\right\} . \tag{4.54}$$

The fireball luminosity I represents the total energy emitted by the meteor across the whole spectrum per unit time. To convert it to a measure of the panchromatic absolute magnitude, we use the relationship derived by Ceplecha and Revelle (2005) and Gritsevich and Koschny (2011):

$$\mathcal{M} = -2.5\left(\log_{10} I - 3.185\right) . \tag{4.55}$$

Therefore, converting Eqs. 4.54 and 4.55 to normalized variables and replacing the term ρ_a with Eqs. 4.39 and 4.47, we obtain:

$$\mathcal{M} = \mathcal{M}_0 - \frac{2.5}{\ln 10}\left\{3\ln v + \ln\left[\mathrm{Ei}(\beta) - \mathrm{Ei}(\beta v^2)\right] + \ln\left(1 + \Omega v^2\right) + \Omega(\mu v^2 - 1)\right\} , \tag{4.56}$$

where:

$$\mathcal{M}_0 = -2.5\left[\log_{10}\left(\frac{\tau M_\infty V_\infty^3 \sin\gamma}{2H_0}\right) - 3.185\right] . \tag{4.57}$$

The fitting of this equation to the observed magnitude data allows to derive an estimation for both τ and μ. Then, the final ensemble of parameters of this model is $(V_\infty, \alpha, \Omega, \mu, \mathcal{M}_0)$, which are the inputs for Eqs. 4.48 and 4.56 and account for both speed and magnitude data.

4.2.5 Physical parameters of the meteoroid

To apply the analytical solution of Eqs. 4.48 and 4.56 to the results of the event's triangulation and derive the physical parameters of the body, we are still missing two key ingredients. These are an estimation for the values of the drag coefficient Γ, the atmospheric density at sea level ρ_0 and the scale height H_0. All of them are included in the expression for the ballistic coefficient α of Eq. 4.41 and H_0 is needed to compute the normalized height $h = H/H_0$.

The most difficult parameter to estimate is indeed the drag coefficient Γ, being mainly dependent on the shape of the meteoroid and the flow regime, directly linked to the speed of the meteoroid. The problem of the unknown shape of the meteoroid is almost impossible to solve. Even in the case of a successful meteorite recovery, little to no information can be deduced about the preatmospheric shape of the meteoroid from the morphology of the fragments. In few selected cases, the features of the fusion crust can be used only to infer if the entry of meteoroid was oriented or not (Taricco et al., 2019), suggesting a value for μ. Then, if $\mu \neq 2/3$, the shape of the meteoroid will change as it ablates affecting the drag coefficient too, while we made the assumption of a constant-parameters flight. About the flow regime (see Sect. 2.5.2), few results are available in the literature discussing the value of Γ as a function of the Re and Ma (Khanukaeva, 2004; Carter et al., 2009; Yager, 2014) or the Knudsen number Kn (Macrossan, 2007). For example, Carter et al. (2009) suggest an analytical expression for Γ as a function of the preatmospheric Mach number based on experimental data. For a meteoroid of spherical shape travelling at $Ma > 4$, they estimate $\Gamma = 0.46$, but for a cubic shape in the same flow conditions the result is $\Gamma = 0.84$ (Carter et al., 2011). This scenario is further complicated if we consider the possible presence of a vapour cap around the meteoroid, due to the sublimation of material from its surface, and the subsequent formation of a shock layer around the body. This strongly affects the local flow conditions and can result in much lower Reynolds numbers compared to the case of an unperturbed atmosphere (Moreno-Ibáñez et al., 2018). As a consequence of the complexity of this problem, different authors adopt different values for the drag coefficient: $\Gamma = 0.5$ (Gritsevich, 2009; Jeanne et al., 2019), 0.6 (Gritsevich and Koschny, 2011), 0.65 (Peña-Asensio et al., 2021), 0.75 (Moilanen et al., 2021), just to cite a few examples. For the PRISMA pipeline, we adopted the value of $\Gamma = 0.75 \pm 0.08$. The corresponding 3σ range of $[0.5, 1]$ reflects the variability of the drag coefficient for high Ma numbers and across the possible range of Re, as presented in Yager (2014) for an object of spherical shape, and encloses most of the values usually assumed by other authors, stretching towards and higher Γ for the case of a non-spherical meteoroid.

Similarly, most authors usually assume fixed values for ρ_0 and H_0 to describe the exponential profile of an isothermal atmosphere. Widely used values are $\rho_0 = 1.29$ kg/m^3 and $H_0 = 7.16$ km (Gritsevich, 2009). However, the atmospheric density profile is known to have seasonal variations and may also depend on the geographic location of the event. To check for the significance of these variations and implement a more accurate estimation for ρ_0 and H_0, we considered the NRLMSIS 2.0 global empirical atmospheric model (Emmert et al., 2021), an upgrade of the standard NRLMSISE-00 (Picone et al., 2002) that allows computing the atmospheric conditions as a function of the location, day of year, time of day, solar activity, and geomagnetic activity. In particular, we implemented in the PRISMA pipeline the automatic run of this model, since the Fortran source code is publicly available[18] for academic usage. As the input for it, we use the starting UT time of the event and the middle latitude and longitude point of its trajectory as derived from the triangulation. Solar and geomagnetic data are retrieved by live-time URL access to the CelesTrak[19] portal, which provides space weather data and in particular

---

[18] `https://map.nrl.navy.mil/map/pub/nrl/NRLMSIS/NRLMSIS2.0/`

[19] `https://celestrak.org/SpaceData/`

daily values of the F10.7, F107a and Ap indices[20] used by the NRLMSIS 2.0 model to determine the solar energy input at the top of the atmosphere. To derive an estimation for ρ_0 and H_0, we apply a log-linear fit over the atmospheric density profile ρ_a in the range $H \in [0, 100]$ km, as presented in Fig. 4.19a. In this case, we fix $\rho_0 = \rho_a(H = 0 \text{ km})$, so that only H_0 is free to vary within the fitting procedure. We limit the fit to $H < 100$ km since the exponential approximation of the density profile is not applicable above this limit, as evident from the plot of the relative residuals of the fit of panel b, reaching ±100% for $H > 100$ km. Fig. 4.19c,d plots the variation of ρ_0 and H_0 in the location of the ITPI01 - Pino Torinese station of PRISMA for the year 2020, evaluated at midnight UT of each day. A prominent seasonal oscillation accounting for a relative variation of ±5% is present for both parameters, which are anticorrelated, with a minimum of ρ_0 and a maximum of H_0 in the summer, between July and August. Hourly results also exhibit a small oscillation with an amplitude of ±0.5%, with a minimum of ρ_0 and a maximum of H_0 around late afternoon (h15–17 UT, not shown). Also, Fig. 4.20 shows the spatial variation of these parameters over the Italian territory (for the day 01/01/2020), outlining a predominantly latitudinal variation with higher values of ρ_0 and lower values of H_0 in the northern regions with respect to the South. This latitudinal variation is of a similar magnitude as the seasonal oscillation of Fig. 4.19c,d.

The importance of an accurate estimation of the atmospheric conditions for the determination of the physical parameters of meteoroids from optical data was already underlined in the literature (Pecina and Ceplecha, 1984; Lyytinen and Gritsevich, 2016). While the exponential approximation of the atmospheric density profile may look satisfying at first look, Fig. 4.19b shows important systematics of ±30% even for $H < 100$ km. Such deviations are even worst for altitudes between 100 and 130 km, reaching a value of more than 100%, and this range is still interesting for high-altitude meteors generated by smaller objects. However, an analytical expression for $\rho_a(H)$ is needed for the solution of the deceleration equation presented in Sect. 4.2.4. To free this assumption, a second approach to the problem is to directly address the differential equation's set of Eq. 4.35 with a numerical solution. With the last considerations we made in Sect. 4.2.4, the final version of this set is:

$$
\begin{cases}
\frac{\mathrm{d}H}{\mathrm{d}t} = -V \sin\gamma \\
D\frac{\mathrm{d}V}{\mathrm{d}t} = -\Gamma \rho_a V^2 \\
D = D_\infty \exp\left\{\frac{1}{2}\sigma(1-\mu)\left(V^2 - V_\infty^2\right)\right\} \\
\mathcal{M} = -2.5\left\{\log_{10}\left[\left(\frac{\tau M_\infty \Gamma}{D_\infty}\right)\rho_a V^3\left(1 + \frac{\sigma V^2}{2}\right)\exp\{\frac{\sigma\mu}{2}(V^2 - V_\infty^2)\}\right] - 3.185\right\} ,
\end{cases} \tag{4.58}
$$

---

[20] The F10.7 index is a measure of the solar radio flux at $\lambda = 10.7$ cm and it is widely used as an indicator of the solar activity, being closely correlated with the sunspot number (Tapping, 2013). The F10.7a index is the 81-days average of F10.7 centred on the day of interest. The Ap index provides a measure daily average level of geomagnetic activity (Rostoker, 1972).

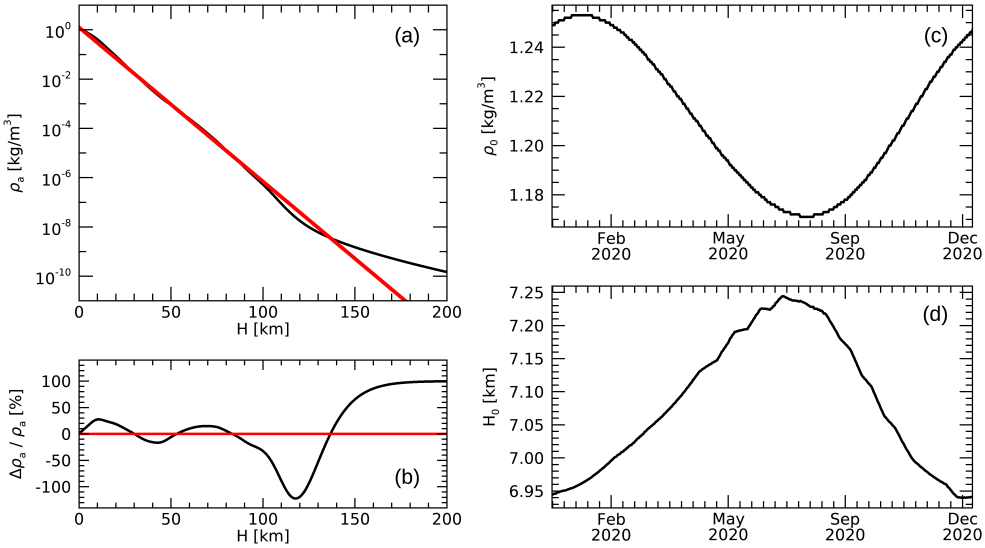

Fig. 4.19: Atmospheric density profile $\rho_a(H)$ deduced by the NRLMSIS 2.0 global atmospheric model. (a) Comparison of the modelled atmospheric profile (black line) with the fitted exponential approximation (red line) for the location of the ITPI01 - Pino Torinese station of PRISMA ($\lambda = 7.76494°$E, $\phi = 45.04124°$N) on the day 01/01/2020 at midnight UT, for which $\rho_0 = 1.249$ kg/m^3 and $H_0 = 6.94 \pm 0.03$ km; (b) Relative residuals between modelled and fitted density profile from panel a; (c) Variation of the atmospheric density at sea level ρ_0 for the ITPI01 station during the year 2020 computed each day at midnight UT; (d) same as panel c but for the scale height H_0.

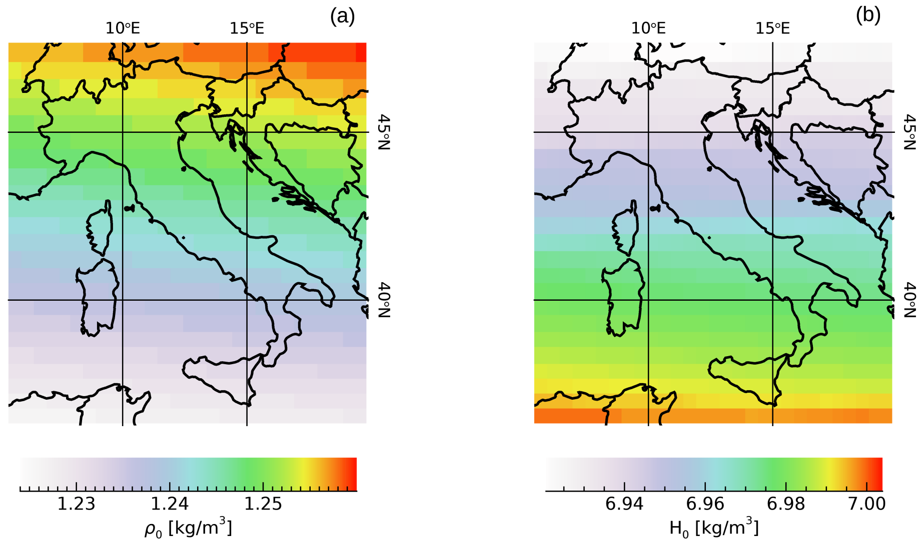

Fig. 4.20: Map of the values of (a) the atmospheric density at sea level ρ_0 and (b) the scale height H_0 over the Italian territory at 0.5° grid step for the day 01/01/2020 at midnight UT, as deduced from the exponential fit of the atmospheric density profile computed with the NRLMSIS 2.0 model.

where ρ_a is now given by the spline interpolation of the NRLMSIS 2.0 model results, gridded at 1 km step. This approach is also more general since it can also allow the solution of a dynamic model with variable parameters during the flight. For the numerical approximation of the first two equations, we use a fourth-order Runge-Kutta solver implemented in IDL[21]. The full numerical solution of Eq. 4.58 is therefore implemented within each step of the fitting procedure, that is the usual LAV-modified LM optimization algorithm. In this case, the unknowns of the problem also include the initial conditions, *i.e.* the beginning altitude H_b and speed V_b. In particular, V_b may be significantly different from V_∞ due to a partial deceleration of the meteoroid before the visible flight (Vida et al., 2020). Then, the set of parameters in this formulation is $(H_b, V_b, V_\infty, D_\infty, \gamma, \sigma, \mu, \tau M_\infty)$[22]. With respect to the analytical formulation presented in Sect. 4.2.4, D_∞ and γ are included in the ballistic coefficient α, σ corresponds to Ω and the term τM_∞ is included within $\mathcal{M}_0$. For shortening the notation, we will refer to the analytical solution of Sect. 4.2.4 as the "GRIT" model (from the first author of the reference papers, Gritsevich, 2009; Gritsevich and Koschny, 2011), while we call "NUM" the numerical implementation just discussed.

Usually, the physical parameters of the meteoroid are estimated on the speed data only through the fitting of the deceleration equation (Eq. 4.48) to estimate (α, β) from the GRIT model, or with the NUM approach. The deduced preatmospheric mass M_∞ is therefore called *dynamical mass*, for example computed from the expression of α of Eq. 4.41 assuming a value for Γ, ρ_0 and H_0 (as discussed above), considering the trajectory inclination γ from the triangulation results and a particular shape of the meteoroid. We implemented this purely dynamic approach in the PRISMA pipeline, which is named "DYN" for future reference and accounts for the deceleration's measure only. The GRIT_DYN model consists in the fitting of Eq. 4.48, while NUM_DYN considers Eq. 4.58 excluding the last equation of the system. Of course, we cannot estimate a value for both μ (which is assumed to be 2/3) and τ in this case. Then, a few authors make use of the magnitude data to estimate (μ, τ) with Eq. 4.56 but where β is fixed from the results on speed data (Gritsevich and Koschny, 2011; Drolshagen et al., 2021). We choose to adopt a different methodology, that is the simultaneous fit of both the V_k and $\mathcal{M}_k$ data. This is possible if considering the parameters Ω and μ separately in the model and results in a new formulation, that we named *photo-dynamic* model (PHD). The GRIT_PHD model consists of the simultaneous fitting of Eq. 4.48 and 4.56 and NUM_PHD in the full set of Eq. 4.58. The PHD approach allows estimating at the same time all parameters, including μ and τ, if the fit algorithm successfully converges. Therefore, the practical implementation of the dynamic model in the PRISMA pipeline is as follows:

---

[21] `https://www.l3harrisgeospatial.com/docs/rk4.html`

[22] An value of τ can be given only after estimating the preatmospheric mass M_∞, since these two parameters appear only once and are multiplied in the intensity equation of Eq. 4.58.

1. We start by fitting the GRIT_DYN model on the speed data (H_k, V_k). The starting points (α, Ω) for this fit can be easily given by Eqs. 4.51 and 4.53, assuming $\mu = 2/3$, and a first estimate of V_∞ is given by Eq. 4.30. If we cannot find a real solution for the Eq. 4.51, we use default starting points of $\alpha = 20$ and $\beta = 10$.
2. Then, we fit the GRIT_PHD model on $(H_k, V_k, \mathcal{M}_k)$. If GRIT_DYN converged, we update the starting points of (α, Ω) to the fitted DYN values. The shape-change parameter is therefore allowed to vary within $\mu \in [0, 1]$ and a starting point for $\mathcal{M}_0$ term can be given as $\min_k\{\mathcal{M}_k\}$.
3. We then repeat the same procedure for both the NUM_DYN and NUM_PHD models. The starting points for these fits are updated with the estimations by the GRIT results, if available (that is, if GRIT_DYN and GRIT_PHD converged). Concerning the initial conditions, a starting point for H_b is easily given by $\max_k\{H_k\}$, and for V_b as V_∞.

We choose to start the computation with the GRIT model since it comes with relevant benefits over the NUM approach. The model includes fewer and adimensional parameters to be estimated, making it easier for the fit procedure to converge to a solution, and an independent and in most cases reliable estimation for most of them is already available, thanks to the analytical solution of the χ^2 problem (Eqs. 4.51, 4.52 and 4.53). However, the NUM approach does not rely on the exponential approximation of the atmospheric density profile and we therefore prefer its estimates to give the final values of the physical parameters of the meteoroid. It is to be noted that the convergence of the NUM approach greatly benefits from a more accurate estimation of its parameters' starting point thanks to the results of the fitting of the GRIT model. In conclusion, we believe to have exploited the most important strengths of both approaches with this original implementation.

Figures 4.21, 4.22 and Table 4.1 show the results of the dynamic model for the 20190415T194950_UT event detected by PRISMA. In particular, Figure 4.21 shows the results of the fitting procedure for all four considered models. The left column report the results of the GRIT model, which considers H as the independent variable and assumes the exponential atmospheric density profile (panel a, blue line). The right column plots the results of the NUM model, this time having the t as the independent variable and using the NRLMSIS 2.0 atmospheric density (panel a, black line). In the plots of the speed profile, the dotted line represents the results of the DYN model, whereas the solid line is from the PHD model. In this case, the two solutions are superimposed and the DYN fit for $V(H)$ is not visible. This suggests that the DYN and PHD models return compatible parameters, as outlined in Tab. 4.1. While the deceleration curve is well described by the fitting results, few systematics can be visible in the magnitude data of 4.21c,f that are not reproduced by the photo-dynamic model. For example, a "knee" in the lightcurve is visible $H \sim 65$ km ($t \sim 1.5$ s), while the model accounts for a constant-slope magnitude increase before

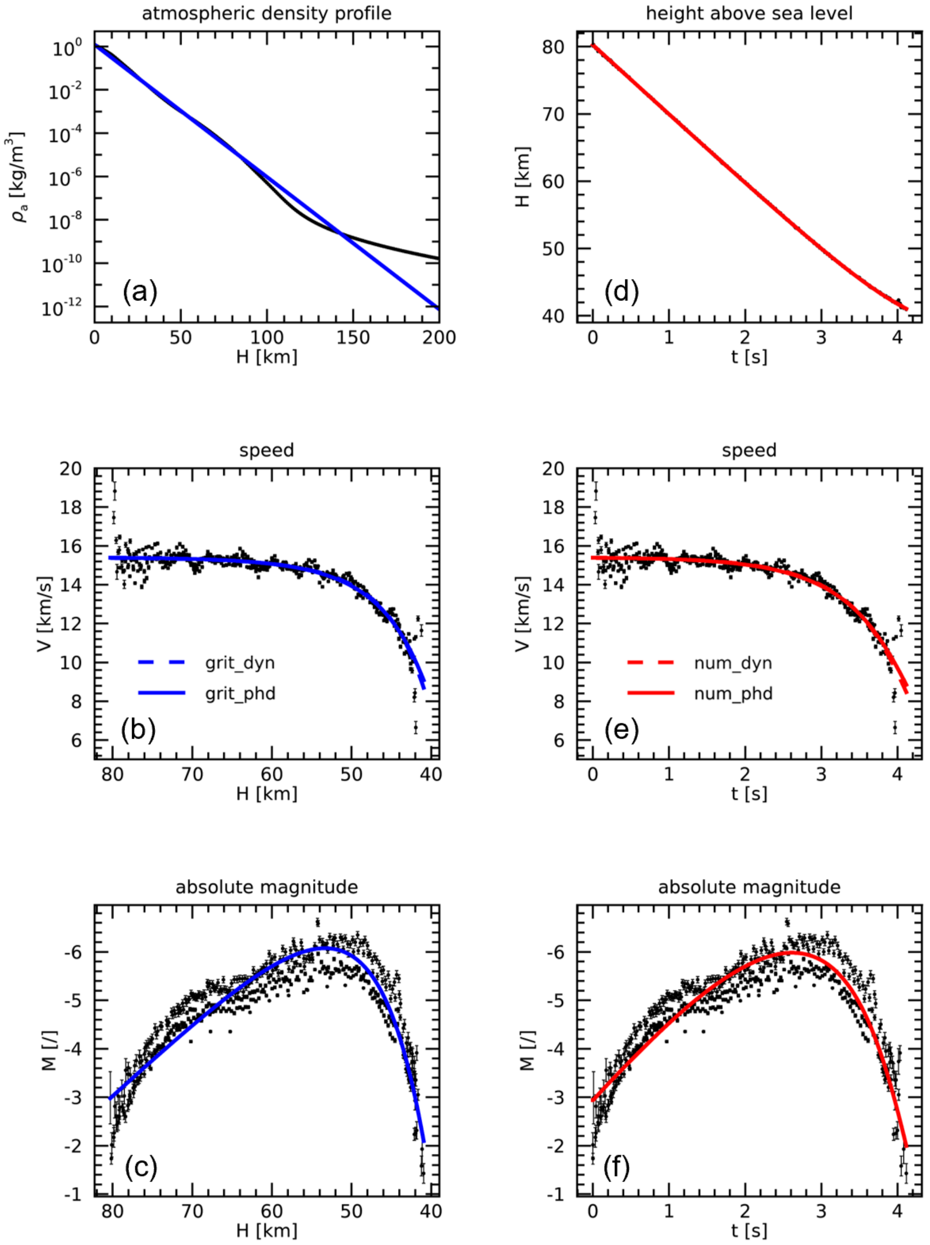

Fig. 4.21: Results of the fitting procedure of the dynamic model for the 20190415T194950_UT event. These are plots automatically produced by the PRISMA pipeline to have a visual report of the results, exported in PDF format. (a) Comparison between the NRLMSIS 2.0 atmospheric density profile (black line) with the fitted exponential profile for the GRIT model (blue line); (b) Fit of the GRIT_DYN (blue dashed line) and GRIT_PHD (blue solid line) models over the speed data (points with error bars); (c) Fit of the GRIT_PHD model (blue solid line) on the magnitude data; (d-e) same as panels b and c but for the NUM_DYN and NUM_PHD models, with the addition of the altitude equation (panel d).

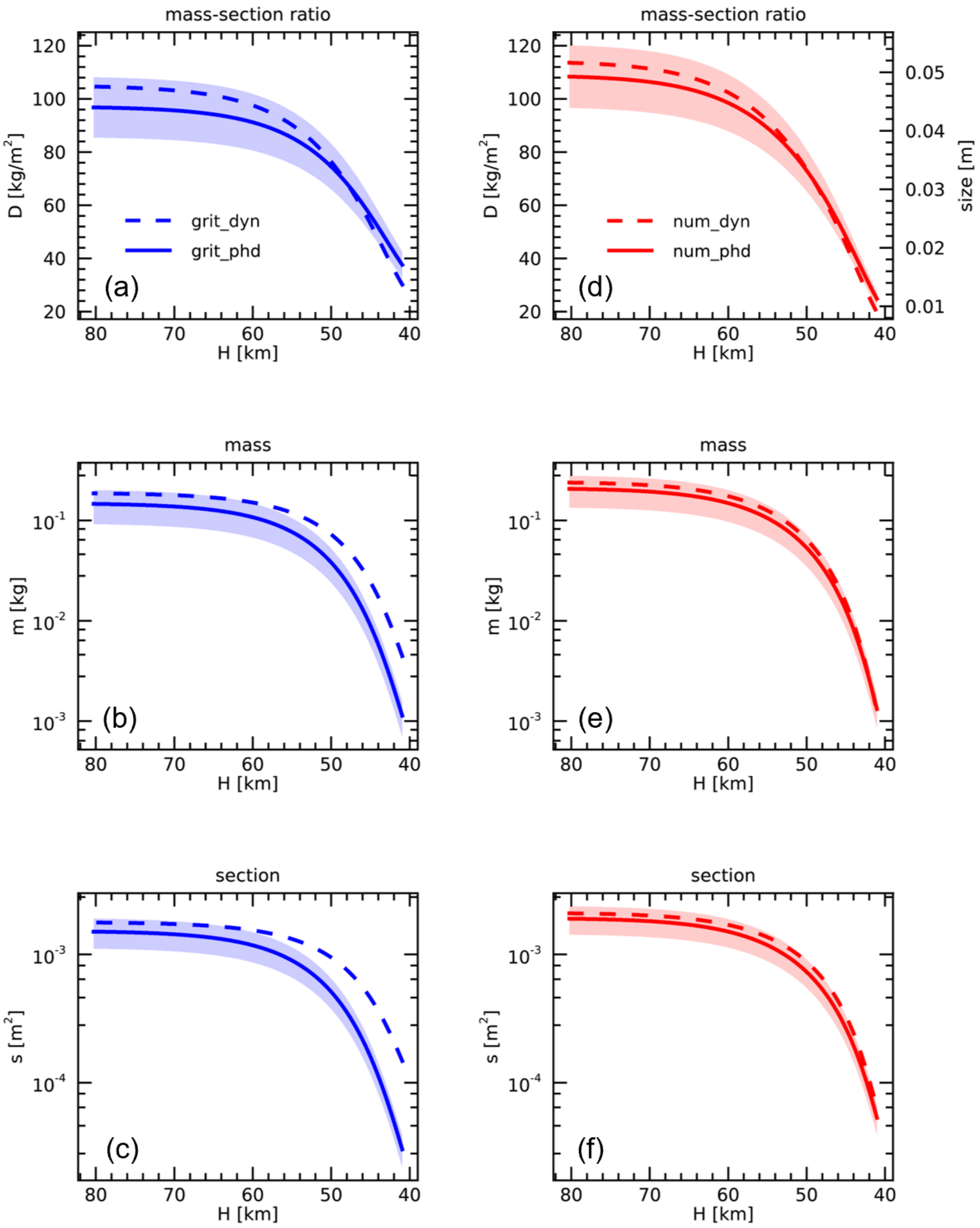

Fig. 4.22: Values of meteoroid's MSR (a, d), mass (b, e) and section (c, d) as a function of the altitude (left column, GRIT models) or time (right column, NUM models) deduced with the dynamic model of the 20190415T194950_UT event (see Fig. 4.21). The right y axis of panel d shows the conversion between MSR and size of the meteoroid (estimated as $2r$) according to Eq. 4.60. Dashed lines refer to the DYN model and solid lines to PHD model. The shaded area on solid lines represents the 1σ confidence interval for each quantity for the PHD model. These are plots automatically produced by the PRISMA pipeline to have a visual report of the results, exported in PDF format.

		GRIT_DYN	GRIT_PHD	NUM_DYN	NUM_PHD
V_∞	[km/s]	15.39 ± 0.08	15.41 ± 0.08	15.41 ± 0.05	15.40 ± 0.05
γ	[deg]	42.00 ± 0.20	42.00 ± 0.20	42.02 ± 0.04	42.09 ± 0.04
α	[/]	92 ± 11	100 ± 12	85 ± 10	89 ± 10
β	[/]	1.8 ± 0.1	1.5 ± 0.1	2.50 ± 0.07	2.21 ± 0.07
Ω	[/]	5.5 ± 0.4	7.5 ± 0.2	7.5 ± 0.2	7.6 ± 0.1
σ $(\cdot 10^2)$	[s^2/km^2]	4.6 ± 0.4	6.3 ± 0.2	6.3 ± 0.2	6.4 ± 0.1
μ	[/]	2/3	0.80 ± 0.01	2/3	0.71 ± 0.01
τ	[%]	–	4.5 ± 1.7	–	3.1 ± 1.1
D_∞	[kg/m^2]	105 ± 12	97 ± 11	114 ± 12	109 ± 12
D_{fin}	[kg/m^2]	30 ± 4	38 ± 5	20 ± 2	25 ± 3
M_∞	[g]	190 ± 70	150 ± 60	240 ± 80	210 ± 70
M_{fin}	[g]	4 ± 2	1.1 ± 0.4	1.3 ± 0.5	1.3 ± 0.5
S_∞	[cm^2]	18 ± 5	15 ± 4	21 ± 5	19 ± 5
S_{fin}	[cm^2]	1.5 ± 0.4	3.0 ± 0.9	0.7 ± 0.2	0.5 ± 0.2
$2r_\infty$	[cm]	4.8 ± 0.6	4.4 ± 0.6	5.2 ± 0.6	5.0 ± 0.6
$2r_{fin}$	[cm]	1.4 ± 0.2	1.7 ± 0.2	0.9 ± 0.1	1.1 ± 0.1

Tab. 4.1: Physical parameters of the 20190415T194950_UT event as deduced by the 4 approaches to the solution of the dynamic model implemented in the PRISMA pipeline (Figs. 4.21 and 4.22). The meaning of each symbol is described in the text.

the maximum intensity at about 55 km of altitude. These kinds of features are often visible in lightcurves of PRISMA data and may be due to variable parameters during the flight, for example of the atmospheric drag coefficient Γ, that cannot be acknowledged by the model in its current version. They may also be attributable to fragmentation events, that require ad-hoc dedicated corrections to adapt the model to the lightcurve of each event (Borovička et al., 1998; Ceplecha and Revelle, 2005; Register et al., 2017). If the general behaviour of the magnitude lightcurve is well described by the fitting results, we consider the results of the NUM_PHD model as the final reference values for the parameters of the event. Otherwise, the NUM_DYN results may be considered as well, if significantly different from the PHD version. This is not the case for our example, since DYN and PHD estimates are mutually compatible for the vast majority of the meteor's parameters (see Tab. 4.1). In this table, the reported 1σ uncertainties account for the standard errors computed by the optimization algorithm of the dynamical model, together with the contributions coming from the assigned uncertainties on the parameters Γ, ρ_0, H_0 and ρ_m (see next paragraphs).

It is to be underlined that we can deduce D_∞ only from the dynamic model, being an explicit parameter in the NUM approach and computing it from α in the case of the GRIT model. Then, we are still missing a way to compute M_∞ from D_∞, that is by specifying a preatmospheric shape and a bulk density ρ_m for the meteoroid. We choose to spherical shape in this case, which results in the following:

$$M_\infty = \frac{9}{16}\pi\frac{D_\infty^3}{\rho_m^2}\ . \tag{4.59}$$

This choice was made considering also the fact that a sphere minimizes the surface area among all 3D shapes for a given enclosed volume. That is, we will overestimate the value of M_∞ from Eq. 4.59 if this assumption is not valid. This is the least problematic scenario when having the final aim of recovering meteorites, since it will lead to an overestimation of the final mass too. In the worst case, we will point towards possible meteorites to be found on the ground when there is none (or the expected fragments are too little to be recovered), and not the other way around that may result in not identifying meteorite-droppers. With this assumption, we can determine the preatmospheric section S_∞ and radius r_∞:

$$S_\infty = \frac{9}{16}\pi\frac{D_\infty^2}{\rho_m^2} \quad , \quad r_\infty = \frac{3}{4}\frac{D_\infty}{\rho_m} \; . \tag{4.60}$$

In particular, the estimate of the characteristic dimensions of the meteoroid can be given by $2r_\infty$. We must underline that this assumption only targets the preatmospheric shape of the body, while this can change according to the μ parameter along the flight. For sure, this allows for a higher degree of generality of the model with respect to assuming $\mu = 2/3$ and considering a spherical body preserving its shape during the whole ablation phase.

About the meteoroid's density ρ_m, we assume the average bulk density of ordinary chondrites of 3.3 ± 0.2 g/cm^3 (Consolmagno et al., 2008) since this meteorite class represents the vast majority of recovered meteorites (see Sect. 2.6.1 and Tab. 2.1). This is the heaviest assumption that we need to make after the one about the value of the drag coefficient Γ. Experimental results suggest that meteoroids can have bulk densities from 0.5 up to 6 g/cm^3 (Kikwaya et al., 2011; Moorhead et al., 2017), and this is strongly correlated with the Tisserand's parameter of their pre-atmospheric orbit, that is the asteroidal or cometary origin of the body (see Sect. 4.2.6). The assumed value for ρ_m is in the middle of this wide range and should be the most appropriate for the analysis of meteorite-dropper bolides. Nevertheless, a significant systematic can originate from this strong assumption that has to be accounted for when considering the meteoroid's masses estimated by the optical observations only.

With these assumptions, we estimate a preatmospheric mass of $M_\infty = 210 \pm 70$ g for the meteoroid of the 20190415T194950_UT event, corresponding to a characteristic size of 5.0 ± 0.6 cm. Since for this event we estimated a μ value quite close to 2/3 (Tab. 4.1), the spherical shape hypothesis appears to be even more realistic. The evolution of the mass-to-section ratio, mass and section are presented in Fig. 4.22. The final mass, evaluated at the end of the visible flight imaged by the PRISMA network, is then estimated to be $M_{fin} = 1.3 \pm 0.5$ g, corresponding to 99.5% of the preatmospheric mass being ablated and making it highly unlikely to recover such a small mass on the ground. In fact, it was already evident that this event did not represent a meteorite-dropper, since it does not fulfil the empirical conditions of $V_{fin} < 4$ km/s and $H_{fin} < 25$ km (see Sect. 2.5.1).

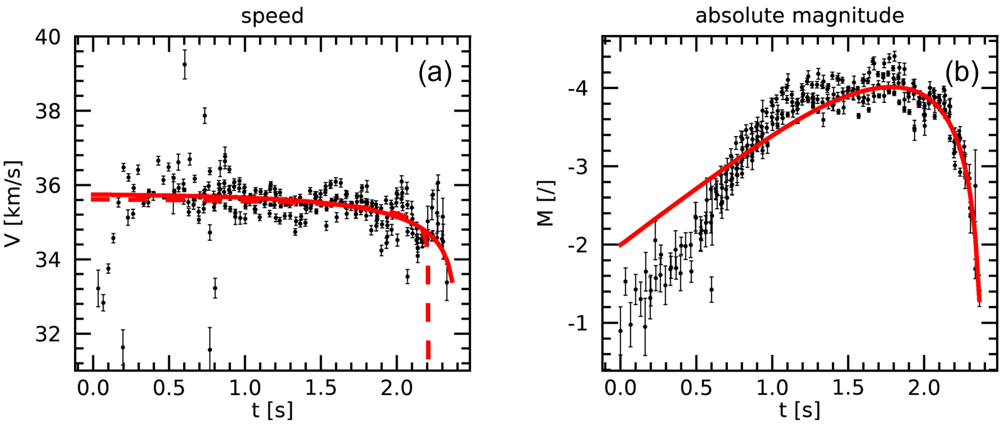

Fig. 4.23: Results of the NUM dynamic (DYN, red dashed line) and photo-dynamic (PHD, red solid line) models over the data (black points with error bars) of speed (a) and magnitude (b) of the 20181214T181546_UT event, observed by 6 PRISMA cameras.

The photo-dynamical approach is particularly advantageous when dealing the events that show little to no deceleration. In these conditions, the fitting of the dynamical model struggles to converge when relying on the speed data only. One example is presented in Fig. 4.23 for the 20181214T181546_UT event[23]. The result of the DYN fitting of the speed (dashed line on panel a) is not appropriate, showing a steep deceleration at $t \sim 2.2$ s ($H \sim 80.5$ km, not shown) that is not observed in the data. On the other hand, the PHD fitting (solid line on panel a and b) takes advantage of the additional data of the magnitude lightcurve and manages to converge to a result that better matches the observations, with a drastic improvement on the χ^2 of a factor 150 (from ~3000 for DYN to 20 for PHD). For these reasons, the dynamic and photo-dynamic estimations of the preatmospheric mass of the meteoroid are significantly different in this case. The DYN model estimates $M_\infty = 11 \pm 4$ g, while that PHD result is 1.5 ± 0.6 g. A similar difference occurs for the fitted value of the ablation coefficient, being $\sigma = 0.3 \pm 0.1$ s^2/km^2 (DYN) against 0.087 ± 0.007 s^2/km^2 (PHD). In these cases, we strongly prefer the photo-dynamic results, since the purely dynamic ones are not reliable due to the small observed deceleration of the meteoroid.

4.2.6 Preatmospheric orbit of the meteoroid

The last task to be performed within the processing of one event detected by PRISMA is the computation of the preatmospheric orbit of the observed meteoroid. Apart from the time UT of the event and its geographical coordinates (beginning longitude λ_b and latitude ϕ_b), we only need two more ingredients, which are: (1)

---

[23] `https://fireball.fripon.org/displaymultiple.php?id=1387`

the speed versor $\overline{w}_R$ in the ECI reference frame as computed with the triangulation (Sect. 4.2.2) and; (2) the preatmospheric speed module V_∞ estimated from the dynamic model (Sect. 4.2.5). Both elements come with the associated uncertainties, that are the covariance matrix $\overline{\Sigma}_R$ of the components of $\overline{w}_R$ (see Sect. 4.2.3) and the standard error of the preatmospheric speed as derived from the dynamic model. The *apparent speed* vector of the meteoroid is then simply given as $\overrightarrow{V_a} = V_\infty \overline{w}_R$, and the *apparent radiant* (at the epoch of observation) is defined by the spherical angles of $\overrightarrow{V_a}$ as the inverses of Eq. 4.17:

$$\alpha_a = \text{atan2}\,(V_{ay}, V_{ax}) \quad , \quad \delta_a = \text{atan2}\left(V_{az}, \sqrt{V_{ax}^2 + V_{ay}^2}\right) \ . \tag{4.61}$$

To be able to estimate the orbital elements of the meteoroid's orbit, we need to compute the heliocentric speed vector $\overrightarrow{V_h}$ starting from $\overrightarrow{V_a}$. The first correction to be considered is about the Earth's gravity, which accelerates the meteoroid's motion approaching the Earth. Following the method of Ceplecha (1987), we have to make the assumption that the meteoroid is not gravitationally bound to the Earth, so that the collision of the meteoroid is hyperbolic. Then, we can consider the *geocentric speed* vector $\overrightarrow{V_g}$, that is the speed of the meteoroid not influenced by the gravitational attraction of the Earth (before the collision). Its module can be simply given by the conservation of energy as:

$$V_g = \sqrt{V_a^2 - \frac{2GM_0}{R_0 + H_b}} \ , \tag{4.62}$$

where G is the gravitational constant, M_0 and R_0 are respectively the mass and radius of the Earth and H_b is the observed beginning height of the meteor. The direction of $\overrightarrow{V_g}$ is modified according to the *zenithal attraction* effect, that is, the speed vector is attracted towards the local zenith direction due to the Earth's gravitational force. The zenith distance of the geocentric radiant z_g can be therefore computed as:

$$z_g = z_a + 2\text{atan}\left[\frac{(V_a - V_g)\tan\frac{z_a}{2}}{(V_a + V_g)}\right] \ . \tag{4.63}$$

The proof of this formula can be found in Chap. 12, Sect. 97 of Dubyago (1961). To apply Eqs. 4.62 and 4.63, we need to convert the ECI components of $\overrightarrow{V_a} = (V_{ax}, V_{ay}, V_{az})$ into equatorial coordinates $(V_a, \alpha_a, \delta_a)$ and then into horizontal coordinates (V_a, a_a, z_a). After having applied the geocentric corrections, we therefore convert the horizontal coordinates (V_g, a_g, z_g) back into the ECI components of $\overrightarrow{V_g} = (V_{gx}, V_{gy}, V_{gz})$. In doing all these transformations, it is important to propagate the full covariance matrix $\overline{\Sigma}$ to not lose the information about its non-diagonal elements. For example, in the conversion between rectangular ECI components and equatorial coordinates EQ the covariance propagation is in the form of:

$$\overline{\Sigma}_{\text{EQ}} = \overline{J}\,\overline{\Sigma}_{\text{ECI}}\,\overline{J}^T \ , \tag{4.64}$$

where $\overline{J}$ is the jacobian matrix of the ECI $\rightarrow$ EQ transformation from Eqs. 4.61 and together with the expression of the module of the apparent speed vector $V_a = \sqrt{V_{ax}^2 + V_{ay}^2 + V_{az}^2}$. After correcting for the Earth's gravity, we can precess $\overrightarrow{V_g}$ to the J2000 epoch and compute the heliocentric speed $\overrightarrow{V_h}$ simply as:

$$\overrightarrow{V_h} = \overrightarrow{V_g} + \overrightarrow{V_0} \, , \tag{4.65}$$

where $\overrightarrow{V_0}$ is the Earth's revolution speed and can be estimated, for example, using the BARYVEL[24] procedure implemented in the IDLAstro library from NASA. The reader should be aware that the speed vectors we are considering are pointing towards the arrival direction (that is the radiant) and not the motion direction, so this applies also for $\overrightarrow{V_0}$ in Eq. 4.65.

Then, the Keplerian orbital elements of the meteoroid are uniquely defined by the meteoroid's position $\overrightarrow{X_h} = (X_h, Y_h, Z_h)$ and speed $\overrightarrow{V_h} = (V_{hx}, V_{hy}, V_{hz})$ in the assumption of a two-body problem. The meteoroid's heliocentric position vector $\overrightarrow{X_h}$ can be well approximated by the Earth's position $\overrightarrow{X_0} = (X_0, Y_0, Z_0)$ at the time of the meteoroid's impact, which is also provided by the IDLAstro library in the XYZ[25] procedure as a function of the modified Julian date of the event. Considering the average Sun-Earth distance of 1 AU $\sim$ 1.5·10^8 km against the meteoroid's distance from the Earth's centre of $R_0 + H_b \sim$ 6500 km, the systematic introduced by this approximation is less than 0.05%. Since orbital elements are usually given in ecliptic coordinates, we finally convert $\overrightarrow{X_h}$ and $\overrightarrow{V_h}$ into this reference frame by using the EULER[26] procedure and scale them to the units of AU and AU/year respectively, for the sake of simplicity. We choose the ensemble of primary orbital elements to compute in our case as $(h, e, i, \Omega, \omega, \nu)$. The first element is the specific angular momentum:

$$\overrightarrow{h} = \overrightarrow{X_h} \times \overrightarrow{V_h} \quad \rightarrow \quad h = \left| \overrightarrow{h} \right| . \tag{4.66}$$

This vector is perpendicular to the orbital plane of the meteoroid and the sign of its Z component indicates if the orbit is prograde ($h_z > 0$) or retrograde ($h_z < 0$). Then, the inclination i of the meteoroid's orbit with respect to the ecliptic is given as:

$$i = \text{acos}\left(\frac{h_z}{h}\right) \, . \tag{4.67}$$

The orbital eccentricity e can be computed as the module of the eccentricity vector $\overrightarrow{e}$ that points from the aphelion towards the perihelion:

$$\overrightarrow{e} = \frac{\overrightarrow{V_h} \times \overrightarrow{h}}{\mu} - \frac{\overrightarrow{X_h}}{\left|\overrightarrow{X_h}\right|} \quad \rightarrow \quad e = |\overrightarrow{e}| \, , \tag{4.68}$$

---

[24] https://idlastro.gsfc.nasa.gov/ftp/pro/astro/baryvel.pro

[25] https://idlastro.gsfc.nasa.gov/ftp/pro/astro/xyz.pro

[26] https://idlastro.gsfc.nasa.gov/ftp/pro/astro/euler.pro

where $\mu = GM_S \simeq 39.477$ AU^3/yr^2 is the heliocentric gravitational parameter. From the definition of eccentricity vector, the true anomaly ν at the time of impact can be easily computed as the angle between $\overrightarrow{e}$ and $\overrightarrow{X_h}$:

$$\nu = \begin{cases} \text{atan2}\left(\left|\overrightarrow{e} \times \overrightarrow{X_h}\right|, \overrightarrow{e} \cdot \overrightarrow{X_h}\right) & \text{IF } \overrightarrow{V_h} \cdot \overrightarrow{X_h} \geq 0 \\ 2\pi - \text{atan2}\left(\left|\overrightarrow{e} \times \overrightarrow{X_h}\right|, \overrightarrow{e} \cdot \overrightarrow{X_h}\right) & \text{IF } \overrightarrow{V_h} \cdot \overrightarrow{X_h} < 0 \,, \end{cases} \tag{4.69}$$

where the two cases determine the sign of the radial component of $\overrightarrow{V_h}$ to understand if the meteoroid was flying away ($\overrightarrow{V_h} \cdot \overrightarrow{X_h} \geq 0$, $\nu \in [0, \pi]$) or approaching its perihelion ($\overrightarrow{V_h} \cdot \overrightarrow{X_h} < 0$, $\nu \in [\pi, 2\pi]$) when it collided with the Earth. To compute the last two elements, we need to define the ascending node vector $\vec{n}$ as:

$$\vec{n} = \hat{k} \times \overrightarrow{h} \,, \tag{4.70}$$

where $\hat{k}$ is the Z versor of the ecliptic reference frame. By definition, $\vec{n}$ lays in both the ecliptic plane and the orbital plane of the meteoroid, so that it points towards the ascending node of the orbit. The longitude of the ascending node Ω can be therefore computed as:

$$\Omega = \text{atan2}\left(n_y, n_x\right) \,. \tag{4.71}$$

Similarly, the argument of perihelion ω is the angle from the ascending node $\vec{n}$ to the eccentricity vector $\overrightarrow{e}$, that indeed points towards the perihelion:

$$\omega = \begin{cases} \text{atan2}\left(|\overrightarrow{e} \times \vec{n}|, \overrightarrow{e} \cdot \vec{n}\right) & \text{IF } e_z \geq 0 \\ 2\pi - \text{atan2}\left(|\overrightarrow{e} \times \vec{n}|, \overrightarrow{e} \cdot \vec{n}\right) & \text{IF } e_z < 0 \,, \end{cases} \tag{4.72}$$

In this equation, the two cases determine if the perihelion is within the branch of the orbit between the ascending and descending node ($e_z \geq 0$, $\omega \in [0, \pi]$) or in the opposite branch ($e_z < 0$, $\omega \in [\pi, 2\pi]$).

From this set of primary orbital elements, we can compute all the other quantities of interest to characterize the meteoroid's preatmospheric orbit. The semi-major axis of the orbit is given as:

$$a = \frac{h^2}{\mu(1 - e^2)} \,. \tag{4.73}$$

While most authors use a as a primary orbital element, we prefer to keep h since the specific angular momentum is always well-defined, while a can be not finite for $e = 1$. The perihelion distance q and aphelion distance Q are computed as:

$$\begin{cases} q = a(1 - e) = \frac{h^2}{\mu(1+e)} \\ Q = a(1 + e) = \frac{h^2}{\mu(1-e)} \,, \end{cases} \tag{4.74}$$

For closed orbits ($e < 1$) we can compute the orbital period as:

$$T = 2\pi\sqrt{\frac{a^3}{\mu}} = \frac{2\pi h^3}{\mu^2(1-e^2)^{3/2}} \,, \tag{4.75}$$

and we can also give the eccentric anomaly E_ν and mean anomaly M_ν:

$$\begin{cases} E_\nu = 2\text{atan}\left[\sqrt{\frac{1-e}{1+e}}\tan\frac{\nu}{2}\right] \\ M_\nu = E_\nu - e\sin E_\nu \end{cases} \tag{4.76}$$

The mean anomaly is particularly useful when drawing the orbit since it scales linearly with the time:

$$\Delta t = \sqrt{\frac{a^3}{\mu}}\Delta M_\nu = \frac{T}{2\pi}\Delta M_\nu \,. \tag{4.77}$$

For the case of a hyperbolic orbit ($e > 1$), the eccentric anomaly is replaced by the hyperbolic anomaly F_ν and Eq. 4.76 is modified accordingly:

$$\begin{cases} F_\nu = 2\text{atanh}\left[\sqrt{\frac{e-1}{e+1}}\tan\frac{\nu}{2}\right] \\ M_\nu = e\sinh F_\nu - F_\nu \,, \end{cases} \tag{4.78}$$

while Eq. 4.77 is modified into:

$$\Delta t = \sqrt{-\frac{a^3}{\mu}}\Delta M_\nu \,. \tag{4.79}$$

For a parabolic orbit ($e = 1$) we use the parabolic anomaly D_ν:

$$\begin{cases} D_\nu = \tan\frac{\nu}{2} \\ M_\nu = D_\nu + \frac{D_\nu^3}{3} \,, \end{cases} \tag{4.80}$$

and Eq. 4.77 now encloses the perihelion distance instead of the semi-major axis a which is not defined for a parabolic orbit:

$$\Delta t = \sqrt{\frac{q^3}{\mu}}\Delta M_\nu \,. \tag{4.81}$$

Finally, we can compute the Tisserand's parameter T_J with respect to Jupiter:

$$T_J = \frac{a_J}{a} + 2\cos i\sqrt{\frac{a}{a_J}(1-e^2)} = \frac{a_J\mu}{h^2}(1-e^2) + \frac{2h}{a_J\mu}\cos i \,, \tag{4.82}$$

where $a_J \simeq 5.2038$ AU is the semi-major axis of Jupiter's orbit. This parameter is related to the three-bodies problem (the Sun, the meteoroid and Jupiter), it is quasi-conserved along the meteoroid's orbit and is frequently used to distinguish between asteroidal orbits ($T_J > 3$) and cometary orbits ($T_J \in [2,3]$).

Speed and radiant

V_a	[km/s]	15.40 ± 0.05			
α_a	[deg]	64.98 ± 0.05	δ_a	[deg]	63.73 ± 0.04
V_g	[km/s]	10.67 ± 0.07			
α_g	[deg]	47.45 ± 0.15	δ_g	[deg]	59.68 ± 0.06
V_h	[km/s]	36.06 ± 0.06			
α_h	[deg]	106.65 ± 0.03	δ_h	[deg]	33.61 ± 0.06
λ_h	[deg]	104.07 ± 0.03	ϕ_h	[deg]	10.99 ± 0.06

Orbital elements

h	[AU^2/yr]	7.49 ± 0.01	a	[AU]	1.89 ± 0.02
e	[/]	0.500 ± 0.004	q	[AU]	0.9477
i	[deg]	11.19 ± 0.06	Q	[AU]	2.84 ± 0.03
Ω	[deg]	25.28251 ± 0.00008	T	[yr]	2.61 ± 0.03
ω	[deg]	146.5 ± 0.1	T_J	[/]	3.77 ± 0.02
ν	[deg]	33.5 ± 0.1	M_ν	[deg]	10.1 ± 0.2

Tab. 4.2: Radiant and orbital elements of the preatmospheric orbit of the 20190415T194950_UT event. Radiants are given in FK5 equatorial coordinates at J2000 epoch, except for λ_h and ϕ_h which are the ecliptic heliocentric longitude and latitude.

Figures 4.24, 4.25 and Table 4.2 report the results of the computation of the preatmospheric orbit for the 20190415T194950_UT event. In particular, the blue histograms of Fig. 4.24 plot the distributions of the primary orbital elements $(h, e, i, \Omega, \omega, \nu)$ deduced from a Monte Carlo (MC) simulation with 1k repetitions that accounts for the error propagation within the orbit computation. This is done starting from the uncertainties of the ECI components of $\overrightarrow{V_a}$ and generating replicas of random apparent speed vectors normally distributed according to the covariance matrix $\overline{\Sigma}_{\mathrm{ECI}}$. These are therefore fed to the orbit computation procedure to check the standard error propagation (solid black lines of Fig. 4.24). The agreement between the two results is good, confirming the validity of the linearization hypothesis (Eq. 4.64) within the error propagation of the nominal orbital elements, that are reported in Tab. 4.2 with their 1σ uncertainty range. Similarly, Fig. 4.25a,b plots the nominal orbit (black thick line) projected on the (x, y) and (x, z) planes in ecliptic coordinates, together with major planets' orbits and the region of the MAB (grey shaded area). The red shaded bands around the nominal orbit plot the 1,2 and 3σ nominal confidence regions, which are again to be compared by the dispersion of the MC ensemble plotted in panels c and d (red ellipses) from the nominal orbit (black thick ellipse). In this figure we plot 300 replicas, so that the width of their distribution is directly comparable with the 3σ confidence region (which encloses 99.7% of the possible orbits, that is approximately 1 - 1/300), and the agreement is quite good by a visual inspection. This meteoroid had an Apollo-type orbit (see Sect. 2.3), since its semi-major axis was determined to be 1.89 ± 0.02 (larger than 1 AU) and its perihelion of 0.9477 AU is just inside the Earth's orbit, and crossed it nearly tangential. It had a moderate eccentricity of 0.500 ± 0.004 and a low inclination on

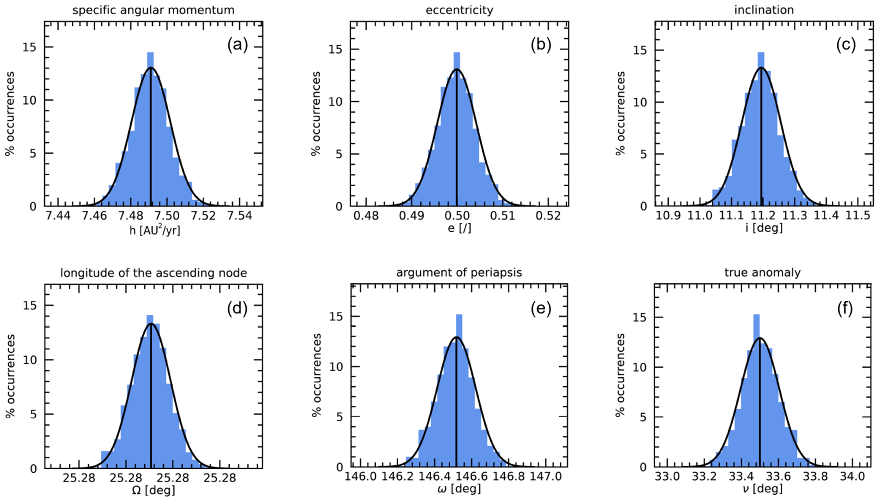

Fig. 4.24: Orbital elements $(h, e, i, \Omega, \omega, \nu)$ computed for the preatmospheric orbit of the 20190415T194950_UT event. Each panel plots the distribution computed by a Monte Carlo simulation based on the measured covariance matrix $\overline{\Sigma}_{\text{ECI}}$ of the apparent speed vector $\overrightarrow{V_a}$ (blue histograms), compared to the nominal results of the error propagation (black thick line).

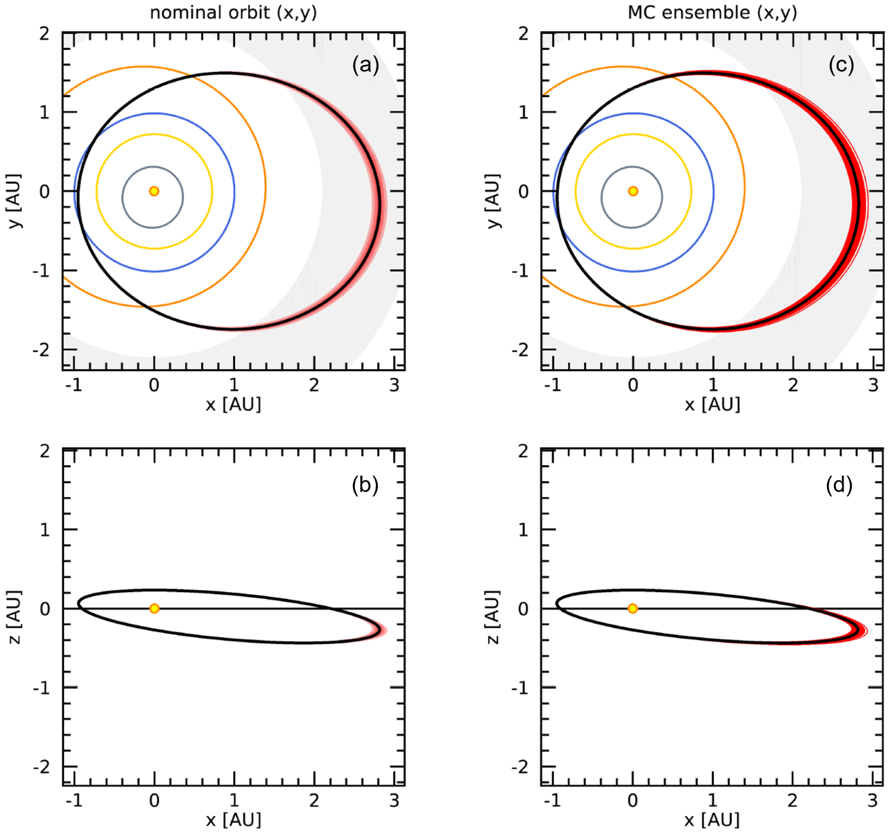

Fig. 4.25: Preatmospheric orbit of the 20190415T194950_UT event. The left column (a,b) plots the orbit's projection (x, y) and (x, z) in the ecliptic reference frame of the nominal orbit (black thick line) together with the 1,2 and 3σ confidence bands (red shaded areas) around it. The right column (c,d) plots the same projections but for 300 replicas of the Monte Carlo. In panels a and c, the big yellow dot represents the position of the Sun on the ecliptic plane, the coloured ellipses plot the orbits of inner planets (grey - Mercury, gold - Venus, blue - Earth, orange - Mars) and the shaded grey annular region represents the MAB, from 2.1 to 3.3 AU of distance from the Sun.

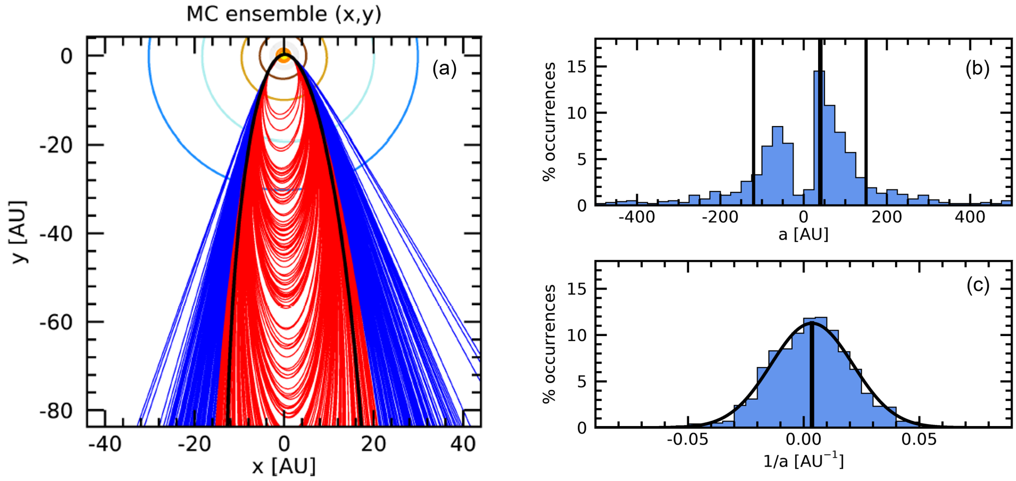

Fig. 4.26: An example of preatmospheric orbit computation for a meteoroid close to the parabolic limit, for the 20190327T232558_UT event. (a) A plot of the orbits of 300 replicas of the MC ensemble in the (x, y) ecliptic plane, showing that 41.2% of the computed orbits are open (blue lines) while the remaining 58.8% are closed (red ellipses). (b) Distribution of the semi-major axis values a for the MC ensemble, with the equivalent 1σ range indicated with the black vertical lines (15.87%–84.13% percentile with respect to the ensemble median). (c) Distribution of $1/a$ for the MC ensemble compared to the nominal value (black vertical line) and distribution from the standard error propagation method (black curve).

the ecliptic of 11.19 ± 0.06°, with its aphelion of 2.84 ± 0.03 AU inside the middle MBA. Together with a Tisserand's parameter of 3.77 ± 0.02, these results suggest an asteroidal origin for this meteoroid.

The comparison of the results of the MC ensemble with the nominal orbit and its standard errors is particularly relevant in the case of orbits close to the parabolic limit ($e = 1$). An example of this case is presented in Fig. 4.26 for the 20190327T232558_UT event[27], observed by 15 PRISMA cameras. The eccentricity of the nominal orbit is $e = 0.998 \pm 0.008$ and 41.2% of the MC replicas are open, over the parabolic limit. This is shown in panel a, presenting the ecliptic (x, y) projection of the MC ensemble of orbits. In this figure, closed orbits are plotted in red and open orbits are in blue. The nominal orbit is indeed closed. However, the standard error propagation for derived orbital parameters is not appropriate in this case. For example, Eq. 4.73 for the semi-major axis diverges for $e = 1$ and the nominal confidence range of $a = 300 \pm 1400$ AU is not really representative of the width of the distribution because the distribution itself is far from being normal, as shown in Fig. 4.26b. On the other hand, we can use the statistics of MC replica and give the equivalent 1σ range as the 15.87%–84.13% percentile with respect to the ensemble median, that in this case is $a = 40^{+110}_{-160}$ AU and is plotted as the black vertical lines in panel b. If wanting to refer to nominal values, one can refer to the inverse of the semi-major axis, being $1/a = 0.0036 \pm 0.018$ AU^{-1} (panel c). Even if

---

[27] https://fireball.fripon.org/displaymultiple.php?id=1909

the nominal orbit was found to be open, a careful inspection of the MC ensemble will finally confirm or disprove the significance of this result. The topic of open orbits deduced from optical data and their significance, related to the discovery of interstellar meteoroids, is discussed in Chap. 7.

The method by Ceplecha (1987) discussed in this section and implemented in the PRISMA pipeline for the computation of the originating preatmospheric orbit of meteoroids is the most widely used for the analysis of optical data of meteor and fireball networks. However, it comes with some limitations. For example, this method makes the assumption of a hyperbolic impact with the Earth (Eqs. 4.62 and 4.63) to correct for the influence of the Earth's gravitational field and neglects the perturbations due to third bodies, such as the Moon and other planets of the Solar System. The most complete approach consists in the numerical back-integration of the meteoroid's state vector $(\overrightarrow{X_h}, \overrightarrow{V_h})$ in a N-body problem that accounts for the gravitational perturbations of the major planets along the meteoroid's orbit. Clark and Wiegert (2011), Dmitriev et al. (2015), and Jansen-Sturgeon et al. (2019) compared the precision and accuracy of the Ceplecha (1987) method with different numerical solvers of this sort and all concluded that the analytical method is appropriate to compute the preatmospheric orbit of meteoroids from optical data. While the numerical approaches showed a greater accuracy level in general, the results were often compatible due to the random error if the atmospheric drag is correctly taken into account, so that a proper estimate of V_∞ is given instead of just using the first observed speed value V_b.

5

The recovery of the Cavezzo and Matera meteorites

The technological and scientific efforts deployed by the PRISMA collaboration in the development of the first professional Italian fireball network allowed for the recovery of two meteorites on the national soil. The first one was recovered on 04/01/2020 in the municipality of Cavezzo (MO) in Emilia Romagna, after a meteorite-dropping bolide was detected by eight PRISMA cameras just three days before, on the evening of the New Year's Day. Two meteorite's specimen of a total mass of 55.3 g were recovered by a local inhabitant, Mr. Davide Gaddi, on an embankment along the Secchia river in the area of the strewn-field delimited by the observations of PRISMA. The finder eventually donated to INAF the two fragments, which are now preserved at the Museo di Scienze Planetarie in Prato, Toscana. The second meteorite was recovered on 17/02/2023 in the city of Matera, in Basilicata. The bolide was captured on the evening of Saint Valentine's Day (14/02) by three PRISMA cameras only, due to the non-optimal coverage of the network in the southern part of Italy. Nevertheless, the analysis of these data allowed to confine an area of probable fall. In this case we received a report of a peculiar finding, since the meteorite landed on the roof of a house in a rural area in the North of Matera (Contrada Rondinelle). One fragment landed on the balcony of the house, damaging one tile, and another fragment impacted a solar panel installed on the roof, shattering its glass surface. Most probably originating from these impacts, dozens of fragments were found by the two owners of the house, the brothers Mr. Gianfranco e Pino Losignore, in the neighbouring area, amounting to 117.5 g of total recovered mass.

With an average rate of only 1 fall meteorite every ten years acknowledged by The Meteoritical Bulletin on the Italian soil in the last century and just one recovered fall in the last 20 years before Cavezzo, the work of PRISMA significantly increased the efficiency in meteorite's recovery in Italy. Moreover, Cavezzo is one of the smallest "pedigree" meteorites ever recovered (see Tab. 2.2) and this demonstrates the effectiveness of accurate processing of fireball network data even on challenging events generated by small-size meteoroids. Also, the PRISMA collaboration adopted a novel citizen science approach to maximize the recovery efficiency when a meteorite-dropping bolide is detected, consisting of informing and involving the local population in the on-field search activity. This strategy proved to be successful in both cases. In this chapter, I describe the analysis of the two events and the recovery of the two meteorites, together with the analysis of the Cavezzo meteorite.

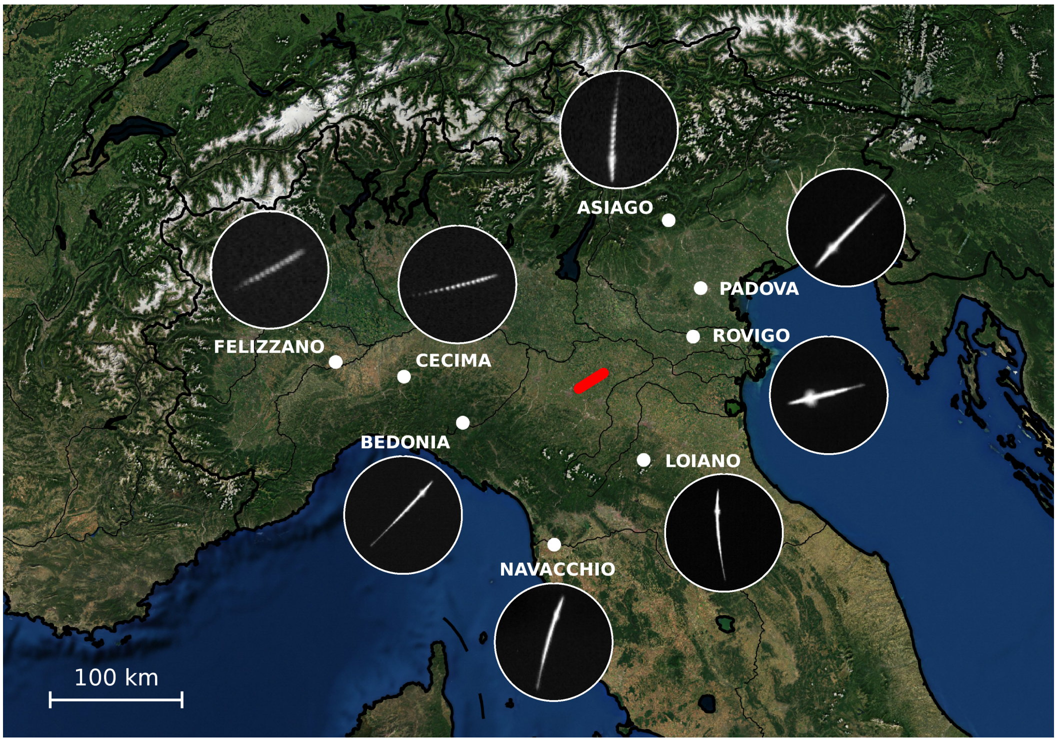

Fig. 5.1: Map of the PRISMA stations (white dots) involved in the detection of the IT20200101 fireball (Gardiol et al., 2021). The red line plots the fireball bright trajectory projected on the ground, and white circles enclose the fireball trail seen by each camera (reconstructed from video records). The fireball trails are oriented accordingly to the specific in-situ hardware installation and may be not strictly consistent with one another (all-sky images, from which meteor trails are cropped, were approximately oriented with N direction upward and E direction rightward). Background map was generated using the Matplotlib Basemap Toolkit (Hunter, 2007, `https://matplotlib.org/basemap/users/index.html`).

5.1 The IT20200101 event

Eight PRISMA stations detected a bright bolide in the skies of Northern Italy on 01/01/2020 at 18:26:53 UT, which we will name IT20200101 in the text from now on. Figure 5.1 presents the map of PRISMA stations that detected this event (white dots) together with the on-ground projection of the reconstructed trajectory (red line) and the images of the meteor trail seen by each camera (enclosed in white circles). The list of the involved stations is reported in Tab. 5.1. The FRIPON alert system initially performed a preliminary data analysis based on the data of four of these stations (ITPI03, ITTO02, ITER04, ITVE02), since the remaining ones had been installed just prior to the detection and were not yet configured in the automatic pipeline. The results of this preliminary analysis already indicated that meteorite fragments were likely to be found on the ground. This was evident from the beginning since the bolide entered the atmosphere with a high inclination angle of about 66° with respect to the ground, reaching a final altitude of 21 km at a low speed of 3.4 km/s. In order to get a preliminary estimate of the strewn-field,

Station name	Lat. N [°]	Long. E [°]	El. [m]
ITER04 - Bedonia	44°30’27.7”	09°37’57.0”	550
ITVE02 - Rovigo	45°04’54.0”	11°47’42.2”	15
ITPI03 - Felizzano	44°54’45.0”	08°26’14.0”	114
ITER01 - Loiano	44°15’23.7”	11°19’54.4”	787
ITLO03 - Cecima	44°48’52.7”	09°04’43.6”	670
ITTO02 - Navacchio	43°40’59.5”	10°29’29.9”	15
ITVE01 - Padova	45°24’07.0”	11°52’06.7”	64
ITVE03 - Asiago	45°50’57.9”	11°34’06.0”	1370

Tab. 5.1: PRISMA stations that observed the IT20200101 fireball. From left to right: station name, latitude, longitude and elevation above sea level.

we reprocessed the data manually adding two of the missing cameras (ITLO03 and ITER01). In the meantime, we also started to receive many reports from visual observers. In particular, 52 observations were reported through the PRISMA website on the International Meteor Organization online form[1].

The results of the analysis of the IT20200101 bolide and the circumstances of the meteorite recovery were published in Gardiol et al. (2021). It must be noted that, at the beginning of the year 2020, the full analysis pipeline presented in Chap. 4 had not been fully developed yet. As a consequence, the results presented in this section might slightly differ from the one published in 2021 (the same reported in Tab. 2.2), even if we did not find very significant differences between the two versions. The results of Gardiol et al. (2021) refer to an alternative pipeline developed by PRISMA and presented in Carbognani et al. (2020). This method includes also the computation of the strewn-field, which is not yet implemented in the automatic pipeline on the PRISMA servers. If a meteorite-dropping bolide is detected by PRISMA, we always compare these two versions of the data analysis to cross-check our results, including also a third independent analysis provided by FRIPON[2], which method is described in Jeanne et al. (2019).

As shown in Fig. 5.1, the IT20200101 fireball was observed with a homogeneous coverage from all directions, thanks to the good spatial density of the PRISMA network in Northern Italy. The results of the triangulation are reported in Fig. 5.2 and in the first part of Tab. 5.2. The fireball’s trajectory was observed from a starting altitude of 75.86 ± 0.04 km and ended at a terminal height of 21.40 ± 0.03 km from the ground (panel a). The total length of the luminous atmospheric path is 59.42 ± 0.03 km, which was covered in about 5.6 s. The meteoroid followed an atmospheric trajectory inclined by an angle of 66.4 ± 0.2° with respect to the horizontal plane, with an azimuth of 237.8 ± 0.2° travelling from WSW to ENE, and rapidly entered into the denser layers of the atmosphere. The distance residuals of the trajectory fit plotted in panel b (see Sect. 4.2.2) have a standard deviation of

---

[1] `https://prisma.imo.net/members/imo_view/event/2020/18`

[2] `https://fireball.fripon.org/displaymultiple.php?id=12529`

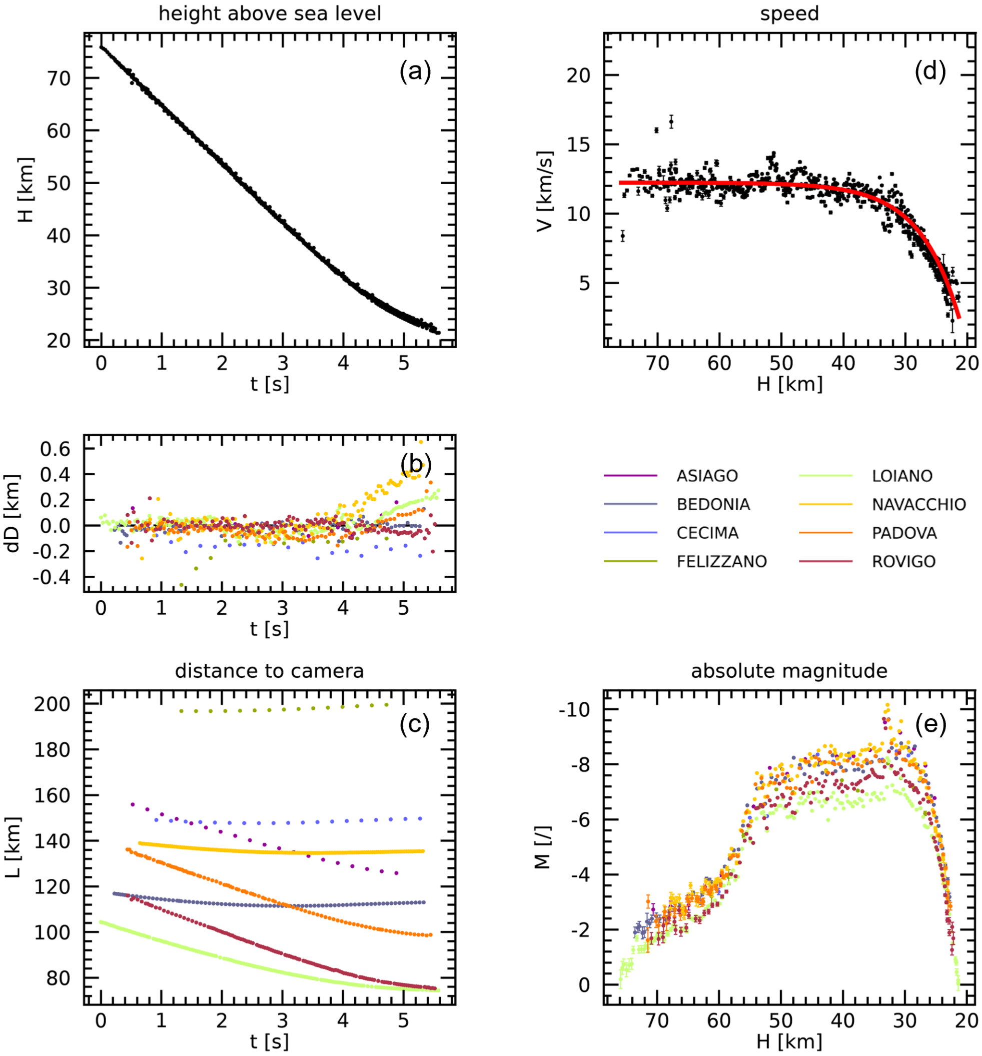

Fig. 5.2: Results of the triangulation processing for the IT20200101 event. (a) Height above sea level; (b) distance residuals of the LoS fitting procedure from Eq. 4.27; (c) distance of the trajectory from the various stations that detected the event; (d) speed profile reconstructed from the triangulated positions (dots with error bars) together with the result of the exponential fit of Eq. 4.30 (red thick line); (e) absolute magnitude lightcurve from Eq. 4.31.

0.1 km, corresponding to an angular separation of ~3 arcmin at an average distance of 130 km (panel c). This results is compatible with the astrometric precision level, as discussed in Sects. 4.1.4, 4.2.1 and 4.2.2. However, a significant systematic is visible in the last second of the flight, when the residuals of a few cameras progressively drift towards higher altitudes. Thanks to the brightness of the bolide, this event was recorded at quite a low elevation from most of the stations, reaching values less than 10° from the horizon in the last frames. As discussed in Sect. 4.1, most PRISMA cameras are not able to detect stars in this region, suffering from the low sky quality and light pollution which is particularly intense in the Po valley. While residual systematic effects are numerically addressed (Sect. 4.1.4), this correction can be only tentative below 10° of elevation and the positional accuracy for these last points is questionable. To assess the potential effect of this bias over the final result, we first excluded these points and verified that the overall results (*i.e.*, the trajectory computation) were unchanged within the measurement errors. We finally included them since they provide important photometric data for the trailing edge of the fireball light curve.

The computed speed profile is reported in Fig. 5.2d. The meteoroid entered the atmosphere at a low beginning speed $V_b = 12.23 \pm 0.08$ km/s, reaching a final speed of 2.5 ± 0.5 km/s at 21.4 km of altitude. Finally, the magnitude lightcurve of the bolide is plotted in Fig. 5.2e. In the first 2 s from the beginning of the event, the brightness grew rapidly and reached a plateau of about $\mathcal{M} = -7.5$ until 4.7 s, followed by a sudden fading in the last second. The photometric analysis highlighted that the PSF of the fireball saturated, in almost all cameras, in correspondence of this plateau. We applied in this case the tentative correction presented in Sect. 4.2.1, that unveiled a flux loss fraction of ~40% at the brightest point of the trajectory. Two rapid flares are also visible at 3.95 and 4.15 s with absolute magnitudes close to -9.5 and -8.5 respectively, which may be related to fragmentation events. In Gardiol et al. (2021), we discussed that this evidence suggests a particular weakness of the meteoroid which may be caused, for instance, by fractures already present when it was entering the atmosphere or by the porosity of the material. As a matter of fact, the dynamic pressure at that altitude (~30 km) was approximately 1 MPa, while a stony meteorite should be able to withstand a pressure of the order of 10 MPa if monolithic.

The results of the dynamic model for IT20200101 are reported in Fig. 5.3 and in the second part of Tab. 5.2. We report here the results of the NUM_DYN and NUM_PHD approaches. While we usually prefer the PHD results, strong systematic effects are visible for the fit of the magnitude lightcurve (5.3b). This may be due to the saturation cut-off (even if a tentative correction was applied), which can alter the shape of the lightcurve around its maximum and flatten it. Also, the evidence for fragmentation complicates the interpretation of the data based on the single-body theory that is assumed for the dynamic model (Sect. 4.2.4), in light of the underlying hypothesis of a constant-parameter flight. Nevertheless, the overall shape of the

Triangulation

			Beginning	Ending
Time	t	(UT)	18:26:52.9	18:26:58.45
Latitude	ϕ	[deg N]	44.7344 ± 0.0003	44.8401 ± 0.0003
Longitude	λ	[deg E]	10.7192 ± 0.0003	10.9543 ± 0.0003
Height	H	[km]	75.86 ± 0.04	21.40 ± 0.03
Speed	V	[km/s]	12.23 ± 0.08	2.4 ± 0.4
Time of Flight	ToF	[s]	5.58 ± 0.05	
Trajectory Length	L	[km]	59.42 ± 0.03	
Trajectory Inclination	γ	[deg]	66.4 ± 0.2	
Trajectory Azimuth	a	[deg]	237.8 ± 0.2	
Min. Abs. Magnitude	$\mathcal{M}_{min}$	[/]	-10.2 ± 0.1	

Dynamic model

			NUM_DYN	NUM_PHD
Preatm. speed	V_∞	[km/s]	12.28 ± 0.05	12.25 ± 0.05
Ablation coeff.	σ	[$\mathrm{s}^2/\mathrm{km}^2$]	0.038 ± 0.003	0.043 ± 0.002
Shape-change coeff.	μ	[/]	2/3	0.65 ± 0.02
Luminous efficiency	τ	[%]	–	0.24 ± 0.08
Preatm. MSR	D_∞	[$\mathrm{kg/m}^2$]	440 ± 50	470 ± 50
Preatm. mass	M_∞	[kg]	14 ± 5	17 ± 6
Preatm. size	$2r_\infty$	[cm]	20 ± 3	21 ± 3
Final MSR	D_{fin}	[$\mathrm{kg/m}^2$]	180 ± 20	170 ± 20
Final mass	M_{fin}	[kg]	1.0 ± 0.4	0.8 ± 0.3
Final size	$2r_{fin}$	[cm]	8 ± 1	8 ± 1

Tab. 5.2: Summary of the results of the triangulation and dynamic model for the IT20200101 event. The two columns of the first half of the table (triangulation) refer to values at the beginning and end of the bright flight, respectively (when applicable), and in the second half (dynamic model) they refer to the results of the two approaches NUM_DYN and NUM_PHD. Values of mass and size are computed from the mass-section ratio D by assuming a spherical shape of the meteoroid and the measured meteorite bulk density of $\rho_m = 3.322$ g/cm^3.

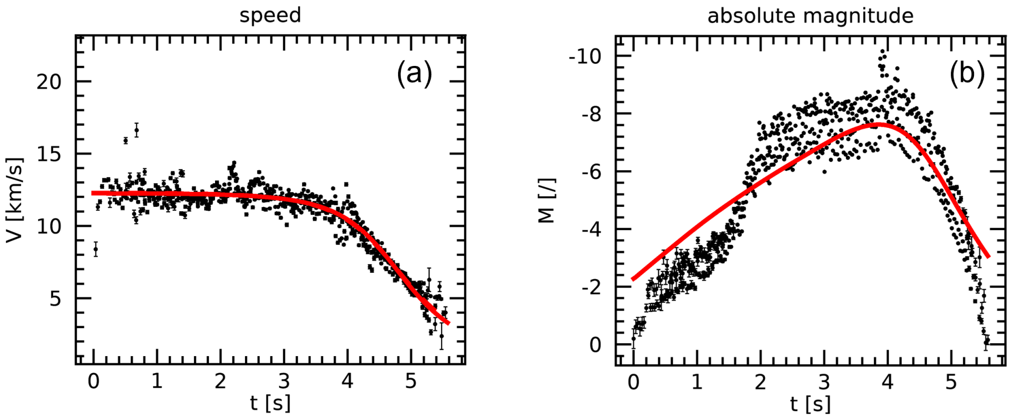

Fig. 5.3: Results of the dynamic model fitting on the data of (a) speed and (b) absolute magnitude for the IT20200101 event. The solid red line represents the fit of the NUM_PHD model in both panels. The speed profile of NUM_DYN is hidden below the solid line of panel a being virtually identical to the NUM_PHD result.

lightcurve is consistent with an isotropic ablation of the meteoroid and the shape-change coefficient is estimated to be $\mu = 0.65 \pm 0.02$, compatible with the reference value of $2/3$ assumed in the DYN model. As a consequence, the DYN and PHD results are fully compatible within their 1σ confidence intervals. The preatmospheric mass-section ratio was therefore deduced to be 470 ± 50 kg/m^2, with an ablation coefficient of 0.043 ± 0.002 s^2/km^2. In this case, we were also able to measure the density of the main mass of the meteorite (F2, see Sect. 5.2) by means of an accurate and precise 3D scanning of its outer surface, resulting in $\rho_m = 3.332$ g/cm^3, which is within the range of assumed density within the PRISMA pipeline (3.3 ± 0.2 g/cm^3, see Sect. 4.2.5). However, even this estimate of the density may be questioned due to the evidence of fragmentation at a quite low dynamic pressure that may suggest a higher porosity of the body and a consequent lower bulk density of the meteoroid with respect to the recovered meteorite, resulting in higher mass values (Eq. 4.59). Using the measured density value, we infer a preatmospheric meteoroid mass of $M_\infty = 17 \pm 6$ kg, corresponding to a size of 21 ± 3 cm and compatible at 68% confidence with the result of 10 ± 5 kg given by the independent analysis of FRIPON. These values are greater by a factor of approximately 3 with respect to the estimation of the preatmospheric MSR and mass given in Gardiol et al. (2021), which refers to the method of Carbognani et al. (2020). As a comparison, the previously estimated value of the preatmospheric MSR was 280 ± 20 kg/m^2. These results are barely compatible at the 99.7% confidence level. However, they refer to two methods that differ in many aspects, such as the assumed atmospheric model (Carbognani et al., 2020 use the 1976 US standard atmosphere), the drag coefficient (Carbognani et al., 2020 assume $\Gamma = 0.58$) and the χ^2 minimization algorithm used for the optimization of the dynamic model. This difference is also linked to the deduced value for the ablation coefficient, which is estimated as $\sigma = 0.043 \pm 0.002$ s^2/km^2 in this work and 0.012 ± 0.003 s^2/km^2 in Gardiol et al. (2021), with again difference by a factor 3. On the other hand, the final mass estimated in both methods is compatible, with 1.5 ± 0.4 kg (9 ± 1 cm of size) computed by Gardiol et al. (2021) and 0.8 ± 0.3 kg (8 ± 1 cm of size) obtained with the NUM_PHD model. However, in this case the result of FRIPON is significantly lower, with an estimated final mass of 0.15 ± 0.17 kg. These heterogeneous results show the sensitivity of the results of the dynamic model with respect to the various assumptions that have to be given to obtain a full solution of the differential equations' set describing the problem (see Sect. 4.2.4), linked to the impossibility of directly estimating many parameters, like the drag coefficient Γ and the shape of the body, just to cite a few. However, all results suggest a high probability for meteorite fragments to be recovered on the ground.

The preatmospheric orbit of the IT20200101 event was also discussed in Gardiol et al. (2021), together with the search for a candidate progenitor body for the Cavezzo meteoroid. This was done by following the procedure described in Carbognani et al. (2020), that is, using the orbital similarity criterion D_N introduced

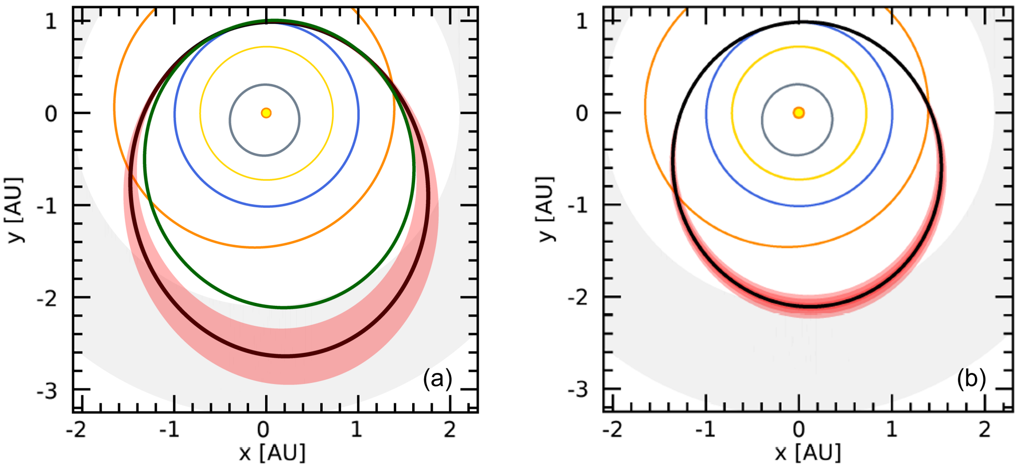

Fig. 5.4: Projection on the ecliptic plane of the preatmospheric orbit of the IT20200101 meteoroid. (a) Results of Gardiol et al. (2021) obtained with the method of Carbognani et al. (2020) (black ellipse) with 1σ uncertainty band (red shaded area), together with the orbit of 2013 VC$_{10}$ plotted as the dark green ellipse. (b) The updated preatmospheric orbit of IT20200101 from this work (black curve) computed from the method of Sect. 4.2.6), with 1,2 and 3σ intervals plotted as the shaded band around the nominal orbit with decreasing transparency. In both panels, the big yellow dot graphically represents the Sun's position on the ecliptic plane and the coloured ellipses plot the orbit of the inner planets of the Solar System (from Mercury to Mars), while the shaded grey annular region represents the MBA (from 2.1 to 3.3 AU distance from the Sun).

		This work	FRIPON	G-2021	2013 VC$_{10}$
Epoch		J2000	J2000	J2000	MJD59000
a	[AU]	1.55 ± 0.02	1.545 ± 0.007	1.82 ± 0.22	1.566
e	[/]	0.366 ± 0.009	0.364 ± 0.003	0.46 ± 0.06	0.365
i	[deg]	3.20 ± 0.08	3.17 ± 0.01	4.0 ± 1.6	2.044
Ω	[deg]	280.652 ± 0.003	280.676 ± 0.003	280.52311 ± 0.00001	224.068
ω	[deg]	178.29 ± 0.09	178.26 ± 0.03	179 ± 5	240.264
q	[AU]	0.9832	0.9832	0.983 ± 0.001	0.9944
Q	[AU]	2.12 ± 0.04	2.11 ± 0.01	2.66 ± 0.41	2.1379
T_J	[/]	4.37 ± 0.04	4.38 ± 0.02	4.1 ± 0.2	4.344

Tab. 5.3: Elements of the preatmospheric orbit of the IT20200101 meteoroid as computed by this work, the FRIPON pipeline and the results of Gardiol et al. (2021), based on the method of Carbognani et al. (2020). The last column reports the elements of the orbit of 2013 VC$_{10}$ (as provided by the NEOSyS database).

by Valsecchi et al. (1999) against the NEODyS database[3] (Gronchi and Milani, 2001) that lists the orbital elements and secular quantities for all known NEAs to date. This analysis resulted in only one possible candidate progenitor body for the IT20200101 meteoroid. This asteroid is named 2013 VC$_{10}$ and is a 50-m size NEA ($H = 24.8$) observed for 54 days only between 2013 and 2014[4]. For this pair, the similarity parameter was $D_N = 0.115$, compared to the maximal acceptance value of 0.15 that was set for the association (see Sect. 4 of Gardiol et al., 2021 for more details). The orbits of IT20200101 computed in Gardiol et al. (2021) and the one of 2013 VC$_{10}$ are plotted in Fig. 5.4a. A comparison of the orbital elements deduced in this work, by the FRIPON processing and in Gardiol et al. (2021) is presented in Tab. 5.3, together with the ones of 2013 VC$_{10}$. The agreement with the results of this work (method of Sect. 4.2.6, Fig. 5.4b) and the ones of FRIPON is good and always within the 1σ intervals (apart from the longitude of the ascending node Ω). The preatmospheric orbit of IT20200101 has an asteroidal origin, as clearly indicated by the Tisserand's parameter of $T_J = 4.37 \pm 0.04$, with its aphelion at the very edge of the region of the inner MBA. The results of Gardiol et al. (2021) are in general compatible within 2σ, also because of the significantly bigger random errors attributed to most of the entries of Tab. 5.3. However, they suggest an orbit with a more pronounced eccentricity (e) and a slightly larger semi-major axis (a). It is then to be noted than the differences between the results presented here and the ones of Gardiol et al. (2021) go towards an even better match with the orbit of 2013 VC$_{10}$, as also evident from Fig. 5.4, with its values of both a and e fully contained within the 1σ confidence region of the updated orbit of the IT20200101 meteoroid.

5.1.1 Computation of the strewn-field

To project the motion of the residual meteoroid towards the ground and estimate the strewn-field of meteorite fragments, we used the method described in Carbognani et al. (2020) and the results are presented in Gardiol et al. (2021). Starting from the final point of the visible trajectory (see Tab. 5.2), it is possible to continue to numerically integrate the deceleration equation (Eq. 2.23) during the dark flight. Because the meteoroid's motion was greatly decelerated by the atmospheric drag, the gravitational acceleration term must be included at this time since it starts to become relevant. In doing so, it is assumed that the ablation phenomenon ended after the last observation. Moreover, we must consider the influence of the wind speed $\overrightarrow{V}_w$ in this equation. This means that the term V of Eq. 2.23 must be replaced with the meteoroid's speed with respect to the fluid, that is $\overrightarrow{V} - \overrightarrow{V}_w$. The meteoroid's motion is therefore decomposed into a longitudinal component (l) and two transverse components, one pointing towards the ground (h) and the third one given by the

---

[3] NEODyS-2 database – `https://newton.spacedys.com/~neodys2/propneo/encounter.cond`.

[4] `https://newton.spacedys.com/neodys/index.php?pc=1.1.0&n=2013VC10`

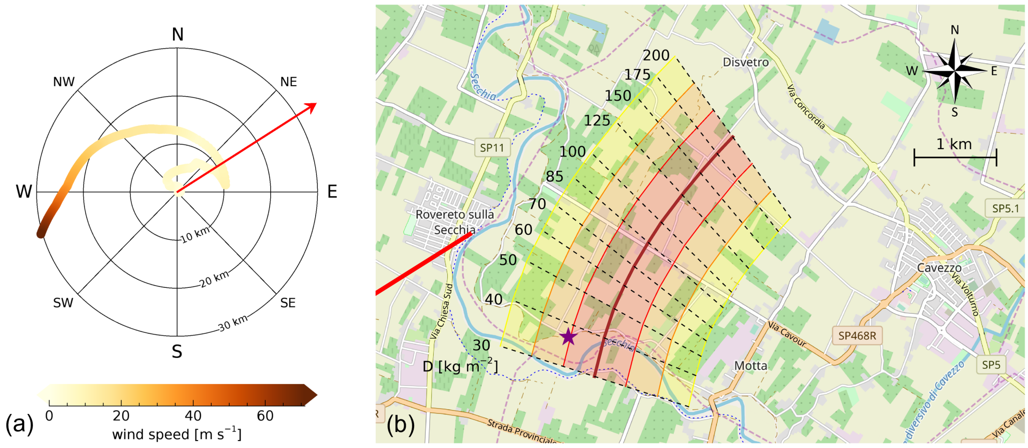

Fig. 5.5: Computation of the strewn-field for meteorites of the IT20200101 event (Gardiol et al., 2021). (a) Wind vertical profile at 18 UTC in the area of the event computed at MeteoExpert and used for the strewn-field computation. The red arrow shows the fireball motion direction. (b) Map of the strewn-field computed according to the method of Carbognani et al. (2020) as a function of different MSR values $D \in [30, 200]$ kg/m^2 represented by the dashed transverse lines. The brown thick line shows the nominal impact point and the shaded areas enclose 1σ (red), 2σ (orange), and 3σ (yellow) uncertainties in the transverse x direction. The purple star shows where the two Cavezzo fragments F1 and F2 were recovered (see Sect. 5.2), and the thick red line plots the terminal part of the bright flight trajectory, projected on the ground. Background map data copyrighted OpenStreetMap contributors and available from `https://www.openstreetmap.org`.

right-hand rule (x). The gravitational term acts over the h component and the atmospheric drag acts on the l component. The computation can also include the Coriolis force and the effect of the Earth's rotation, even if the magnitude of these corrections is usually small compared to the random uncertainty originating from the unknown of the phenomenon. In fact, we again face the problem of giving a value of the drag coefficient Γ (see details in Carbognani et al., 2020). Also, an accurate determination of the wind speed intensity and direction at the precise location of the meteoroid's trajectory is challenging.

The knowledge of the atmospheric conditions plays a key role in the computation of the strewn-field of meteorite fragments that could be possibly found on the ground. The wind effect is even more important in this case, given the small residual mass and size of meteorite's fragments after ablation of the order of 1 to 10 cm of size, considering that the main mass most probably fragmented during the ablation phase. For the computation of the strewn-field for the IT20200101 event, we were able to account for the specific state of the atmosphere thanks to the meteorological data elaborated at Meteo Expert, a private organization providing meteorological services where weather models are internally developed and applied. Figure 5.5a shows the wind intensity and direction values at 18 UTC in the area of the IT20200101 event as a function of the altitude. The wind was particularly intense at about 22 km, which is the last observed point of the luminous path, reaching a speed of about 28 m/s, and blowing at 45° clockwise with respect to the meteoroid motion direction. The wind intensity decreases to reach a speed of about 20 m/s at 20 km altitude, and is confined below 10 m/s from 13 km downwards. This led to a significant shift of the strewn-field compared to a situation with zero wind, especially in the transverse x direction.

The map of the computed strewn-field is reported in Fig. 5.5b, together with the terminal part of the visible atmospheric trajectory of IT20200101, projected on ground, and the location where the two fragments were found (purple star, see Sect. 5.2). Since the observational data suggested that fragmentation occurred during the ablation phase, we computed the impact point for different masses, *i.e.*, for different MSR values ranging from 30 to 200 kg/m^2, that is of the order of D_{fin} (see Tab. 5.2). The nominal impact point as a function of the MSR is plotted by the thick brown line on the map and the red, orange and yellow bands represent the 1,2 and 3σ uncertainties in the transverse x direction. The 1σ uncertainty in the longitudinal direction was estimated to be 300 m. Due to the intense winds at that time, the lateral displacement can be as high as 2.3 km for smaller fragments. The expected impact velocity ranges from 28 to 71 m/s.

5.2 The recovery of the Cavezzo meteorite

A preliminary estimation of the strewn-field was available the day following the fall, *i.e*, on 02/01/2020 in the early afternoon. Then, we had to decide a strategy for the meteorite search. A team of volunteers within the PRISMA collaboration is indeed trained for meteorite hunting. However, the strewn-field was located in a rural territory with many cultivated fields, groves and houses spread over the area, the vast majority of which is on private property. Because of this, we notified the local authorities that teams of hunters would be there to search for meteorites on behalf of the PRISMA collaboration, and we seek for the help of the local Civil Protection to help searchers enter private terrains and areas. Nevertheless, we were aware that the limited number of people in our team of hunters had little chance to systematically cover the whole extension of the strewn-field by themselves in a reasonable time. Therefore, we undertook a parallel approach. The Project Office of PRISMA prepared a press release[5] to be published on the project's website and on the outreach platform of INAF (MediaINAF[6]), providing all the necessary information about the most probable area where fragments could be found and also a brief tutorial on how to recognize a freshly fallen meteorite. The goal of this strategy was to maximize the probability of a successful recovery by involving a larger number of people, even if not specially trained. The news was made public in the late afternoon

---

[5] `http://www.prisma.inaf.it/index.php/2020/01/02/una-meteorite-in-emiliaromagna`

[6] `https://www.media.inaf.it/2020/01/02/forse-e-caduta-una-meteorite-in-emilia-romagna`

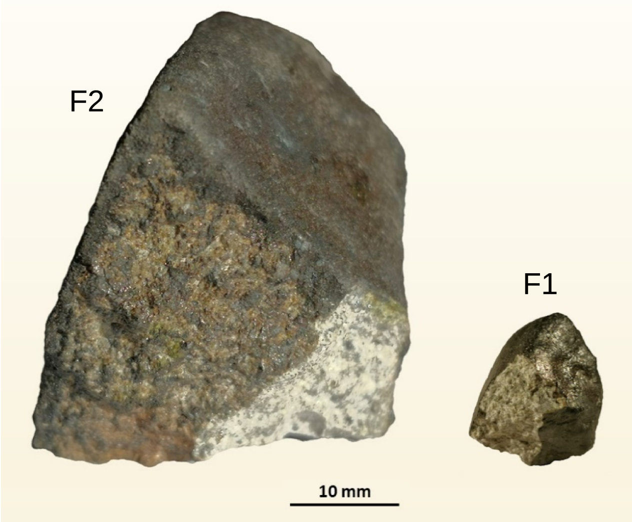

Fig. 5.6: The two recovered samples of the Cavezzo meteorite (Gardiol et al., 2021). On the right hand side, the first recovered fragment (F1, 3.1 g); on the left-hand side, the second and larger one (F2, 52.2 g).

of 02/01/2020 and was quickly covered by local and national mass media. By the morning of 04/01/2020, a team of about twenty hunters was ready to start searches, while a small scouting group from the Università di Bologna led by Romano Serra was already on-site. At 3 PM of the same day, we received an email with the first reliable meteorite candidate from Mr. Davide Gaddi, reporting the recovery of a small fragment (the size of a fingernail) on an embankment along the Secchia river. In the time we arranged a meeting on the site with Romano Serra, Mr. Gaddi found a second and bigger fragment, the size of a walnut. Both fragments were immediately recognized to be freshly fallen meteorites.

The two fragments were recovered at coordinates 44°49’43.7” N 10°58’19.5” E (purple star on Fig. 5.5b), at the border of a narrow country road that runs parallel to the left main embankment of the Secchia river, in the municipality of Cavezzo. Fragment n.1 (F1), the first one to be found, has a tetrahedral form and weighs 3.1 g. Fragment n.2 (F2), the largest one, weighs 52.2 g. A composite picture of both is presented in Fig. 5.6. The MSR values for the two fragments can be estimated to be 30–70 kg/m^2 for F1 and 35–85 kg/m^2 for F2, considering that we ignore the orientations of the meteorites during the fall. For both fragments, this is compatible with the predicted values of the dark-flight model, also considering the longitudinal uncertainty of 300 m (see Fig. 5.5). Both fragments clearly present a recently formed fusion crust on most of their surface. They also show a light grey chondritic pattern on one of their sides, which was probably due to fragmentation that most likely occurred when they hit the ground. In addition, F2 presents a darker grey colouration on one side, apparently a less pronounced secondary fusion crust, which is compatible with exposure due to a fragmentation event most probably associated to the flares which occurred at a height of around 30 km (Sect. 5.1).

5.3 The analysis of the Cavezzo meteorite

Immediately after the finding, the meteorite specimens were transported to the Earth Science Department of the Università di Firenze to be analyzed. Both fragments were donated to INAF by the finder, Mr. Davide Gaddi. Two samples from F1 and one sample from F2 are held by the museum "La Specola" of the Università di Firenze[7], and two samples from F1 and F2 and the main mass F2 are deposited at the Museo Italiano di Scienze Planetarie[8] in Prato (Toscana). Both museums are included in The Meteoritical Society official repositories list. The analysis of the Cavezzo meteorite was carried out at various institutes: Università di Firenze, Museo di Storia Naturale "Filippo Olmi", CRIST and MEMA Laboratories; Museo di Scienze Planetarie of Prato; Open University, Milton Keynes (UK), and; Università di Torino, Laboratorio del Monte dei Cappuccini in Torino. The results of this extended analysis were presented in Pratesi et al. (2021). A detailed report on this fall was sent to the Nomenclature Committee of the Meteoritical Society. On September 5, 2020, the meteorite was approved as a new Italian meteorite with the name Cavezzo (Gattacceca et al., 2021) and classified as an L5-anomalous chondrite (L5-an). This is the first meteorite of this class. Let us summarize here the most important results that led to this peculiar classification, which originates from the various differences found in the analysis of the two fragments.

Petrography

Figure 5.7 shows the backscattered electron (BSE) images of three samples of Cavezzo meteorite, two from F1 (top) and one from F2 (bottom). In the samples collected from F1, the amount and appearance of chondrules vary significantly, from being well-delineated and with clear boundaries from the enclosing matrix (*e.g.*, sample 1a, 70 vol%) to being scarce or even absent (*e.g.*, sample 1c, 20% vol) in an achondritic texture. On the other hand, the sample from the main mass F2 shows the typical distribution for L chondrites, characterized by not well-delineated and partially melted chondrules.

Modal mineralogy and crystal chemistry

The modal mineral abundance of both fragments was measured by means of SEM/EDS microanalyses and elemental mapping and gave the most outstanding difference between the two Cavezzo specimens, as presented by the pie charts of Fig. 5.8a. The most puzzling result is the high content of olivine of about 65 vol% of F1, which is remarkably far from the ranges of ordinary chondrites, being 29.8–35.7 vol% for H, 40.7–43.0 vol% for L, and 49.7–52.5 vol% for LL chondrites. Similarly, F1 exhibits a content of low-Ca pyroxene of 5.8 wt%, extremely low with respect to

---

[7] https://www.sma.unifi.it/vp-245-la-specola.html#

[8] https://www.fondazioneparsec.it/it/il-museo-di-scienze-planetarie/

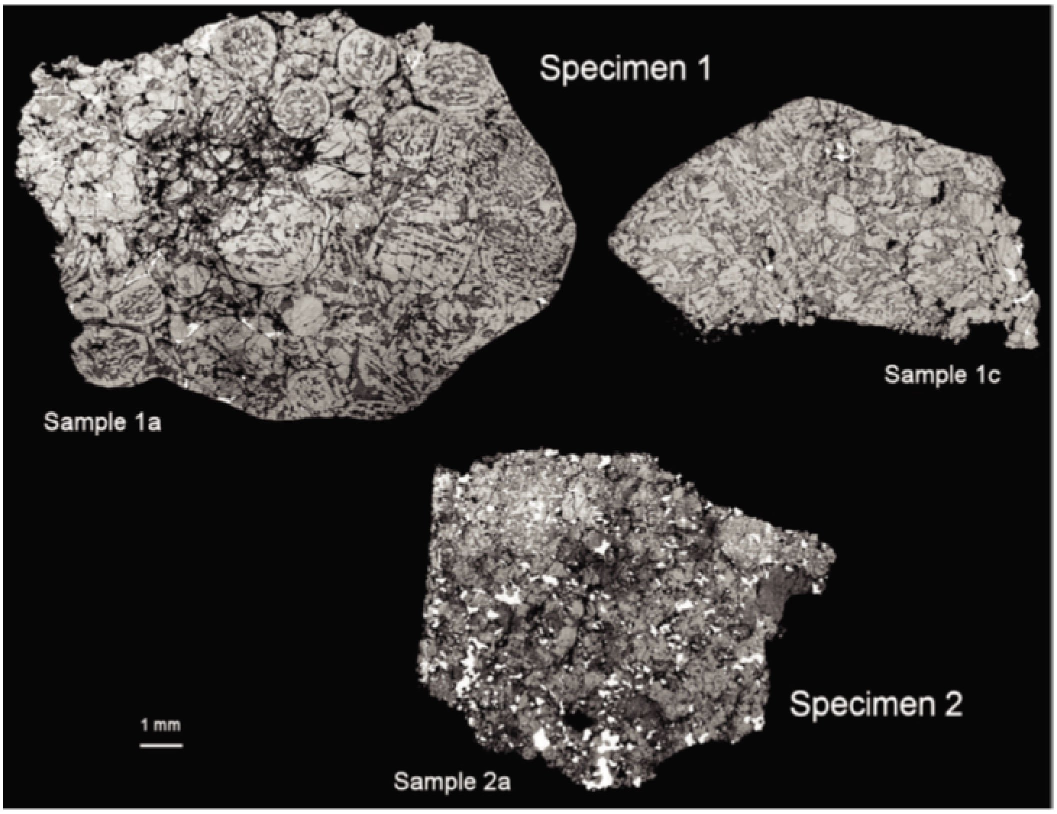

Fig. 5.7: BSE photomosaic of three samples of Cavezzo meteorite, two from the F1 specimen (1a and 1c, on the upper part of the image) and one from F2 (2a, bottom part). F1 exhibits a transition from chondritic to achondritic texture, while F2 shows a homogeneous and chondritic texture typical of a high petrological type (Pratesi et al., 2021).

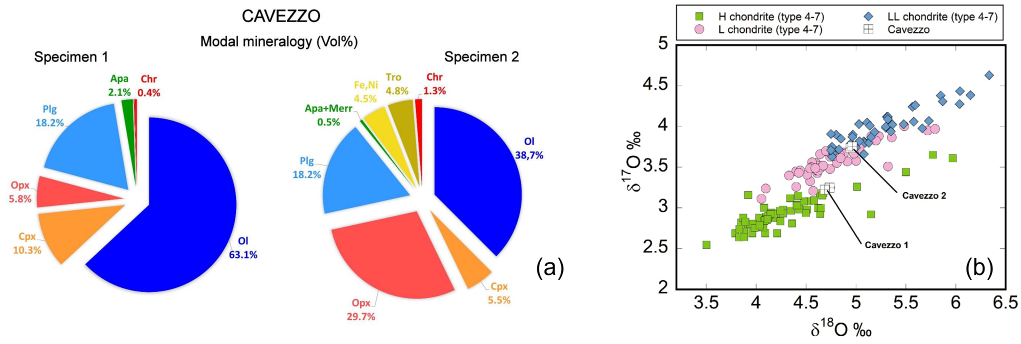

Fig. 5.8: (a) Pie charts of the modal mineralogy Cavezzo F1 (left) an F2 (right); (b) Chart of the oxygen isotopes composition of the F1 and F2 fragments of Cavezzo (white squares) compared with the typical ranges of H (green points), L (pink) and LL chondrites (blue), showing a dichotomy in the isotopic fractioning of the two fragments (Pratesi et al., 2021).

ranges of chondrites groups, of 27.0–24.9 wt% for H, 24.2–21.7 wt% for L and 22.6–18.9 wt% for LL chondrites. At the same time, the measured modal mineralogy of F2 is much more similar to ordinary chondrites. The compositions of the main and accessory mineral phases in F1 and F2 are both quite similar and comparable with those of ordinary chondrites of the L group (not shown).

Oxygen isotopes

As discussed in Sect. 2.6.1, the bulk oxygen isotopic composition is one of the most important parameters to be considered to classify a meteorite. Figure 5.8b plots the diagram of δ^{17}O against δ^{18}O (the same of Fig. 2.18) with the populations of H, L and LL chondrites plotted as the green, pink and blue points respectively, and the values for Cavezzo F1 and F2 as the white squares. The result for F1 plots at the boundary between H and L chondrites, whereas F2 is located at the opposite boundary, between L and LL chondrites.

Classification

The main mass F2 shows all the features of an L5 chondrite. Fragment F1 also belong to the chondritic class, but its analysis pointed towards many peculiarities. In particular, the data of oxygen isotopes suggest that F1 is derived from isotopically distinct material compared to that of F2. Since none of the two specimens shows signs of fragmentation or discontinuity and they do not contain fragments of each other, these features cannot be attributed to brecciation and Cavezzo cannot be classified as an ordinary breccia chondrite. Instead, the F1 specimen may be xenolithic material and represent a previously unsampled portion of the parent body of L chondrites, with F2 being the enclosing host material. For these reasons, Cavezzo was officially classified by The Meteoritical Society as the first L5-an chondrite ever discovered.

5.3.1 Cosmogenic radionuclides in Cavezzo

The γ-activity of the main mass F2 of the Cavezzo meteorite was measured at the Monte dei Cappuccini Laboratory in Torino. The results of these measurements were published in Bizzarri et al. (2023), and I have actively participated in this analysis. As a matter of fact, I carried out my Master's Thesis within the Cosmogeophysics group that operates in this underground laboratory. During my study and work period there, I developed a toolkit for the analysis of the data of the two spectrometers (Gardiol et al., 2017) that was also used for the analysis of the γ-spectrum of Cavezzo.

Radionuclides activity in meteorites is of particular interest since it can unveil information about the progenitor body of the meteorite and also on the cosmic-ray (CR) flux and solar activity at the time of fall. In fact, a large number of stable and

Fig. 5.9: The F2 specimen of Cavezzo just before the measurement, placed on the top of the GEM90 HPGe detector and surrounded by the NaI(Tl) annulus. The six photomultiplier tubes on the top of the NaI annulus are also visible (Bizzarri et al., 2023).

unstable isotopes is produced when the meteoroid is exposed to the galactic CR flux in the interplanetary space, by the interactions of energetic particles (mainly protons and α particles) within the meteoroid's mass (Michel et al., 1991; Bhandari et al., 1993). The production of these cosmogenic radionuclides is therefore in secular equilibrium during the CR exposure time of the body but ceases when the meteoroid falls to the Earth due to the atmospheric shielding of CR. Then, freshly-fallen meteorites are of great interest in planetary science since they give the unique opportunity to measure radionuclides with a very short half-life (days or weeks) that cannot be revealed in any other natural sample and that will decay if the meteorite is not measured just after the fall, within the shortest possible time. On the other hand, it is possible to study the variation of galactic CR flux over different timescales by measuring the activity of cosmogenic radionuclides in meteorites, according to their half-life. Since the CR flux in the interplanetary space is modulated by the heliospheric magnetic field, the activity of cosmogenic radionuclides is anticorrelated to the solar activity, being an indirect proxy for it (Bonino et al., 1995; Beer et al., 2012; Asvestari et al., 2017; Mancuso et al., 2019).

The F2 sample of Cavezzo was measured with the large-volume, high-efficiency HPGe-NaI(Tl) γ-spectrometer named GEM90 installed at the Monte dei Cappuccini underground laboratory (Taricco et al., 2006). This detector consists of a hyperpure germanium (HPGe) crystal (2 kg, 95% relative efficiency, resolution $\sim$2 keV) operating in coincidence with an umbrella of NaI(Tl) scintillator (55 kg). The natural shielding of the mount under which the laboratory is located (70 m water equivalent) provides a cosmic muon flux 30 times less than at the surface level, thus considerably reducing the background counts. Together with a second detector, named GEM150, several meteorites have been measured at this facility (*e.g.*, Taricco et al., 2006; Taricco et al., 2008; Taricco et al., 2016; Taricco et al., 2019).

The measurement of the F2 specimen of Cavezzo took place about three weeks after the fall and lasted for 45 days. A picture of the sample positioned for the

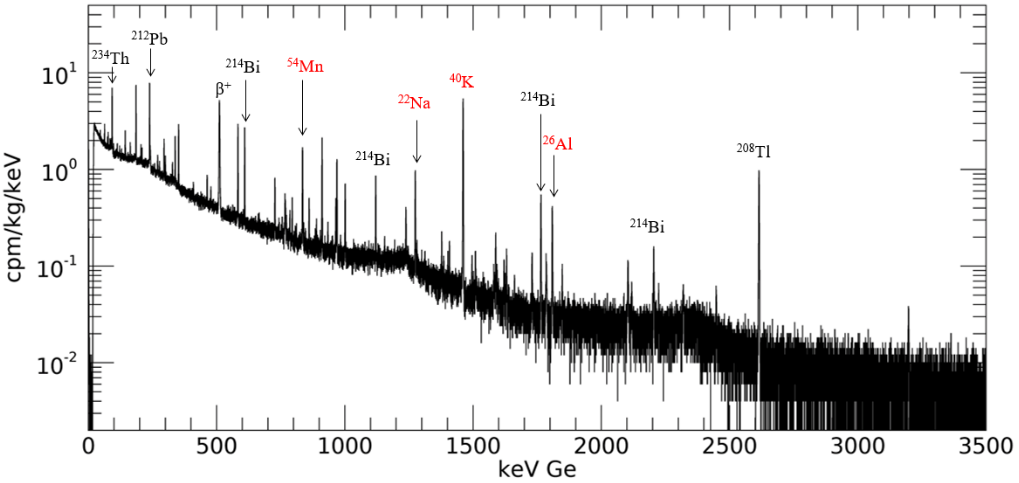

Fig. 5.10: The γ-spectrum of the Cavezzo main mass F2 in normal mode (HPGe alone, $\sim$45 days counting time). Some peaks are highlighted and associated with the related cosmogenic (red) or naturally occurring (black) radionuclides (Bizzarri et al., 2023).

Nuclide	Decay	Half-life	E$_\gamma$ [keV]	BR [%]	cpd	Eff. [%]	dpm/kg
^{47}Ca	β^-	4.5 d	1297.09	75	137 ± 71	1.75 ± 0.01	104 ± 54
^{52}Mn	$\epsilon + \beta^+$	5.6 d	1434.06	99.99	50 ± 42	1.56 ± 0.01	43 ± 36
^{48}V	$\epsilon + \beta^+$	16.0 d	983.52	99.85	51 ± 7	2.13 ± 0.02	32 ± 4
			1312.10	97.5	35 ± 8	1.73 ± 0.02	27 ± 6
^{51}Cr	ϵ	27.7 d	320.08	9.89	25 ± 6	0.56 ± 0.01	59 ± 14
^{7}Be	ϵ	53.2 d	477.60	10.44	31 ± 3	0.47 ± 0.01	88 ± 10
^{58}Co	$\epsilon + \beta^+$	70.9 d	810.76	99.44	13 ± 2	3.19 ± 0.02	5.4 ± 0.7
^{56}Co	$\epsilon + \beta^+$	77.2 d	846.76	99.94	15 ± 2	2.44 ± 0.01	9 ± 1
			1238.27	66.41	7 ± 2	1.19 ± 0.01	8 ± 2
^{46}Sc	β^-	83.8 d	889.28	99.98	21 ± 2	2.71 ± 0.02	10 ± 1
			1120.55	99.97	8 ± 2	2.38 ± 0.01	5 ± 1
^{57}Co	ϵ	271.8 d	122.06	85.49	28 ± 3	4.30 ± 0.02	9 ± 1
^{54}Mn	ϵ	312.2 d	834.85	99.98	195 ± 3	1.66 ± 0.01	156 ± 3
^{22}Na	$\epsilon + \beta^+$	2.6 y	1274.54	99.94	130 ± 2	1.83 ± 0.01	95 ± 1
^{60}Co*	β^-	5.3 y	1173.23	99.85	1.52 ± 0.36	2.34 ± 0.02	0.9 ± 0.2
			1332.49	99.98	1.54 ± 0.44	2.17 ± 0.01	1.0 ± 0.3
^{44}Ti*	ϵ	60 y	1157.02*	99.88	4.4 ± 0.8	3.03 ± 0.02	1.9 ± 0.3
^{26}Al	$\epsilon + \beta^-$	717 ky	1129.67	2.5	3 ± 1	0.060 ± 0.002	58 ± 22
			1808.65	99.76	64.6 ± 0.9	1.53 ± 0.01	56.2 ± 0.8
^{40}K	$\epsilon + \beta^-$	1250 My	1460.82	10.55	327 ± 4	0.258 ± 0.002	1680 ± 20

Tab. 5.4: Results of the measurement of the activity of cosmogenic radionuclides in the Cavezzo main mass (F2). The columns are, in order: nuclide, decay mode, half-life, energy of the detected γ line, branching ratio (BR) of that photon, counts per day (cpd) reported to the date of fall and normalized to the branching ratio, simulated decay efficiency of the detector and final massic activity value, given in decays per minute (dpm) per kg.
(*) Measured with the coincidence technique.
($\star$) Gamma emitted by its short-lived daughter ^{44}Sc.

measurement on the top of the HPGe crystal and surrounded by the NaI scintillator is shown in Figure 5.9. The counted γ-ray spectrum in normal mode (*i.e.*, only the counts on the HPGe crystal) is plotted in Fig. 5.10. Most of the visible peaks are due to the γ decay of naturally occurring radioisotopes (some of them are marked with black arrows in the plot), that are contained in both the meteorite and the material surrounding the detector (*i.e.*, background signal). Most of them originate from the decay chains of ^{238}U and ^{232}Th. Thanks to the high selectivity and low background of the instrument and exploiting the coincidence technique between the HPGe and NaI detectors, we were able to detect 15 cosmogenic radioisotopes. They are listed in Tab. 5.4 together with the information about the decay channel, half-life and measured activity. Some of them are indicated in red in Fig. 5.10. The most intense peak, at the energy of about 1461 keV, is due to the decay of ^{40}K and its attributable to both the background and meteorite components. This isotope of potassium is indeed cosmogenic but has a half-life of $\sim$1.25 Gy, being therefore still present on the Earth from its formation.

In the γ-spectrum of Cavezzo, we were able to detect cosmogenic radionuclides with a half-life of the order of a few days, such as ^{47}Ca, ^{52}Mn and ^{48}V, thus undoubtedly confirming the recent fall of the meteorite and its link with the IT20200101 fireball. It is also to be noted that two of the radionuclides listed in Tab. 5.4 were not detected in the normal spectrum of Fig. 5.10. These are ^{60}Co and ^{44}Ti, which have the lowest counting rates among all detected radionuclides in the meteorite. An estimation of the activity of both was possible thanks to the advanced coincidence techniques between the HPGe detector and the NaI scintillator (Colombetti et al., 2013). In short, this consists in detecting two (or more) photons, emitted in coincidence by the same decay of one radionuclide, separately in the two detectors to filter out background events that may affect their detection. This method is routinely applied for the detection of ^{44}Ti, which γ at 1157 keV[9] is heavily affected by the interference of the line at 1155 keV of ^{214}Bi, a naturally occurring radioisotope of the ^{238}U decay chain (Taricco et al., 2006). To filter out the counts coming from the ^{214}Bi decay, we select events that occur in the region of 1157.02 keV on the HPGe detector in coincidence with 511 or 1022 keV counts on the NaI scintillator, since the β^+ decay of ^{44}Sc (the daughter of ^{44}Ti) emits a positron that almost instantly annihilates, generating two anti-collinear photons with an energy of 511 keV each. On the other hand, the detection of ^{60}Co does not suffer from any interference of the sort, but its activity in the Cavezzo meteorite was too low to produce a visible peak on the normal spectrum, above the background fluctuations. We therefore exploited the same techniques for the measurement of ^{44}Ti but applied with the coincident emission of the two γs at the energy of 1173 and 1332 keV from the decay of ^{60}Co, one detected in the HPGe crystal and the other in the NaI scintillator (and the other

---

[9] The decay of ^{44}Ti can emit three γs at 68 keV, 78 keV and 146 keV, but their energy is too low to be detected on the HPGe detector. We therefore consider the decay of its daughter ^{44}Sc, which emits a γ at the energy of 1157 keV within an half-life of 4 hours.

way around). This coincidence technique allowed to lower the background under the ^{60}Co peaks by a factor of $\sim$30, enabling their detection. Since the GEM90 detector is equipped with a fully digital acquisition chain that records the channels of the HPGe and NaI detectors independently, it is possible to optimize the coincidence parameter after the measurement to retrieve the best configuration (the position and width of the coincidence window on the NaI spectrum, not shown). This innovative optimization method is described in Gardiol et al. (2017) and was applied for the measurement of Cavezzo, to deduce the activity of both ^{44}Ti and ^{60}Co radionuclides.

Finally, an estimation of the detector efficiency is needed to convert the experimental counting rates (counts per day - cpd in Tab. 5.4) into a measure of the activity of each radionuclide (decays per minute per kg - dpm/kg in Tab. 5.4). For this purpose, we used the Monte Carlo simulation toolkit Geant4[10] (Agostinelli et al., 2003; Allison et al., 2006; Allison et al., 2016), widely used to simulate the passage of particles through the matter and developed by the Geant collaboration at CERN. We used the measurement of three standards (^{26}Al, ^{40}K and ^{60}Co) to calibrate these simulations. Then, we reproduced the measurement of the Cavezzo meteorite with Geant4. For each detected radionuclide, we simulated 1 million decays for 100 times to compute the mean value of the decay efficiency and a measure of its uncertainty (computed as the standard deviation of the 100 runs), and the results are reported in Tab. 5.4. Further details about the measurement and the efficiency simulations are reported in Bizzarri et al. (2023).

The scientific analysis of these experimental results is still ongoing at this time of writing. I report here two preliminary results about the activity of two radionuclides measured in the Cavezzo main mass F2, which are ^{22}Na and ^{26}Al. It is well-known that the activity of ^{22}Na in meteorites is modulated by solar activity. This is because its half-life of 2.6 yr makes its production rate sensitive to the decadal oscillation of the solar activity (known as *Schwabe cycle*). To compare the data of ^{22}Na activity among different meteorites, we can use the approach introduced by Bhandari et al. (1989) and consider the ^{22}Na/^{26}Al ratio. Being the ^{26}Al activity insensitive to decadal variation of the CR flux and generated from the same target elements as ^{22}Na, this ratio ratio preserves the ^{22}Na response to the Schwabe cycle and is independent of the shielding conditions of the meteorite sample within the progenitor body. From the values of Tab. 5.4, the ^{22}Na/^{26}Al ratio for the Cavezzo main mass is estimated to be 1.69 ± 0.03, and it is plotted in Fig. 5.11. This high ratio reflects the low activity of the last solar cycle (n. 24), in comparison with the previous ones, as shown by the lower green line of Fig. 5.11 which plots the series of sunspot number, an indirect proxy for the solar activity.

Finally, the measured activity of ^{26}Al can provide an estimation of the preatmospheric (equivalent) radius r of the meteoroid and of the shielding depth ΔX of our meteorite sample within the body during its CR exposure age. With a half-life of

---

[10] `https://geant4.web.cern.ch/`

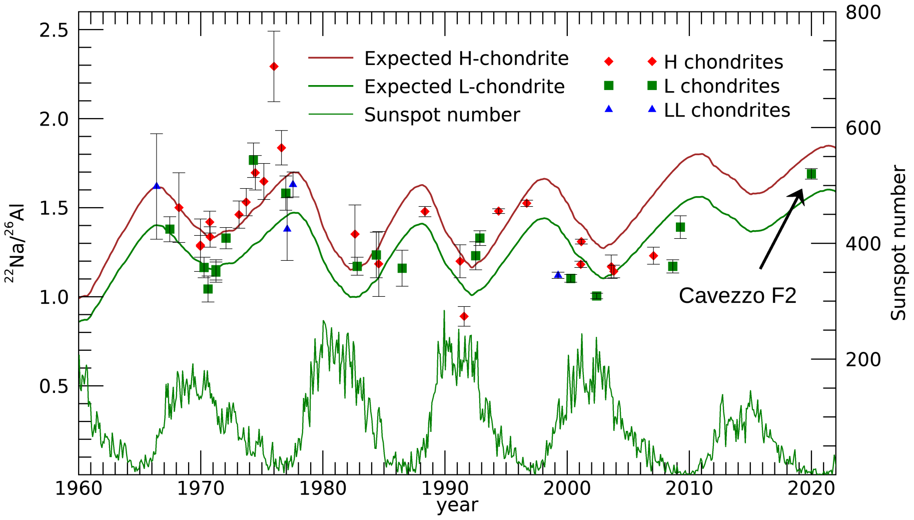

Fig. 5.11: The ^{22}Na/^{26}Al activity ratio in the Cavezzo main mass (F2), together with those measured in meteorites which fell during the last five solar cycles (Bhandari et al., 1994; Dhingra et al., 2004; Shukla et al., 2005; Taricco et al., 2010) and later measurements carried out at the Physical Research Laboratory, India. Calculated activity ratios expected for L and H chondrites are shown by a solid line. As a comparison, the monthly sunspot number series (ISN v2.0) is also shown, which indicates a phase difference of 1 to 2 yr between the sunspot minimum and the ^{22}Na peak.

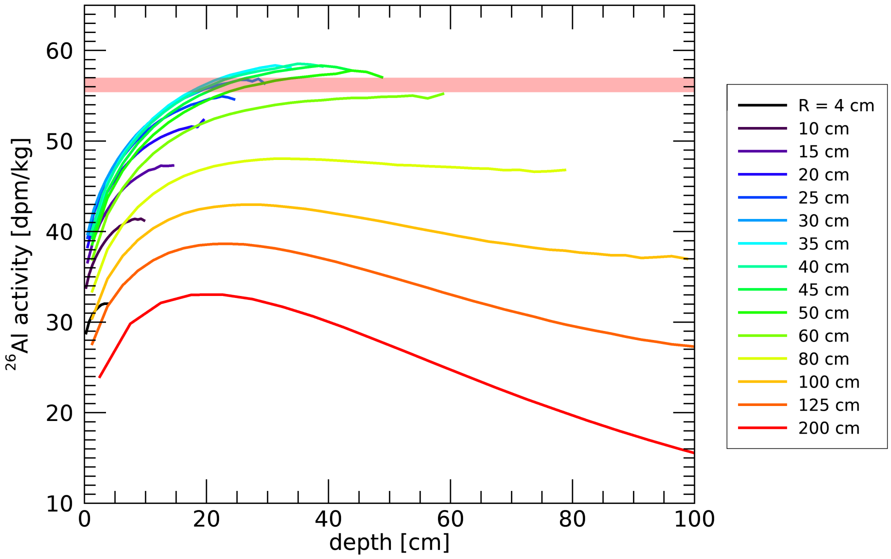

Fig. 5.12: ^{26}Al production rate computed for the long-term averaged galactic CR spectrum (Leya et al., 2021) and accounting for the measured bulk composition of the Cavezzo main mass F2 (see text), as a function of the shielding depth ΔX and for different preatmospheric sizes of the meteoroid ($r \in [5, 120]$ cm). The horizontal red band shows the 1σ confidence interval for the ^{26}Al activity (56.2 ± 0.8 dpm/kg) experimentally determined for Cavezzo F2, compatible with $r \in [30, 50]$ cm and $\Delta X \in [15, 35]$ cm.

717 ky, the production rate of ^{26}Al is insensitive to short-term CR flux variations and its expected activity in chondrites can be computed as a function of the long-term galactic CR flux and of the shielding parameters (Michel and Neumann, 1998). The expected ^{26}Al production profiles are plotted in Fig. 5.12 as a function of the shielding depth ΔX for different preatmospheric radii $r \in [5, 120]$ cm, computed with the model of Leya et al. (2021) adapted for the measured bulk composition of the Cavezzo main mass (O - 41.54%, Fe - 21.19%, Si - 18.22%, Mg - 14.20%, Ni - 1.31%, Ca - 1.28%, Al - 0.98%, Cr - 0.32%, Mn - 0.25%, Na - 0.25%, K - 0.09%, P - 0.07%, Ti - 0.06%, S - 0.04%, neglecting elements with concentration <0.01%). The measured activity value of the ^{26}Al activity, with its 1σ confidence interval, is plotted as the red shaded band. This analysis suggests a preatmospheric size for the Cavezzo meteoroid of $r \in [30, 50]$ cm and a shielding depth of the main mass F2 of $\Delta X \in [15, 35]$ cm within it. Therefore, there is a significant disagreement between this result and the photo-dynamical estimation of the meteoroid's size, that is $r_\infty = 10.5 \pm 1.5$ cm (see Tab. 5.2). The detailed reason for this mismatch is still being investigated, also in light of recent results about the estimation of the CR exposure age by measurements of noble gases concentration in Cavezzo. Generally speaking, this evidence could be explained by a complex exposure history of the Cavezzo meteoroid, with significant impact events during the time scale of the last millions of years.

5.4 The IT20230214 event

On 14/02/2023 (Saint Valentine's Day) at 17:68:29 UT, the PRISMA network detected a brilliant event, named IT20230214 from now on, over the Puglia and Basilicata regions in Southern Italy. Unfortunately, the network has not reached a dense coverage in this part of the country until today, and three cameras only detected this event. These are the stations ITPU01 - Castellanagrotte (40°52'32.2" N, 17°08'52.0" E, 337 m), ITPU03 - Tricase (39°55'25.0" N, 18°21'58.3" E, 122 m) and ITAB01 - Vasto (42°05'58.7" N, 14°42'08.9" E, 190 m). The reconstructed tracks detected by these cameras are reported in Fig. 5.13. The ITPU03 and ITAB01 stations recorded the bolide very close to the horizon, at a distance of ~200 km. The terminal part of the bright flight was detected below 10° from both cameras, negatively affecting the astrometric precision and accuracy of these measures (see Sect. 4.1.4). Also, the light of the bolide saturated on all three cameras and we applied the correction for the PSF saturation to this case as well (see Sect. 4.2.1). The results of the triangulation processing are shown in Fig. 5.14 and summarized in the first part of Tab. 5.5, in a similar way to what was presented for the IT20200101 event in the previous sections. The poor astrometric performance of ITPU03 and ITAB01 for this case is evident from the residuals of the trajectory fit (Fig. 5.14b),

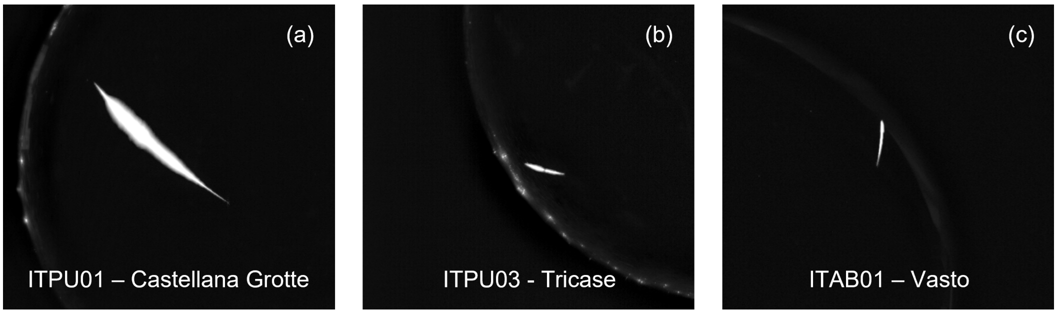

Fig. 5.13: Reconstruction of the tracks of the IT20230214 bolide as seen from the three cameras (a) ITPU01 - Castellana Grotte, (b) ITPU03 - Tricase and (c) ITAB01 - Vasto.

which show a significant systematic for these cameras. As a consequence, the evaluation of the effective number of degrees of freedom resulted in $N_{DOF} = 3$ (*i.e.*, the number of cameras), showing again that a significant bias is present within the data of each camera (see Sect. 4.2.3). Also, the magnitude lightcurve (panel e) shows important deviations among the three cameras. From a visual inspection of the captures of that day, we found that the protective domes of all cameras were dirty (in particular the one of Tricase), significantly impacting their transparency. The IT20230214 event was detected from a starting altitude of 85.5 $\pm$ 0.1 km at an initial speed of 16.3 $\pm$ 0.1 km/s. It traversed the atmosphere for about 5.3 s at an inclination angle of 56.7 $\pm$ 0.3°, for a total trajectory length of 75.0 $\pm$ 0.1 km, arriving from the NNE direction and travelling towards SSW with an azimuth angle of 24.3 $\pm$ 0.1°. Projected on the ground, its trajectory began SW of Bari and ended NE of Matera, where the visible flight terminated at an altitude of 22.8 $\pm$ 0.1 km, while the meteoroid was travelling at a low speed of 3 $\pm$ 1 km/s.

The results of the dynamical model fitting are presented in Fig. 5.15 and in the second part of Tab. 5.5. Again, we compare the results of the dynamic and photo-dynamic approaches. The shape-change coefficient μ from the lightcurve is estimated to be compatible with 2/3, which is isotropic ablation. However, the magnitude data of this event are not of a good quality and we do not strictly prefer the NUM_PHD results over the DYN ones. The meteoroid had a preatmospheric speed of $V_\infty = 16.4 \pm 0.2$ km/s and an MSR of 310–510 kg/m^2, corresponding to M_∞ in the range 5–21 kg and a preatmospheric size of 15–24 cm. These estimates are given by considering the two 1σ confidence intervals of the DYN and PHD approaches, which are compatible at this significance level. The two values for the ablation coefficient σ significantly differ by a factor of two, resulting in a very different estimate of the final mass at the end of the bright flight. The purely dynamic model suggests a residual mass of 0.6 $\pm$ 0.3 kg (7 $\pm$ 1 cm of size), while the photo-dynamic results in a much more modest mass of 0.10 $\pm$ 0.04 kg (4.4 $\pm$ 0.7 cm). It is worth noticing that this last estimate is compatible with the total known weight (TWK) of the recovered meteorite of 117.5 g (see Sect. 5.5). We can also compare

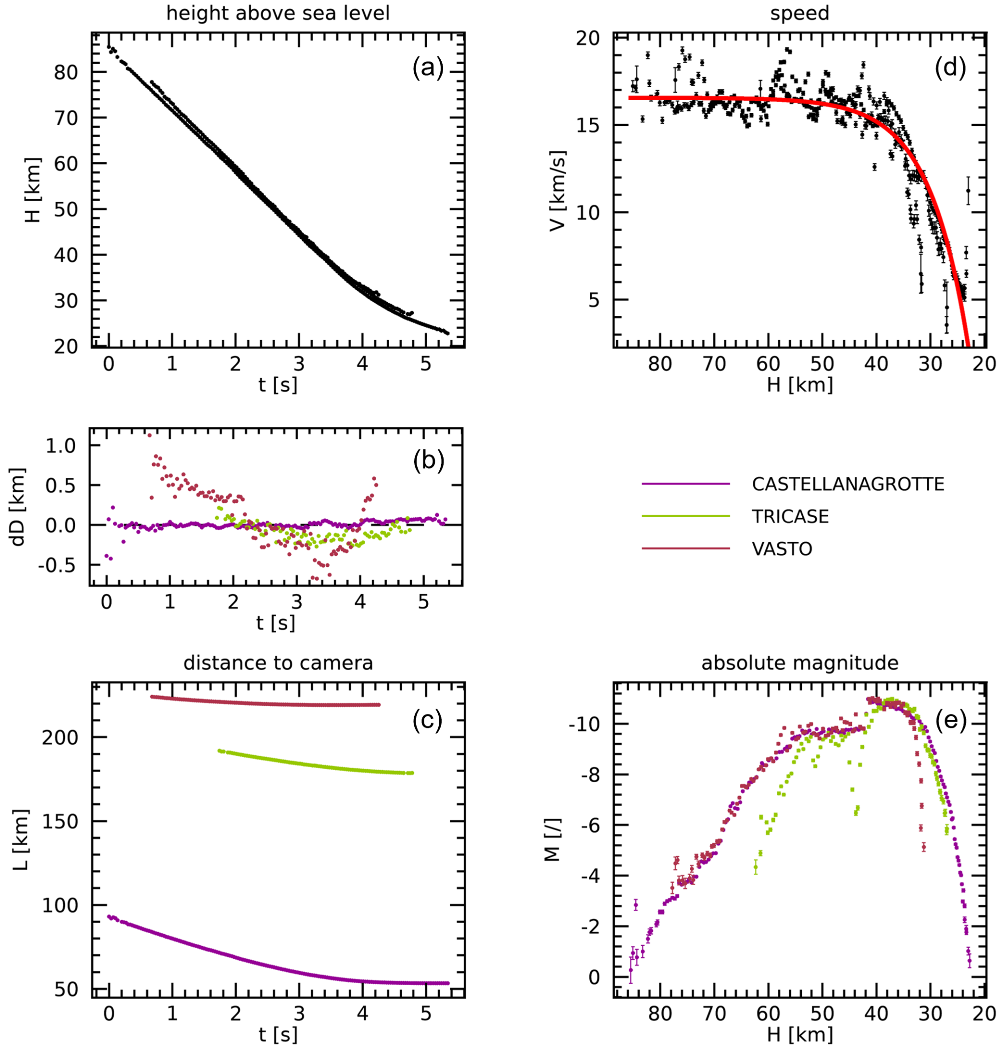

Fig. 5.14: Results of the triangulation processing for the IT20230214 event. (a) Height above sea level; (b) distance residuals of the LoS fitting procedure from Eq. 4.27; (c) distance of the trajectory from the various stations that detected the event; (d) speed profile reconstructed from the triangulated positions (dots with error bars) together with the result of the exponential fit of Eq. 4.30 (red thick line); (e) absolute magnitude lightcurve from Eq. 4.31.

Triangulation

			Beginning	Ending
Time	t	(UT)	17:58:29.54	17:58:34.89
Latitude	ϕ	[deg N]	41.0893 ± 0.0006	40.7496 ± 0.0006
Longitude	λ	[deg E]	16.8053 ± 0.0004	16.5996 ± 0.0004
Height	H	[km]	85.5 ± 0.1	22.8 ± 0.1
Speed	V	[km/s]	16.3 ± 0.1	3 ± 1
Time of Flight	ToF	[s]	5.34 ± 0.05	
Trajectory Length	L	[km]	75.0 ± 0.1	
Trajectory Inclination	γ	[deg]	56.7 ± 0.3	
Trajectory Azimuth	a	[deg]	24.3 ± 0.1	
Min. Abs. Magnitude	$\mathcal{M}_{min}$	[/]	-11.1 ± 0.1	

Dynamic model

			NUM_DYN	NUM_PHD
Preatm. speed	V_∞	[km/s]	16.4 ± 0.2	16.4 ± 0.2
Ablation coeff.	σ	[s^2/km^2]	0.020 ± 0.005	0.038 ± 0.002
Shape-change coeff.	μ	[/]	2/3	0.69 ± 0.03
Luminous efficiency	τ	[%]	–	1.5 ± 0.5
Preatm. MSR	D_∞	[kg/m^2]	360 ± 50	460 ± 50
Preatm. mass	M_∞	[kg]	8 ± 3	15 ± 6
Preatm. size	$2r_\infty$	[cm]	17 ± 2	21 ± 3
Final MSR	D_{fin}	[kg/m^2]	150 ± 30	100 ± 10
Final mass	M_{fin}	[kg]	0.6 ± 0.3	0.10 ± 0.04
Final size	$2r_{fin}$	[cm]	7 ± 1	4.4 ± 0.7

Tab. 5.5: Summary of the results of the triangulation and dynamic model for the IT20230214 event. The two columns of the first half of the table (triangulation) refer to values at the beginning and end of the bright flight, respectively (when applicable), and in the second half (dynamic model) they refer to the results of the two approaches NUM_DYN and NUM_PHD. Values of mass and size are computed from the mass-section ratio D by assuming a spherical shape of the meteoroid and for the measured meteorite bulk density of $\rho_m = 3.3 \pm 0.2$ g/cm^3.

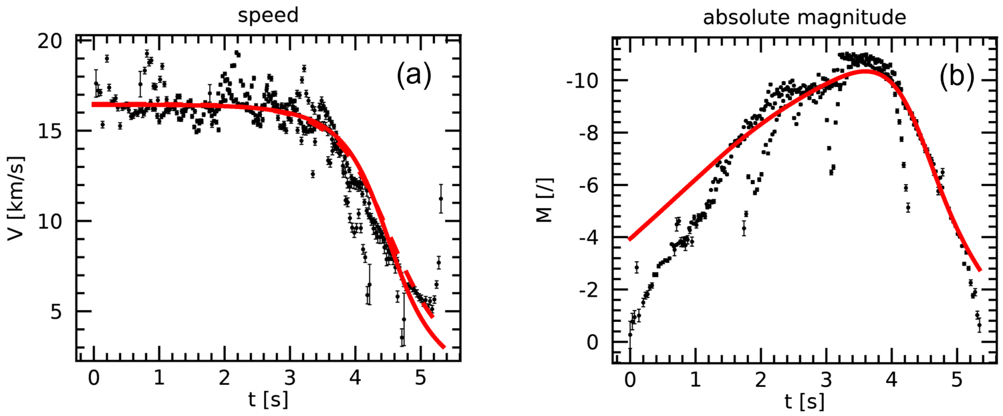

Fig. 5.15: Results of the dynamic model fitting on the data of (a) speed and (b) absolute magnitude for the IT20230214 event. The solid red line represents the fit of the NUM_PHD model in both panels, and the dashed red line in panel a is the result of the NUM_DYN model.

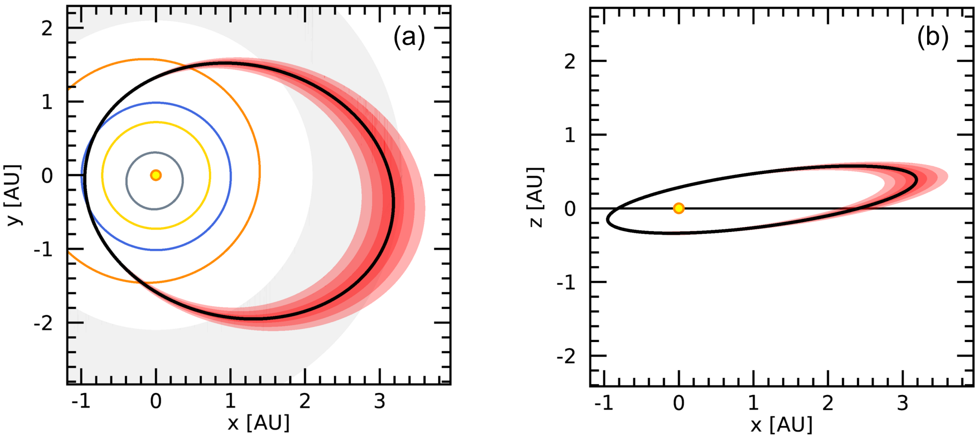

Fig. 5.16: Heliocentric preatmospheric orbit of the IT20230214 meteoroid computed in this work. (a) Plot of the (x, y) ecliptic projection. (b) Plot of the (x, z) ecliptic projection. In both panels, the red shaded bands enclose the 1, 2 and 3σ confidence intervals.

		This work	FRIPON
Epoch		J2000	J2000
a	[AU]	2.10 ± 0.07	2.32 ± 0.02
e	[/]	0.54 ± 0.02	0.586 ± 0.003
i	[deg]	14.5 ± 0.2	14.8 ± 0.1
Ω	[deg]	325.4660 ± 0.0001	325.4601 ± 0.0004
ω	[deg]	204.33 ± 0.07	202.87 ± 0.2
q	[AU]	0.9566 ± 0.0004	0.9588 ± 0.0005
Q	[AU]	3.2 ± 0.1	3.68 ± 0.03
T_J	[/]	3.51 ± 0.08	3.229 ± 0.03

Tab. 5.6: Elements of the preatmospheric orbit of the IT20230214 meteoroid as computed by this work and the FRIPON pipeline, with their 1σ nominal uncertainties.

our results with the ones provided by the independent processing of FRIPON[11]. Their estimate of the preatmospheric speed is slightly higher, being $V_\infty = 16.8 \pm 0.2$ km/s but compatible with the one presented in this work at 1σ confidence level. They also provide a lower pre-atmospheric mass of 3 ± 2 kg (which is purely dynamic), which can be considered in agreement with our estimated range for the preatmospheric mass. At the same time, FRIPON estimates a final mass of 0.18 ± 0.19 kg, similar to our photo-dynamic estimate and compatible with the TKW of the Matera meteorite.

The computed preatmospheric heliocentric orbit of the IT20230214 meteoroid is plotted in Fig. 5.16 and its elements are reported in Tab. 5.6. It has a moderate eccentricity of 0.54 ± 0.02 and an inclination on the ecliptic plane of 14.5 ± 0.2°, with a semi-major axis of 2.10 ± 0.07 AU and its aphelion on the outer region of the MAB (represented as the grey shaded region of panel a). Together with a Tisserand's parameter of 3.51 ± 0.08, this points towards an asteroidal origin for

---

[11] `https://fireball.fripon.org/displaymultiple.php?id=19980`

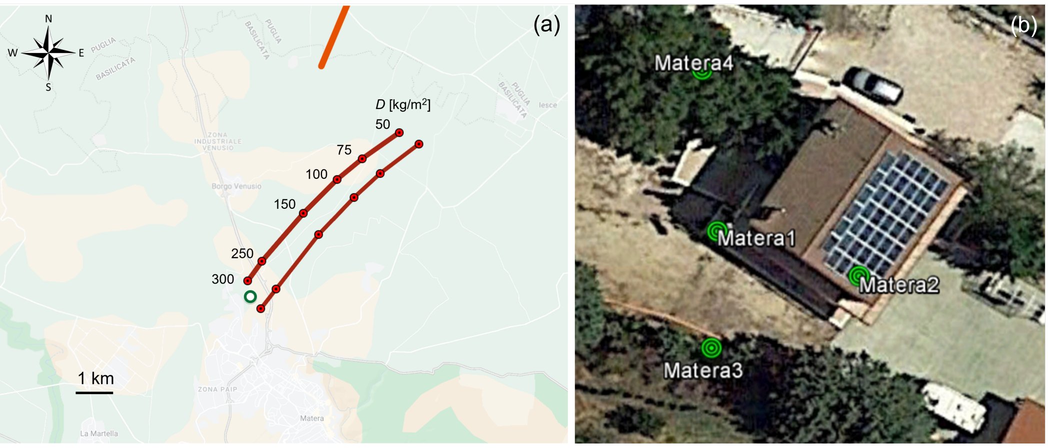

Fig. 5.17: The strewn-field of the IT20230314 event. (a) Computed nominal impact points of meteorites fragments as a function of their MSR value. The distance between the two lines represents a preliminary estimation of the transverse uncertainty of the impact point. The orange line plots the terminal part of the trajectory projected on the ground and the green points indicate the coordinates of the recovery of the Matera meteorite (background map credits: Google Maps). (b) A picture from Google Earth of the house of the Losignore brother, where the green dots plot the position of the recovery of the main fragments.

the orbit of this meteoroid. Compared to the performance achieved on the orbit of Cavezzo, we notice here significantly larger random errors and, mainly due to the higher uncertainty of the measures of the preatmospheric speed and radiant direction (*i.e*, the triangulation results) with respect to the IT20200101 event, as already pointed out in this section. The search for candidates for a progenitor body within the population of known NEAs is still ongoing. Finally, the comparison of the orbital elements of this work with the ones provided by FRIPON (last column of Tab. 5.6) results in significant but still relatively confined differences between these two solutions, mainly for the values of the semi-major axis and inclination. This results in an aphelion distance $\sim$0.5 AU greater than the one deduced in this work. The reason for this mismatch is still being investigated at this time of writing, but may originate from the higher preatmospheric speed estimate of the meteoroid given by FRIPON with respect to the one presented in this work.

5.5 The recovery of the Matera meteorite

Despite the experimental limitations in the detection of this event, it was possible to estimate the probable area of fall of meteorite fragments. Similarly to the case of Cavezzo, the data of the wind speed and direction came from Meteo Expert (see Sect. 5.1.1). Figure 5.17a shows the preliminary version of the strewn-field, together with the terminal part of the trajectory projected on the ground (orange line). The area of fall is located north of the Matera city, the capital of the Basilicata

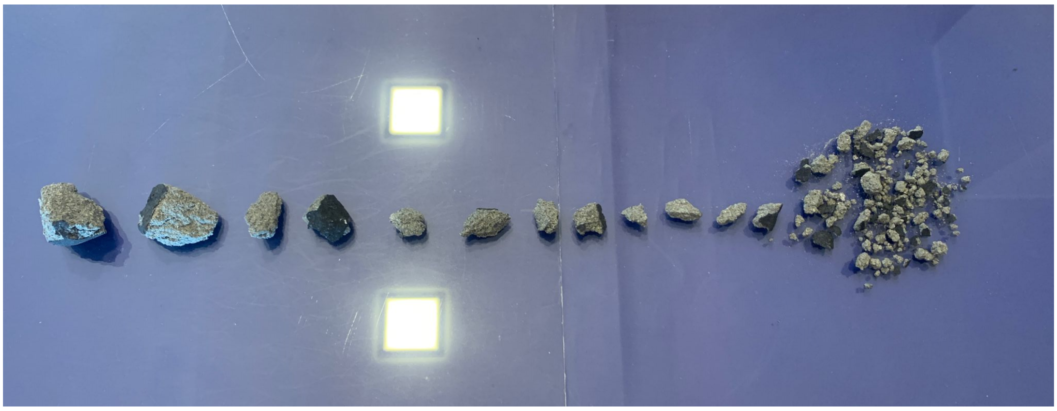

Fig. 5.18: A picture of (not all) the fragments of the Matera meteorite (`http://www.prisma.inaf.it/index.php/2023/02/18/eccola-trovata-la-meteorite-di-san-valentino/`).

region. The effect of the wind drag caused the strewn-field to be shifted towards East compared to the geometrical prolongation of the trajectory. The two red curves represent an estimation of the transverse uncertainty in this computation, and the red dots along them indicate the nominal impact points for fragments with different MSR values. Adopting the same successful approach of the case of the Cavezzo meteorite, the Project Office of PRISMA prepared and disclosed a press release[12] on the morning of 16/02/2023. It is worth noticing that we initially gave a less extended version of the strewn-field compared to the one of Fig. 5.17a, since the results of the dynamic model indicated a final MSR in the range of 90–180 kg/m^2 (see Tab. 5.5).

On 17/02/2023 we were travelling to Matera, and one member of the Project Office (Dr. Carmelo Falco) was already there to start organizing the on-field search campaign. On the evening of that day, he was contacted by the brothers Mr. Gianfranco e Pino Losignore, who reported an interesting finding over their property (Fig. 5.17b), located in Contrada Rondinelle on the municipality of Matera (green point of panel a). The approximate coordinates of the recovery are 40°41’43.9” N and 16°35’4.2” E. They found a bunch of rocky fragments, of tens of grams of total mass, on the balcony of their house (Matera 1 on panel b) and one tile of the pavement was damaged by what looked like a violent impact. We immediately recognized these fragments as freshly-fallen meteorite pieces. On the morning of the next day, it was also discovered that one fragment landed on the roof of their house (Matera 2) and damaged one solar panel, shattering its outer glass surface. Further searches in the neighbouring area led to the discovery of a third fragment, and a fourth one was recovered by two volunteers of the search campaign (Mr. Pierluigi Cox and Mrs. Silvia Yadira Padilla Leon). To date, the total recovered mass of the

---

[12] `http://www.prisma.inaf.it/index.php/2023/02/16/la-mappa-della-meteorite-di-san-valentino/`

Matera[13] meteorite is 117.5 g, distributed in 4 main specimens and dozens of small fragments from the impact on the balcony (see Fig. 5.18). This is compatible with the final mass estimated by the photo-dynamic model (see Tab. 5.5). However, the coordinates of the recovery suggest an MSR value that is not compatible with the final mass-to-section ratio of the single-body ablation hypothesis. This is to be compared with the longitudinal uncertainty on the impact points of Fig. 5.5a, which is to be evaluated yet. A significant mismatch between these results may be due to the shape of the fragments during the dark flight being considerably different than spherical. Unfortunately, the geometry of the recovered specimen cannot be helpful in this analysis, since most of them originated from fragmentation on the ground.

The day after the recovery, all fragments were moved to the Istituto Nazionale di Fisica Nucleare - Laboratori Nazionali del Gran Sasso[14] to measure their γ-activity with the HPGe detectors of the STELLA[15] facility, and the geochemical analysis of the meteorite is being carried out at the Dipartimento di Scienze della Terra of the Università di Firenze.

---

[13] This is a provisional designation only. The official recognition and naming of this meteorite have yet to be approved by The Meteoritical Society.

[14] `https://www.lngs.infn.it/`

[15] SubTErranean Low-Level Assay (`https://www.lngs.infn.it/en/div-ric/special-techniques`)

Analysis of the meteors detected by Mini-EUSO

6

Since its first operations in October 2019, Mini-EUSO regularly took data during dedicated observative sessions (about twice a month), being installed by the cosmonauts on the ISS in front of a UV-transparent window of the Russian Zvezda module looking in the nadir direction towards the Earth. Until early 2023, Mini-EUSO performed 81 of such data-taking sessions, and half of this data has been already brought back to the Earth by two Soyuz spacecrafts in 2020 and 2021. In this chapter, I describe the analysis of Mini-EUSO data with the aim of identifying meteors on the D3 continuous acquisition at 40.96 ms time resolution and reconstructing their atmospheric path, to estimate their physical parameters. While observing the same phenomenon, the data of PRISMA and Mini-EUSO are completely different and I had to develop ad-hoc reduction procedures for the analysis of meteors detected by Mini-EUSO. Since Mini-EUSO implements a monocular vision only, it is not possible to triangulate the three-dimensional trajectory of the observed meteors and we have to make a few assumptions about the geometry of the observation. With a statistics of 24k events detected in the first 44 sessions by two independent trigger algorithms, it was possible to compute the meteor's flux as a function of the absolute magnitude. To do this, I developed dedicated numerical simulations to estimate the trigger efficiency as a function of the meteor's magnitude and the background illumination level of Mini-EUSO. This allowed to compute the effective exposure of Mini-EUSO for the detection of meteors, therefore correcting the recorded flux for the differential efficiency bias due to the very diverse observational conditions of Mini-EUSO during its operation.

6.1 Meteor trigger

Let us briefly recall here a few technical specifications and the data format of Mini-EUSO observations, that was presented in Sect. 3.4.3. The focal plane (PDM - Photon Detection Module) of Mini-EUSO is made of 6 × 6 MAPMTs (Multi-Anode Photomultiplier Tubes, referred to as PMT in the following), each one consisting of 8 × 8 individually separated pixels and therefore summing up to a matrix of 48 × 48 pixels. Each of these pixels has single-photon counting capabilities, with a photon collection efficiency of ∼10% and a FoV projected on the ground of about

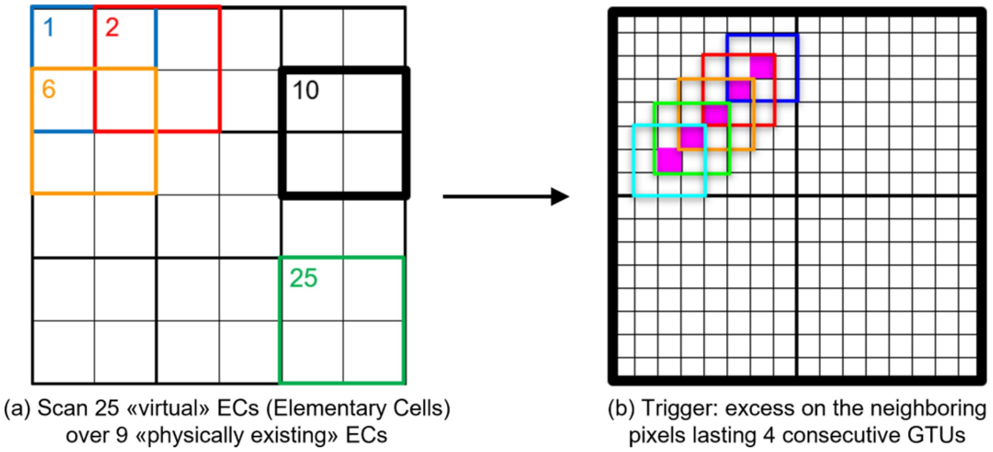

(a) Scan 25 «virtual» ECs (Elementary Cells) over 9 «physically existing» ECs

(b) Trigger: excess on the neighboring pixels lasting 4 consecutive GTUs

Fig. 6.1: Graphical representation of the trigger scheme adapted for the detection of meteors in D3 data from Mini–EUSO. (a) Subdivision of the PDM in 25 virtual ECs, allowed to overlap by 1 PMT.(b) In each virtual EC, the algorithm searches for over-threshold excesses on neighbouring pixels lasting at least 4 GTUs.

6.3×6.3 km^2 and corresponding to 4.7×4.7 km^2 at the typical meteor altitude of 100 km, varying slightly with the altitude of the ISS and the pointing direction of the pixel. Mini-EUSO acquires data in three timescales, which are D1 (2.5 μs), D2 (320 μs, that is 128 D1) and D3 (40.96 ms, 128 D2). The time unit is named GTU (Gate Time Unit). In the text, we will refer to frame and GTU with the same meaning. While the D1 and D2 data are internally triggered by the system and saved to the local disk space of the instrument only in this case, the acquisition of D3 data is not triggered and therefore consists in a ∼24 Hz continuous monitoring of the UV emission from the Earth's surface and atmosphere.

To detect meteors on D3 data, we then had to develop an offline trigger logic able to recognize a moving source on the focal plane. As a first approach, we adapted a trigger algorithm that was originally designed for the onboard detection of space debris in future missions of the JEM-EUSO program. A detailed description of the algorithm and its performance for space debris search can be found in Miyamoto et al. (2019). While meteors (11–72 km/s) are typically faster than space debris (7–9 km/s), the apparent speed of these two classes of events, as seen from Mini-EUSO, is not so different due to the higher distance at which meteors are expected (∼100 km of altitude, *i.e.*, about 300 km of distance from the ISS) with respect to space debris (tens of kilometres from the ISS). The concept of this trigger algorithm is presented in Fig. 6.1. The PDM is divided into 25 *virtual* ECs (Fig. 6.1a), which are allowed for 1 PMT overlapping between one another. For each pixel, the algorithm

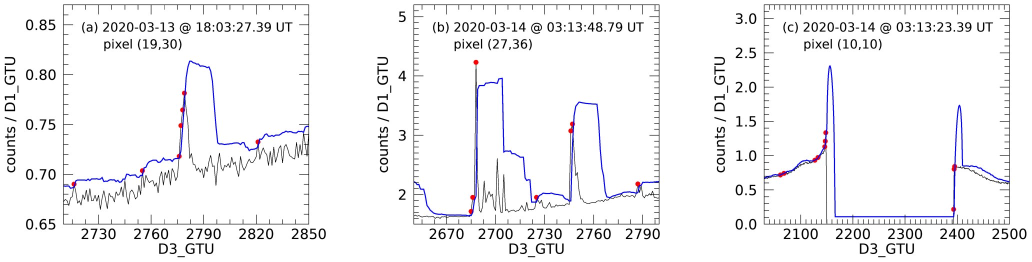

Fig. 6.2: Three example cases of results from the Mini-EUSO meteor trigger (Fig. 6.1), from data session n. 13 (13-14/03/2020). In all subpanels, the black curve plots the single-pixel lightcurve and the blue thick line plots the computed threshold according to the algorithm described in Sect. 6.1. Red points mark GTUs where the counts on the selected pixel overcome the given threshold. (a) A pixel lightcurve of a meteor event, that overcame the threshold on 4 consecutive GTUs and generated a trigger, whereas neighbouring isolated GTUs that happen to be over-threshold are discarded. (b) Lightcurve of a thunderstorm imaged by Mini-EUSO. (c) An example of cathode-2 transition.

evaluates the detection threshold (T_{xy}) as the running mean (μ_{xy}) plus three times the standard deviation (σ_{xy}), both computed over the last 16 GTUs:

$$\begin{cases} \mu_{xy}(t) = \frac{1}{16}\sum_{k=t-16}^{t-1} C_{xy}(k) \\ \sigma_{xy}(t) = \sqrt{\frac{1}{16}\sum_{k=t-16}^{t-1}[C_{xy}(k) - \mu_{xy}(t)]^2} \end{cases} \quad \rightarrow \quad T_{xy}(t) = \mu_{xy}(t) + 3\sigma_{xy}(t) \ , \tag{6.1}$$

where t is the GTU index and C_{xy} are pixel counts on D3 data (in the units of counts/px/D1_GTU[1]) for each pixel in the PDM. Then, the algorithm inspects for any over-threshold excess on neighbouring pixels, in a 3×3 pixel area, lasting at least 4 consecutive GTUs (Fig. 6.1b). If this is the case, information about the position and GTUs of triggered pixels are saved for further processing. This occurrence should represent the case of a moving source, such as a meteor, imaged onto the focal surface of Mini-EUSO. Due to its simple and fast-executable implementation, this algorithm could be employed in the future also as an online meteor trigger for the planned EUSO missions.

Figure 6.2 presents three examples of single-pixel lightcurves acquired in the observation session n. 13, together with the computed thresholds. In particular, Fig. 6.2a plots the light-curve of a meteor event, that successfully triggered according to this algorithm. Particular attention must be given to the detection of false positives in this regard. As detailed in Sect. 3.3.3, Mini-EUSO can record many different types of luminous events in the atmosphere and from the ground, in a greatly varying range of timescales. As an example, lightning can be detected in D3 data (Fig. 6.2b), resulting in a sudden brightening of a vast portion of the PDM, due to stray-light scattering onto the lenses, and triggering the corresponding EC to switch to cathode-2 (Cat2) protection mode (Fig. 6.2c). These events are usually recognizable

---

[1] Values of pixel counts in D2 and D3 data are conventionally normalized to counts over the time integration of D1 (2.5 μs).

against meteors due to their very short duration lightcurves and repetitive patterns. To discard most of these events, we reject any trigger that involves more than 64 pixels (equivalent to 1 PMT) in the same virtual EC. To exclude false positives when an EC is in Cat2, we set a minimum value for T_{xy} corresponding to Poissonian fluctuations for a background value of 0.1 counts/px/D1_GTU, which is the typical lowest count value recorded in D3 data for low illumination conditions in standard cathode-3 (Cat3) acquisition mode (Casolino et al., 2023). For the same reason, we control the variation of the threshold for each pixel to avoid false triggers when switching back from Cat2 to Cat3, by fixing the running threshold value if $C_{xy}(t) > T_{xy}(t-1) + 5\sigma_{xy}(t-1)$, that is, if there is a sudden and steep increase of the counts registered at a certain pixel and GTU.

6.1.1 Event selection and classification

We used the data from the first 9 sessions delivered to the Earth in 2020 with the first Soyuz (n. 05-14, the first four sessions were dedicated to the test of the instrument only) to tune the trigger algorithm and understand its performance for the detection of meteors. All the triggers from a couple of selected sessions (mainly n.11 and 13) were visually inspected (thanks to the ETOS toolkit, see Sect. 3.4.3) and classified according to the following scheme:

- *Meteor* (M): a clear meteor event that shows an evident apparent motion on the PDM within more than 2-3 pixels and has a gaussian-like single-pixel lightcurve, originating by the PSF of the meteor gradually moving in and out of the FoV of that pixel.
- *Meteor candidate* (M?): an event that cannot be indisputably classified as a meteor but shows convincing evidence for it to be considered a meteor. A typical example of an event in this class has a smooth lightcurve but shows a limited and not clear apparent motion on the PDM. This may be caused by various reasons, *e.g.* the meteor crossing the border in between two adjacent PMTs, which corresponds to an inactive region of an equivalent size of one pixel insensitive to incoming light. While we will usually consider the M and M? classes together (and indicate them as M), we preserved this distinction on the database to have a qualitative measure of the confidence of the classification of meteor events.
- *Other / non-meteor event* (U): an event that showed a significant signal in one or more pixels but that is not a meteor, such as a lightning that survived the trigger intensity cut-off and did not triggered more than 64 pixels.
- *Noise* (N): nothing significant is visible at the GTU and position indicated by the trigger, *i.e.*, false positives. This was often the case of isolated GTUs that triggered in a few pixels near the leading edge of the lightcurve of a city

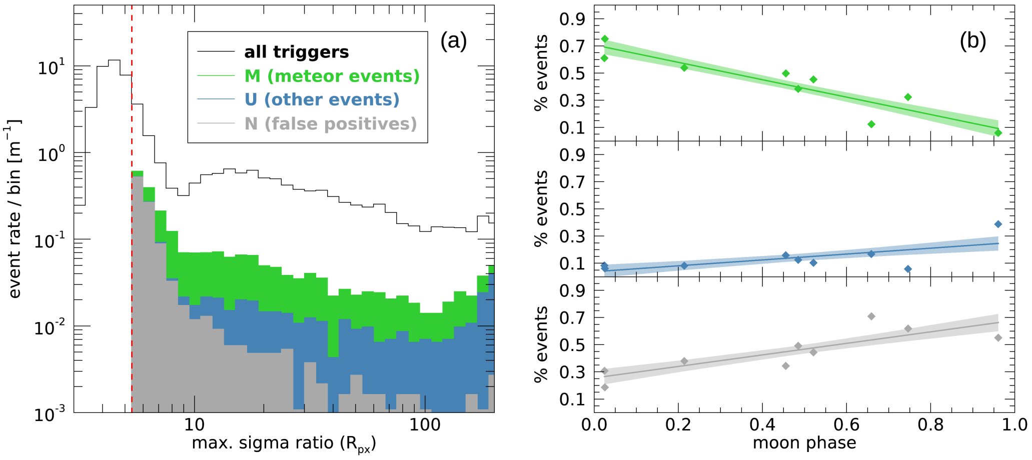

Fig. 6.3: Results of the meteor trigger algorithm on the first 9 data sessions of Mini-EUSO. (a) Histogram of the maximal sigma ratio (R_{xy}) for all triggers (black line) and for the three classes of events (meteors, M – green; other events, U – blue; false positives, N – grey). (b) Percentage of M, U and N events as a function of the moon phase for each session, where points refer to the data from each session and the solid lines plot a least-square linear fit together with the 68% confidence interval.

entering in their FoV. In fact, fixed sources on the ground move in the FoV of Mini-EUSO at an apparent speed that is the ISS speed (~7.66 km/s) along the positive y direction.

Unfortunately, this inspection resulted in a very high percentage (~70%) of N events being detected by the trigger algorithm. We therefore analyzed these results to define a post-processing procedure and automatically discard most events in this class. Within the trigger logic, the intensity of an event can be represented by the ratio between the over-threshold residual and the standard deviation of background fluctuations:

$$R_{xy} = \frac{C_{xy} - T_{xy}}{\sigma_{xy}} \ . \tag{6.2}$$

Since each trigger is made of 4 GTUs, we then consider the maximal sigma ratio in this range. The black-line histogram of Fig. 6.3a plots the distribution of R_{xy} for all triggers in the considered sessions. From the trigger requirement, it must be $R_{xy} > 3$. Two populations are well depicted from this plot, separated at $R_{xy} \sim 8$. From the extensive visual inspection described above, it was clear that most of the triggers below this limit were false positives, mainly due to noise in correspondence to the passage of the FoV over bright cities and artefacts at PMTs borders (Casolino et al., 2023). According to this evidence, we decided to discard every trigger for which $R_{xy} < 5.5$ (red dashed line in Fig. 6.3a). This is an empirical limit and a fraction of faint meteors may be still detected under this value, which represents a trade-off to maximize the ratio between true and false positives. We also discard every trigger that stays in the same pixel for the whole event duration of the event.

Indeed, it would be possible that these cases are faint and short meteors, but we have little to no evidence to discern them from other sources, like impulsive lights from the ground. On the contrary, it is possible that the same meteor generates more than one trigger during its flight, especially in the case of longer events. Overlapping triggers in the same pixel region are therefore automatically regrouped during the post-processing. The selection bias introduced by these limits will be corrected when evaluating the trigger efficiency and the actual instrument exposure for the observation of meteors (see Sect. 6.3).

Figure 6.3a also plots the distribution of R_{xy} for three separate classes that are meteor and candidate meteor events (M+M?, green histogram), non-meteor events (U, blue) and false positives (N, grey). This is the result of a visual classification of the event ensemble resulting from the trigger and the post-processing described above. In a first step, this classification was made with a direct inspection of the video data from the starting pixel position and GTU marked by the trigger. We classified each event by observing the evolution of the PSF on the focal surface, its apparent motion and the shape of the lightcurve of the interested pixels, as already done for the first inspection described above. The result of such visual inspection is of course subject to significant biases due to the subjective impression of each user dedicated to this task. Moreover, the visualization of the event is usually non-trivial, because the background features often suppress the small temporal and spatial dynamic variability of meteor events, especially for the fainter ones. On the other hand, we believe that a dedicated check by a human user is indeed necessary in our case, given the number of non-meteor events that may resemble a straight-line motion on the PDM and that may be consequently mistaken as meteors by a totally automatic processing procedure. For this reason, the first 9 sessions of the data were inspected with a double-blind approach followed by a cross-checking of the classification results from the two users. From this experiment, we found out that $> 90\%$ of the events were assigned to the same class by all users. Most of the difference was indeed attributable to faint events, that were classified in between the M and M? class and for which the apparent motion of the PSF was unclear and hardly visible without a dedicated background subtraction method. From the results of this analysis, we were able to design an analysis algorithm capable of tracking the meteor path through the whole flight by applying several selection criteria on the shape of single-pixel light curves identified by the trigger (see Sect. 6.2). Therefore, the full dataset of triggered events was processed through this algorithm and the visual inspection was conducted against these results, removing most of the subjectivity issues in the process.

We also studied the performance of our meteor trigger with respect to the background illumination conditions. In each session, this can vary significantly due to the observed region on the ground, the cloud coverage and the reflected and stray light from the Sun and Moon. A detailed analysis of the night-time emission of the Earth in the near UV range from the D3 data for Mini-EUSO is presented in

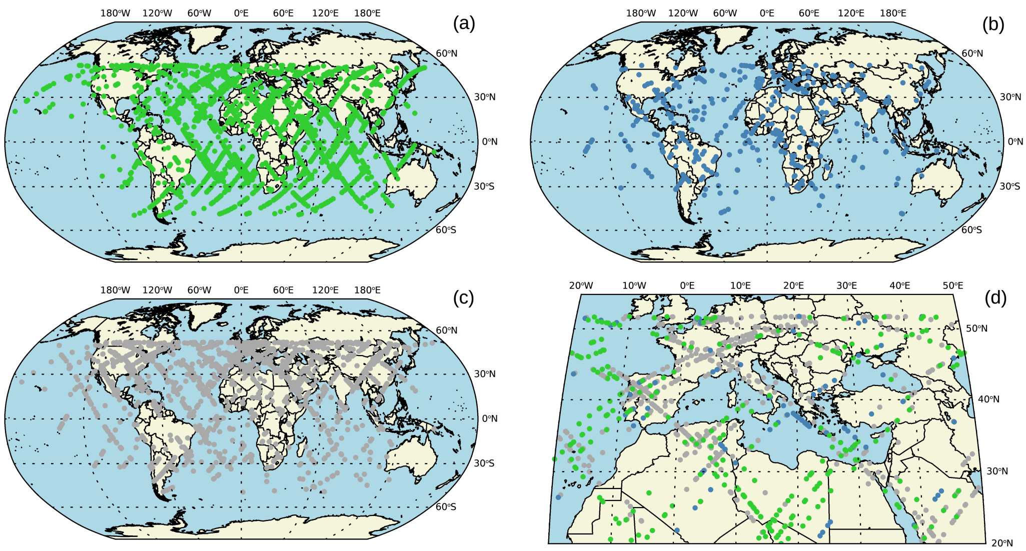

Fig. 6.4: Maps of the positions of the nominal central point of the FoV of Mini-EUSO, projected on the ground, for the starting GTU of triggered events of the sessions n. 01-14 for the three classes: (a) meteors, M – green; (b) other events, U – blue; (c) false positives, N – grey. Panel (d) plots a magnification of the map over Central and Southern Europe and North Africa.

Casolino et al. (2023). The average counts for cloud-free observations vary from $\sim$0.6 cnts/GTU for new moon to $\sim$40 during full moon (also depending on the moon elevation above the local horizon). The effect of this variability is evident from Fig. 6.3b, which plots the fraction of events for the three classes M, U and N as a function of the moon phase. The percentage of identified meteors over the whole triggers ensemble varies from about 70% for new moon down to just a few percent in the case of full moon. In the opposite way, the fraction of both non-meteor events and false positive increases for increasing moon phase values, from 5% to 30% for U and from 20% to 60% for N events, respectively for new and full moon conditions. Moreover, Fig. 6.4 shows the positions on the globe of the triggered events for each class. Overall, 49% of events are triggered on land and 51% over the oceans. This distribution varies if we consider only meteor events, which are more likely triggered over oceans (66%) rather than on land (34%). The opposite is true for U and N events, which are more frequent over land (63%) and less over oceans (37%). This is best shown in Fig. 6.4d, a magnification of the map over Europe and North Africa. From this figure, it is evident that false positives are very often triggered over densely populated and therefore highly light-polluted areas, such as the whole of Western Europe and the coast of North Africa facing the Mediterranean Sea. On the other hand, N events are rarely triggered over the sea, the Atlantic Ocean and darker regions on land, such as the Sahara Desert.

6.1.2 Trigger results

After these operations of fine-tuning to maximize the performance of the meteor trigger on the first sessions of Mini-EUSO, we processed the whole available dataset, that is up until August 2021 (sessions n. 05-44). Table 6.1 reports the meteor trigger counts and rates for each session (Trigger 1), together with the results of an independent trigger algorithm developed for the detection of meteors on Mini-EUSO D3 data (Trigger 2). This second trigger algorithm deploys a dedicated and more refined background subtraction method, that computes a threshold for the i-th GTU accounting also for values in the "future", being therefore not suitable for a potential implementation as an online trigger on future EUSO missions. It also implements an event classification based on a *k-d trees* algorithm and dedicated quality cuts to remove most of the false positives[2]. Trigger 2 generally shows better performances with respect to Trigger 1 in terms of the percentage of false positives, which is always confined to $< 20\%$. The two triggers show a similar events rate (given as events per minute in Tab. 6.1) in all sessions. With a total observation time of 8200 min (corresponding to 136.7 h or 5.7 d), Trigger 1 detected 14.4k events at an average rate of 1.76 min^{-1}, while Trigger 2 detected 18.3 k events at 2.23 min^{-1}. However, the comparison between the two datasets highlights that only $\sim$36% of the events are detected by both triggers (column "CM" of the table). On the other hand, 24% of the meteor events are detected only by Trigger 1 (column "T1"), and 40% only by Trigger 2 (column "T2"). While this evidence may look peculiar at first sight, we have to consider that the majority of events seen by Mini-EUSO are quite faint, between magnitude +4 and +5 and with a limiting magnitude of the telescope for meteors observations of about +7 in the U band (see Sect. 6.2.2). As discussed in Sect. 6.3, the efficiency of Trigger 1 for meteors in this magnitude range at a typical background value of 1 cnts/GTU is $\sim$50%. It is therefore reasonable that two different triggers may detect two sets of events that are only partially overlapping.

Because of this result, we therefore consider the merged version of these datasets ("Total" columns in Tab. 6.1) consisting of 24k meteors detected at an average rate of 2.92 min^{-1}. This rate is quite close to the expected value computed for Mini-EUSO observations of meteors at +5 absolute magnitude of 2.4 min^{-1} (see Tab. 3.1). Finally, Fig. 6.5 shows the spatial density distribution of this meteor dataset. About 30% of the total number of meteors is observed over land, while 70% of them are triggered over the oceans. This is in agreement with the ratio of the land- over ocean-covered area on a global scale. Nevertheless, as already highlighted in Sect. 6.1.1, we can observe that meteors rarely trigger over populated and light-polluted areas like Western and Central Europe, North America and India, just to cite a few.

---

[2] This algorithm was developed by Dr. Lech Wiktor Piotrowsky (University of Warsaw). The details of the algorithm are not published yet.

N.	Date	Obs. T.	M. ph.	Trigger 1		Trigger 2		Total		Comparison		
		[min]		count	rate	count	rate	count	rate	CM	T1	T2
05	19/11/19	176.6	0.48	132	0.75	157	0.89	221	1.25	31%	29%	40%
06	27/11/19	268.9	0.02	447	1.66	439	1.63	673	2.50	31%	35%	34%
07	05/12/19	204.9	0.66	46	0.22	54	0.26	82	0.40	22%	34%	44%
08	30/12/19	209.8	0.21	382	1.82	399	1.90	566	2.70	37%	30%	33%
09	08/01/20	229.6	0.96	21	0.09	12	0.05	33	0.14	0%	64%	36%
11	21/02/20	159.1	0.03	404	2.54	499	3.14	677	4.25	34%	26%	40%
12	02/03/20	199.1	0.52	192	0.96	222	1.11	315	1.58	31%	30%	39%
13	13/03/20	196.3	0.75	142	0.72	195	0.99	262	1.33	28%	26%	46%
14	31/03/20	209.3	0.46	242	1.16	288	1.38	403	1.93	31%	29%	40%
16	25/05/20	297.2	0.11	873	2.94	1132	3.81	1449	4.88	38%	22%	40%
18	24/06/20	321.2	0.16	44	0.14	82	0.26	96	0.30	31%	15%	54%
20	21/07/20	219.8	0.02	910	4.14	1127	5.13	1456	6.63	39%	23%	38%
21	27/07/20	285.4	0.57	1617	5.67	2035	7.13	2640	9.25	38%	23%	39%
22	13/08/20	271.6	0.28	618	2.28	862	3.17	1073	3.95	38%	20%	42%
23	20/08/20	311.3	0.06	1013	3.25	1300	4.18	1655	5.32	40%	21%	39%
24	25/08/20	245.6	0.54	505	2.06	665	2.71	985	4.01	19%	32%	49%
25	14/09/20	237.9	0.08	572	2.40	655	2.75	882	3.71	39%	26%	35%
26	24/09/20	360.5	0.60	811	2.25	1146	3.18	1443	4.00	35%	21%	44%
27	09/12/20	180.0	0.28	131	0.73	205	1.14	252	1.40	33%	19%	48%
28	21/12/20	266.9	0.51	880	3.30	1117	4.19	1432	5.37	39%	22%	39%
29	04/01/21	290.5	0.66	170	0.59	227	0.78	302	1.04	31%	25%	44%
30	08/01/21	273.9	0.21	320	1.17	426	1.56	550	2.01	35%	23%	42%
31	11/01/21	283.6	0.02	395	1.39	425	1.50	587	2.07	39%	28%	33%
32	15/01/21	312.7	0.10	602	1.93	646	2.07	893	2.86	39%	28%	33%
33	20/01/21	253.8	0.51	496	1.95	618	2.43	815	3.21	37%	24%	39%
34	01/02/21	236.0	0.78	98	0.42	147	0.62	190	0.81	29%	23%	48%
35	02/02/21	271.7	0.69	238	0.88	322	1.19	415	1.53	35%	22%	43%
36	05/02/21	310.0	0.36	325	1.05	429	1.38	539	1.74	40%	20%	40%
37	10/02/21	135.4	0.01	155	1.15	140	1.03	207	1.53	43%	32%	25%
38	11/02/21	112.9	0.00	125	1.11	130	1.15	182	1.61	40%	29%	31%
40	03/05/21	269.0	0.47	351	1.31	550	2.04	674	2.51	34%	18%	48%
41	06/05/21	84.3	0.21	66	0.78	131	1.55	158	1.87	25%	17%	58%
43	30/07/21	259.0	0.55	512	1.98	749	2.89	936	3.61	35%	20%	45%
44	11/08/21	256.9	0.14	570	2.22	750	2.92	936	3.64	41%	20%	39%
Sessions 05-44		8200.7	–	14.4k	1.76	18.3k	2.23	24.0k	2.92	36%	24%	40%

Tab. 6.1: Results of the two meteor trigger algorithms (Trigger 1 is the method presented in this work, Trigger 2 is the method of Dr. Lech Wiktor Piotrowsky - University of Warsaw) on the Mini-EUSO data from sessions n. 05-44. Columns are: session code and date; total observation time (minutes); median moon phase of the night; number and rate (events per minute) of triggered meteor events for Trigger 1, Trigger 2 and for the merged database version; percentage of meteors detected by both triggers (CM), only by Trigger 1 (T1) and only by Trigger 2 (T2).

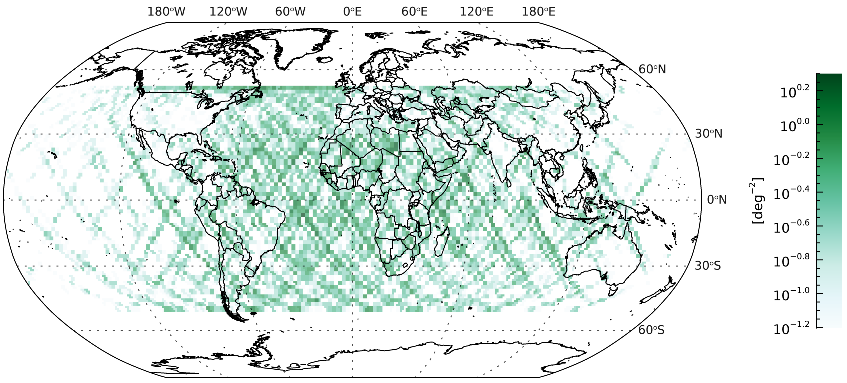

Fig. 6.5: Map of the spatial density (in logarithmic colour scale, bins of 2° × 2°) of meteor events detected by the Mini-EUSO telescope in the data sessions n.05-44 (from November 2019 to August 2021).

6.2 Meteor tracking algorithm and analysis

To reconstruct the dynamic of meteors detected on the focal surface of Mini-EUSO, we designed a tracking algorithm that operates starting from the results of the trigger. In particular, each entry on the trigger list is provided with an estimation of the starting GTU (the index of the first GTU t_0 within the 4 over-threshold frames) and the corresponding (x_0, y_0) position in pixel coordinates. From this information, we need a tool to objectively evaluate if the lightcurve of that pixel, and the ones within its first neighbourhood, registered a significant signal and if this is compatible with the expected features of a meteor observed on the Mini-EUSO PDM. As already introduced in Sect. 6.1.1, we can expect that the single-pixel lightcurve of a meteor resembles a gaussian profile. This is because this signal is given by the progressive motion within the FoV of each pixel of the PSF of the meteor, that can be approximated by a 2D gaussian function with an FWHM of 1.2 px (see Sect. 3.4.1). We therefore select a range of $[-10, 30]$ GTUs from t_0 and fit over this lightcurve portion $C_{xy}(t)$ a gaussian function over a 2nd degree polynomial background:

$$F_{xy}(t) = B_0 + B_1 t + B_2 t^2 + A \exp\left\{-\frac{1}{2}\left(\frac{t-T}{s}\right)^2\right\}. \tag{6.3}$$

For this task, we use the GAUSSFIT[3] function of IDL, that automatically optimize the parameters of Eq. 6.3 according to the standard weighted χ^2 minimization problem and does not need a user-input estimation of the starting values for them. An example of this processing is shown in Fig. 6.6a, where the measured D3 counts are plotted as black dots and the fitted function $F_{xy}(t)$ from Eq. 6.3 is plotted by the red line. The blue line represents the background term of $F_{xy}(t)$, and the shaded blue band plots its 3σ confidence interval. We then define a series of five conditions that the fit results and its parameters have to fulfil to positively evaluate the lightcurve $C_{xy}(t)$ and the pixel (x_0, y_0) as part of the meteor track, which are:

1. the fit reached a successful convergence;
2. the fitted value of the gaussian height $A \pm \sigma_A$ is significantly greater than zero at the 3σ (99.9%, one-sided) confidence level, that is $A - 3\sigma_A > 0$;
3. the ligthcurve $C_{xy}(t)$ has at least one GTU that is over the 3σ confidence band of the background term of $F_{xy}(t)$;
4. the fitted centre T of the gaussian function is determined to be within the allowed range of $[-10, +30]$ GTUs from t_0.
5. the fitted standard deviation s results in a duration of the signal $\Delta t = 2 \cdot 3s$ compatible with the motion of a meteor within the pixel. Since the speed of a meteor is confined within $[11.1, 72.8]$ km/s and given the size of the pixel

---

[3] https://www.l3harrisgeospatial.com/docs/gaussfit.html

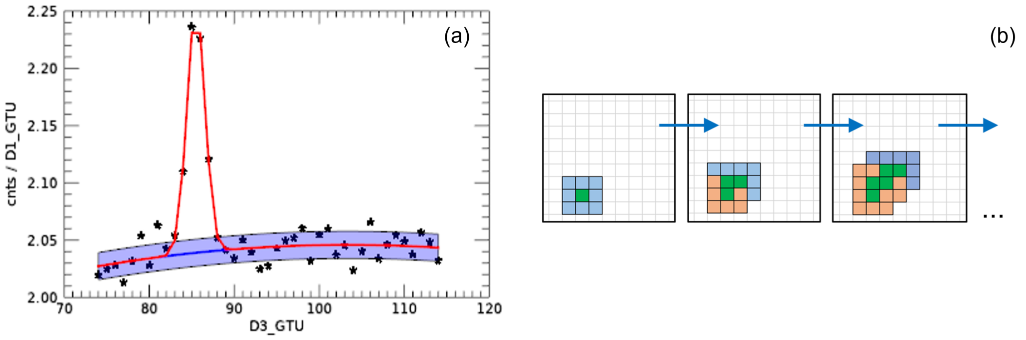

Fig. 6.6: Schematization of the tracking algorithm designed to reconstruct the meteor path imaged on the PDM of Mini-EUSO in D3 data. (a) An example of the fit of the gaussian profile of Eq. 6.3 to identify the meteor signal. Black dots represent the measured lightcurve of the pixel, the red line is the fitted gaussian function and the blue line and shaded band plot the background polynomial term with its 3σ confidence interval. (b) Graphical representation of the iterative process to identify all the pixels within the meteor track. We start from the first pixel provided by the trigger algorithm and evaluate its significance (green square in the first box from the left), then we add to the processing list all of its first neighbours (blue pixels), which are again evaluated by the fitting of panel a. Some of them will be discarded (orange pixels). Every time a new pixel is added to the track, all of its first neighbours are added to the processing list if they had not been checked yet, until no more pixels are found to be significant.

of 4.7 km at an altitude of 100 km, this results in a range of $[2, 11]$ GTUs of duration. Considering that we actually observe the horizontal component of the speed ($V_\infty \cos\gamma$) and that the apparent speed vector of the meteor is summed to the ISS speed (that may results into a lower speed then 11.1 km/s) we allow for a pixel duration of $[2, 20]$ GTUs.

If all of these conditions are matched, we consider this pixel as significant and add it to the list of the meteor track (x_i, y_i, t_{ik}), where $t_{ik} \in [T_i - 3s_i, T_i + 3s_i]$, i is the pixel index and k is there GTU index. This procedure is repeated in an iterative way, as presented in Fig. 6.6b. Once one pixel is added to the track, all its first neighbours are added to the processing list and checked for their significance. For all the pixels except the first, we add a sixth condition to the ones already presented, that is we check if the centre T of the gaussian profile is contained within the duration of one of the other pixels of the track (given by the condition n.5). This is because we expect that the transition between pixels is relatively slow, given the sampling time of 41 ms, the meteor's speed of the order of tens of km/s and the PSF size on the PDM.

An example of the results of this meteor tracking algorithm is presented in Fig. 6.7. Panel a shows the map of pixels on the PDM that were recognized as part of the meteor event, and panel b plots their lightcurves, with the coloured portion highlighting the duration of the event on each of them. The integral lightcurve of the event is plotted in panel c and it is obtained by summing all the single-pixels

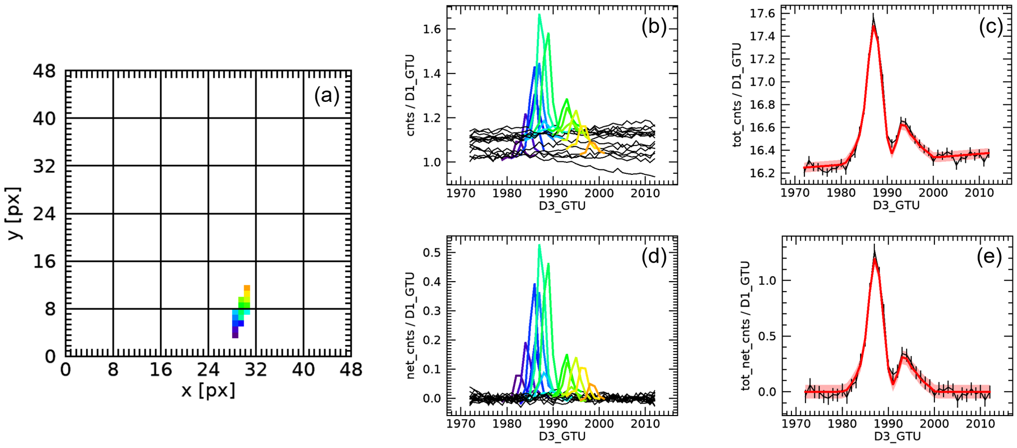

Fig. 6.7: Results of the meteor tracking algorithm on one event of the Mini-EUSO session n. 11, occurred on 21/02/2020 at 20:05:55.15 UT over the Indian Ocean (20°56' S, 93°56' E). (a) Map of the identified pixel within the track on the PDM; (b) measured lightcurves of all the pixels of panel a, with matching colours and highlighting the GTU range interested by the passage of the meteor. (c) integral lightcurve obtained by summing the ones of panel b; (d) lightcurves of net counts of the meteors obtained according to Eq. 6.4; (e) integral net lightcurve. In its apparent motion, the meteor crosses the border between two PMTs, and this is evident from the decreased counts around the GTU 1990 on the plots of panels c and e. The red curves on these panels plot the total lightcurve derived from the fit results, *i.e.*, the gaussian term of Eq. 6.3 summed over all the pixels in the track.

lightcurves. We can then use the polynomial term from Eq. 6.3 to remove the background contribution to single-pixel lightcurves:

$$\overline{C}_{xy}(t) = C_{xy}(t) - B_0 - B_1 t - B_2 t^2 \ , \tag{6.4}$$

plotted in panel d, and also from the integral lightcurve of the event (panel e). In this case, the apparent trajectory of the meteor on the PDM crossed the border between two PMTs. While this is not represented in Fig. 6.7a, each PMT is physically separated from the others, resulting in an inactive region of the width of $\sim$1 px at all of its borders. When the PSF of the meteor on the PDM is projected on these borders, a substantial fraction of its light is lost, as evident from the integral lightcurve of panels c and e.

The net counts $\overline{C}_{xy}(t)$, *i.e.*, the signal attributed only to the meteor captured on the PDM, can be therefore used to compute the barycentre position of the meteor along its apparent trajectory, that is simply given as:

$$x_b(t) = \frac{1}{\sum_i \overline{C}_i(t)} \sum_i \overline{C}_i(t) x_i \ , \tag{6.5}$$

for the x coordinate and where the sum over i extends over all the identified pixels (x_i, y_i) of the meteor track. The same formula is valid for the y coordinate as well. We then have to convert the derived pixel positions into physical coordinates, *i.e.*,

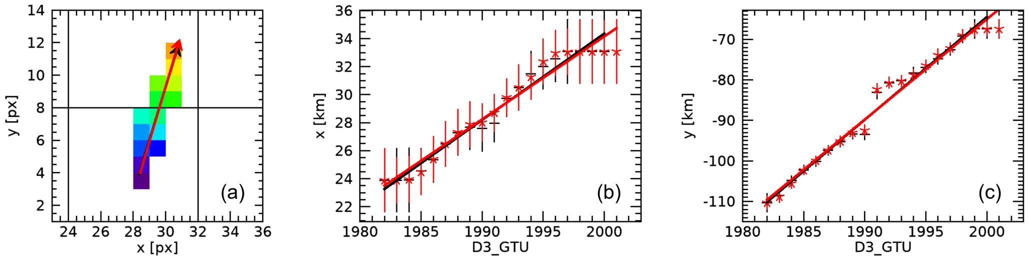

Fig. 6.8: Results of the barycentre computation for the event presented in Fig. 6.7. In all panels, the black points and lines represent the results of the computation over the net measured counts $\overline{C}_{xy}$, whereas the red ones are the results from the gaussian fitting of Eq. 6.3 (as for Fig. 6.7c,e). Both of these versions are computed during the analysis for a consistency check and a posteriori verification of the goodness of the fit. In this case, the two results are completely overlapping. (a) Map of the pixels interested by the meteor track, with the arrow indicating the apparent motion direction on the PDM. (b) Barycentre x positions computed from Eq. 6.5 (dots with error bars) as a function of the GTU index and converted to km assuming an altitude of the meteor of $H = 100$ from the ground level. The result of the linear fitting is plotted by the solid line. (c) Same as panel b but for the y positions.

the distance from the FoV centre measured in km in the x and y directions. The footprint of each pixel depends on the distance of the meteor from Mini-EUSO, that is $d = H_{ISS} - H$. While the altitude of the ISS orbit H_{ISS} is reported in the metadata of the observations (see Sect. 3.4.3), we do not have any evidence to deduce the altitude H of the meteor since Mini-EUSO implements a monocular vision only and cannot triangulate the 3D trajectory of the event. We are then forced to make the assumption of a typical meteor altitude of $H_0 = 100$ km. The effects of this assumption on the accuracy and precision of the physical parameters of the meteor measured by Mini-EUSO are discussed in Sect. 6.2.3. Even at a fixed altitude, the footprint of each pixel is not homogeneous on the PDM due to optical distortions. Therefore, we use the results of the simulations of the optical system of Mini-EUSO to take into account these secondary effects. For example, the footprint on the ground ($d \simeq 420$ km) of Mini-EUSO pixels varies from ~35 km^2 at the very centre of the FoV to ~26 km^2, corresponding to a variable linear dimension from 6 to 5 km approximately (Bacholle et al., 2021; Casolino et al., 2023).

The resulting barycentre positions for the event presented in Fig. 6.7 are plotted in Fig. 6.8. The effect of the PMT gap crossing is again evident on panel c, where the computed y position has a sudden variation of ~10 km, *i.e.*, a "jump" of approximately 2 pixels, when the PSF of the meteor transits between the two PMTs, as shown in panel a. We can therefore compute the V_x and V_y speed components of the meteor by applying a linear fit over these positions (solid lines of panels b and c) and estimate the apparent horizontal speed V and azimuth direction a. For both these quantities, we need to correct for the apparent speed of the ISS

($V_{ISS} \simeq 7.66$ km/s) and azimuth, which is also provided in the metadata and, in a first approximation[4], is oriented along the positive y direction of the PDM:

$$V = \sqrt{V_x^2 + (V_y - V_{ISS})^2} \,, \tag{6.6}$$

$$a = a_{ISS} + \text{atan2}(-V_x, -V_y + V_{ISS}) \,. \tag{6.7}$$

Eq. 6.7 represents the arrival direction of the meteor counted clockwise from the North, and a_{ISS} is the local azimuth of the ISS orbit. For the event of Fig. 6.8, we computed a horizontal speed of 53.8 km/s and an azimuth angle of 53.9°. The uncertainties affecting these values are discussed in Sect. 6.2.3.

6.2.1 Magnitude system for Mini-EUSO

The event presented in Fig. 6.7 shows a maximum luminosity of 1.2 cnts/GTU, which is to be converted into a measure of the magnitude of the meteor. In order to do so, we need to define the zero-point of the magnitude system of Mini-EUSO, that is, the reference flux of a source of absolute magnitude $\mathcal{M} = 0$ observed at a distance of 100 km. Figure 3.14 plots the quantum efficiency curve of the telescope, which observes in the near-UV wavelength range, from 260 to 480 nm. Within the standard photometric systems, the closest bandpass filter is the Johnson-Cousins U band (see Fig. 3.4), which has a maximum at $\lambda \simeq 370$ nm in close agreement with the one of the Mini-EUSO bandpass (365 nm). However, the U band is a bit narrower and spans approximately from 310 to 410 nm of wavelength. Since Mini-EUSO does not observe any standard calibration sources (*i.e.*, stars) in its FoV during regular operations, we rely on the reference flux of the U band to estimate the zero-point flux as:

$$F_0 = \frac{f_\lambda \cdot A \cdot \Delta t_{D1} \cdot \Delta\lambda \cdot \eta}{E_\gamma} \simeq 165 \text{ cnts} \,, \tag{6.8}$$

where:

- $f_\lambda = 4.175 \cdot 10^{-8}$ erg/cm^2/s/nm is the zero-point flux of the U band[5];
- $A = \pi(12.5 \text{ cm}^2) = 490.6 \text{ cm}^2$ is the photon collecting (lenses) area of the Mini-EUSO telescope;
- $\Delta t_{D1} = 2.5$ µs is integration time of D1 data;
- $\Delta\lambda = 220$ nm is the width of the Mini-EUSO bandpass;
- $\eta \simeq 7\%$ is the integral average efficiency of Mini-EUSO over $\Delta\lambda$;
- $E_\gamma = 5.45 \cdot 10^{-12}$ erg is the nominal energy of a photon at $\lambda = 365$ nm.

---

[4] The actual 3D orientation of the ISS along its orbit is given by the values of the roll, pitch and yaw angles. In particular, a non-zero value of the yaw angle results in the ISS vector not exactly aligned along the y axis. However, the magnitude of this effect is below the precision level of the speed measurement of meteors from Mini-EUSO, and we will assume that V_{ISS} is totally along the apparent y direction on the PDM.

[5] https://www.astronomy.ohio-state.edu/martini.10/usefuldata.html

Therefore, the absolute magnitude $\mathcal{M}(t)$ of the meteor is computed according to the following:

$$\mathcal{M}(t) = -2.5\log_{10}\left[\frac{\sum_i \overline{C}_i(t)}{F_0}\right] - 5\log_{10}\left[\frac{\sqrt{x_b(t)^2 + y_b(t)^2 + (H_{ISS} - H_0)^2}}{100 \text{ km}}\right] , \tag{6.9}$$

where x_b and y_b are the barycentre positions from the centre of the FoV measured in km (Fig. 6.8b,c). To give a measure of the overall intensity of the meteor, we consider the minimum absolute magnitude over the duration of the event:

$$\mathcal{M} = \min_{t\in\Delta t}\{\mathcal{M}(t)\} . \tag{6.10}$$

For the example of Figs. 6.7 and 6.8, the resulting minimum absolute magnitude is $\mathcal{M} = +2.67$.

6.2.2 Statistics of meteor's physical parameters

From the analysis procedure described in the previous sections, we can deduce four physical parameters of meteors observed by Mini-EUSO, which are: (1) the horizontal speed V, (2) the duration Δt, (3) the azimuth angle a and (4) the minimum absolute magnitude $\mathcal{M}$. Figure 6.9 shows the distribution of these parameters on the whole dataset of 24k meteors (see Tab. 6.1), and Fig. 6.10 shows the same distributions but divided for the two classes of M (undoubted meteors, 12.5k events) and M? events (meteor candidates, 11.5k events, see Sect. 6.1.1). Of course, we are not able to see the typical bimodal distribution of the meteor's speed in panel a, since we are missing a measure of the z component of the vector. For the same reason, the distribution of V goes also below the lower limit of 11.1 km/s, with a maximum in correspondence of this value. At the other end of the distribution, we did not record any meteor with a speed significantly higher than the maximum value of 72.8 km/s (see Sect. 2.5.1). Only three events are geometrically above this limit, but all of them are provided with a high error on V (85 $\pm$ 15, 87 $\pm$ 33 and 98 $\pm$ 21 km/s). Also, the distributions for meteors and meteor candidates (Fig. 6.10a) highlight that M events are typically faster (mode value at $\sim$20 km/s) compared to M? ($\sim$10 km/s). This is compatible with the classification scheme presented in Sect. 6.1.1, since M events correspond to a more evident motion on the PDM which will result in a higher horizontal speed value.

The distribution of the duration Δt is not very informative. The modal value is $\sim$0.5 s, corresponding to about 12 GTUs, and the maximum duration of a meteor is 2.25 s (55 GTUs). Similarly to what was already outlined for the V distribution, Fig. 6.10b shows that M? have usually a shorter duration compared to M events. On the contrary, the distribution of the azimuth angle looks quite interesting. Four evident peaks are visible at $a = 35°$, $145°$, $215°$ and $325°$ of azimuth angle. At first

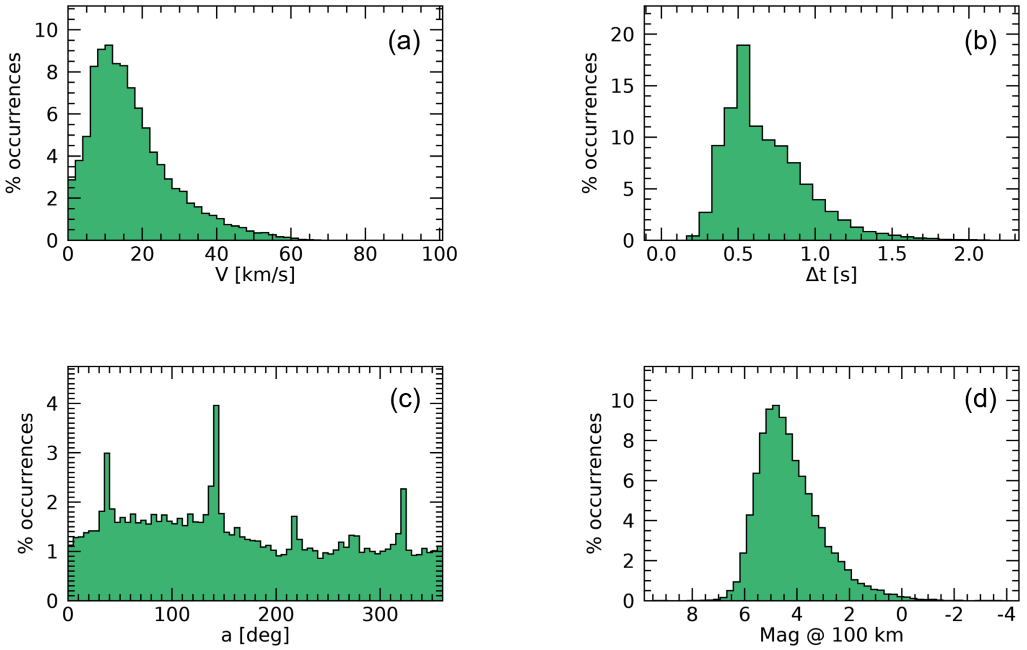

Fig. 6.9: Distribution of the physical parameters of 24k meteors detected by Mini-EUSO during the data-taking sessions n. 05-44 (see Tab. 6.1). (a) Horizontal speed V (Eq. 6.6) at a 100 km reference altitude; (b) duration Δt of the event on the Mini-EUSO PDM. (c) arrival azimuth angle a (Eq. 6.7), and (d) minimum absolute magnitude $\mathcal{M}$ (Eq. 6.10).

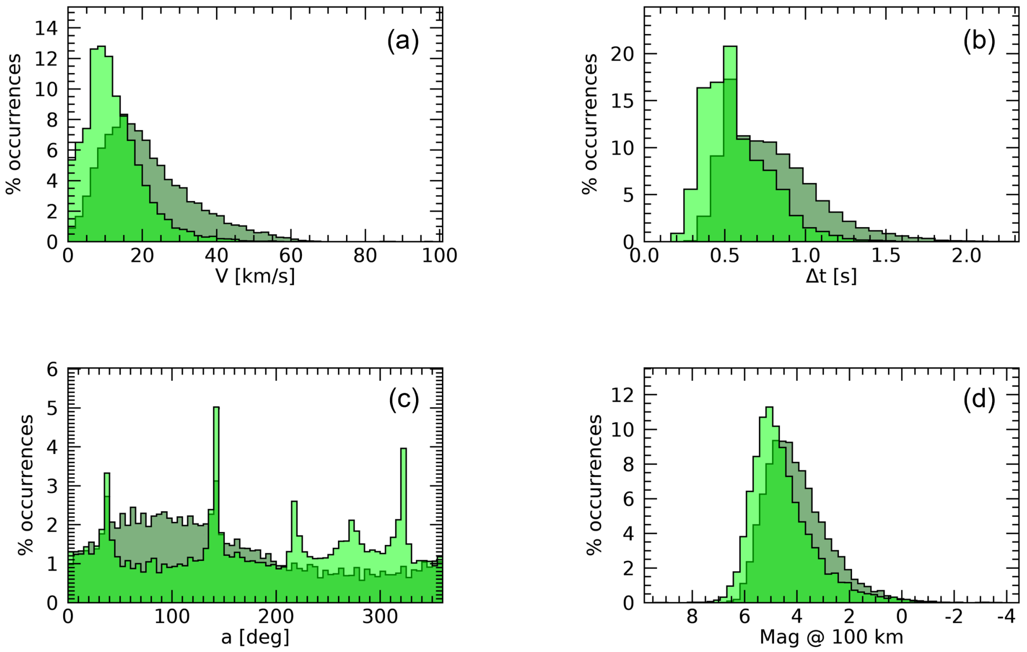

Fig. 6.10: The same distributions of Fig. 6.9 but separated for M (undoubted meteors, 12.5k events - dark green histogram) and M? (meteor candidates, 11.5k events - light green). From these plots, it is evident that meteor candidates are characterized by a typically lower speed and duration, and a higher magnitude.

sight, one may think that these features could be due to the detection of meteor showers during the data acquisition of Mini-EUSO. However, we concluded that these peaks are due to an instrumental effect. A clue for this is evident from Fig. 6.10c, which plots the two distributions of a for the subsets of M (dark green) and M? (light green). It is evident that these peaks mostly originate from M? events. As detailed in Sect. 6.1.1, these are events displaying the typical features of a meteor but have, in most cases, a limited apparent motion on the PDM confined within just a few pixels. By inspecting Eq. 6.7 we can see that $a = a_{ISS} + a_{app}$, where a_{app} is the apparent azimuth angle of the meteor on the PDM. Due to the motion of the ISS along the y direction, this will result in a "preference" for $a_{app} = 0^\circ$ $(+y)$ and 180° $(+y)$ for M? events. Furthermore, due to the orbital configuration of the ISS with respect to the ground, the distribution of a_{ISS} presents two prominent peaks at 215° and 325° (see Fig. 6.15). Then, it is clear that the a values in correspondence with the four peaks of Fig. 6.10 arise from the combination of $a_{ISS} = 215^\circ, 325^\circ$ and $a_{app} = 0^\circ, 180^\circ$. Therefore, the reconstruction of the azimuth direction for M? events is not really reliable because of this bias, which is beyond what is discussed in Sect. 6.2.3. On the other hand, the azimuth distribution for M events shows the expected maximum for $a = 90^\circ$, arising from the effect of the Earth's rotation.

Finally, Fig. 6.9 plots the distribution of the absolute magnitude of meteors detected by Mini-EUSO. No events are detected above $\mathcal{M} \gtrsim +7$, which can be regarded as the limiting magnitude for the observations of meteors by Mini-EUSO. Such a faint magnitude corresponds to a signal of the meteor of ~0.04 cnts/GTU above the background level. This is consistent with the requirement of $R_{px} > 5.5$ of Eq. 6.2 for the meteor trigger, taking into account the typical background level of ~1 cnts/GTU that corresponds to a standard deviation of the background level fluctuations (see Sect. 6.2.3) of $\sigma \sim 0.008$ cnts/GTU ($5.5\sigma \sim 0.043$ cnts/GTU). The opposite end of the distribution is limited to $\mathcal{M} \lesssim -2.5$, that is a flux of about 165 cnts/GTU and for which we can expect the instrument to trigger the Cat2 protection mode. The distributions of $\mathcal{M}$ for M and M? events (Fig. 6.10d) are again compatible with the classification scheme and outline that M? are typically fainter (with a mode value of +5) with respect to M events (+4).

6.2.3 Uncertainty analysis

Let us discuss here the uncertainties affecting the physical parameters of meteors computed from the observations of Mini-EUSO. For the measure of the horizontal speed, the nominal error on V_x and V_y in Eq. 6.6 comes from the linear fit, implementing the solution of a χ^2 minimization problem over the barycentre positions x_b

and y_b. This will depend upon the uncertainties assigned to x_b. Referring to Eq. 6.5, the nominal variance of x_b can be given as:

$$\sigma_{xb}^2 = \frac{\sum_i \left[\sigma_{Ci}(x_i - x_b)\right]^2}{\left(\sum_i \overline{C}_i\right)^2} , \tag{6.11}$$

In doing so, we assume that the counts C_i on each GTU and each pixel follow a Poissonian statistics. Considering that the counts on D3 are normalized to the D1 acquisition time ($\Delta t_{D3} = 128^2 \Delta t_{D1}$), the standard error on C in D3 data can be computed as:

$$\sigma_{C(D3)} = \frac{\sqrt{C(D1)}}{128^2} = \frac{\sqrt{C(D3)}}{128} . \tag{6.12}$$

In its actual implementation, Eq. 6.12 is further complicated by two factors. Pixels of the Mini-EUSO PDM receiving the same amount of light will not display the same value of counts because they do not have exactly the same quantum efficiency. Prior to the analysis, the D3 data are then processed to account for the differential gain of each pixel. This process is known as *flat-fielding* and the details about this correction are given in Casolino et al. (2023). In summary, the counts C_{xy} of each pixel are normalized to a *superflat* matrix S_{xy} computed for each orbit of the ISS when Mini-EUSO takes data, enclosing the response of each pixel to an unitary flux:

$$C_{xy} \to \frac{C_{xy}}{S_{xy}} . \tag{6.13}$$

An example of the effect of this normalization is shown in Fig. 6.11a. Also, panel b of this figure presents the non-linearity of the response of the PDM, due to the readout time (deadtime) of $\tau = 5$ ns of each Spaciroc-3 ASICs. This effect consists in the detector *pile-up* effect, that is, only one photon is counted if two or more arrive at the PDM within a time interval of τ due to a limited double-pulse resolution. In the case of a Poissonian statistic, the number of counts registered by the telescope n scales as a function of the actual number of photoelectrons n_{pe} as:

$$n = n_{pe} \exp\left\{-\frac{\tau}{\Delta t_{D1}} n_{pe}\right\} . \tag{6.14}$$

The maximum n is ~180/GTU which corresponds to $n_{pe} \simeq 500$ pe/GTU produced by the PMT cathode. Defining the pile-up factor $p = \Delta t_{D1}/\tau$, the inverse of Eq. 6.14 can be used to deduce the actual number of photoeletrons at the PDM:

$$n_{pe} = -pW\left(-\frac{n}{p}\right) , \tag{6.15}$$

using the Lambert W function. Eq. 6.15 is valid for $n \leq 180$ cnts/GTU and assumes the first branch of the W function, while a much higher value of n_{pe} is theoretically possible when considering the second branch of W (Fig. 6.11d). While this indeterminacy may look problematic, we must notice that such a high value of

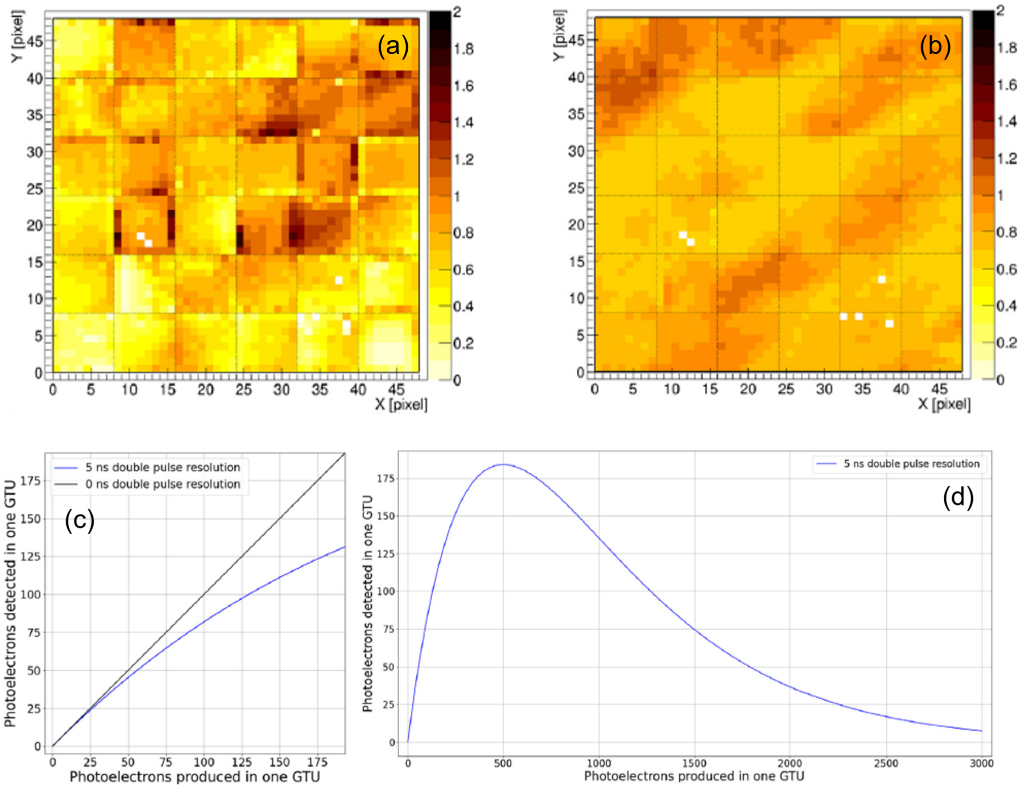

Fig. 6.11: Pre-processing corrections of Mini-EUSO D3 data. Top: An example of the results of the flat-fielding procedure, before (a) and after (b) the correction of Eq. 6.13. In panel b, details like the slightly more luminous bands produced by the clouds are visible. Bottom: pile-up correction on D1 data, that is, the number of detected photoelectrons n as a function of the photoelectrons n_{pe} produced in one GTU (2.5 μs). (c) The effect of non-linearity due to the effect of the double-pulse resolution ($tau = 5$ ns); (d) plot of Eq. 6.14 on the full range, showing the value of the maximum $n \sim 180$ cnts/GTU separating the two branches of Eq. 6.15 (Casolino et al., 2023).

counts on the PDM will trigger the Cat2 protection mode of the instrument (see Sect. 3.4.1), altering the detector response. For the meteor analysis, we always exclude Cat2 data since they will correspond to a drastically lower detector efficiency η, significantly affecting the zero-point flux value (see Sect. 6.2.1). We can therefore correct the counts C_{xy} for the pile-up factor P_{xy}:

$$C_{xy} \to \frac{C_{xy}}{P_{xy}} \quad , \quad P_{xy} = -\frac{C_{xy}}{pW\left(-\frac{C_{xy}}{p}\right)} \, . \tag{6.16}$$

Equation 6.16 is strictly valid on D1 data, whereas to apply it to D3 data we have to make the further assumption that the average light detected is uniformly spread on the D1 frames which compose the corresponding D3 frame. Both corrections of Eq. 6.13 and 6.16 are applied to D3 counts C_{xy} during the pre-processing of the data

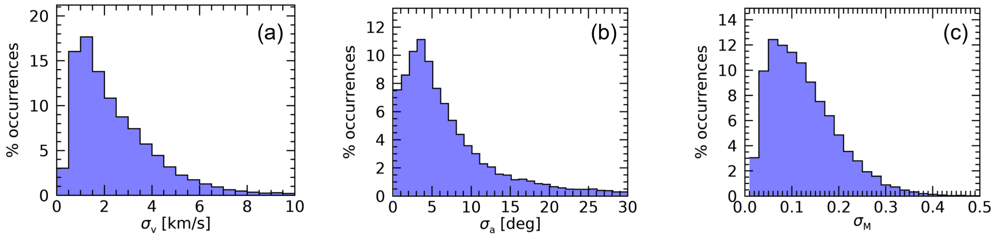

Fig. 6.12: Distribution of nominal uncertainties on the reconstruction of (a) the horizontal speed V, (b) the arrival direction azimuth a and (c) the absolute magnitude $\mathcal{M}$ for the whole dataset of meteors observed by Mini-EUSO in sessions n. 05-44.

(before the meteor analysis), and the standard error for D3 counts of Eq. 6.12 is therefore modified accordingly:

$$\sigma_C = \frac{1}{128}\sqrt{\frac{C_{xy}}{S_{xy}P_{xy}}} \, . \tag{6.17}$$

This equation is then used to compute the nominal error σ_{Ci} on the measured lightcurve (presented as the error bars of Fig. 6.7c,e) and to estimate standard errors σ_x and σ_y on the barycentre positions from Eq. 6.11 (error bars of Fig. 6.8b,c). Finally, these are fed to the fitting procedure to estimate $V_x \pm \sigma_{Vx}$ and $V_y \pm \sigma_{Vy}$, and the nominal confidence interval $V \pm \sigma_V$ from Eq. 6.6. For the example event of Fig. 6.7 and 6.8, the result is $V = 54 \pm 2$ km/s. The same reasoning is valid for the measure of the meteor's azimuth direction (Eq. 6.7) and absolute magnitude (Eq. 6.10), resulting respectively in $a = 54 \pm 1^\circ$ and $\mathcal{M} = 2.66 \pm 0.05$ for this event. The distributions of the reconstructed nominal uncertainties on V, a and $\mathcal{M}$ for the whole dataset of meteors observed by Mini-EUSO are reported in Fig. 6.12. The speed is determined with a typical precision of $\sigma_V = 1.5$ km/s, the arrival direction with $\sigma_a = 5^\circ$ and the absolute magnitude with $\sigma_\mathcal{M} = 0.1$.

That being said, the nominal uncertainty σ_V is not really representative of the actual indetermination of the horizontal speed of the meteor measured by Mini-EUSO. As already mentioned, this is because the projection of x_b and y_b from pixels to km units depends on the altitude of the meteor, which is unknown. This is of course a systematic error because we always assume $H = H_0 = 100$ km but each meteor will have a different beginning altitude H_{beg}. An example of the expected distribution of H_{beg} is shown by Fig. 6.13 for the EDMOND[6] database of meteors' observations (Kornoš et al., 2014). The green histogram represents the distribution measured on a dataset of ~320k meteors with a magnitude mostly within $[-2, 4]$ in the visual wavelength range. The mean of this distribution is indeed 100 km (the assumed nominal value for our analysis) with a standard deviation of 10 km. This distribution is far from being normal, as evident from the solid black line plotted

---

[6] European viDeo Meteor Observation Network (`https://www.meteornews.net/edmond/edmond/edmond-database/`)

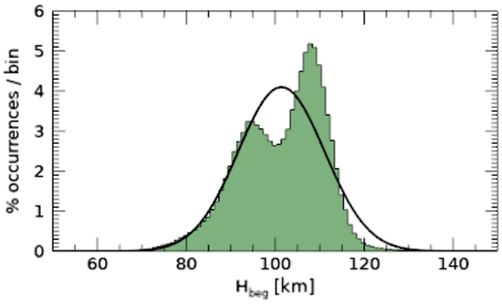

Fig. 6.13: Distribution of the beginning altitude H_{beg} for ~320k meteors in the EDMOND database (Kornoš et al., 2014), plotted as the green histograms. The solid black line plots a gaussian distribution with $\mu = 100$ km and $\sigma = 10$ km, as deduced from the mean and standard deviations of H_{beg}.

over the histogram of Fig. 6.13. However, we use $\Delta H_0 = 10$ km as a measure of the uncertainty on H_0, since the 3σ interval of $[70, 130]$ km represents the extrema of the distribution and is indeed the typical altitude range of meteors. Then, this systematic is converted into a second equivalent random error Δ_V that affects the measure of V as follows:

$$\Delta_V = \frac{\Delta H_0}{H_{ISS} - H_0} V \simeq 0.03V \ . \tag{6.18}$$

Each measure of the horizontal speed is therefore expressed in terms of $V \pm \sigma_V \pm \Delta_V$. At the 3σ confidence level, the indetermination on H introduces a relative uncertainty on V of ~10%, that is summed over the nominal error σ_V. To provide a final estimation of the confidence interval from σ_V and Δ_V, we have to consider the sum (and not the square sum) of these two contributions. This is because they are not independent but, on the contrary, they are exactly correlated (σ_V linearly scales with the altitude, that is with ΔH_0). For the example event of Fig. 6.7, the final result is $V = 54 \pm 4$ km/s.

The apparent azimuth direction is not affected by a systematic on the meteor altitude, since a factor of ΔH_0 on Eq. 6.7 applies to both V_x and V_y and get simplified, that is, a virtual contraction or expansion of the FoV due to ΔH_0 does not modify the measured direction of the event. On the contrary, a systematic on H affects the measure of the absolute magnitude in Eq. 6.10, requiring to add a second contribution to its nominal error as:

$$\Delta_{\mathcal{M}} = 5 \log_{10} e \frac{\Delta H_0}{H_{ISS} - H_0} \simeq 0.07 \ . \tag{6.19}$$

At the 3σ confidence level, the indetermination on H introduces an uncertainty on $\mathcal{M}$ of ~0.2 mag. For the example event of Fig. 6.7, this results in a final value of $\mathcal{M} = 2.66 \pm 0.12$.

Finally, the meteor should be travelling towards the ground through the atmosphere within the duration of the event. Apart from the deceleration due to atmospheric drag, we should also notice an apparent deceleration of the event seen on the PDM of Mini-EUSO due to the meteor's travelling away from the detector, at lower altitudes. However, we never detected a significant deceleration in the computed positions (x_b, y_b) of meteors in Mini-EUSO data, probably because the spatial resolution of the detector is not enough to record such a small variation of the speed. This evidence justifies the choice of applying a linear fit to (x_b, y_b) to deduce the speed components (V_x, V_y), which would be not appropriate otherwise. Then, it is worth noticing that we cannot compute the pre-atmospheric speed V_∞, and V will be always an underestimation of it since we do not correct for the deceleration due to atmospheric drag.

6.3 Simulation of the trigger efficiency

The distribution of the absolute magnitude of meteors detected by Mini-EUSO (Fig. 6.9d) outlines the presence of a certain degree of trigger inefficiency for higher magnitudes. From a theoretical point of view, we would indeed not expect a decrease in the flux of meteors with increasing magnitude, which is finally related to the mass of the meteoroid, but rather a constant power-law increase similar to the size-frequency distribution (SFD) of minor bodies in the Solar System (see Sect. 2.1.2 and Fig. 2.3). On the other hand, we already highlighted the presence of a selection bias introduced to filter false positives during the post-processing of the trigger results (see Sect. 6.1.1), together with the intrinsic inefficiency of the trigger itself. The distribution of the number of meteors n as a function of the minimum absolute magnitude $\mathcal{M}$ is usually given as (Hawkins and Upton, 1958):

$$\mathrm{d}n = n_0 r^{\mathcal{M}} \mathrm{d}\mathcal{M} \ , \tag{6.20}$$

where r is the *population index* and represents the slope of the distribution and a is a scaling parameter related to the absolute flux of meteors at 0 magnitude. Referring to the cumulative number of meteors $N = n(< \mathcal{M})$, *i.e.*, the cSFD, we get a usual power-law function in the form of:

$$\log_{10} N = \log_{10} N_0 + \mathcal{M} \log_{10} r \ , \tag{6.21}$$

where $N_0 = n(\mathcal{M} < 0)$. To provide an unbiased measure of the absolute flux of meteors in our magnitude range, we therefore need to estimate the trigger efficiency ϵ, which will be a function of (1) the meteor's magnitude $\mathcal{M}$ and (2) the illumination background level b. This information is usually enclosed in the *exposure* of the instrument, that is:

$$X(\mathcal{M}, b) = \epsilon(\mathcal{M}, b) T_{obs} A_{obs} \ , \tag{6.22}$$

being T_{obs} the total observing time (from Tab. 6.1) and A_{obs} the observed area. The last term of Eq. 6.22 can be easily given by the area of the atmosphere at 100 km altitude observed by Mini-EUSO in one frame, that is $A_{obs} \simeq 6.25 \cdot 10^4$ km^2 (250 km × 250 km). The term $T_{eff}(\mathcal{M}, b) = \epsilon(\mathcal{M}, b)T_{obs}$ instead represents the effective (or active) observation time of the instrument. The exposure can be therefore written as the following:

$$X(\mathcal{M}, b) = T_{eff}(\mathcal{M}, b)A_{obs} \ . \tag{6.23}$$

To estimate the trigger efficiency $\epsilon(\mathcal{M}, b)$ for Mini-EUSO, we designed a dedicated simulation toolkit and discuss here the main steps involved in this processing. The first step is the definition of the meteor's dynamic to be observed in the FoV of Mini-EUSO. To do so, we use the approach of Gritsevich and Koschny (2011) which provides an analytical formulation of the speed and magnitude of a meteor as a function of a set of physical parameters, as discussed in Sect. 4.2.4. We are therefore interested to simulate an ensemble of events representing the whole population of meteors potentially observable by Mini-EUSO. This requires the definition of a distribution for all the parameters enclosed in the dynamical model.

Geometrical parameters

These are the preatmospheric speed V_∞, the azimuth angle a and the inclination γ with respect to the ground. To define the distribution of these quantities, we analyzed four big databases of meteor's observations, which are: EDMOND (Kornoš et al., 2014), SonotaCo[7] (SonotaCo, 2009), GMN[8] (Vida et al., 2022) and CAMS[9] (Jenniskens et al., 2018b). The distributions for the EDMOND database are plotted by the green histograms of Fig. 6.14 and can be empirically described as:

$$\begin{cases} V_\infty \propto \alpha\mathcal{N}(\mu_{V1}, \sigma_{V1}) + (1-\alpha)\mathcal{N}(\mu_{V2}, \sigma_{V2}) \\ a \propto \mathcal{N}(\mu_a, \sigma_a) \ \mathrm{mod}\ 360^\circ \\ \gamma \propto \beta\mathcal{N}(\mu_{\gamma1}, \sigma_{\gamma1}) + (1-\beta)\mathcal{N}(\mu_{\gamma2}, \sigma_{\gamma2}) \ , \end{cases} \tag{6.24}$$

where $\mathcal{N}$ is the normal distribution. For V_∞, the bimodal distribution is loosely related to the asteroidal (μ_{V1}, σ_{V1}) and cometary (μ_{V2}, σ_{V2}) components, and α represents the relative abundance of the first over the second. Also, the prominent peaks of the distributions in panels a and b of $V_\infty \sim 60$ km/s and $a \sim 50^\circ$ are due to the detection of the Perseid's shower (of which related events account for a considerable fraction of all databases) and were neglected for our case. The fitting results of Eq. 6.24 over the EDMOND database are plotted as the solid black lines of Fig. 6.14. We estimated the parameters of Eq. 6.24 for the four databases and use their weighted average to generate the meteors' ensemble. These values are:

---

[7] SonotaCo Network Simultaneously Observed Meteor Data Sets SNM2007B-SNM2020A (`http://sonotaco.jp/doc/SNM/`).

[8] Global Meteor Network (`https://globalmeteornetwork.org/`)

[9] Cameras for Allsky Meteor Surveillance (`http://cams.seti.org/`).

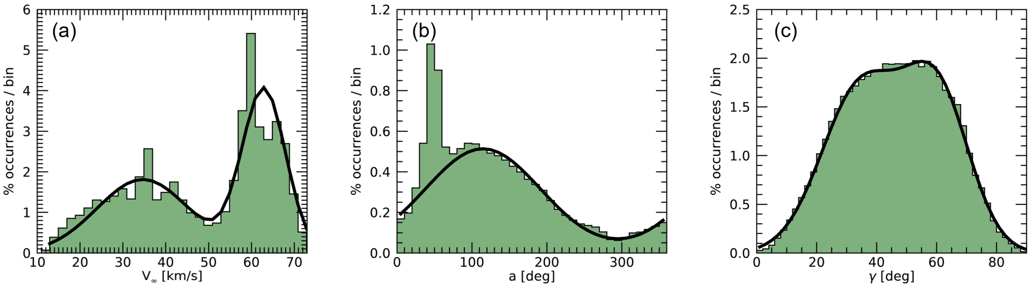

Fig. 6.14: The distributions of (a) preatmospheric speed, (b) azimuth angle and (c) inclination with respect to the ground for ~320k meteors in the EDMOND database (Kornoš et al., 2014). The solid black lines on all panels plot the empirical distribution fitted from Eq. 6.24.

$\alpha = 0.53 \pm 0.02$, $\mu_{V1} = 32.5 \pm 0.5$ km/s, $\sigma_{V1} = 10.1 \pm 0.6$ km/s, $\mu_{V2} = 62.3 \pm 0.3$ km/s, $\sigma_{V2} = 5.2 \pm 0.2$ km/s, $\mu_a = 103.4 \pm 0.6°$, $\sigma_a = 83.9 \pm 0.4°$, $\beta = 0.54 \pm 0.03$, $\mu_{\gamma 1} = 33.7 \pm 0.6°$, $\sigma_{\gamma 1} = 13.2 \pm 0.5°$, $\mu_{\gamma 2} = 59.6 \pm 0.5°$, $\sigma_{\gamma 2} = 11.4 \pm 0.2°$.

Meteoroid's parameters

These are the physical parameters of the body, namely the meteoroid's preatmospheric mass M_∞ and its bulk density ρ_m. The mass of the meteoroid is chosen accordingly to the desired absolute magnitude $\mathcal{M}$ from Eq. 4.56. Then, we link the value of the bulk density to the value of the preatmospheric speed according to the results of Moorhead et al. (2017), who estimated the distribution of ρ_m as a function of the Tisserand's parameter T_J. In particular, they deduced a bimodal distribution for $T_J \geq 2$ (1 - asteroidal) and $T_J < 2$ (2 - cometary), as:

$$\begin{cases} \log_{10} \rho_{m1} \propto \mathcal{N}(\log_{10} \rho_1, \sigma_{\rho 1}) & \text{IF } T_J \geq 2 \\ \log_{10} \rho_{m2} \propto \mathcal{N}(\log_{10} \rho_2, \sigma_{\rho 2}) & \text{IF } T_J < 2 \end{cases} \tag{6.25}$$

Then, we choose ρ_{m1} if V_∞ was generated in the asteroidal component (with a probability of α) or ρ_{m2} for the cometary one $(1 - \alpha)$. The values of the parameters of Eq. 6.25 are: $\rho_1 = 3792$ kg/m^3, $\sigma_{\rho 1} = 0.093$, $\rho_2 = 857$ kg/m^3 and $\sigma_{\rho 1} = 0.127$. We also assume a spherical preatmospheric shape of the meteoroid, as detailed in Sect. 4.2.5 for the analysis of PRISMA data.

Meteor's parameters

These parameters describe the evolution of the meteor through the atmospheric transit (deceleration and light emission) and are the ablation coefficient σ, the shape-change coefficient μ and the luminous efficiency τ. From σ and τ we adopted the approach of Bouquet et al. (2014), that is:

$$\begin{cases} \log_{10} \sigma = A_\sigma + B_\sigma \rho_m \\ \ln \tau = A_\tau + B_\tau \ln(V_\infty - V_0) + C_\tau \ln(100\sigma)\ , \end{cases} \tag{6.26}$$

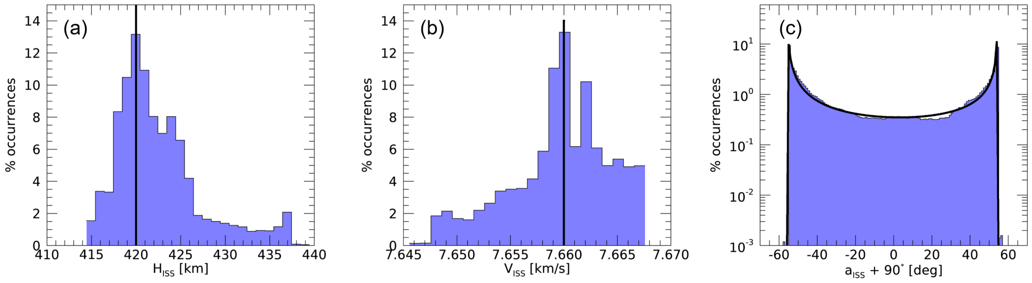

Fig. 6.15: Distributions of the parameters describing the ISS orbital motion with respect to the ground (a - altitude, b - speed module and c - azimuth with respect to the North direction) evaluated for the Mini-EUSO data sessions n. 05-44. Within the simulation, we assume $H_{ISS} = 420$ km and $V_{ISS} = 7.66$ km/s as constants, whereas a_{ISS} is randomly sorted according to a 4-parameters Beta distribution (Eq. 6.28, plotted as the thick black line of panel c).

where σ is given in $\mathrm{s}^2/\mathrm{km}^2$ units and τ in %. Eq. 6.26 relates the ablation coefficient to the density of the meteoroid and the luminous efficiency to both the preatmospheric speed and the ablation coefficient. This phenomenology reflects quite simple concepts. The expression for the ablation coefficient implies that a larger fraction of mass is ablated if ρ_m is lower, *i.e.*, if the meteoroid's material is more fragile. Similarly, a meteoroid with a fixed preatmospheric mass emits more light as its speed increases (since the kinetic energy scales with V_∞^2) and if a lower fraction of the total energy is consumed for ablating its mass (see Sect. 2.5.3). The value of τ is confined in the range $[0.001, 100]$%, and $V_0 = 10$ km/s defines the condition of $\tau(V_\infty \leq V_0) = 0$. The parameters' values for Eq. 6.26 are: $A_\sigma = -0.8 \pm 0.3$, $B_\sigma = -0.000283$, $A_\tau = -5.28 \pm 0.66$, $B_\tau = 0.87 \pm 0.26$ and $C_\tau = -1.46 \pm 0.20$. Finally, the shape change-parameter μ is uniformly sorted within $[0, 1]$ (see Sect. 4.2.4).

ISS parameters

These are the parameters of the ISS orbital motion with respect to the ground, namely the altitude H_{ISS}, the speed V_{ISS} and the azimuth angle a_{ISS} of the ISS orbit. Their distributions obtained for the metadata of the Mini-EUSO observations during sessions n. 05-44 are plotted in Fig. 6.15. Given the narrow variability range of both the altitude and speed module (panels a and b) of the ISS of this dataset, we fix $H_{ISS} = 420$ km and $V_{ISS} = 7.66$ km/s. On the other hand, the azimuth of the orbit is variable within the range $[215, 325]^\circ$, with two predominant peaks corresponding to these extrema, due to the orbital inclination of the ISS. The distribution plotted in 6.15c can be empirically described using the 4-parameters Beta distribution. Considering $\theta_{ISS} = a_{ISS} + 90^\circ$, then:

$$\theta_{ISS} \propto \frac{(\theta_{ISS} - \theta_0)^{p-1}(\theta_1 - \theta_{ISS})^{q-1}}{(\theta_1 - \theta_0)^{p+q-1}B(p,q)} \,, \tag{6.27}$$

where $B(p, q)$ is the beta function (Euler integral of the first kind). The fit of Eq. 6.28 is plotted as the thick black line on panel c. The deduced parameters of Eq. 6.28 are: $\theta_0 = -\theta_1 = -55.2 \pm 0.2°$, $p = 0.025 \pm 0.009$ and $p = 0.155 \pm 0.008$.

Finally, the atmospheric parameters Γ (drag coefficient), ρ_0 (atmospheric density at the sea level) and H_0 (scale height) are fixed to their reference value (see Sect. 4.2.5). Fixing a value for $\mathcal{M}$ (minimum absolute magnitude) and b (expressed in cnts/GTU), which are the inputs of the simulation, we evaluate the dynamic model of Eqs. 4.48 and 4.56 and obtain $[H(t), V(t), \mathcal{M}(t)]$. For the sake of clarity, $V(t)$ now represents the total module of the meteor's speed, that is including the vertical component V_z (along the altitude direction), and t can be integrated from $H(t)$ using Eq. 2.25. The simulation steps can be therefore summarized as follows:

- We compute the counts $C(t)$ recorded by Mini-EUSO from $\mathcal{M}(t)$ thanks to the inverse of Eq. 6.9.
- The beginning altitude H_{beg} of the meteor is defined according to the maximum value of $H(t)$ for which $C(t) \geq 3\sqrt{b}/128$, that is 3 times over the standard deviation of the background counts (Eq. 6.12). This also defines the starting time of the event.
- We generate the starting points (x_{beg}, y_{beg}) of the meteor track, uniformly within the extension of the Mini-EUSO FoV at $H = H_{beg}$, that is $\pm(H_{ISS} - H_{beg}) \tan 22°$ from the zenith direction in both the x and y direction. We also allow for an enlarged area equivalent to ± 1 PMT (∼41 km for $H_{beg} = 100$ km) around the nominal FoV to simulate the cases of meteors partially entering or exiting the FoV of the instrument. Starting from (x_{beg}, y_{beg}), we can now evaluate the horizontal motion of the meteor within the FoV, by numerically integrating the following differential equations (*i.e.*, the inverse of Eq. 6.7):

$$\begin{cases} \mathrm{d}x = -\left[V(t)\sin(a - a_{ISS})\cos(\gamma)\right]\mathrm{d}t \\ \mathrm{d}y = -\left[V(t)\cos(a - a_{ISS})\cos(\gamma) - V_{ISS}\right]\mathrm{d}t\ . \end{cases} \tag{6.28}$$

- To simulate the response of the PDM to the incoming light from the meteor, we implement the PSF (assumed as a 2D gaussian function with an FWHM of 1.2 px) on an oversampled spatial grid with a step of 1/20 of the Mini-EUSO pixel (∼230 m at $H = 100$ km), covering the whole FoV. With this approach, we can mask the regions of the focal plane that are not sensitive to light (the gaps between PMTs), similar to what was discussed for the photometric response of PRISMA cameras (see Sect. 4.1.7 and Fig. 4.12). An increasing portion of the PSF gets progressively masked if the meteor transits over these inactive regions, simulating the corresponding photon collection inefficiency. We can therefore project from physical units (km from the FoV centre) to instrumental units (px on the Mini-EUSO PDM) by resampling this grid, accounting for the

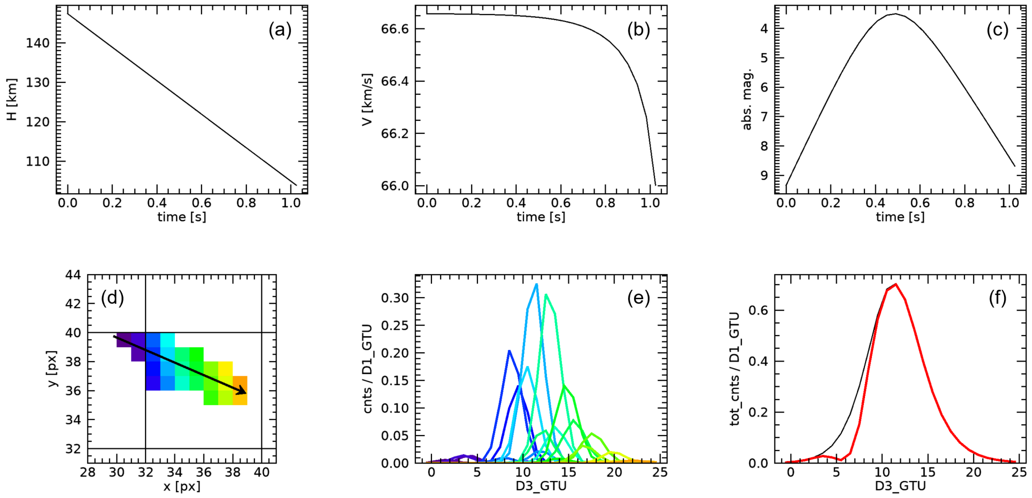

Fig. 6.16: An example of simulated meteor of minimum absolute magnitude $\mathcal{M} = +3.5$ as seen by the Mini-EUSO telescope. The meteoroid had a preatmospheric mass of $M_\infty = 0.02$ g and entered the atmosphere at $V_\infty = 66.6$ km/s with an inclination angle of $\gamma = 39.6°$. (a) Altitude from ground as a function of the time; (b) speed module; (c) absolute magnitude lightcurve, peaking at +3.5; (d) map of pixels on the PDM that were interested by the signal of the meteor; (e) single-pixel lightcurves with the colour code of panel (d); total integrated lightcurve (black curve, inverse of Eq. 6.9 from panel c) compared to the actual counts recorded on the PDM (red curve), that are lower in the first part of the event because the apparent path of the meteor crossed the corner between 4 PMTs.

optical distortion and variable footprint of each pixel (see Sect. 6.2). Also, the atmospheric transit is sampled in time at a resolution of $\Delta t_{D3}/20 \simeq 2$ ms. This approach allows reproducing the PSF elongation in the case of fast-moving meteors, when sampling back at the D3 resolution.

- We then add to the output video the illumination background level b, which is assumed as flat over the whole FoV and, finally, we generate the Poissonian noise component (Eq. 6.12).

An example of the results of this simulation is reported in Fig. 6.16 for a meteor of $\mathcal{M} = +3.5$, due to a meteoroid of $M_\infty = 0.02$ g entering the atmosphere at a speed of $V_\infty = 66.6$ km/s with an inclination angle of $\gamma = 39.6°$. Since its apparent motion on the PDM started at the corners between 4 PMTs, a significant fraction of counts was lost during the first 19 GTUs (panel f, red curve). However, the maximum value of the lightcurve of $\sim$0.7 cnts/GTU (defining the peak absolute magnitude $\mathcal{M}$) corresponded to the centre of the PMT and was correctly recorded by the instrument.

This workflow was enclosed into an IDL procedure, which takes as arguments $(\mathcal{M}, b)$. The simulation was run for 300 meteors for each $(\mathcal{M}_i, b_j)$ combination, with $\mathcal{M}_i \in [-2, +8]$ at 0.5 mag steps and $b_j \in [0.1, 100]$ cnts/GTU logarithmically sampled with 28 steps. The ensemble of simulated meteor videos was then fed to the meteor trigger algorithm. For each $(\mathcal{M}_i, b_j)$, we evaluate the efficiency $\epsilon(\mathcal{M}_i, b_j)$ as the fraction of triggered events over the total number of simulated meteors. This

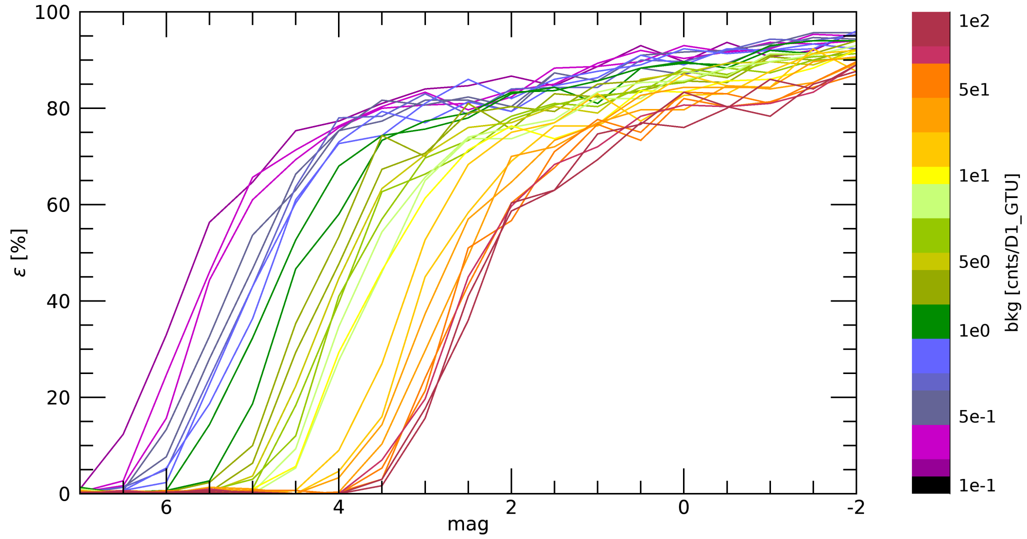

Fig. 6.17: Results of the efficiency simulations for the detection of meteors by the Mini-EUSO telescope, for the peak absolute magnitude $\mathcal{M} \in [-2, +8]$ and background level $b \in [0.1, 100]$ cnts/GTU. Each curve plots the $\epsilon(\mathcal{M})$ corresponding to a fixed value of b, given by the colour table on the right of the figure. The errors on each curve are not plotted here to ease the visualization but an example is reported in Fig. 6.18.

approach was tested against Trigger 1 (see Tab. 6.1, method detailed in Sects. 6.1 and 6.1.1) and not yet for Trigger 2. The results for Trigger 1 are reported in Fig. 6.17, which plots the $\epsilon(\mathcal{M}_i)$ curves for each b_j value. The overall phenomenology is as expected, with a transient-like drop of ϵ for increasing $\mathcal{M}$ (*i.e.*, lower counts on the PDM), while $\epsilon(\mathcal{M})$ shifts towards lower $\mathcal{M}$ as the background level b increasing. However, the trigger efficiency does not reach 100% even at the lowest magnitude and is confined within 85–95% at $\mathcal{M} = -2$. That is, a $\sim$10% of the meteors are not detected even at the bright end of the magnitude distribution. We found that the efficiency curve $\epsilon(\mathcal{M})$ can be appropriately modelled with a *generalized logistic function*, in the form of:

$$\epsilon(\mathcal{M}) = \epsilon_M + \frac{\epsilon_m - \epsilon_M}{\left[1 + (2^\nu - 1)e^{-B(\mathcal{M}-\mathcal{M}_0)}\right]^{1/\nu}} \,, \tag{6.29}$$

where ϵ_m and ϵ_M are respectively the lower (left) and upper (right) horizontal asymptotes, $\mathcal{M}_0$ is defined as $\epsilon(\mathcal{M}_0) = (\epsilon_M - \epsilon_m)/2$, B if the efficiency growth rate and ν is related to the asymmetry of the curve near the two asymptotes. An example of the fit result of Eq. 6.29 on the simulated efficiency curve $\epsilon(\mathcal{M}_i)$ for $b_j = 2$ cnts/GTU is presented in Fig. 6.18a. Varying b_j, we found approximately constant values for the parameters $\epsilon_m = 0.0 \pm 0.2\%$, $B = 7 \pm 1$ and $\nu = 9 \pm 2$. On the

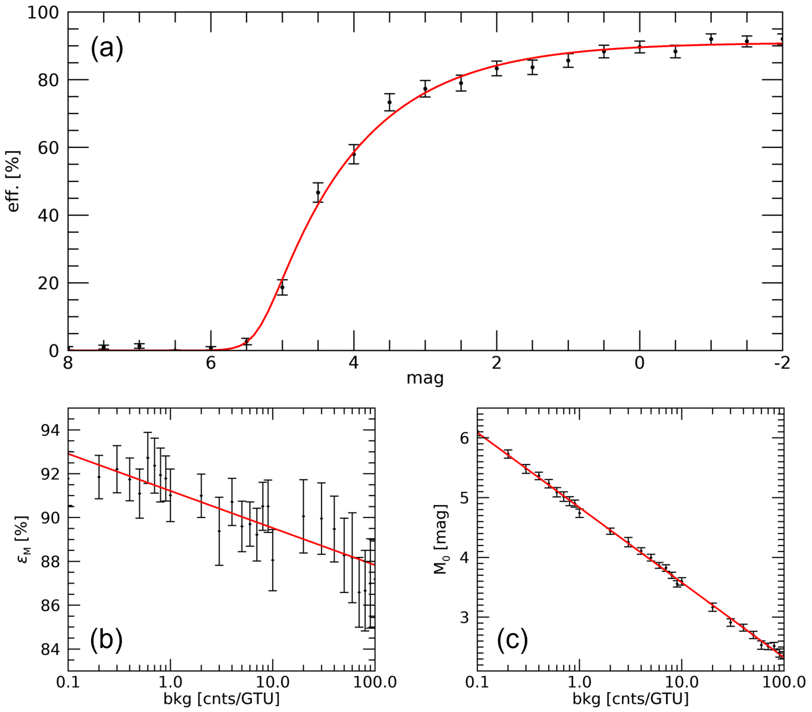

Fig. 6.18: Analytical description of the efficiency $\epsilon(\mathcal{M}, b)$ of Mini-EUSO by a generalized logistic function. (a) Results of the fit of Eq. 6.29 to the data of $\epsilon(\mathcal{M})$ for a background level $b = 2$ cnts/GTU; (b) variation of the maximum efficiency ϵ_M as a function of b as deduced from the fitting procedure, and parametrized with Eq. 6.30 (red line); (c) same as panel b but for the parameter $\mathcal{M}_0$.

contrary, both ϵ_M and $\mathcal{M}_0$ vary as a function of the background value (Fig. 6.18b,c) and can be modelled as:

$$\begin{cases} \epsilon_M(b) = A_\epsilon + B_\epsilon \log_{10} b \\ \mathcal{M}_0(b) = A_\mathcal{M} + B_\mathcal{M} \log_{10} b \, , \end{cases} \tag{6.30}$$

where we determined $A_\epsilon = 91.2 \pm 0.8$ %, $B_\epsilon = -1.7 \pm 0.9$ %, $A_\mathcal{M} = 4.83 \pm 0.05$ and $B_\mathcal{M} = -1.26 \pm 0.05$.

6.4 Meteor's flux estimated by Mini-EUSO

Thanks to the simulations described in the previous section, we deduced a fully analytical formulation for the trigger efficiency of Mini-EUSO $\epsilon(\mathcal{M}, b)$ as a function of the minimum absolute magnitude of the meteor and the background level on the PDM. We then need to compute the exposure from Eq. 6.22 over the whole period of observation of sessions n. 05-44 (see Tab. 6.1). However, even if we consider one D3 frame (40.96 ms) at a time, it is not reasonable to assume that the background level is constant over the whole FoV of Mini-EUSO, since it covers an area projected on the ground of about 330 km × 330 km. We therefore consider the pixel-wise average of the measured counts C_{xy} over $\delta t = 25$ consecutive GTUs:

$$b_{xy}(t_i) = \frac{1}{\delta t} \sum_{t=\delta t(t_i)}^{\delta t(t_i+1)} C_{xy}(t) \ . \tag{6.31}$$

This time interval of ∼1 s is larger than the expected maximum duration of the signal of a meteor over one pixel (20 GTU), allowing to average the contribution of fast transient signals (like meteors), and, at the same time, corresponds to an apparent motion of fixed ground sources confined to the approximate pixel dimension. Considering that the observations are organized in data files of 3200 GTUs (∼131.1 s), the time index varies in the range $t_i \in [0, 127]$ for each file. From this approach, we can then compute the exposure for each δt as the average of $\epsilon(\mathcal{M}, b_{xy})$ on the PDM. In doing so, we still have to consider that the flat-field normalization affects the amplitude of the background fluctuations according to the superflat matrix S_{xy} (see Sect. 6.2.3, Eq. 6.17), that is computed along the data of each ISS orbit and is therefore constant over one data file[10]. This effect was not yet taken into account, since it was assumed a purely Poissonian statistic (Eq. 6.12) within the simulation[11]. Finally, the portion of the PDM that is in the Cat2 protection mode does not contribute to the total exposure of Mini-EUSO, since the gain of the detector is drastically decreased in this condition and we excluded these data from the trigger processing. Then, we need to include only pixels in Cat3 (the normal operating mode) within the exposure computation. To account for this, we scan the pixels within each EC on the PDM and check for the condition $C_{xy} < 10^{-3}$ cnts/GTU over each D3 frame. If more than 15 pixels are characterized by such a low count value, we consider that the corresponding EC is in Cat2 mode for that time interval at that GTU. For each t_i, we then define a matrix $\Omega_{xy}(t_i)$ that encloses the fraction of GTUs for which each pixel (x, y) was found in Cat3 (with respect to the total, that is 25 GTUs). Therefore, the exposure of Mini-EUSO for one data file as a function of the absolute magnitude can be given as:

$$X(\mathcal{M}) = A_{px} \delta t \sum_{t_i=0}^{127} \sum_{x,y}^{\mathrm{PDM}} \Omega_{xy}(t_i) \epsilon \left[\mathcal{M}, \frac{b_{xy}(t_i)}{S_{xy}} \right] \ , \tag{6.32}$$

where $A_{px} = A/48^2$ is the equivalent area of one pixel and accounts for the sum over (x, y) on the PDM, instead of the average. Here, we are implicitly neglecting

---

[10] We neglected here the secondary effect due to the double-pulse resolution (Eq. 6.16).

[11] It is interesting to notice that a second approach is possible to deduce a different version of Eq. 6.32. If we consider the non flat-fielded version of b_{xy}, these counts fluctuate around the mean value according to Eq. 6.12. On the other hand, the signal of a meteor will be enhanced or reduced according to the value of S_{xy} Then, the efficiency term of Eq. 6.32 might be replaced by $\epsilon[\mathcal{M} - 2.5 \log_{10} S_{xy}, b_{xy}(t_i)]$. It is then easily provable that, if one neglects the slight dependence of ϵ_M from b (Eq. 6.30), the analytical expression of Eq. 6.29 has the following symmetry: $\epsilon(\mathcal{M} - 2.5 \log_{10} S, b) = \epsilon(\mathcal{M}, b/S^2)$. Even if we consider that $\epsilon_M = \epsilon_M(b)$, these two formulations return the same total exposure within a negligible difference.

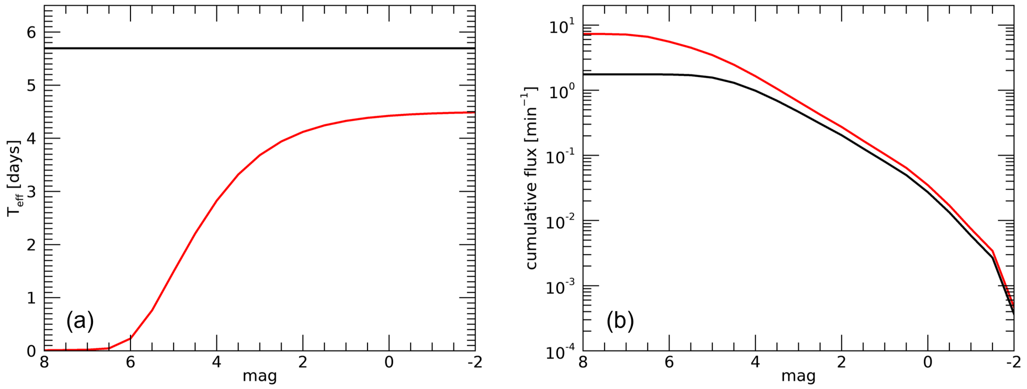

Fig. 6.19: Results of the exposure computation for the meteor's observations of Mini-EUSO of sessions n.05-44. (a) Total effective measurement time T_{eff} (red line) as a function of the peak absolute magnitude of the meteor obtained from Eq. 6.32 (apart from the A factor). As a comparison, the total observing time $T_{obs} = 5.69$ days is given by the black horizontal line. (b) Cumulative flux from Eq. 6.33 considering the bias correction provided by T_{eff} (red curve) against the nominal time T_{obs} (black curve).

that each pixel has a slightly different footprint area at $H = 100$ km and therefore would weigh differently in the term $\sum_{x,y}$ of Eq. 6.32.

Figure 6.19a plots the effective measurement time (that is the exposure apart from the A factor, Eq. 6.23) for the total observing period of sessions n.05-44 (red line), with respect to the nominal observing time of $T_{obs} \simeq 5.69$ days (black horizontal line, see Tab. 6.1). Even at the brightest magnitude, the effective time is only ~79% of T_{obs}. This is due to both a significant fraction of Cat2 acquisition time and to the fact that the maximum efficiency ϵ_M is not 100% (Fig. 6.18). We can then estimate the flux (given as meteors per minute, panel b) as the cumulative distribution $N(\mathcal{M})$ computed from the magnitude histogram $n(M)$ of Fig. 6.9d dividing each bin for $T_{eff}(\mathcal{M})$, that is:

$$N(M) = \sum_{\mathcal{M}_i=-2}^{\mathcal{M}} \frac{n(\mathcal{M}_i)}{T_{eff}(\mathcal{M}_i)} \; . \tag{6.33}$$

In doing so, we select the events detected by Trigger 1, which are ~14.4k (60% of the 24k total events). By repeating the same processing also for Trigger 2, it will be possible to compute the meteor's flux accounting for the total Mini-EUSO database. The red curve of Fig. 6.19 plots the result of Eq. 6.33, and the black curve is the corresponding flux if considering $T_{eff}(\mathcal{M}) = T_{obs}$, given as a reference to visualize the importance of the efficiency correction. We notice that $N(M)$ reaches a steady value for $\mathcal{M} \geq +6.5$, which may indicate an overestimation of the trigger efficiency at this level. However, only 90 events are detected in this magnitude range (that is only ~0.6% of the database), corresponding to a very small effective measurement time of $T_{eff} \simeq 1.1$ hours. Because of this, we consider only $\mathcal{M} \leq +6$ to provide a significant measure of the meteors' flux[12]. Considering that we analyzed here only half of the total data acquired by Mini-EUSO (which performed 81 sessions until early 2023), an increased statistics above this magnitude will allow estimating the flux above this limit.

We finally compared our results with available meteors' flux estimations in literature. The major problem in this comparison is that the measure of flux is usually given as a function of the meteoroid's preatmospheric mass rather than the absolute magnitude. To this purpose, we used the tabulated values of Tab. 3.1 (Robertson and Ayers, 1968). These values must be only regarded as a qualitative indication (since they account for the peak magnitude and not the integral lightcurve) and correspond to an analytical conversion in the form of:

$$\log_{10} M_\infty = -2.985 - 0.4\mathcal{M} \; . \tag{6.34}$$

Also, Verniani (1973) proposed a similar conversion as:

$$\log_{10} M_\infty = 11.09 - 0.4\mathcal{M} - 10\log_{10} V_\infty \; , \tag{6.35}$$

where V_∞ is given in km/s units and M_∞ in kg. Eq. 6.35 corresponds to 6.34 if assuming an average meteoroid's speed of $V_\infty \simeq 26$ km/s. Therefore, Figure 6.20 plots the derived cumulative flux density computed from the Mini-EUSO meteors' observations as a function of the meteoroid's mass using Eq. 6.34. Our result (red squares) is in close agreement in the range $M_\infty \in [10^{-5}, 10^{-1}]$ kg with the flux estimation provided by Grun et al. (1985), deduced from the study of micro-craters on returned lunar samples (black dashed line). The series of brown, green and blue dots are three flux estimations by Koschny et al. (2017), who estimated the cumulative flux density based on a dataset of ~20k double-station observations of meteors over a period of about 3.5 years with the Canary Island Long-Baseline Observatory (CILBO). Similarly to our case at $M_\infty < 10^{-5}$ kg, all these three series present a decreasing slope at their lower end of the distribution. This may be due to a residual overestimation of the exposure of the instrument for the population of these faint events. For the case of Mini-EUSO, we are currently testing an alternative approach for the exposure computation, directly implementing the simulated meteors over observed D3 data from all the considered sessions. This work requires a remarkable computational effort, since we are dealing with a set of ~5.7 days of observations sampled at 40.96 ms resolution. On the other hand, it represents a more general solution to the problem and does not require any further assumptions on the response of the detector, the counting statistics and the flat normalization. Preliminary results of the comparison of $X(\mathcal{M})$ from these two approaches, carried out on few data files from session n. 08, pointed out a general agreement within ~10 % relative accuracy. However, a more significant

---

[12] We also exclude the point at $\mathcal{M} = -2$ since it corresponds to 3 events only.

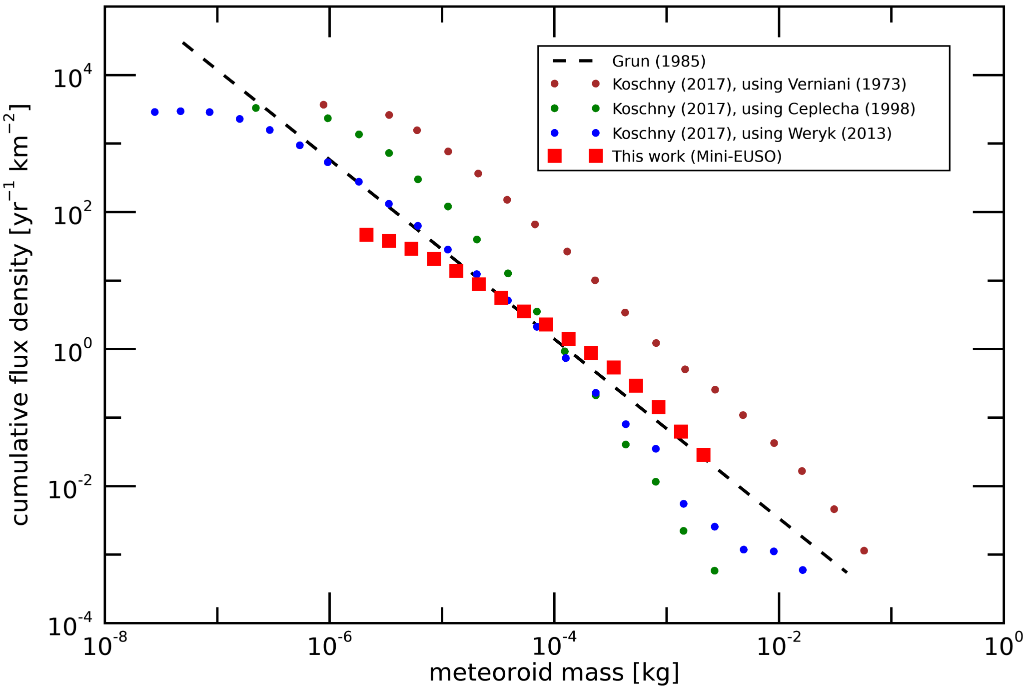

Fig. 6.20: Cumulative flux density of meteors as a function of the preatmospheric mass of the meteoroid estimated from the observations of Mini-EUSO of sessions n. 05-44 (red squares) and using Eq. 6.34 for the conversion of the peak absolute magnitude to the preatmospheric mass of the meteoroid. As a comparison, the black dashed line plots the flux estimated from Grun et al. (1985), deduced from the study of micro-craters on returned lunar samples, and the three series of dots (brown, green and blue) plot the results of Koschny et al. (2017), computed from double-stations observations of ~20k meteors over a period of about 3.5 years with the Canary Island Long-Baseline Observatory (CILBO). The three series correspond to different methods used by Koschny et al. (2017) to compute the preatmospheric mass from the absolute magnitude (Verniani, 1973; Ceplecha and McCrosky, 1976; Weryk and Brown, 2013, see legend).

difference was highlighted for the case of the background D3 maps being highly variable within the FoV of Mini-EUSO and with time, for example corresponding to the transit of Mini-EUSO over cities and densely populated areas. A possible explanation of this mismatch is that a significant variation of the background counts within short time intervals (< 1 s) may negatively affect the progressive adjustment of the threshold value of the trigger (Eq. 6.1). This effect is not considered within the simulations presented in this work, for which we make the assumption that C_{xy} is not significantly varying along a fixed time interval $\delta t = 1$ s.

7

Interstellar meteoroids

As discussed in Sect. 4.2.6 for the analysis of PRISMA data, the measurement of the speed and radiant of an incoming meteoroid through the observation of the related meteor phenomenon allows to estimate its preatmospheric orbit and, finally, its dynamic origin. Then, the result of open (*i.e.*, hyperbolic) orbits is particularly interesting and deserves a deeper analysis, since these objects should come from outside our Solar System. However, this was a matter of long debate since the very first scientific meteor's obsevations. The recent review of Hajduková et al. (2019) provided a deep and detailed analysis of the problem. Today, the vast majority of the scientific community agrees that the subset of open orbits found in meteor databases mostly originates from measurement errors, both random and systematic ones. Nevertheless, the topic of meteoroids measured beyond the parabolic limit is of utmost importance, because of two main reasons. First, the analysis of the significance of these orbits within meteor observations datasets provides a unique tool to test the goodness of the error treatment process and the actual reliability of the orbital data. On the other hand, it will be indeed possible to reach precision and accuracy levels sufficient to enable a confident discovery of interstellar objects from the optical observations of meteors in the Earth's atmosphere, thanks to the technological advancement and to the refinement of the data analysis techniques.

In this chapter, I give a brief summary on the topic of interstellar meteoroids and present a statistical analysis tool designed to test the significance of open orbits within meteor databases, that was also applied to the observations of FRIPON. I then discuss the potentiality of Mini-EUSO observations in identifying interstellar meteors. Finally, I discuss my contribution to the activities of DIMS, a project born in 2017 with the main focus of investigating interstellar meteoroids and other exotic events that may occur in the Earth's atmosphere, such as nuclearites.

7.1 Observations of interstellar meteors

Since the very first scientific observations of meteors, a large number of orbits were determined to be hyperbolic and therefore thought to originate from interstellar meteoroids. A whopping fraction of 79% of observed meteors was found to be hyperbolic in the catalogue of visual observations of Von Niessl and Hoffmeister (1925). In the subsequent years, other observational programs also found a consistent percentage of hyperbolic orbits. Öpik (1940) reported a 60% of open orbits in the observations of the Arizona Expedition by the Harvard University (1931-1933), and defended these conclusions for nearly thirty years. However, with the advent of photographic observations in 1940, the thesis of the predominance of interstellar objects with respect to the interplanetary matter of the Solar System became unreasonable. On the contrary, it was even suggested that none of the detected events over the parabolic limit were real (Lovell, 1954). The research efforts then shifted towards trying to determine the actual fractions of observed interstellar meteors, if any. A range of values within few to tens percents were determined by several authors (a detailed review is given in Hajduková et al., 2019) and these results are controversial and questioned until today.

A new era for the science of interstellar meteoroids came with the in situ dust measurements of the detectors on board the Ulysses and Galileo spacecrafts. Grun et al. (1993) reported the confident and multi-coincident identification of interstellar dust grains in the heliosphere from the data of Ulysses. The interest then shifted towards smaller particles (ISD - Interstellar Dust), that are too small to be detected by the optical observations of meteors in the Earth's atmosphere. It then became fundamental to theoretically understand the dynamic of such object, that is, if and how they can penetrate to the inner Solar System to be detected in the Earth's vicinity. A deep analysis of this aspect is beyond the purpose of this manuscript, for which the reader can refer to Hajduková et al. (2019). The most likely source for ISD is the Local Interstellar Cloud (LIC), through which the Sun travels at a relative speed of ~26 km/s. Large particles (> 0.2 µm of size) can then pierce through into the heliosphere, while the smaller ones are shielded by the heliospheric magnetic field and deflected outwards. Once penetrating within the Solar System, they travel through the Interplanetary Magnetic Field and are subject to the solar radiation pressure, Lorentz and gravitational forces. The ratios between the magnitudes of solar radiation and gravity forces (*i.e.*, the β parameter) determines the fate of these particles, and the largest ones (> 1 µm) can reach an heliocentric speed of 49 km/s.

Considering finally interstellar meteoroids (> 10 µm), they are not coupled to the LIC and ultimately originate from other star systems in the vicinity of the Sun. Their speed is then due to the relative star's speed and the ejection speed from their system, which might range within tens of km/s. If we consider an interstellar meteoroid moving at $V_a = 25$ km/s at the edge of the Solar System, its measured heliocentric speed at the Earth's position will be further influenced by the Sun's gravity and will be $V_h = \sqrt{42^2 + V_a^2} \simeq 49$ km/s, that is 7 km/s over the parabolic limit. In general, we expect them to impact the Earth's with an excess speed of few km/s only. It is also worth noticing that some cases of hyperbolic orbits might have been accelerated by Jupiter or other planets (Wiegert, 2014) and few (especially long period stream meteoroids) might have became truly hyperbolic due to an appropriate combination of the size and ejection direction from the comet.

7.2 The Kresak's diagram

To determine the significance of resulting hyperbolic orbits computed from meteor's observations, the analysis of measurement errors is of utmost importance. In particular, the optical observation of meteors allows to measure the initial speed of the meteoroid at the top of the atmosphere, from which one can infer its preatmospheric value V_∞ correcting for the atmospheric drag, if significant before the meteor's visible flight (see Sect. 4.2.4). The 3D orientation of the atmospheric trajectory allows to define the apparent radiant (α_a, δ_a), that defines the preatmospheric speed vector $\overrightarrow{V_\infty}$ from its module. We then account for the zenith attraction effect due to the Earth's gravity and compute the geocentric speed vector $\overrightarrow{V_g}$. Finally, the heliocentric speed vector $\overrightarrow{V_h}$ is simply given as the vectorial sum of the geocentric speed and the Earth's revolution speed $\overrightarrow{V_0}$ (see Sect. 4.2.6). The module of the heliocentric speed vector is already diagnostic about the nature of the meteoroid's orbit, since it directly refers to the value of the semi-major axis a of its orbit in the hypothesis of a two-body problem:

$$V_h^2 = \mu \left(\frac{2}{R_0} - \frac{1}{a} \right) , \tag{7.1}$$

where $\mu = GM_S$ is the heliocentric gravitational parameter and R_0 is the Earth's distance from the Sun. The parabolic limit is then given by the condition $1/a \to 0$, that is $V_p = 42.1$ km/s and varies within 41.8–42.5 km/s since R_0 also varies from 0.983 to 1.017 AU along the Earth's orbit. It is therefore clear that the extension of the confidence region of V_h with respect to V_p will determine the significance of the orbit being hyperbolic. Since the uncertainty on V_h originates from both the error on the module V_g and its direction in ECI coordinates, Hajduková et al. (2019) proposed a graph based on geocentric quantities which facilitates the visualization of the dispersion beyond the parabolic limit, based on the original work of Kresak and Kresakova (1976). This is done by considering the square module of the heliocentric speed vector (Eq. 4.65) as follows:

$$V_h^2 = V_g^2 + V_0^2 - 2V_g V_0 \cos \epsilon_A , \tag{7.2}$$

where the minus sign in the double-product terms now refers to the Earth's apex (*i.e.*, the direction of motion) and ϵ_A is the angular elongation of the geocentric radiant from the apex. We can then consider the plot (V_g, ϵ_A), of which an example is given in Fig. 7.1 for the IAU MDC[1] database (Lindblad et al., 2003). Since the original idea of this graphical representation came from Kresak and Kresakova (1976), we named this as the *Kresak's diagram*. The red curve represents the parabolic limit, and the other coloured lines represent the value of ϵ_A versus V_g (or V_∞) for elliptic

---

[1] Meteor Data Center of the International Astronomical Union (`https://www.iaumeteordatacenter.org/`).

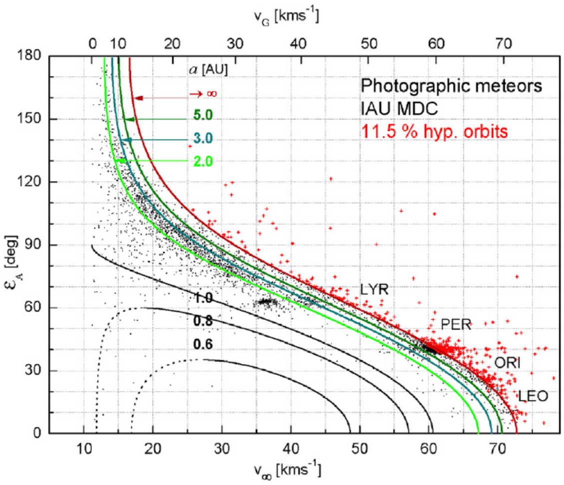

Fig. 7.1: An example of the Kresak's diagram, originally proposed by Kresak and Kresakova (1976), that is the plot of meteoroid's orbit in the (V_g, ϵ_A) parameters' space. V_g is the geocentric speed (upper x axis, the preatmospheric speed V_∞ is reported on the lower axis) and ϵ_A is the radiant's elongation with respect to the Earth's apex. This figure plots the data (black points and red crosses) of photographic meteors' observations listed in the IAU MDC database (Lindblad et al., 2003). The red curve represents the parabolic limit, and the other colours plots the position along the Kresak's diagram of elliptic orbits with varying semi-major axis a. Red crosses represent observations above the parabolic limit, *i.e*, determined with hyperbolic orbits (Hajduková et al., 2020). It is worth noticing that most of them are accumulated in correspondence of the radiant of meteor showers, close to the parabolic limit since originating from cometary bodies on highly eccentric orbits.

orbits with a variable semi-major axis. It is then evident that Solar System's orbits are confined on the portion of the graph on the left of the red curve (black dots). On the other hand, the red crosses plot events that are *geometrically* above the parabolic limit. We use this term to highlight that this result refers to the nominal value of V_h, and nothing is specified about its confidence region on the Kresak's diagram up to now. Indeed, the extensions of the errors on V_g and ϵ_A may result in the event still being compatible with a closed orbital configuration, that is, on the left of the parabolic limit in Fig. 7.1 (as also discussed in Sect. 4.2.6).

7.2.1 On the significance of hyperbolic orbits

Hajduková et al. (2019) and Hajduková et al. (2020) discussed the resulting features evident on different meteors databases also according to the interpretation of the Kresak's diagram. The most interesting one concerns the fact that a considerable fraction of hyperbolic events are accumulated in correspondence of known meteor showers (such as Perseids, see Fig. 7.1). In fact, these showers are usually very close to the parabolic limit, having comet-like orbits with an high semi-major axis. It is then clear that a small measurement error on both V_g or ϵ_A may cause one

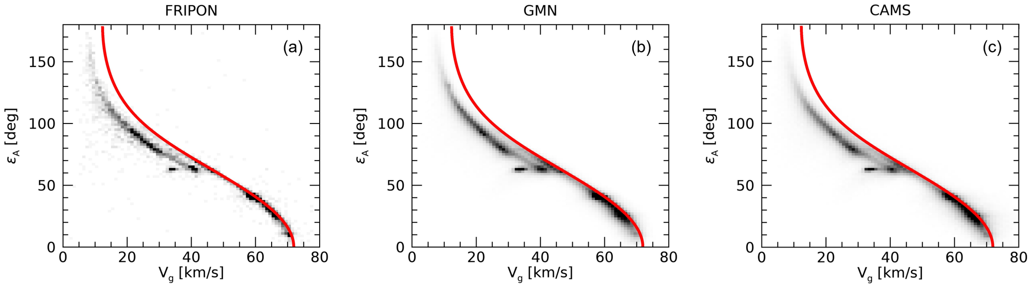

Fig. 7.2: Density representation of the Kresak's diagram for the databases of (a) FRIPON, (b) GMN and (c) CAMS, given in logarithmic colour scale. The red curve plots the parabolic limit.

point on the Kresak's diagram to be artificially moved to the right of the parabolic limit and being identified as interstellar. The presence of an high percentage of hyperbolic orbits among observed meteors that are associated to a shower speaks itself against the significance of points beyond the parabolic limit to be interpreted as true interstellar events. Based on simulations of Perseid-like orbits affected by measurement errors of varying magnitude, Hajduková and Kornoš (2020) suggested that a precision and accuracy level of ~0.1 km/s for the preatmospheric speed and ~0.1° for the radiant is needed to confidentially distinguish interstellar meteors within these datasets.

Following the footprint of these works, we analysed in detail the dataset of meteor's observations available in literature that are provided with an estimation of the measurement errors on the speed (preatmospheric or geocentric) and the radiant position of their entries. We considered the following databases:

- FRIPON (Jeanne et al., 2019; Colas et al., 2020), consisting of ~7k bright bolides detected mainly over Europe from 2016 to 2022 (see Sect. 3.1.1). The observations of PRISMA are included in this database[2].
- GMN (Vida et al., 2021a), an amateur-professional collaboration project with over 600 video meteor cameras in more than 30 countries. From 2019 to 2020, GMN detected ~575k meteors, with a stellar limiting magnitude of +6.
- CAMS (Jenniskens et al., 2018b), an international project that studies meteors with a particular attention to meteor showers. From 2010 to 2016, CAMS observed ~472k meteors with a limiting magnitude of +5.

Figure 7.2 shows the density plots of these three databases in the Kresak's diagram representation, together with the curve of the parabolic limit. The three distributions are similarly shaped, and all of them are characterized by the presence of a "tail" above the parabolic limit that is particularly visible in the range $V_g > 50$ km/s. The percentage of geometrically hyperbolic events in the three datasets is similar, and is

---

[2] The processing of the PRISMA database, which accounts for ~2.5k event, is still ongoing at this time of writing. We plan to repeat this analysis with our results and comparing the two versions.

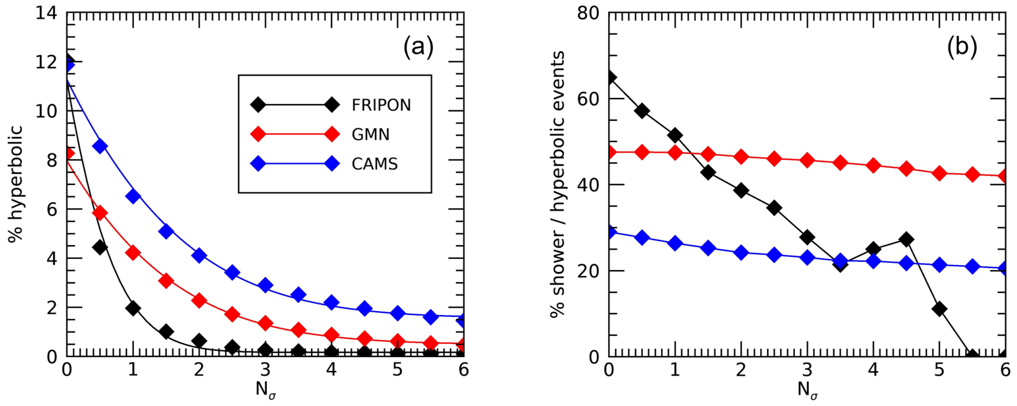

Fig. 7.3: Results of the statistical analysis to determine the significance of hyperbolic orbits in meteor databases (given in the legend of panel a). (a) Fraction of hyperbolic events as a function of the confidence level expressed as N_σ, that is the number of standard deviations used to define the confidence interval in the Kresak's diagram. The coloured curves represent the fitting of Eq. 7.3 over the results of each database. (b) Fraction of meteors associated to known showers contained within the hyperbolic subset as a function of N_σ.

12.05% (835 events) for FRIPON, 8.27% (47.5k) for GMN and 11.86% (55.9k) for CAMS, that is also comparable to the case of the IAU MDC database of Fig. 7.1. As discussed above, it is also interesting to understand how many of these hyperbolic events were indeed associated to a known meteor showers and therefore most likely to be artificially hyperbolic ones. In all cases the percentage of shower meteors among the hyperbolic events is quite high, and that is 64.9% for FRIPON, 47.6% for GMN and 29.0% for CAMS.

Then, let us understand how the inclusions of measurement errors in this analysis affects these results. To do so, we progressively vary the confidence level, *i.e.*, the number N_σ of standard deviations that is used to define the confidence interval in the Kresak's diagram, and evaluate the fraction of events in each database that survives this filtering process. Similarly, we evaluate the fraction of shower-related events within the hyperbolic subset for each confidence level. The results of this simple but enlightening analysis are reported in Fig. 7.3. Panel a plots the decay of the hyperbolic fraction for the three databases. This is finally linked to the distribution of events above the parabolic limit, but where the distance (*i.e.*, the parabolic excess) of each event is weighted according to the extension of its confidence interval. In all cases, the percentage of hyperbolic events drops as N_σ increases. However, this decrease is much steeper for FRIPON with respect to GMN and CAMS, which on the other hand are characterized by a very similar trend. Taking $N_\sigma = 3$ as a reference (that is, one-sided 99.9% confidence level), the percentage of hyperbolic events is as low as 0.27% (18 events) for FRIPON, compared to 1.08% and 2.52% respectively for GMN and CAMS data. However, this evidence alone cannot reveal whether the residual events can be effectively addressed as candidates of interstellar meteoroids or not. For example, CAMS probably has an intrinsicly higher fraction of hyperbolic events since its observations are more focused towards meteor showers, which orbits are more likely to artificially trespass the parabolic limit due to measurement errors because of their higher geocentric speed. On the other hand, it is not reasonable to simply state that those events are not hyperbolic "by decree", also because they survived to a quite selective 3σ filtering.

A quite relevant indication in this respect is evident from Fig. 7.3b. For the case of FRIPON, shower-related meteors within the hyperbolic subset are efficiently filtered as N_σ increases, even in spite of the fact that FRIPON shows the higher fraction of geometrically hyperbolic shower meteors among the three databases. At $N_\sigma = 5.5$, all shower events are removed from the hyperbolic subset. On the other hand, this percentage is quite steady as a function of N_σ for the case of GMN and CAMS, with a relative drop of 5–10% only. This represents a clear evidence that the filtering process according to the measurement errors is not being effective, and the events that survive this selection still do not represent real candidates of interstellar meteors. On the same topic, it is also quite interesting to notice that the fraction of hyperbolic events at $N_\sigma = 3$ for FRIPON is of the same order as the expected percentage of events that one would expect to lay outside the one-sided 3σ confidence interval, that is 100 - 99.86 = 0.14%. Highlighting this strong evidence, we can make one step further, that is interpreting the shape of the relative drop of the hyperbolic fraction with N_σ of Fig. 7.3b. If we make the hypothesis that any of the events in these datasets can be significantly identified as hyperbolic, we can expect that their distribution above the parabolic limit can be given in the form of:

$$f(N_\sigma) = f_0 + \frac{1-f_0}{2}\mathrm{erfc}\left[\frac{1}{\sqrt{2}}\left(\frac{N_\sigma}{R} + B\right)\right] , \qquad (7.3)$$

that is valid if the measurement errors can be assumed to represent the width of a normal distribution. Within Eq. 7.3, f_0 represents the real fraction of hyperbolic events[3], while R can be interpreted as an estimator of the goodness of the errors determination within the problem. In fact, $R = 1$ corresponds to the case for which the fraction of hyperbolic events drops above the parabolic limit as the cumulative function of a normal distribution. On the other hand, $R > 1$ outlines that this drop is slower and may suggests that the measurement errors are being underestimated (or overestimated if $R < 1$). Finally, B is related to the fraction of geometrically hyperbolic events (at $N_\sigma = 0$) and can vary among different datasets for various reasons, as already mentioned. The results of the fitting of Eq. 7.3 over the data of FRIPON, GMN and CAMS are plotted as the coloured curves on Fig. 7.3a. We determined $R = 1.19 \pm 0.05$ for FRIPON and $R = 3.10 \pm 0.02$ for both GMN and

---

[3] From its mathematical definition of Eq. 7.3, $f_0 = \lim_{N_\sigma \to \infty} f(N_\sigma)$. However, it is physically unreasonable to think that any event would survive to a selection with an indefinitely large confidence level. For its practical meaning, f_0 is the fraction of hyperbolic events that survive to the highest confidence level considered, for example, when giving an upper limit estimation of the flux of interstellar meteoroids.

CAMS. This evidence further supports our previous conclusions, indicating that a good error estimation is provided in the FRIPON database. On the other hand, this model suggests that the magnitude of errors given in the GMN and CAMS databases is significantly underestimated, and this is in accordance with the results of Fig. 7.3b.

Our analysis highlighted what was already pointed out by authors but from another point of view, with a direct approach to the measurement errors with the aim of testing the significance of hyperbolic orbits that are commonly found by the reduction of meteor observations. A real interstellar meteor could be indeed detected just above the parabolic limit. In fact, interstellar meteoroids are expected to have a quite small parabolic excess speed (see Sect. 7.1). However, their orbit must be determined with sufficient precision and accuracy to finally prove the significance of these detections, and distinguish them from the background of Solar System's meteors that artificially cross the parabolic limit due to measurement errors. Therefore, the real challenge consists in (1) improving the quality of the error treatment processing within the reduction pipelines, so that the uncertainties assigned to the database's entries reflect the actual indeterminacy on those parameters, and (2) improving the overall quality of the observations, that is, deploying more advanced detector enabling to reach precision and accuracy levels sufficient to confidentially detect the interstellar component of meteoroids close to the parabolic limit.

7.3 Identification of interstellar meteors with Mini-EUSO

In light of what we discussed in the previous sections about ground-based optical observations of meteors, the reader might then think that a space-based monocular telescope such as Mini-EUSO does not have any chance to significantly contribute in the topic of interstellar meteors. As a matter of fact, we discussed in Chap. 6 the various limitations of the analysis of meteors detected by such instrument. On the other hand, the observations of Mini-EUSO come with remarkable benefits over ground-based observations (Sect. 3.3.2). For instance, a space-based observatory provides an uniform coverage of the meteor's flux on the whole Earth and can reach large exposure values within a little observation time. If compared to ground-based instrument, Mini-EUSO observed a remarkable number of meteors (∼24k) within a total of only ∼5.7 days of operation, since it observed only during dedicated sessions about twice a month. In the future, a space telescope dedicated to a continuos monitoring of the meteor's flux have the potentiality to provide an invaluable large amount of observations, remarkably increasing the available statistics. We already demonstrated that, despite the limitations of the instrument, it was possible to give a measure of the flux density of meteors from Mini-EUSO observations that is

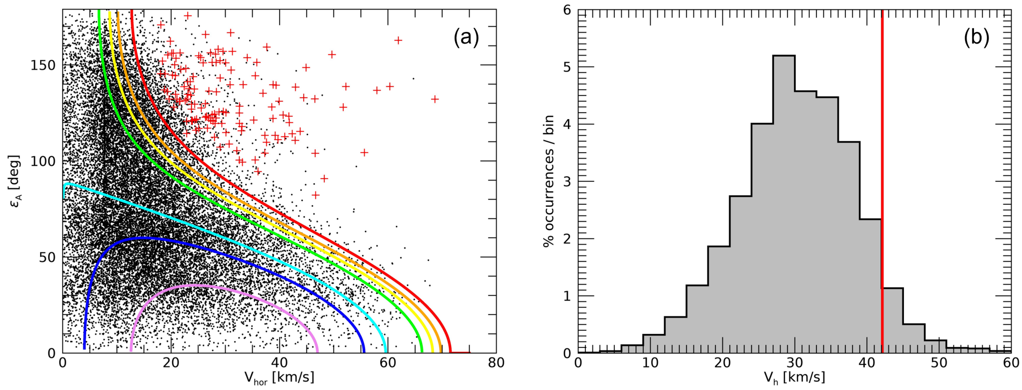

Fig. 7.4: First step of the identification of interstellar meteor candidates within the Mini-EUSO database of meteor's observations. (a) Scatter plot of the observed meteors (black dots) on the Kresak's diagram (see Sect. 7.2). The parabolic limit is drawn by the red curve, and other coloured curves plots corresponds to different values of the orbital semi-major axis (see Fig. 7.1). Events that survived the first 3σ filtering assuming $V_g = V_{hor}$ are plotted as red crosses. (b) Distribution of the heliocentric speed module neglecting the zenith attraction effect. The vertical red line draws the parabolic limit ($V_p = 42.1$ km/s).

in nice agreement with other estimates available in literature (Sect. 6.4). In this section, we demonstrate the potentiality of Mini-EUSO in regard of the identification of interstellar meteor candidates. Again, this is possible only thanks to a detailed analysis of the uncertainties of the problem.

The major limitation of meteor's observations with Mini-EUSO is due to the fact that the instrument does not have the capabilities to triangulate the three-dimensional atmospheric path of the detected events. Sect. 6.2.3 gave a detailed overview on how this reflects into the uncertainties given for the measurement of speed, azimuth and absolute magnitude. We then approached the identification of interstellar meteors in the following way. In a first step, let us neglect that we are missing a measure of the speed component along the altitude direction, and consider that $V_g = V_{hor}$ (that is the horizontal speed of the meteor measured by Mini-EUSO). This is equivalent of assuming that $\gamma = 0°$, that is physically unreasonable because a small inclination will be always provided by the zenith attraction effect due to Earth's gravitation. However, V_{hor} will be an underestimation of the actual geocentric speed V_g (Eq. 4.62). The same is valid for the fact that we are not correcting for the atmospheric drag. Then, the effect of this simplification on the Kresak's diagram will be a shift of the events to the left side of the plot, that is towards the region of meteors originating within the Solar System, and this will not generate artificial interstellar meteors. The Kresak's diagram for the meteor's database of Mini-EUSO (Tab. 6.1) is presented in Fig. 7.4a, and panel b plots the corresponding distribution of heliocentric speed V_h. It is clear that the distribution of points on the Kresak's diagram is very different from what we saw in Fig. 7.1 and 7.2. Since $V_{hor} < V_g$, a considerable number of events are distributed in regions of the

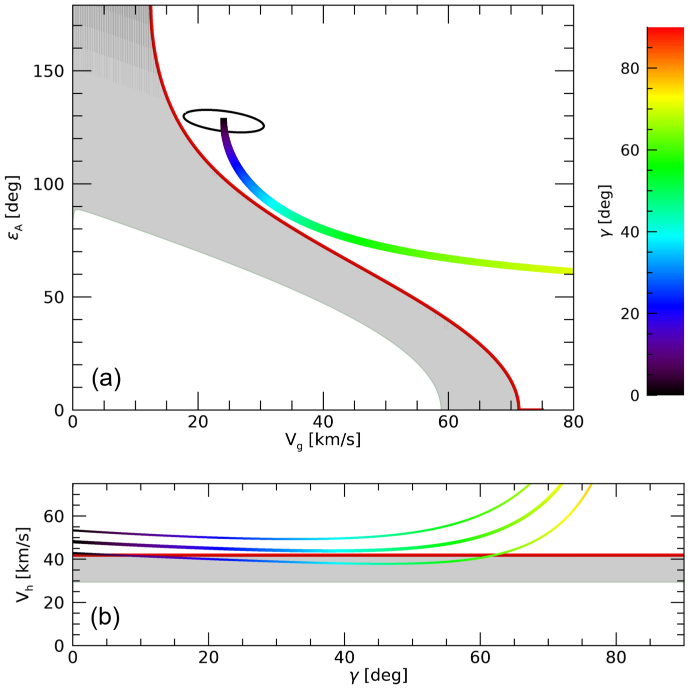

Fig. 7.5: The effect of the indeterminacy on the trajectory inclination γ for meteors detected by Mini-EUSO, represented on the Kresak's diagram for an example of event which survived the first filtering process assuming $V_g = V_{hor}$ (see Fig. 7.4). (a) The black ellipse encloses the 3σ confidence region for $\gamma = 0°$, that is moved in the (V_g, ϵ_A) plane along the coloured line by varying $\gamma \in [0, 90]°$. The confidence region crosses on the left side of the parabolic limit (red curve) for $\gamma \in [7, 62]°$ and is then compatible with a Solar System origin (shaded grey area). (b) Same as panel a but presented as the variation of the heliocentric speed module V_h as a function of γ.

plane that would be scarcely populated otherwise. For example, this is the case of the portion corresponding to $a < 1$ AU below the light blue curve on Fig. 7.4a, that represents the orbits of NEOs in the classes of Atens or Atiras (see Sect. 2.3). This effect is evident also in panel b, since the heliocentric speed distribution significantly extends below $V_h < 30$ km/s. On the other hand, the percentage of geometrically hyperbolic orbit is 5.83% (1397 events) and is comparable to the value obtained for ground-based observations (see Sect. 7.2.1). The red crosses in Fig. 7.4 plot the events that survived the 3σ selection and are 135 only, corresponding to 0.56% of the whole database. We choose this specific confidence level since it also relates to the systematic uncertainty on the assumed meteor altitude (see Sect. 6.2.3).

We then focus our attention to these 135 events that apparently overcome the parabolic limit even if provided with an underestimated geocentric speed. It is to be noticed that they are accumulated mostly below 40 km/s and not towards higher apparent speed values as we saw for ground-based observations. However, until now we did not considered that the radiant position, and therefore its elongation ϵ_A

Date	Time UT	Lat. [deg]	Lon. [deg]	N_{px}	Δt [s]	V_{hor} [km/s]	a [deg]	$\mathcal{M}$ [mag]	$\overline{V}_h$ [km/s]
25/05/20	23:49:24.83	06°33'N	31°45'E	9	0.70	33 ± 2	223 ± 3	2.7 ± 0.1	50 ± 2
28/07/20	08:04:48.02	25°47'S	80°30'W	22	0.82	47 ± 4	292 ± 4	3.3 ± 0.1	64 ± 4
16/01/21	07:12:43.96	38°40'N	69°11'W	10	0.78	37 ± 3	231 ± 1	2.9 ± 0.1	51 ± 3

Tab. 7.1: Relevant data about the three interstellar meteor candidates identified in the Mini-EUSO database. From left to right: Date and time UT of the detection, latitude and longitude of the ISS at that time, number of pixels on the PDM that were interested by the meteor signal, duration of the event, horizontal speed module at a 100 km altitude, azimuth direction from the North, absolute magnitude and minimum heliocentric speed (Eq. 7.5).

will be also affected by a variable trajectory inclination. We then assume that γ can vary in the range $[0, 90]^\circ$ and compute the preatmospheric speed as:

$$V_\infty(\gamma) = \frac{V_{hor}}{\cos\gamma} \ . \tag{7.4}$$

Similarly, we can compute the actual apparent radiant (α_a, δ_a) from the measured value of the azimuth angle a and the assumed inclination γ. Therefore, the indeterminacy on γ will results in a set of points $[V_g(\gamma), \epsilon_A(\gamma)]$ instead of a single point on the Kresak's diagram. An example is given in Fig. 7.5 for an event that survived the initial 3σ filtering. The black ellipse on panel a plots the 3σ confidence confidence region on the Kresak's diagram for $\gamma = 0^\circ$, that is indeed totally on the right side of the parabolic limit (red curve). However, as γ increases (given by the colour scale), the point approaches the parabolic limit since V_g increases but ϵ_A decreases. This is also shown in panel b, that plots $V_h(\gamma)$ again with its 3σ interval. Therefore, the event is compatible with a Solar System origin for $\gamma \in [7, 62]^\circ$, and it is ruled out from the list of potential interstellar meteors. Of course, this is a conservative indication since we are heavily constrained by the indeterminacy on γ. This event could have been an interstellar meteor, if its trajectory inclination was actually greater than 62°, but we do not have sufficient data to prove it.

After this screening, 9 events survived because their confidence region never crossed on the left of the parabolic limit for any γ value. We excluded 6 of them since they were classified in the M? class (meteor candidates, see Sect. 6.1.1) and exhibited a limited motion on the focal surface of 2 or 3 pixels. As discussed in Sect. 6.2.2, the azimuth direction might be significantly biased in this case due to the limited spatial resolution of the instrument. The apparent horizontal speed could also be overestimated for these events, since the PSF extends over only 1-2 pixels only and the barycentre position might be artificially biased towards the centre of the pixel (similarly to what discussed for the case of PRISMA, see Sect. 4.1.4). The remaining 3 events are presented in Fig. 7.6, 7.7 and 7.8. From their observed features, they are undoubted meteor events. Their relevant data are reported in

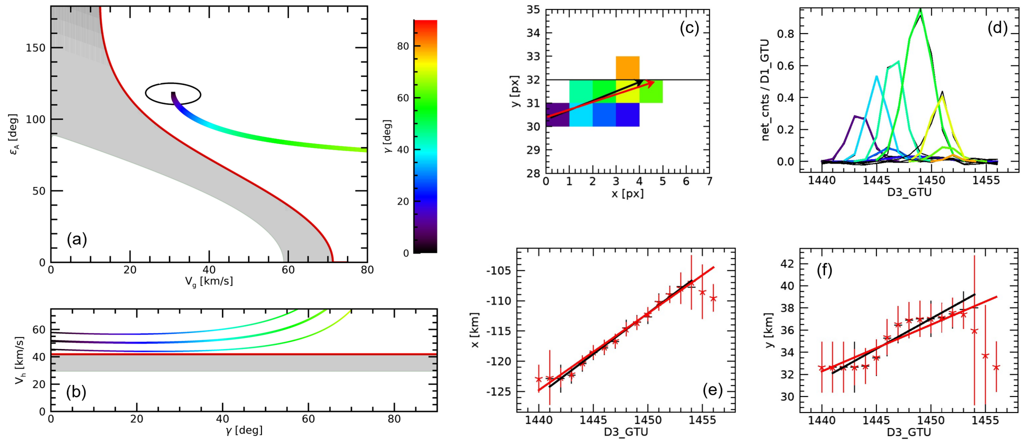

Fig. 7.6: Results of the analysis for the first interstellar meteor candidate listed in Tab. 7.1). Panels a and b reports the analysis of the event onto the Kresak's diagram (see Fig. 7.5), while panels c-e present the results of the analysis of the event (see Fig. 6.7 and 6.8).

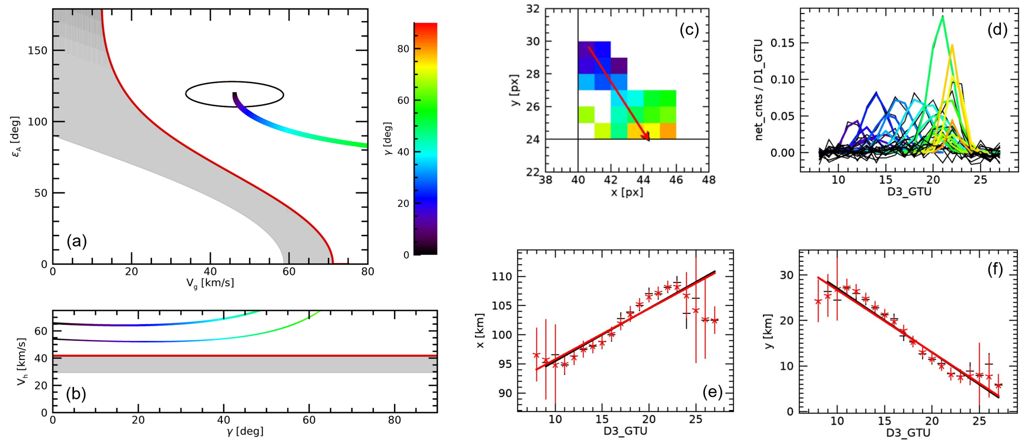

Fig. 7.7: Same as Fig. 7.6 for the second event listed in Tab. 7.1.

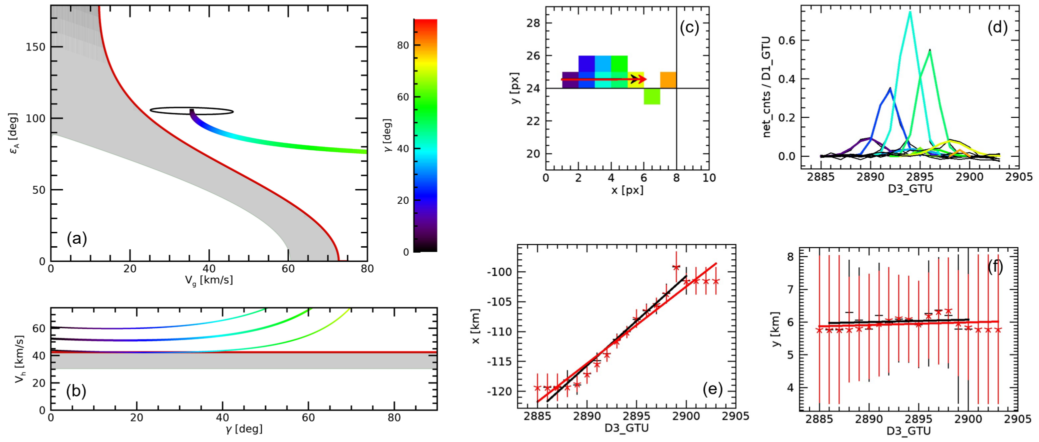

Fig. 7.8: Same as Fig. 7.6 for the third event listed in Tab. 7.1.

Tab. 7.1. In particular, a conservative estimation of their heliocentric speed can be provided as:

$$\overline{V}_h = \min_{\gamma \in [0,90]^\circ} V_h(\gamma) \ , \tag{7.5}$$

At this time of writing, a deeper analysis of these interesting events is in progress to further investigate their significance as actual interstellar meteor candidates. For example, we notice that they all occurred in proximity of a PMT border or corner, therefore the estimation of their direction on the PDM could suffer from this condition of observation.

7.4 The DIMS project

During the period of the PhD, part of my work was also dedicated to the data analysis of the DIMS project and was presented in Barghini et al. (2021) and Barghini et al. (2022a). DIMS (Dark matter and Interstellar Meteoroid Study) is a novel experiment born in 2017 and designed to search for such fast-moving particles by observing the sky with wide-field, high-sensitivity CMOS cameras. Each stations of DIMS mainly consists of a Canon ME20F-SH monochrome camera, a computer to control the camera and a solar power supply and environmental control system (Shinto et al., 2022). The camera is equipped with Canon EF 35mm, f/1.4L lenses and a 1920 × 1080 pixels high-sensitivity CMOS sensor and can be operated at a 30 or 60 Hz frame rate. This system is installed in a stainless steel box with an acrylic dome and can be operated remotely. A detailed description of the project is given in Kajino et al. (2017) and Abe et al. (2022).

Apart from interstellar meteors, similar events beyond the parabolic limit might have other exotic sources. For example, in the wide landscape of dark matter (DM) candidates, it is hypothesized that macroscopic strange quark matter (SQM) nuggets may collide with the atmosphere and generate luminous events similar to meteors. The original idea was proposed by Witten (1984), suggesting that macroscopic SQM aggregates of up, down and strange quarks might be more stable than ordinary matter. These hypothetical objects were first named nuclearites (De Rujula and Glashow, 1984), while today they are included in a broader class of macroscopic DM candidates named macros (Jacobs et al., 2015). If existing, they should generate optical atmospheric events remarkably distinguishable from meteors, thanks to their peculiar characteristics such as very low altitude and very high speed. During the last decays, theoretical and experimental efforts have been made to constrain their flux at the Earth's position by various techniques (see Sect. 3.3.3).

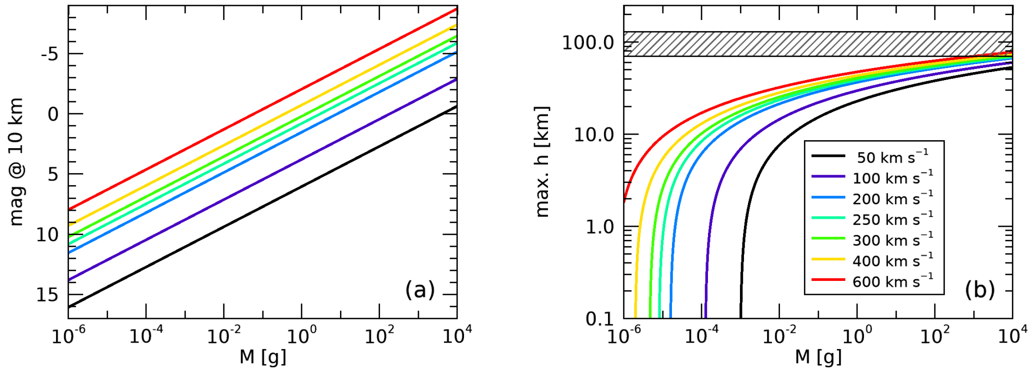

Fig. 7.9: Apparent visual magnitude at 10 km of altitude (a) and maximum height of light emission (b) as a function of the nuclearite mass, for different velocities within 50 and 600 km/s (Eqs. 7.6 and 7.7). The grey dashed region in panel b marks the altitude range in which meteors typically occur, from 70 to 130 km (Barghini et al., 2022a).

7.4.1 Nuclearites in the Earth's atmosphere

The theoretical description of the phenomenology of a nuclearite traversing the Earth's atmosphere was first provided by De Rujula and Glashow (1984). The nuclearite is thought to have a nuclear density ($\rho_N = 3.6 \cdot 10^{14}$ g/cm^3) and to be surrounded by an electron cloud to preserve overall neutrality. Then, it should lose energy via quasi-elastic collisions with the air molecules and form an expanding thermal cylindrical shock wave, which emits black-body radiation. In these conditions, the luminous efficiency is estimated to be ~4% and independent from the mass and speed of the object. The original formulation by De Rujula and Glashow (1984) considered that the nuclearite collides with the atmosphere at a speed of about 250 km/s, that is the typical rotation speed of the Galaxy and does not consider the Earth motion. However, it has been suggested that these objects might travel at a speed up to the escape limit from the Galaxy at the Sun's position, that is approximately 550 km/s. In this case, the apparent visual magnitude m of a nuclearite of mass M, travelling at a speed V and observed from the ground at an altitude H can be given as (Barghini et al., 2022a):

$$m = 0.80 - 1.67\log_{10}\left(\frac{M}{1\text{ g}}\right) + 5\log_{10}\left(\frac{H}{10\text{ km}}\right) - 7.5\log_{10}\left(\frac{V}{250\text{ km/s}}\right) . \quad (7.6)$$

The variation of the apparent magnitude at 10 km of altitude as a function of the nuclearite's mass is presented in Fig. 7.9a for different speed values. In this hypothesis, it is assumed that the nuclearite is not significantly decelerated by the atmospheric drag. Also, the light emission from a nuclearite is expected to be almost constant within its whole flight in the atmosphere and the apparent magnitude should change only as a function of the distance from the observer. This is one of the main features that should enable to discern between the observation of nuclearites and meteors, the latter having a much larger intrinsic variability in terms of lightcurve morphology due to their complex physical evolution while crossing the atmosphere. Moreover, the maximal height at which a nuclearite is supposed to generate light, according to this formulation, can be computed as:

$$H_{max} = 3.3 \left[\ln\left(\frac{M}{1\ \text{g}}\right) + 3\ln\left(\frac{V}{250\ \text{km/s}}\right)\right] . \tag{7.7}$$

The variation of H_{max} as a function of the nuclearite's mass for different speed values in given in Fig. 7.9b. From this result, we can see that the height of light emission for a nuclearite event should be much lower than the typical range for meteors (from 70 to 130 km, dashed band on the figure). It is confined below 40 km for $M < 1$ g and reaches 70 km only for very massive nuclearites ($M > 1$ kg). In any case, the most remarkable feature of events generated by nuclearites is that they may move upwards within the Earth's atmosphere, since a massive nuclearite should be able to pierce through the Earth's diameter and emerge from the ground. The observation of a luminous event moving upwards in the atmosphere would then be an indisputable proof for its non-meteor origin. On the contrary, very light nuclearites ($M < 0.3$ ng) would be able to reach the Earth's crust and accumulate therein.

A different model for the phenomenology of a nuclearite traversing the Earth's atmosphere was proposed in recent years by Sidhu et al. (2019). In this case, the nuclearite (and a macro in general) is considered as a straight-moving point-like source which creates a hot plasma channel, expanding by heat diffusion. Considering that the plasma should be optically thin (except only for very massive macros), the luminous efficiency can be computed from the plasma recombination rate. According to this model, the expected visual magnitude can be given as:

$$m = 39.66 - 5\log_{10}\left(\frac{M}{1\ \text{g}}\right) + 5\log_{10}\left(\frac{H}{10\ \text{km}}\right) + 5\log_{10}\left(\frac{\rho}{\rho_N}\right) + \frac{1}{\ln 10}\left(\frac{H}{1\ \text{km}}\right) . \tag{7.8}$$

Then, a macro with nuclear density $\rho = \rho_N$ at $H = 10$ km would shine at a visual magnitude of $m = +44$, against the value given by Eq. 7.6 of $m = +0.8$ for $V = 250$ km/s. This huge difference significantly impacts the detectability of such events. According to Sidhu et al. (2019), they should produce a signal way too dim to be detected by any kind of ground-based detector, but in the case of very massive objects or much below the nuclear density.

7.4.2 Preliminary analysis of DIMS data

DIMS carried out several observation campaigns since 2017, mainly in Japan and USA. In this preliminary analysis we considered the data taken, mainly for a testing purpose, during the night of 01/09/2019 at the TA sites with two stations. The cameras, named N1 and N2, were installed at the Hinckley and Black Rock Mesa sites, respectively, at a distance of about 17 km and pointing towards Polaris, and continuously observed the sky for 6.5 hours. Such a limited distance between the stations is chosen accordingly to the fact that nuclearite events should occur lower in the atmosphere with respect to meteors. As a drawback, meteors are observed with a lower parallax between the two stations, and this may affect the accuracy of the triangulation processing (see Sect. 4.2.2). The triggering system on DIMS cameras is managed by UFOCapture[4], a software developed by the SonotaCo collaboration for the detection of meteors. During this night, the two cameras detected 422 events in coincidence mode. Since the instrumental setup and configuration is quite similar to the case of the PRISMA network, we adapted the reduction methods described in Chap. 4 for the case of DIMS for both the calibration of the sensor and the analysis of the events[5]. A detailed description of implemented methods is given in Barghini et al. (2021).

Thanks to its highest sensitivity with respect to PRISMA cameras, DIMS can observe stars down to magnitude +9 in the visual wavelength range. Furthermore, stars and meteors are observed in the same data, which are stored as 8-bit AVI files with a typical duration of a few seconds. While this would lead to prefer a differential approach to derive the astrometric solution, the wide field of DIMS cameras ($57^\circ \times 34^\circ$) introduces heavy optical distortions. Therefore, we still adopted an absolute astrometric solving of the plate for the reduction of DIMS data. The algorithm of source finding and correlation with catalogues positions is essentially the same as for PRISMA (see Sect. 4.1.2). The most important difference is that we can directly work with equatorial coordinates (α, δ), since the cameras are conveniently pointed towards Polaris. A first comparison with the reference catalogue is therefore performed by considering a simple spherical and undistorted projection in equatorial coordinates as the one of Eq. 4.7, but where the azimuth angle a is replaced with the right ascension α and the zenith distance z with $90^\circ - \delta$ (precessed to the current epoch). After the iterative process of source finding and correlation with the catalogue, the final astrometric solution is given by a standard CD matrix approach, accounting for plate rotation and scaling, plus an 8th degree TNX[6] complete polynomial distortion. The photometric reduction of DIMS data is the same presented for PRISMA (see Sect. 4.1.6).

Figure 7.10 shows an example of the astrometric and photometric reduction of one video captured by the N1 camera. The image of panel a displays a portion of the total FoV around the detected meteor together with the identified stars positions onto the frame, which are circled in red. It is evident that a greater number of stars is visible above the sky background, while we imposed a magnitude limit of +8 on the V band for the source finding algorithm. This setting allows finding ~900 stars for

---

[4] https://sonotaco.com/soft

[5] The analysis of DIMS data presented here was obtained with a preliminary version of the PRISMA pipeline which included the triangulation computation only. At this time of writing, we are processing the new observations of DIMS from 2022 with the complete pipeline.

[6] https://fits.gsfc.nasa.gov/registry/tnx.html

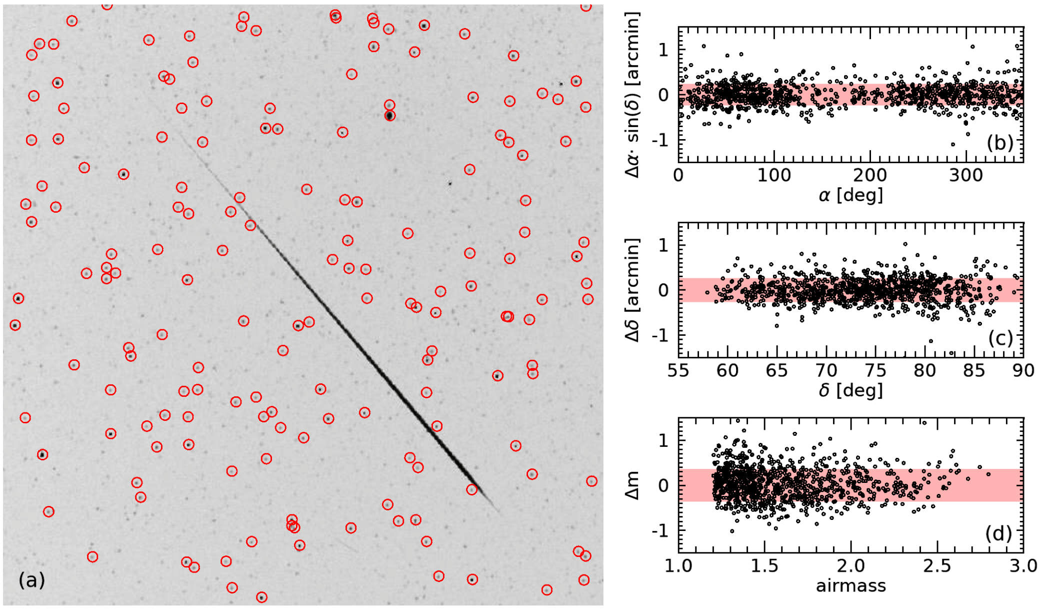

Fig. 7.10: Calibration results on a sample event captured from N1 camera at the Hinckley TA site on 01/01/2019 at 08:16:17 UT. (a) A portion of the FoV (with inverted colour scale) with the track of the triggered meteor together with positions of identified stars, as red circles, up to magnitude +8; (b) right ascension residuals between calibrated and catalogued stars positions; (c) same as panel b, but for declination; (d) magnitude residuals as a function of the airmass (Barghini et al., 2022a).

each video, that is already more than sufficient to provide an accurate and precise calibration for our purposes. Figure 7.10b-d plot the astrometric and photometric residuals for the final solution of that video. No systematic deviations are evident, and residuals are normally distributed around zero with a standard deviation of about 0.25 arcmin (*i.e*, 0.15 px considering the linear plate scale of 1.8 arcmin/px), highlighting that we are already achieving a sub-pixel positional precision.

We then applied the triangulation processing described in Sect. 4.2.2 to the 422 events detected in the considered night by both N1 and N2 DIMS cameras. Figure 7.11 summarizes the results of this analysis. Panels a, b and c plot the distributions of the reconstructed beginning height and entry speed, and none of the events shows indisputable signatures for a non-meteor origin. Beginning heights are confined in the usual meteor range of 70–130 km from the ground, and the histogram of entry speed displays the typical bi-variated distribution for low (asteroidal) and high (cometary) components. Only 8 events showed a median speed above the 72.8 km/s (*i.e.*, the maximum allowed speed for a meteoroid from the Solar System at the Earth's position) but, after a careful revision of their analysis, they were found to be badly reconstructed from triangulation and therefore discarded. The magnitude distribution shown in panel c also suggests that DIMS cameras are not completely efficient in the detection of meteors above +4 magnitude, and the limiting magnitude for DIMS observations is +6. These results can be then used to define the expected constraints to the flux of macro that could be established by the DIMS experiment,

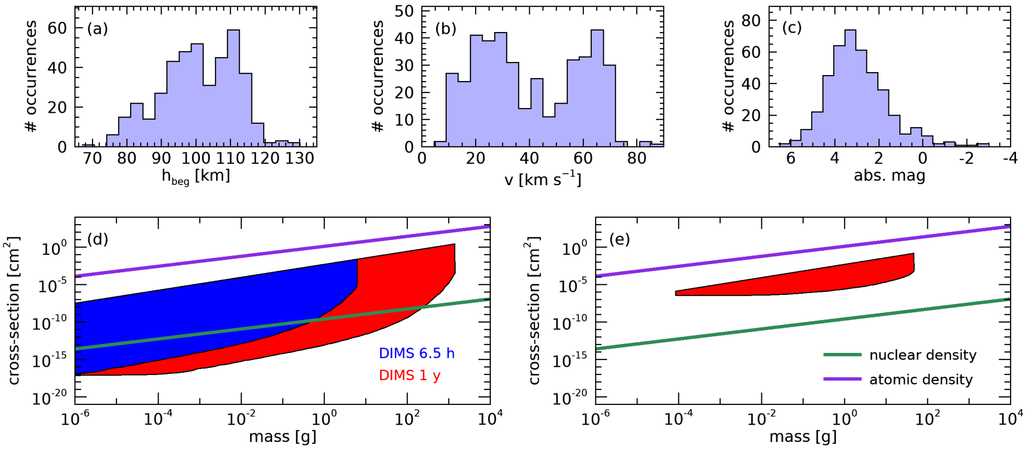

Fig. 7.11: Results of the preliminary analysis of the 422 meteor events detected on 01/09/2019 by two DIMS cameras installed at the TA site. Top: distributions of beginning height (a), atmospheric entry speed (b) and absolute magnitude (c). Bottom: constraints of macro's observation by DIMS for 6.5 hours exposure of the current dataset (blue area) and for 1-year projection with 10% duty cycle (red area), according to De Rujula and Glashow (1984) - panel d, and to Sidhu et al. (2019) - panel e. The green and purple lines in panels d,e plot the cross-section respectively for macros with nuclear and atomic density (Barghini et al., 2022a).

following the approach described in Sidhu and Starkman (2019) and detailed in Barghini et al. (2022a). In particular, not having observed any anomalous event in our dataset allows to rule out a certain region in the macro parameters space of mass and cross-section. The boundary of this region depends upon which model we consider for the macro phenomenology (see Sect. 7.4.1). Figure 7.11d plots this region, according to the model of De Rujula and Glashow (1984) corresponding to the exposure of the night of 01/09/2019 (6.5 hours, blue area) and the expected limits for 1 year of DIMS observations assuming a 10% duty cycle (red area). In this projection, DIMS would be able to probe macros with nuclear density up to 1 kg. However, this result is drastically different if considering the model of Sidhu et al. (2019) plotted in panel e, according to which DIMS cannot rule out any region of the parameter's space with one night of observations, and reaches only $\sim$0.1 kg in the 1-year projection. This preliminary analysis does not yet consider the actual efficiency of the current DIMS trigger in detecting very fast events, that was not tested against the UFOCapture algorithm up to now, together with the decrease in the efficiency below +4 magnitude (similarly to what was done for the Mini-EUSO data, see Sect. 6.3).

Finally, we repeated the analysis for the identification of interstellar meteor candidates also on this limited dataset of observations. The resulting Kresak's diagram is reported in Fig. 7.12. The fraction of geometrically hyperbolic events is 8.8%, which is in line with other optical surveys (see Sect. 7.2.1). A dedicated inspection of such events showed that some problems occurred in the automatic reduction pipeline (typically, very short events with bad triangulation outcome).

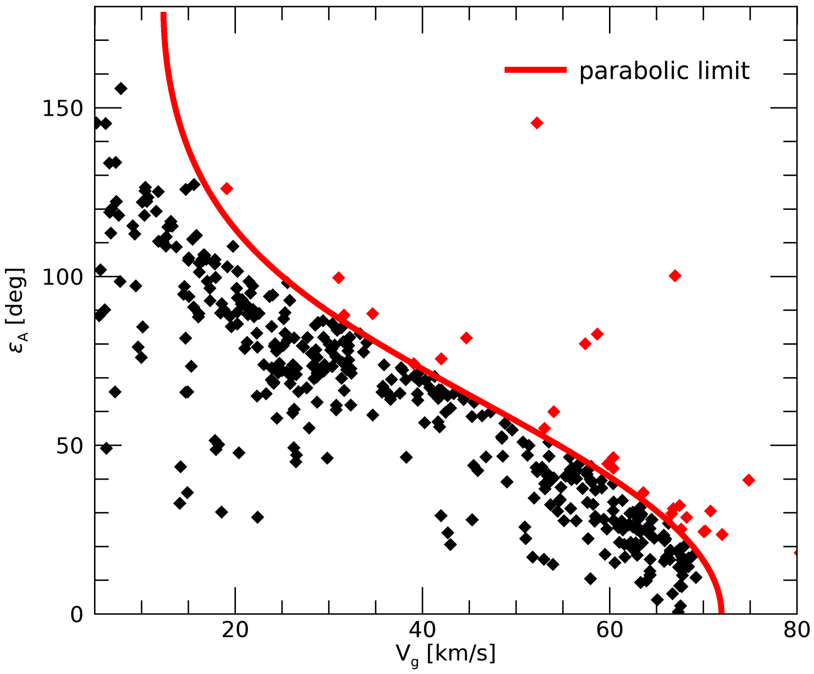

Fig. 7.12: Scatter plot on the Kresak's diagram of the 422 meteors detected on 01/09/2019 by two DIMS cameras installed at the TA site. Black diamonds correspond to elliptic orbits, while red ones are above the parabolic limit (red curve) and therefore geometrically hyperbolic, corresponding to 8.8% of the current dataset.

However, a detailed error estimation was not carried out for this preliminary analysis. During 2021 and 2022, DIMS deployed 3 cameras in Japan (at Kiso Observatory, Shinshu University and Akeno Observatory) and 2 cameras in Utah, USA at the TA site. These instruments, operating in automatic acquisition mode, will provide a very large database of meteor observations in next years. The analysis of these observations will be the argument of further work, thanks to the application of the complete version of PRISMA pipeline on this new dataset.

8

Conclusions

In this thesis, I discussed the importance of meteor studies in the framework of modern planetary sciences. The observation of meteors in the Earth's atmosphere provides an unique tool to probe the population of NEOs beyond the detectability limits of direct telescopic observations, and the invaluable opportunity to reconstruct their atmospheric trajectory. This enables the computation of their preatmospheric orbit, finally linked to the region of origin within the Solar System, and to estimate the area of probable fall for meteorite fragments, if a significant portion of the mass survived the atmospheric ablation. This concept is fully implemented in the PRISMA fireball network, partner of the FRIPON collaboration. I demonstrated that the technology deployed by FRIPON and PRISMA allows to constrain the trajectory of observed fireballs within a typical precision of $\sim$100 m and their preatmospheric speed within $\sim$0.1 km/s. Under reasonable assumptions about the state of the atmosphere and the geometry of the body, it is then possible to estimate the preatmospheric mass of the meteoroid, together with a wide set of secondary physical parameters that characterize the phenomenon. In particular, I discussed in detail the importance of an appropriate error estimation, that is crucial when evaluating the residual mass of the meteoroid and the likehood of meteorites to be recovered on the ground, just to cite one example.

Within 6 years of operations, the observations of PRISMA and the analysis pipeline presented in this manuscript enabled the recovery of two freshly-fallen "pedigree" meteorites, named Cavezzo and Matera, over the Italian soil. The analysis of the Cavezzo meteorite unveiled peculiar results that led to its classification as an L5-anomalous chondrite. Cavezzo is the first meteorite ever classified in this class. In particular, the two recovered specimens showed significant differences in their petrological features, bulk and isotopic composition, that led to believe that the smaller fragment of Cavezzo originated from a previously unsampled portion of the parent body of L chondrites. These results show how the meteoritic science benefits from an increasing recovery efficiency of fall meteorites, that is achieved by the operation of networks such as PRISMA and FRIPON. Also, the results of the γ-activity measurements of the main mass of Cavezzo highlighted a considerable discrepancy between the meteoroid's preatmospheric size, just before the fall, and the average dimensions of the body evaluated during its cosmic ray exposure age by the measured ^{26}Al concentration. While still being investigated, this evidence may suggest a recent impact event of the Cavezzo meteoroid in the last millions of years.

From the analysis of the data of the Mini-EUSO telescope, I also demonstrated the capabilities of space-based instruments in contributing to the field of meteoritic sciences. Within a quite limited observing time of 5.7 days, the observations of Mini-EUSO provided an extensive database of meteor events up to a +7 limiting absolute magnitude, proving the potentiality of space-based observations to significantly increase the statistics achievable with instruments operating on the ground. I reviewed the technical limitations of Mini-EUSO in the observation of meteors and explained how these can be overcome with reasonable assumptions, and how they reflect on the uncertainty on the physical parameters of observed events. Mini-EUSO is able to measure the horizontal speed to the precision of few km/s, the azimuth direction within few degrees and the absolute luminosity of meteors within few tenths of magnitude. Thanks to the development of dedicated simulations to estimate the total exposure time of Mini-EUSO for the observation of meteors, it was possible to provide an estimation of the absolute flux density of meteors that was found to be compatible with other results available in the literature.

Finally, I discussed the importance of the error treatment in the identification of candidates for interstellar meteors in meteor observation databases. A new statistical analysis suggested that the high fraction of hyperbolic events is artificially given by an underestimation of the errors on the measured speed and radiant position values. This was not the case for the data of FRIPON, for which I proved that an appropriate error estimation is provided, leading to a fraction of hyperbolic events that is indeed compatible with the expected residual outlier fraction at the chosen confidence level. The same technique was adapted for the case of Mini-EUSO, and the statistical analysis of its meteor database revealed three potential candidates of interstellar meteors, that are now subject of further investigations to definitively test the significance of this finding. I also adapted the same reduction procedure developed for the case of PRISMA to the observations of DIMS, a new experiment specifically designed for the detection of interstellar meteors. Beyond the field of meteoritic science, the night-time monitoring of meteors of DIMS was used to provide an upper limit to the flux of exotic hypothetical objects such as nuclearites, a candidate of macroscopic dark matter.

Bibliography

Abbasi, R. U., Abe, M., Abu-Zayyad, T., et al. (2018). “Evidence of Intermediate-scale Energy Spectrum Anisotropy of Cosmic Rays E $\geq 10^{19.2}$ eV with the Telescope Array Surface Detector”. In: *The Astrophysical Journal* 862.2, 91, p. 91. arXiv: `1802.05003 [astro-ph.HE]` (cit. on p. 63).

Abdellaoui, G., Abe, S., Acheli, A., et al. (2017a). “Cosmic ray oriented performance studies for the JEM-EUSO first level trigger”. In: *Nuclear Instruments and Methods in Physics Research A* 866, pp. 150–163 (cit. on p. 66).

Abdellaoui, G., Abe, S., Acheli, A., et al. (2017b). “Meteor studies in the framework of the JEM-EUSO program”. In: *Planetary and Space Science* 143, pp. 245–255 (cit. on pp. 69, 70, 72).

Abdellaoui, G., Abe, S., Adams, J. H., et al. (2018). “EUSO-TA - First results from a ground-based EUSO telescope”. In: *Astroparticle Physics* 102, pp. 98–111 (cit. on p. 65).

Abdellaoui, G., Abe, S., Adams, J. H., et al. (2019). “Ultra-violet imaging of the night-time earth by EUSO-Balloon towards space-based ultra-high energy cosmic ray observations”. In: *Astroparticle Physics* 111, pp. 54–71 (cit. on p. 66).

Abdul Halim, A., Abreu, P., Aglietta, M., et al. (2023). “A Catalog of the Highest-energy Cosmic Rays Recorded during Phase I of Operation of the Pierre Auger Observatory”. In: *The Astrophysical Journal Supplement Series* 264.2, 50, p. 50 (cit. on p. 63).

Abe, S., Arahori, M., Barghini, D., et al. (2022). “DIMS Experiment for Dark Matter and Interstellar Meteoroid Study”. In: *37th International Cosmic Ray Conference*, 554, p. 554 (cit. on p. 217).

Adams, J. H., Ahmad, S., Albert, J. N., et al. (2015a). “JEM-EUSO: Meteor and nuclearite observations”. In: *Experimental Astronomy* 40.1, pp. 253–279 (cit. on pp. 69, 72).

Adams, J. H., Ahmad, S., Albert, J. N., et al. (2015b). “JEM-EUSO observational technique and exposure”. In: *Experimental Astronomy* 40.1, pp. 117–134 (cit. on p. 63).

Adams, J. H., Ahmad, S., Albert, J. N., et al. (2015c). “Space experiment TUS on board the Lomonosov satellite as pathfinder of JEM-EUSO”. In: *Experimental Astronomy* 40.1, pp. 315–326 (cit. on p. 66).

Adams, J. H., Ahmad, S., Albert, J. N., et al. (2015d). “The EUSO-Balloon pathfinder”. In: *Experimental Astronomy* 40.1, pp. 281–299 (cit. on p. 66).

Adams, J. H., Ahmad, S., Albert, J. N., et al. (2015e). “The JEM-EUSO mission: An introduction”. In: *Experimental Astronomy* 40.1, pp. 3–17 (cit. on p. 64).

Adams, J. H., Ahmad, S., Allard, D., et al. (2022). "A Review of the EUSO-Balloon Pathfinder for the JEM-EUSO Program". In: *Space Science Reviews* 218.1, 3, p. 3 (cit. on p. 66).

Agostinelli, S., Allison, J., Amako, K., et al. (2003). "GEANT4 - a simulation toolkit". In: *Nuclear instruments and methods in physics research section A: Accelerators, Spectrometers, Detectors and Associated Equipment* 506.3, pp. 250–303 (cit. on p. 161).

Allison, J., Amako, K., Apostolakis, J., et al. (2006). "Geant4 developments and applications". In: *IEEE Transactions on Nuclear Science* 53.1, pp. 270–278 (cit. on p. 161).

Allison, J., Amako, K., Apostolakis, J., et al. (2016). "Recent developments in GEANT4". In: *Nuclear Instruments and Methods in Physics Research A* 835, pp. 186–225 (cit. on p. 161).

Alvarez, Luis W., Alvarez, Walter, Asaro, Frank, and Michel, Helen V. (1980). "Extraterrestrial Cause for the Cretaceous-Tertiary Extinction". In: *Science* 208.4448, pp. 1095–1108 (cit. on p. 24).

Andrade, Manuel, Docobo, José Á., García-Guinea, Javier, et al. (2023). "The Traspena meteorite: heliocentric orbit, atmospheric trajectory, strewn field, and petrography of a new L5 ordinary chondrite". In: *Monthly Notices of the Royal Astronomical Society* 518.3, pp. 3850–3876 (cit. on p. 52).

Astapovich, I. S. (1958). *Meteor Phenomena in the Earth Atmosphere* (cit. on p. 27).

Asvestari, E., Usoskin, I. G., Kovaltsov, G. A., et al. (2017). "Assessment of different sunspot number series using the cosmogenic isotope ^{44}Ti in meteorites". In: *Monthly Notices of the Royal Astronomical Society* 467, pp. 1608–1613 (cit. on p. 158).

Audureau, Y., Marmo, C., Bouley, S., et al. (2014). "FreeTure: A Free software to capTure meteors for FRIPON". In: *Proceedings of the 33th International Meteor Conference, Giron, France, 18-21 September 2014*. Ed. by J.-L. Rault and P. Roggemans, pp. 39–41 (cit. on p. 57).

Babadzhanov, P. B. (2002). "Fragmentation and densities of meteoroids". In: *Astronomy and Astrophysics* 384, pp. 317–321 (cit. on p. 32).

Bacholle, S., Barrillon, P., Battisti, M., et al. (2021). "Mini-EUSO Mission to Study Earth UV Emissions on board the ISS". In: *The Astrophysical Journal Supplement Series* 253.2, 36, p. 36. arXiv: `2010.01937 [astro-ph.IM]` (cit. on pp. 72–76, 183).

Bagheri, M., Bertone, P., Fontane, I., et al. (2022). "Overview of Cherenkov Telescope onboard EUSO-SPB2 for the Detection of Very-High-Energy Neutrinos". In: *37th International Cosmic Ray Conference*, 1191, p. 1191. arXiv: `2109.01789 [astro-ph.IM]` (cit. on p. 66).

Bannister, S. M., Boucheron, L. E., and Voelz, D. G. (2013). "A Numerical Analysis of a Frame Calibration Method for Video-based All-Sky Camera Systems". In: *Publications of the Astronomical Society of the Pacific* 125, p. 1108 (cit. on pp. 84, 85).

Barghini, D., Gardiol, D., and Carbognani, A. (2019a). "Improving astrometry and photometry reduction for PRISMA all-sky cameras". In: *International Meteor Conference, Pezinok-Modra, Slovakia*. Ed. by Regina Rudawska, Jurgen Rendtel, Charles Powell, et al., pp. 41–45 (cit. on pp. 59, 82).

Barghini, D., Gardiol, D., Carbognani, A., and Mancuso, S. (2019b). "Astrometric calibration for all-sky cameras revisited". In: *Astronomy and Astrophysics* 626, A105, A105 (cit. on pp. 82, 83, 86–93, 107, 108).

Barghini, D., Valenti, S., Abe, S., et al. (2021). “Meteor observation with the DIMS project: sensor calibration and first results”. In: *WGN, Journal of the International Meteor Organization* 49.6, pp. 173–180 (cit. on pp. 217, 220).

Barghini, D., Valenti, S., Abe, S., et al. (2022a). “Characterization of the DIMS system based on astronomical meteor techniques for macroscopic dark matter search”. In: *37th International Cosmic Ray Conference*, 500, p. 500 (cit. on pp. 72, 217, 218, 221, 222).

Barghini, Dario, Bertaina, Mario, Cellino, Alberto, et al. (2022b). “UV telescope TUS on board Lomonosov satellite: Selected results of the mission”. In: *Advances in Space Research* 70.9, pp. 2734–2749 (cit. on p. 66).

Battisti, M., Barghini, D., Belov, A., et al. (2022a). “Onboard performance of the level 1 trigger of the mini-EUSO telescope”. In: *Advances in Space Research* 70.9, pp. 2750–2766 (cit. on p. 76).

Battisti, M., Bayer, J., Bertaina, M., et al. (2019). “Performance results of the trigger logic implemented in EUSO-SPB”. In: *Nuclear Instruments and Methods in Physics Research A* 936, pp. 349–350 (cit. on p. 66).

Battisti, Matteo, Barghini, Dario, Belov, Alexander, et al. (2022b). “An end-to-end in-flight calibration of the Mini-EUSO detector”. In: *44th COSPAR Scientific Assembly. Held 16-24 July*. Vol. 44, p. 2136 (cit. on p. 75).

Battisti, Matteo, Belov, A., Bertaina, M. E., et al. (2023). “EUSO-SPB2 Fluorescence Telescope trigger test within the EUSO@TurLab Project”. In: *Nuclear Instruments and Methods in Physics Research A* 1045, 167611, p. 167611 (cit. on p. 66).

Beer, J., McCracken, K., and Steiger, R. (2012). *Cosmogenic radionuclides: theory and applications in the terrestrial and space environments*. Springer Science & Business Media (cit. on p. 158).

Bell, Jeffrey F., Davis, Donald R., Hartmann, William K., and Gaffey, Michael J. (1989). “Asteroids: the big picture.” In: *Asteroids II*. Ed. by Richard P. Binzel, Tom Gehrels, and Mildred Shapley Matthews, pp. 921–945 (cit. on p. 17).

Belov, Alexander, Bertaina, Mario, Capel, Francesca, et al. (2018). “The integration and testing of the Mini-EUSO multi-level trigger system”. In: *Advances in Space Research* 62.10, pp. 2966–2976. arXiv: `1711.02376 [astro-ph.IM]` (cit. on p. 76).

Benedix, G. K., Haack, H., and McCoy, T. J. (2014). “Iron and Stony-Iron Meteorites”. In: *Meteorites and Cosmochemical Processes*. Ed. by Andrew M. Davis. Vol. 1, pp. 267–285 (cit. on p. 44).

Benson, R. and Linsley, J. (1981). “Satellite Observation of Cosmic-Ray Air Showers”. In: *International Cosmic Ray Conference*. Vol. 8. International Cosmic Ray Conference, p. 145 (cit. on p. 63).

Bertaina, M. E. et al. (2022). “An overview of the JEM-EUSO program and results”. In: *37th International Cosmic Ray Conference*, 406, p. 406. arXiv: `2112.09954 [physics.space-ph]` (cit. on pp. 64, 65).

Bertaina, Mario (2019). “Results from the first missions of the JEM-EUSO program”. In: *European Physical Journal Web of Conferences*. Vol. 210. European Physical Journal Web of Conferences, 05009, p. 05009 (cit. on p. 65).

Bessell, Michael and Murphy, Simon (2012). “Spectrophotometric Libraries, Revised Photonic Passbands, and Zero Points for UBVRI, Hipparcos, and Tycho Photometry”. In: *Publications of the Astronomical Society of the Pacific* 124.912, p. 140. arXiv: `1112.2698 [astro-ph.SR]` (cit. on pp. 58, 97, 98).

Bhandari, N., Bonino, G., Callegari, E., et al. (1989). “The Torino, H6, Meteorite Shower”. In: *Meteoritics* 24.1, p. 29 (cit. on p. 161).

Bhandari, N., Bonino, G., Castagnoli, G. Cini, and Taricco, C. (1994). “The 11-Year Solar Cycle Variation of Cosmogenic Isotope Production Rates in Chondrites”. In: *Meteoritics* 29.4, p. 443 (cit. on p. 162).

Bhandari, N., Mathew, K. J., Rao, M. N., et al. (1993). “Depth and size dependence of cosmogenic nuclide production rates in stony meteoroids”. In: *Geochimica Cosmochimica Acta* 57, pp. 2361–2375 (cit. on p. 158).

Binzel, R. P. and Xu, S. (1993). “Chips off of Asteroid 4 Vesta: Evidence for the Parent Body of Basaltic Achondrite Meteorites”. In: *Science* 260.5105, pp. 186–191 (cit. on p. 46).

Bischoff, Addi, Barrat, Jean-Alix, Bauer, Kerstin, et al. (2017). “The Stubenberg meteorite—An LL6 chondrite fragmental breccia recovered soon after precise prediction of the strewn field”. In: *Meteorit. Planet. Sci.* 52.8, pp. 1683–1703 (cit. on p. 52).

Bischoff, Addi, Dyl, Kathryn A., Horstmann, Marian, et al. (2013). “Reclassification of Villalbeto de la Peña—Occurrence of a winonaite-related fragment in a hydrothermally metamorphosed polymict L-chondritic breccia”. In: *Meteorit. Planet. Sci.* 48.4, pp. 628–640 (cit. on p. 52).

Bischoff, Addi, Jersek, Miha, Grau, Thomas, et al. (2011). “Jesenice—A new meteorite fall from Slovenia”. In: *Meteorit. Planet. Sci.* 46.6, pp. 793–804 (cit. on p. 52).

Bisconti, F., Miyamoto, H., Barghini, D., et al. (2022). “Pre-flight qualification tests of the Mini-EUSO telescope engineering model”. In: *Experimental Astronomy* 53.1, pp. 133–158 (cit. on pp. 79, 80).

Bizzarri, I., Barghini, D., Colombetti, P., et al. (2023). “Cosmogenic radionuclides in the Cavezzo meteorite: Gamma-ray measurement and detection efficiency simulations”. In: *Applied Radiation and Isotopes*, p. 110651 (cit. on pp. 157–159, 161).

Bland, P. A. and Artemieva, N. A. (2006). “The rate of small impacts on Earth”. In: *Meteoritics and Planetary Science* 41, pp. 607–631 (cit. on p. 45).

Bland, P. A., Towner, M. C., Sansom, E. K., et al. (2016). “Fall and Recovery of the Murrili Meteorite, and an Update on the Desert Fireball Network”. In: *79th Annual Meeting of the Meteoritical Society*. Vol. 79, 6265, p. 6265 (cit. on p. 52).

Bland, Philip A., Spurný, Pavel, Towner, Martin C., et al. (2009). “An Anomalous Basaltic Meteorite from the Innermost Main Belt”. In: *Science* 325.5947, p. 1525 (cit. on p. 52).

Blin, S., Barrillon, P., de La Taille, C., et al. (2018). “SPACIROC3: 100 MHz photon counting ASIC for EUSO-SPB”. In: *Nuclear Instruments and Methods in Physics Research A* 912, pp. 363–367 (cit. on p. 76).

Bonino, G., Cini Castagnoli, G., Bhandari, N., and Taricco, C. (1995). “Behavior of the Heliosphere over Prolonged Solar Quiet Periods by ^{44}Ti Measurements in Meteorites”. In: *Science* 270, pp. 1648–1650 (cit. on p. 158).

Borovicka, J. (1993). “A fireball spectrum analysis”. In: *Astronomy and Astrophysics* 279.2, pp. 627–645 (cit. on p. 35).

Borovicka, J. (1994). “Two components in meteor spectra”. In: *Planetary and Space Science* 42.2, pp. 145–150 (cit. on p. 35).

Borovička, J. (1990). “The Comparison of Two Methods of Determining Meteor Trajectories from Photographs”. In: *Bulletin of the Astronomical Institutes of Czechoslovakia* 41, pp. 391–396 (cit. on pp. 109–111).

Borovička, J. (1992). “Astrometry with all-sky cameras”. In: *Publications of the Astronomical Institute of the Czechoslovak Academy of Sciences* 79 (cit. on pp. 83, 84).

Borovička, J. and Kalenda, P. (2003). “The Morávka meteorite fall: 4 Meteoroid dynamics and fragmentation in the atmosphere”. In: *Meteorit. Planet. Sci.* 38.7, pp. 1023–1043 (cit. on p. 52).

Borovička, J., Popova, O. P., Nemtchinov, I. V., Spurný, P., and Ceplecha, Z. (1998). “Bolides produced by impacts of large meteoroids into the Earth’s atmosphere: comparison of theory with observations. I. Benesov bolide dynamics and fragmentation”. In: *Astronomy and Astrophysics* 334, pp. 713–728 (cit. on pp. 52, 131).

Borovička, J., Spurný, P., Kalenda, P., and Tagliaferri, E. (2003a). “The Morávka meteorite fall: 1 Description of the events and determination of the fireball trajectory and orbit from video records”. In: *Meteorit. Planet. Sci.* 38.7, pp. 975–987 (cit. on p. 52).

Borovička, J., Spurny, P., and Keclikova, J. (1995). “A new positional astrometric method for all-sky cameras.” In: *Astronomy and Astrophysics Supplement Series* 112, pp. 173–178 (cit. on pp. 83, 93, 94).

Borovička, J., Weber, H. W., Jopek, T., et al. (2003b). “The Morávka meteorite fall: 3 Meteoroid initial size, history, structure, and composition”. In: *Meteorit. Planet. Sci.* 38.7, pp. 1005–1021 (cit. on p. 52).

Borovička, J. and Charvát, Z. (2009). “Meteosat observation of the atmospheric entry of 2008 TC_3 over Sudan and the associated dust cloud”. In: *Astronomy and Astrophysics* 507.2, pp. 1015–1022 (cit. on p. 52).

Borovička, J., Spurný, P., Šegon, D., et al. (2015). “The instrumentally recorded fall of the Križevci meteorite, Croatia, February 4, 2011”. In: *Meteorit. Planet. Sci.* 50.7, pp. 1244–1259 (cit. on p. 52).

Borovička, Jiří, Bettonvil, Felix, Baumgarten, Gerd, et al. (2021). “Trajectory and orbit of the unique carbonaceous meteorite Flensburg”. In: *Meteoritics and Planetary Science* 56.3, pp. 425–439. arXiv: `2101.02177 [astro-ph.EP]` (cit. on p. 52).

Borovička, Jiří, Popova, Olga, and Spurný, Pavel (2019). “The Maribo CM2 meteorite fall—Survival of weak material at high entry speed”. In: *Meteorit. Planet. Sci.* 54.5, pp. 1024–1041. arXiv: `1902.01112 [astro-ph.EP]` (cit. on p. 52).

Borovička, Jiří, Spurný, Pavel, Brown, Peter, et al. (2013a). “The trajectory, structure and origin of the Chelyabinsk asteroidal impactor”. In: *Nature* 503.7475, pp. 235–237 (cit. on p. 25).

Borovička, Jiří, Spurný, Pavel, Brown, Peter, et al. (2013b). “The trajectory, structure and origin of the Chelyabinsk asteroidal impactor”. In: *Nature* 503.7475, pp. 235–237 (cit. on p. 52).

Borovička, Jiří, Spurný, Pavel, and Shrbený, Lukáš (2020). “Two Strengths of Ordinary Chondritic Meteoroids as Derived from Their Atmospheric Fragmentation Modeling”. In: *The Astronomical Journal* 160.1, 42, p. 42. arXiv: `2006.07080 [astro-ph.EP]` (cit. on p. 52).

Borovička, Jiří, Tóth, Juraj, Igaz, Antal, et al. (2013c). “The Košice meteorite fall: Atmospheric trajectory, fragmentation, and orbit”. In: *Meteorit. Planet. Sci.* 48.10, pp. 1757–1779 (cit. on p. 52).

Botta, Oliver and Bada, Jeffrey L. (2002). “Extraterrestrial Organic Compounds in Meteorites”. In: *Surveys in Geophysics* 23.5, pp. 411–467 (cit. on p. 43).

Bottke William F., Jr., Vokrouhlický, David, Rubincam, David P., and Nesvorný, David (2006). “The Yarkovsky and Yorp Effects: Implications for Asteroid Dynamics”. In: *Annual Review of Earth and Planetary Sciences* 34, pp. 157–191 (cit. on pp. 23, 24).

Bottke, William F., Durda, Daniel D., Nesvorný, David, et al. (2005a). “Linking the collisional history of the main asteroid belt to its dynamical excitation and depletion”. In: *Icarus* 179.1, pp. 63–94 (cit. on pp. 9, 23).

Bottke, William F., Durda, Daniel D., Nesvorný, David, et al. (2005b). “The fossilized size distribution of the main asteroid belt”. In: *Icarus* 175.1, pp. 111–140 (cit. on pp. 9, 10, 23).

Bouquet, Alexis, Baratoux, David, Vaubaillon, Jérémie, et al. (2014). “Simulation of the capabilities of an orbiter for monitoring the entry of interplanetary matter into the terrestrial atmosphere”. In: *Planetary and Space Science* 103, pp. 238–249 (cit. on p. 194).

Bouvier, Audrey, Gattacceca, Jérôme, Agee, Carl, Grossman, Jeffrey, and Metzler, Knut (2017). “The Meteoritical Bulletin, No. 104”. In: *Meteorit. Planet. Sci.* 52.10, pp. 2284–2284 (cit. on p. 52).

Bronshten, V. A. (1983). *Physics of Meteoric Phenomena* (cit. on pp. 30, 33–35).

Brown, P., Ceplecha, Z., Hawkes, R. L., et al. (1994). “The orbit and atmospheric trajectory of the Peekskill meteorite from video records”. In: *Nature* 367.6464, pp. 624–626 (cit. on p. 52).

Brown, P., McCausland, P. J. A., Fries, M., et al. (2011). “The fall of the Grimsby meteorite—I: Fireball dynamics and orbit from radar, video, and infrasound records”. In: *Meteorit. Planet. Sci.* 46.3, pp. 339–363 (cit. on p. 52).

Brown, P., Pack, D., Edwards, W. N., et al. (2004). “The orbit, atmospheric dynamics, and initial mass of the Park Forest meteorite”. In: *Meteorit. Planet. Sci.* 39.11, pp. 1781–1796 (cit. on p. 52).

Brown, P., Spalding, R. E., ReVelle, D. O., Tagliaferri, E., and Worden, S. P. (2002a). “The flux of small near-Earth objects colliding with the Earth”. In: *Nature* 420.6913, pp. 294–296 (cit. on p. 45).

Brown, P. G., Assink, J. D., Astiz, L., et al. (2013). “A 500-kiloton airburst over Chelyabinsk and an enhanced hazard from small impactors”. In: *Nature* 503.7475, pp. 238–241 (cit. on pp. 25, 52).

Brown, P. G., Vida, D., Moser, D. E., et al. (2019). “The Hamburg meteorite fall: Fireball trajectory, orbit, and dynamics”. In: *Meteorit. Planet. Sci.* 54.9, pp. 2027–2045. arXiv: `1907.03008 [astro-ph.EP]` (cit. on p. 52).

Brown, Peter G., Hildebrand, Alan R., Zolensky, Michael E., et al. (2000). “The Fall, Recovery, Orbit, and Composition of the Tagish Lake Meteorite: A New Type of Carbonaceous Chondrite”. In: *Science* 290.5490, pp. 320–325 (cit. on p. 52).

Brown, Peter G., Revelle, Douglas O., Tagliaferri, Edward, and Hildebrand, Alan R. (2002b). “An entry model for the Tagish Lake fireball using seismic, satellite and infrasound records”. In: *Meteorit. Planet. Sci.* 37.5, pp. 661–675 (cit. on p. 52).

Brownlee, D. E. (2014). “Comets”. In: *Planets, Asteriods, Comets and The Solar System*. Ed. by Andrew M. Davis. Vol. 2, pp. 335–363 (cit. on p. 19).

Burbine, T. H. (2014). “Asteroids”. In: *Planets, Asteriods, Comets and The Solar System*. Ed. by Andrew M. Davis. Vol. 2, pp. 365–415 (cit. on pp. 7, 12, 15, 17).

Burbine, Thomas H., Meibom, Anders, and Binzel, Richard P. (1996). “Mantle material in the main belt: Battered to bits?” In: *Meteoritics & Planetary Science* 31.5, pp. 607–620 (cit. on p. 14).

Cambiè, G. and Marcelli, L. (2019). “Integration and testing of the Mini-EUSO telescope”. In: *European Physical Journal Web of Conferences*. Vol. 209. European Physical Journal Web of Conferences, 01047, p. 01047 (cit. on p. 78).

Campbell-Brown, M. D., Kero, J., Szasz, C., Pellinen-Wannberg, A., and Weryk, R. J. (2012). “Photometric and ionization masses of meteors with simultaneous EISCAT UHF radar and intensified video observations”. In: *Journal of Geophysical Research (Space Physics)* 117.A9, A09323, A09323 (cit. on p. 47).

Capel, F., Belov, A., Casolino, M., Klimov, P., and JEM-EUSO Collaboration (2018). “Mini-EUSO: A high resolution detector for the study of terrestrial and cosmic UV emission from the International Space Station”. In: *Advances in Space Research* 62, pp. 2954–2965. arXiv: `1709.00405 [astro-ph.IM]` (cit. on p. 72).

Capel, Francesca, Belov, Alexander, Cambiè, Giorgio, et al. (2019). “Mini-EUSO data acquisition and control software”. In: *Journal of Astronomical Telescopes, Instruments, and Systems* 5, 044009, p. 044009. arXiv: `1907.04938 [astro-ph.IM]` (cit. on pp. 76, 77).

Carbary, J. F., Morrison, D., Romick, G. J., and Yee, J. H. (2003). “Leonid meteor spectrum from 110 to 860 nm”. In: *Icarus* 161.2, pp. 223–234 (cit. on p. 69).

Carbognani, Albino, Barghini, D., Gardiol, D., et al. (2020). “A case study of the May 30, 2017, Italian fireball”. In: *European Physical Journal Plus* 135.2, 255, p. 255. arXiv: `1911.09555 [astro-ph.EP]` (cit. on pp. 145, 149–152).

Carbognani, Albino, Di Martino, Mario, and Stirpe, Giovanna (2023). “Computation of a possible Tunguska’s strewn field”. In: *arXiv e-prints*, arXiv:2302.13620, arXiv:2302.13620. arXiv: `2302.13620 [astro-ph.EP]` (cit. on p. 25).

Carter, R. T., Jandir, P. S., and Kress, M. E. (2009). “Estimating the Drag Coefficients of Meteorites for All Mach Number Regimes”. In: *40th Annual Lunar and Planetary Science Conference*. Lunar and Planetary Science Conference, 2059, p. 2059 (cit. on p. 124).

Carter, R. T., Jandir, P. S., and Kress, M. E. (2011). “Constraining the Drag Coefficients of Meteors in Dark Flight”. In: *Meteoroids: The Smallest Solar System Bodies*. Ed. by W. J. Cooke, D. E. Moser, B. F. Hardin, and D. Janches, p. 243 (cit. on p. 124).

Casolino, M., Barghini, D., Battisti, M., et al. (2023). “Observation of night-time emissions of the Earth in the near UV range from the International Space Station with the Mini-EUSO detector”. In: *Remote Sensing of Environment* 284, p. 113336. arXiv: `2212.02353 [astro-ph.IM]` (cit. on pp. 72, 78, 174, 175, 177, 183, 188, 189).

Casolino, M., Klimov, P., and Piotrowski, L. (2017). “Observation of ultra high energy cosmic rays from space: Status and perspectives”. In: *Progress of Theoretical and Experimental Physics* 2017.12, 12A107, 12A107 (cit. on p. 64).

Cellino, A., Bus, S. J., Doressoundiram, A., and Lazzaro, D. (2002). “Spectroscopic Properties of Asteroid Families”. In: *Asteroids III*, pp. 633–643 (cit. on p. 17).

Cellino, A. and Dell’Oro, A. (2010). “Asteroid Dynamical Families”. In: *Lecture Notes in Physics, Berlin Springer Verlag*. Ed. by J. Souchay and R. Dvorak. Vol. 790, pp. 137–193 (cit. on p. 16).

Ceplecha, Z. (1961). “Multiple fall of Příbram meteorites photographed. 1. Double-station photographs of the fireball and their relations to the found meteorites”. In: *Bulletin of the Astronomical Institutes of Czechoslovakia* 12, p. 21 (cit. on pp. 28, 48, 52, 112).

Ceplecha, Z. (1966). “Dynamic and photometric mass of meteors”. In: *Bulletin of the Astronomical Institutes of Czechoslovakia* 17, p. 347 (cit. on p. 47).

Ceplecha, Z. (1987). “Geometric, dynamic, orbital and photometric data on meteoroids from photographic fireball networks”. In: *Bulletin of the Astronomical Institutes of Czechoslovakia* 38, pp. 222–234 (cit. on pp. 82, 83, 108–110, 117, 134, 141).

Ceplecha, Z. (1996). “Luminous efficiency based on photographic observations of the Lost City fireball and implications for the influx of interplanetary bodies onto Earth.” In: *Astronomy and Astrophysics* 311, pp. 329–332 (cit. on p. 52).

Ceplecha, Z., Borovička, J., Elford, W. G., et al. (1998). “Meteor Phenomena and Bodies”. In: *Space Science Reviews* 84, pp. 327–471 (cit. on pp. 30, 31).

Ceplecha, Z. and McCrosky, R. E. (1976). “Fireball end heights: A diagnostic for the structure of meteoric material”. In: *Journal of Geophysical Research* 81.B35, pp. 6257–6275 (cit. on p. 203).

Ceplecha, Z. and Revelle, D. O. (2005). “Fragmentation model of meteoroid motion, mass loss, and radiation in the atmosphere”. In: *Meteorit. Planet. Sci.* 40, p. 35 (cit. on pp. 52, 123, 131).

Chapman, C. R. (1986). “Implications of the inferred compositions of asteroids for their collisional evolution”. In: *Memorie della Società Astronomica Italiana* 57.1, pp. 103–114 (cit. on p. 14).

Chapman, C. R., Morrison, D., and Zellner, B. (1975). “Surface Properties of Asteroids: A Synthesis of Polarimetry, Radiometry, and Spectrophotometry”. In: *Icarus* 25.1, pp. 104–130 (cit. on p. 17).

Chesley, Steven R., Chodas, Paul W., Milani, Andrea, Valsecchi, Giovanni B., and Yeomans, Donald K. (2002). “Quantifying the Risk Posed by Potential Earth Impacts”. In: *Icarus* 159.2, pp. 423–432 (cit. on p. 26).

Chladni, E. F. F. (1794). *Ueber den Ursprung der von Pallas gefundenen und anderer ihr ähnlicher Eisenmassen und über einige damit in Verbindung stehende Naturerscheinungen*. bey Johann Friedrich Hartknoch (cit. on p. 27).

Clark, D. L. and Wiegert, P. A. (2011). “A numerical comparison with the Ceplecha analytical meteoroid orbit determination method”. In: *Meteoritics and Planetary Science* 46, pp. 1217–1225 (cit. on p. 141).

Clavel, J., Parmar, Arvind N., and Catalano, O. S. A (2003). “The Extreme Universe Space Observatory (EUSO) Mission in the Context of ESA”. In: *International Cosmic Ray Conference*. Vol. 2. International Cosmic Ray Conference, p. 1073 (cit. on p. 64).

Colas, F., Zanda, B., Bouley, S., et al. (2020). “FRIPON: a worldwide network to track incoming meteoroids”. In: *Astronomy and Astrophysics* 644, A53, A53. arXiv: `2012.00616 [astro-ph.IM]` (cit. on pp. 54, 56, 57, 61, 209).

Colas, F., Zanda, B., Vernazza, P., et al. (2012). “(FRIPON) Fireball Recovery and Interplanetary Matter Observation Network”. In: *Asteroids, Comets, Meteors 2012*. Ed. by LPI Editorial Board. Vol. 1667. LPI Contributions, 6426, p. 6426 (cit. on p. 54).

Colas, François (2016). “Official launching of FRIPON”. In: *eMeteorNews* 1.2, pp. 67–68 (cit. on p. 56).

Colas, François, Zanda, Brigitte, Bouley, Sylvain, et al. (2014). “The FRIPON and Vigie-Ciel networks”. In: *Proceedings of the International Meteor Conference, Giron, France, 18-21 September 2014*. Ed. by J. L. Rault and P. Roggemans, pp. 34–38 (cit. on p. 57).

Coleman, A., Eser, J., Mayotte, E., et al. (2023). “Ultra high energy cosmic rays The intersection of the Cosmic and Energy Frontiers”. In: *Astroparticle Physics* 147, 102794, p. 102794. arXiv: `2205.05845 [astro-ph.HE]` (cit. on p. 63).

Colombetti, P., Taricco, C., Bhandari, N., et al. (2013). “Low γ activity measurement of meteorites using HPGe-NaI detector system”. In: *Nuclear Instruments and Methods in Physics Research A* 718, pp. 140–142 (cit. on p. 160).

Connolly, Harold C. and Jones, Rhian H. (2016). “Chondrules: The canonical and noncanonical views”. In: *Journal of Geophysical Research (Planets)* 121.10, pp. 1885–1899 (cit. on p. 43).

Connolly H. C., Jr., Desch, S. J., Ash, R. D., and Jones, R. H. (2006). “Transient Heating Events in the Protoplanetary Nebula”. In: *Meteorites and the Early Solar System II*. Ed. by Dante S. Lauretta and Harry Y. McSween, p. 383 (cit. on p. 42).

Consolmagno, G., Britt, D., and Macke, R. (2008). “The significance of meteorite density and porosity”. In: *Chemie der Erde / Geochemistry* 68.1, pp. 1–29 (cit. on p. 132).

Consolmagno, G. J., Britt, D. T., and Macke, R. J. (2011). “Cautionary tales about comparing meteorites to asteroids”. In: *EPSC-DPS Joint Meeting 2011*. Vol. 2011, p. 578 (cit. on p. 15).

De Rujula, A. and Glashow, S. L. (1984). “Nuclearites-a novel form of cosmic radiation”. In: *Nature* 312.5996, pp. 734–737 (cit. on pp. 71, 217, 218, 222).

DeMeo, Francesca E., Binzel, Richard P., Slivan, Stephen M., and Bus, Schelte J. (2009). “An extension of the Bus asteroid taxonomy into the near-infrared”. In: *Icarus* 202.1, pp. 160–180 (cit. on pp. 13, 14).

Devillepoix, H. A. R., Cupák, M., Bland, P. A., et al. (2020). “A Global Fireball Observatory”. In: *Planetary and Space Science* 191, 105036, p. 105036. arXiv: `2004.01069 [astro-ph.EP]` (cit. on p. 28).

Devillepoix, Hadrien A. R., Sansom, Eleanor K., Bland, Philip A., et al. (2018). “The Dingle Dell meteorite: A Halloween treat from the Main Belt”. In: *Meteorit. Planet. Sci.* 53.10, pp. 2212–2227. arXiv: `1803.02557 [astro-ph.EP]` (cit. on p. 52).

Devillepoix, Hadrien A. R., Sansom, Eleanor K., Shober, Patrick, et al. (2022). “Trajectory, recovery, and orbital history of the Madura Cave meteorite”. In: *Meteoritics and Planetary Science* 57.7, pp. 1328–1338. arXiv: `2202.06641 [astro-ph.EP]` (cit. on p. 52).

Dhingra, D., Bhandari, N., Shukla, P. N., et al. (2004). “Spectacular fall of the Kendrapara H5 chondrite”. In: *Meteoritics and Planetary Science* 39.S8, A121–A132 (cit. on p. 162).

Díaz Damian, A. (2019). “EUSO-SPB1: Flight Data Classification and Air Shower Search Results”. In: *36th International Cosmic Ray Conference (ICRC2019)*. Vol. 36. International Cosmic Ray Conference, 240, p. 240. arXiv: `1909.08323 [astro-ph.IM]` (cit. on p. 66).

Dielman, T. E. (2005). “Least absolute value regression: recent contributions”. In: *Journal of Statistical Computation and Simulation* 75.4, pp. 263–286 (cit. on p. 90).

Dmitriev, V., Lupovka, V., and Gritsevich, M. (2015). “Orbit determination based on meteor observations using numerical integration of equations of motion”. In: *Planetary and Space Science* 117, pp. 223–235 (cit. on p. 141).

Dohnanyi, J. S. (1969). “Collisional Model of Asteroids and Their Debris”. In: *Journal of Geophysical Research* 74, pp. 2531–2554 (cit. on p. 10).

Dones, Luke, Brasser, Ramon, Kaib, Nathan, and Rickman, Hans (2015). “Origin and Evolution of the Cometary Reservoirs”. In: *Space Science Reviews* 197.1-4, pp. 191–269 (cit. on p. 19).

Drolshagen, E., Ott, T., Koschny, D., et al. (2021). “Luminous efficiency based on FRIPON meteors and limitations of ablation models”. In: *Astronomy and Astrophysics* 650, A159, A159 (cit. on p. 127).

Dubyago, A. D. (1961). “The determination of orbits”. In: *New York* (cit. on p. 134).

Duncan, M., Quinn, T., and Tremaine, S. (1988). “The Origin of Short-Period Comets”. In: *Astrophysical Journal Letters* 328, p. L69 (cit. on p. 20).

Durda, Daniel D., Bottke, William F., Nesvorný, David, et al. (2007). “Size-frequency distributions of fragments from SPH/ N-body simulations of asteroid impacts: Comparison with observed asteroid families”. In: *Icarus* 186.2, pp. 498–516 (cit. on p. 9).

Dyl, Kathryn A., Benedix, Gretchen K., Bland, Phil A., et al. (2016). “Characterization of Mason Gully (H5): The second recovered fall from the Desert Fireball Network”. In: *Meteorit. Planet. Sci.* 51.3, pp. 596–613 (cit. on p. 52).

Ebisuzaki, Toshikazu, Quinn, Mark N., Wada, Satoshi, et al. (2015). “Demonstration designs for the remediation of space debris from the International Space Station”. In: *Acta Astronautica* 112, pp. 102–113 (cit. on p. 71).

Edwards, Wayne N (2009). “Meteor generated infrasound: Theory and observation”. In: *Infrasound monitoring for atmospheric studies*, pp. 361–414 (cit. on p. 35).

Emmert, J. T., Drob, D. P., Picone, J. M., et al. (2021). “NRLMSIS 2.0: A Whole Atmosphere Empirical Model of Temperature and Neutral Species Densities”. In: *Earth and Space Science* 8.3, e01321, e01321 (cit. on p. 124).

Eser, J. (2019). “Results of the EUSO-SPB1 flight”. In: *36th International Cosmic Ray Conference (ICRC2019)*. Vol. 36. International Cosmic Ray Conference, 247, p. 247. arXiv: 1909.03005 [astro-ph.IM] (cit. on p. 66).

Farinella, Paolo, Vokrouhlický, David, and Hartmann, William K. (1998). “Meteorite Delivery via Yarkovsky Orbital Drift”. In: *Icarus* 132.2, pp. 378–387 (cit. on p. 23).

Farnocchia, Davide, Tholen, David J., Micheli, Marco, et al. (2017). “Mass estimate and close approaches of near-Earth asteroid 2015 TC25”. In: *AAS/Division for Planetary Sciences Meeting Abstracts #49*. Vol. 49. AAS/Division for Planetary Sciences Meeting Abstracts, 100.09, p. 100.09 (cit. on p. 45).

Fernandez, J. A. (1980). “On the existence of a comet belt beyond Neptune”. In: *Monthly Notices of the Royal Astronomical Society* 192, pp. 481–491 (cit. on p. 20).

Fernández, Y. R., Li, J. Y., and Woodney, . . . L. M. (2015). “Asteroids and Comets”. In: *Treatise on Geophysics*. Ed. by Gerald Schubert, pp. 487–528 (cit. on pp. 7, 13, 19).

Ferrière, Ludovic (2021). *First "Austro" meteorite recovered in Styria since 1977*. https://austria-in-space.at/en/news/2021/austro_meteor_styria_en.php. Accessed: 2023-03-27 (cit. on p. 52).

Ferus, Martin, Petera, Lukáš, Koukal, Jakub, et al. (2020). “Elemental composition, mineralogy and orbital parameters of the Porangaba meteorite”. In: *Icarus* 341, 113670, p. 113670 (cit. on p. 52).

Filippatos, G., Battisti, M., Bertaina, M. E., et al. (2022a). “Expected Performance of the EUSO-SPB2 Fluorescence Telescope”. In: *37th International Cosmic Ray Conference*, 405, p. 405. arXiv: 2112.07561 [astro-ph.IM] (cit. on p. 66).

Filippatos, George, Battisti, Matteo, Belov, Alexander, et al. (2022b). “Development of a cosmic ray oriented trigger for the fluorescence telescope on EUSO-SPB2”. In: *Advances in Space Research* 70.9, pp. 2794–2803. arXiv: 2201.00794 [astro-ph.HE] (cit. on p. 66).

Flamini, E., Di Martino, M., and Coletta, A. (2019). *Encyclopedic Atlas of Terrestrial Impact Craters* (cit. on p. 32).

Foschini, L. (1999). “The meteoroid hazard for space navigation”. In: *IN: 2nd National Meeting of Planetary Sciences. Bormio (Italy) 25-31 January 1998. Proceedings*, pp. 131–138. arXiv: physics/9804026 [physics.space-ph] (cit. on p. 26).

Foschini, L. (2001). “On the atmospheric fragmentation of small asteroids”. In: *Astronomy and Astrophysics* 365, pp. 612–621. arXiv: astro-ph/0012256 [astro-ph] (cit. on p. 48).

Füllekrug, Martin, Mareev, Eugene A., and Rycroft, Michael J. (2006). *Sprites, Elves and Intense Lightning Discharges* (cit. on p. 71).

Gaffey, Michael J., Bell, Jeffrey F., Brown, R. Hamilton, et al. (1993). “Mineralogical Variations within the S-Type Asteroid Class”. In: *Icarus* 106.2, pp. 573–602 (cit. on p. 13).

Gaia Collaboration, Brown, A. G. A., Vallenari, A., et al. (2021). “Gaia Early Data Release 3. Summary of the contents and survey properties”. In: *Astronomy and Astrophysics* 649, A1, A1. arXiv: 2012.01533 [astro-ph.GA] (cit. on p. 85).

Gaia Collaboration, Prusti, T., de Bruijne, J. H. J., et al. (2016). “The Gaia mission”. In: *Astronomy and Astrophysics* 595, A1, A1. arXiv: 1609.04153 [astro-ph.IM] (cit. on p. 84).

Gardiol, D., Barghini, D., Buzzoni, A., et al. (2021). “Cavezzo, the first Italian meteorite recovered by the PRISMA fireball network. Orbit, trajectory, and strewn-field”. In: *Monthly Notices of the Royal Astronomical Society* 501.1, pp. 1215–1227 (cit. on pp. 48, 50, 52, 144, 145, 147, 149–152, 154).

Gardiol, D., Barghini, D., Colombetti, P., et al. (2017). “Improvement of the extraction method of faint signals in γ -activity measurements of meteorites”. In: *European Physical Journal Plus* 132, 269, p. 269 (cit. on pp. 157, 161).

Gardiol, D., Cellino, A., and Di Martino, M. (2016). “PRISMA, Italian network for meteors and atmospheric studies”. In: *Proceedings of the 35th International Meteor Conference Egmond, the Netherlands, 2-5 June 2016*. Ed. by A. Roggemans and P. Roggemans, p. 76 (cit. on p. 54).

Gargaud, M., Amils, R., Quintanilla, J. C., et al. (2011). *Encyclopedia of Astrobiology* (cit. on p. 6).

Gattacceca, Jérôme, MCcubbin, Francis M., Bouvier, Audrey, and Grossman, Jeffrey (2020a). “The Meteoritical Bulletin, No. 107”. In: *Meteorit. Planet. Sci.* 55.2, pp. 460–462 (cit. on p. 52).

Gattacceca, Jérôme, McCubbin, Francis M., Bouvier, Audrey, and Grossman, Jeffrey N. (2020b). “The Meteoritical Bulletin, no. 108”. In: *Meteoritics and Planetary Science* 55.5, pp. 1146–1150 (cit. on p. 52).

Gattacceca, Jérôme, McCubbin, Francis M., Grossman, Jeffrey, et al. (2021). “The Meteoritical Bulletin, No. 109”. In: *Meteoritics and Planetary Scienceps* 56.8, pp. 1626–1630 (cit. on p. 155).

Gattacceca, Jérôme, MCCubbin, Francis M., Grossman, Jeffrey, et al. (2022). “The Meteoritical Bulletin, No. 110”. In: *Meteoritics and Planetary Science* 57.11, pp. 2102–2105 (cit. on pp. 38, 52).

Gianiglio, G., Ostillio, A., and Santangelo, A. (2003). “EUSO in the Context of ESA Human Spaceflight Directorate”. In: *International Cosmic Ray Conference*. Vol. 2. International Cosmic Ray Conference, p. 1093 (cit. on p. 64).

Gladman, B. J., Migliorini, F., Morbidelli, A., et al. (1997). “Dynamical lifetimes of objects injected into asteroid belt resonances”. In: *Science* 277, pp. 197–201 (cit. on p. 23).

Gladman, Brett J., Davis, Donald R., Neese, Carol, et al. (2009). “On the asteroid belt’s orbital and size distribution”. In: *Icarus* 202.1, pp. 104–118 (cit. on p. 9).

Gomes, R., Levison, H. F., Tsiganis, K., and Morbidelli, A. (2005). “Origin of the cataclysmic Late Heavy Bombardment period of the terrestrial planets”. In: *Nature* 435.7041, pp. 466–469 (cit. on p. 24).

Gradie, Jonathan C., Chapman, Clark R., and Tedesco, Edward F. (1989). “Distribution of taxonomic classes and the compositional structure of the asteroid belt.” In: *Asteroids II*. Ed. by Richard P. Binzel, Tom Gehrels, and Mildred Shapley Matthews, pp. 316–335 (cit. on p. 17).

Grady, Monica, Pratesi, Giovanni, and Moggi Cecchi, Vanni (2014). *Atlas of Meteorites* (cit. on pp. 39, 40).

Granvik, M. and Brown, P. (2018). “Identification of meteorite source regions in the Solar System”. In: *Icarus* 311, pp. 271–287. arXiv: `1804.07229 [astro-ph.EP]` (cit. on pp. 48, 91).

Green, Richard F., Luginbuhl, Christian B., Wainscoat, Richard J., and Duriscoe, Dan (2022). “The growing threat of light pollution to ground-based observatories”. In: *The Astronomy and Astrophysics Review* 30.1, 1, p. 1 (cit. on p. 55).

Greenwood, Richard C., Burbine, Thomas H., and Franchi, Ian A. (2020). “Linking asteroids and meteorites to the primordial planetesimal population”. In: *Geochimica et Cosmochimica Acta* 277, pp. 377–406 (cit. on pp. 46, 47).

Gritsevich, M. and Koschny, D. (2011). “Constraining the luminous efficiency of meteors”. In: *Icarus* 212, pp. 877–884 (cit. on pp. 120, 122–124, 127, 193).

Gritsevich, M. I. (2007). “Approximation of the observed motion of bolides by the analytical solution of the equations of meteor physics”. In: *Solar System Research* 41.6, pp. 509–514 (cit. on pp. 120–122).

Gritsevich, M. I. (2009). “Determination of parameters of meteor bodies based on flight observational data”. In: *Advances in Space Research* 44, pp. 323–334 (cit. on pp. 120, 124, 127).

Gronchi, G. F. and Milani, A. (2001). “Proper Elements for Earth-Crossing Asteroids”. In: *Icarus* 152.1, pp. 58–69 (cit. on p. 151).

Grun, E., Zook, H. A., Baguhl, M., et al. (1993). “Discovery of Jovian dust streams and interstellar grains by the Ulysses spacecraft”. In: 362.6419, pp. 428–430 (cit. on p. 206).

Grun, E., Zook, H. A., Fechtig, H., and Giese, R. H. (1985). “Collisional balance of the meteoritic complex”. In: *Icarus* 62.2, pp. 244–272 (cit. on pp. 202, 203).

Haack, H., Sørensen, A. N., Bischoff, A., et al. (2019). “Ejby - A new H5/6 ordinary chondrite fall in Copenhagen, Denmark”. In: *Meteorit. Planet. Sci.* 54.8, pp. 1853–1869 (cit. on p. 52).

Haack, Henning, Grau, Thomas, Bischoff, Addi, et al. (2012). “Maribo—A new CM fall from Denmark”. In: *Meteorit. Planet. Sci.* 47.1, pp. 30–50 (cit. on p. 52).

Hajduková Mária, Jr., Sterken, Veerle, and Wiegert, Paul (2019). “Interstellar Meteoroids”. In: *Meteoroids: Sources of Meteors on Earth and Beyond*. Ed. by Galina O. Ryabova, David J. Asher, and Margaret J. Campbell-Brown, p. 235 (cit. on pp. 205–208).

Hajduková, Mária and Kornoš, Leonard (2020). “The influence of meteor measurement errors on the heliocentric orbits of meteoroids”. In: *Planetary and Space Science* 190, 104965, p. 104965 (cit. on p. 209).

Hajduková, Maria, Sterken, Veerle, Wiegert, Paul, and Kornoš, Leonard (2020). “The challenge of identifying interstellar meteors”. In: *Planetary and Space Science* 192, 105060, p. 105060 (cit. on p. 208).

Halliday, I., Griffin, A. A., and Blackwell, A. T. (1981). “The Innisfree Meteorite Fall: A Photographic Analysis of Fragmentation, Dynamics and Luminosity”. In: *Meteoritics* 16.2, p. 153 (cit. on p. 52).

Harris, Alan W. and Harris, Alan W. (1997). “On the Revision of Radiometric Albedos and Diameters of Asteroids”. In: *Icarus* 126.2, pp. 450–454 (cit. on p. 9).

Hawkins, Gerald S. and Upton, Edward K. L. (1958). “The Influx Rate of Meteors in the Earth’s Atmosphere.” In: *Astrophysical Journal* 128, p. 727 (cit. on p. 192).

Hezel, Dominik C. and Russell, Sara S. (2008). “Comment on “Ancient Asteroids Enriched in Refractory Inclusions””. In: *Science* 322.5904, p. 1050 (cit. on p. 14).

Hildebrand, A. R., Milley, E. P., Brown, P. G., et al. (2009). “Characteristics of a Bright Fireball and Meteorite Fall at Buzzard Coulee, Saskatchewan, Canada, November 20, 2008”. In: *Lunar and Planetary Science Conference*. Lunar and Planetary Science Conference, 2505, p. 2505 (cit. on p. 52).

Hildebrand, Alan R., McCausland, Phil J. A., Brown, Peter G., et al. (2006). “The fall and recovery of the Tagish Lake meteorite”. In: *Meteorit. Planet. Sci.* 41.3, pp. 407–431 (cit. on p. 52).

Hirayama, Kiyotsugu (1918). “Groups of asteroids probably of common origin”. In: *Astronomical Journal* 31, pp. 185–188 (cit. on p. 16).

Hiroi, Takahiro and Hasegawa, Sunao (2003). “Revisiting the search for the parent body of the Tagish Lake meteorite - Case of a T/D asteroid 308 Polyxo”. In: *Antarctic Meteorite Research* 16, pp. 176–184 (cit. on p. 14).

Hiroi, Takahiro, Zolensky, Michael E., and Pieters, Carle M. (2001). “The Tagish Lake Meteorite: A Possible Sample from a D-Type Asteroid”. In: *Science* 293.5538, pp. 2234–2236 (cit. on p. 14).

Høg, E., Bässgen, G., Bastian, U., et al. (1997). “The TYCHO Catalogue”. In: *Astronomy and Astrophysics* 323, pp. L57–L60 (cit. on p. 84).

Høg, E., Fabricius, C., Makarov, V. V., et al. (2000). “The Tycho-2 catalogue of the 2.5 million brightest stars”. In: *Astronomy and Astrophysics* 355, pp. L27–L30 (cit. on p. 84).

Hölker, Franz, Wolter, Christian, Perkin, Elizabeth K, Tockner, Klement, et al. (2010). “Light pollution as a biodiversity threat”. In: *Trends Ecol. Evol* 25.12, pp. 681–682 (cit. on p. 55).

Hughes, C., Denny, P., Jones, E., and Glavin, M. (2010). “Accuracy of fish-eye lens models”. In: *Applied Optics* 49, p. 3338 (cit. on p. 94).

Hull, Pincelli M., Bornemann, André, Penman, Donald E., et al. (2020). “On impact and volcanism across the Cretaceous-Paleogene boundary”. In: *Science* 367.6475, pp. 266–272 (cit. on p. 24).

Hunter, J. D. (2007). “Matplotlib: A 2D graphics environment”. In: *Computer Science and Engineering* 9.3, pp. 90–95 (cit. on p. 144).

Jacobs, David M., Starkman, Glenn D., and Lynn, Bryan W. (2015). “Macro dark matter”. In: *Monthly Notices of the Royal Astronomical Society* 450.4, pp. 3418–3430. arXiv: `1410.2236 [astro-ph.CO]` (cit. on p. 217).

Jansen-Sturgeon, Trent, Sansom, Eleanor K., and Bland, Philip A. (2019). “Comparing analytical and numerical approaches to meteoroid orbit determination using Hayabusa telemetry”. In: *Meteoritics and Planetary Science* 54.9, pp. 2149–2162. arXiv: `1808.05768 [astro-ph.EP]` (cit. on p. 141).

Jeanne, S., Colas, F., Zanda, B., et al. (2019). “Calibration of fish-eye lens and error estimation on fireball trajectories: application to the FRIPON network”. In: *Astronomy and Astrophysics* 627, A78, A78 (cit. on pp. 116–118, 124, 145, 209).

Jechow, Andreas, Kolláth, Zoltán, Ribas, Salvador J., et al. (2017). “Imaging and mapping the impact of clouds on skyglow with all-sky photometry”. In: *Scientific Reports* 7, 6741, p. 6741. arXiv: `1705.04968 [astro-ph.IM]` (cit. on p. 55).

Jenniskens, P., Shaddad, M. H., Numan, D., et al. (2009). “The impact and recovery of asteroid 2008 TC_3”. In: *Nature* 458.7237, pp. 485–488 (cit. on p. 52).

Jenniskens, Peter (2007). “Meteor showers and their parent comets”. In: *Proceedings of the International Meteor Conference, 25th IMC, Roden, Netherlands, 2006*. Ed. by Felix Bettonvil and Javor Kac, pp. 56–62 (cit. on pp. 29, 30).

Jenniskens, Peter, Albers, Jim, Tillier, Clemens E., et al. (2018a). “Detection of meteoroid impacts by the Geostationary Lightning Mapper on the GOES-16 satellite”. In: *Meteoritics and Planetary Science* 53.12, pp. 2445–2469 (cit. on p. 69).

Jenniskens, Peter, Baggaley, Jack, Crumpton, Ian, et al. (2018b). “A survey of southern hemisphere meteor showers”. In: *Planetary and Space Science* 154, pp. 21–29 (cit. on pp. 193, 209).

Jenniskens, Peter, Fries, Marc D., Yin, Qing-Zhu, et al. (2012). “Radar-Enabled Recovery of the Sutter’s Mill Meteorite, a Carbonaceous Chondrite Regolith Breccia”. In: *Science* 338.6114, p. 1583 (cit. on p. 52).

Jenniskens, Peter, Gabadirwe, Mohutsiwa, Yin, Qing-Zhu, et al. (2021). “The impact and recovery of asteroid 2018 LA”. In: *Meteoritics and Planetary Science* 56.4, pp. 844–893. arXiv: `2105.05997 [astro-ph.EP]` (cit. on p. 52).

Jenniskens, Peter, Moskovitz, Nick, Garvie, Laurence A. J., et al. (2020). “Orbit and origin of the LL7 chondrite Dishchii’bikoh (Arizona)”. In: *Meteorit. Planet. Sci.* 55.3, pp. 535–557 (cit. on p. 52).

Jenniskens, Peter, Rubin, Alan E., Yin, Qing-Zhu, et al. (2014). “Fall, recovery, and characterization of the Novato L6 chondrite breccia”. In: *Meteorit. Planet. Sci.* 49.8, pp. 1388–1425 (cit. on p. 52).

Jenniskens, Peter, Tedesco, Ed, Murthy, Jayant, Laux, Christophe O., and Price, Stephen (2002). “Spaceborne ultraviolet 251-384 nm spectroscopy of a meteor during the 1997 Leonid shower”. In: *Meteoritics and Planetary Science* 37.8, pp. 1071–1078 (cit. on p. 69).

Jenniskens, Peter, Utas, Jason, Yin, Qing-Zhu, et al. (2019). “The Creston, California, meteorite fall and the origin of L chondrites”. In: *Meteorit. Planet. Sci.* 54.4, pp. 699–720 (cit. on pp. 48, 52).

Jewitt, D. and Luu, J. (1993). “Discovery of the candidate Kuiper belt object 1992 QB_1”. In: *Nature* 362.6422, pp. 730–732 (cit. on p. 21).

Jones, Rhian H. (2012). “Petrographic constraints on the diversity of chondrule reservoirs in the protoplanetary disk”. In: *Meteoritics and Planetary Science* 47.7, pp. 1176–1190 (cit. on p. 42).

Jopek, Tadeusz J., Hajduková, Mária, Rudawska, Regina, et al. (2023). “New nomenclature rules for meteor showers adopted”. In: *New Astronomy Reviews* 96, 101671, p. 101671 (cit. on p. 30).

Kajino, F., Takami, S., Nagasawa, M., et al. (2017). “Study of Fast Moving Nuclearites and Meteoroids using High Sensitivity CMOS Camera with EUSO-TA”. In: *35th International Cosmic Ray Conference (ICRC2017)*. Vol. 301. International Cosmic Ray Conference, 924, p. 924 (cit. on p. 217).

Kalashev, Oleg, Pshirkov, Maxim, and Zotov, Mikhail (2019). “Prospects of detecting a large-scale anisotropy of ultra-high-energy cosmic rays from a nearby source with the K-EUSO orbital telescope”. In: *Journal of Cosmology and Astroparticle Physics* 2019.9, 034, p. 034. arXiv: `1810.02284 [astro-ph.HE]` (cit. on p. 67).

Kartashova, Anna, Golubaev, Alexander, Mozgova, Alona, et al. (2020). “Investigation of the Ozerki meteoroid parameters”. In: *Planetary and Space Science* 193, 105034, p. 105034 (cit. on p. 52).

Kasuga, T., Watanabe, J., and Ebizuka, N. (2005). “A 2004 Geminid meteor spectrum in the visible-ultraviolet region. Extreme Na depletion?” In: *Astronomy and Astrophysics* 438.2, pp. L17–L20 (cit. on p. 69).

Keller, G., Adatte, T., Gardin, S., Bartolini, A., and Bajpai, S. (2008). “Main Deccan volcanism phase ends near the K-T boundary: Evidence from the Krishna-Godavari Basin, SE India”. In: *Earth and Planetary Science Letters* 268.3-4, pp. 293–311 (cit. on p. 24).

Khanukaeva, D. Yu. (2004). “Calculation of Variable Drag and Heat-Transfer Coefficients in Meteoric Physics Equations”. In: *Earth Moon and Planets* 95.1-4, pp. 433–439 (cit. on p. 124).

Kővágó, G. (2021). “Possible meteorite fall in Austria”. In: *eMeteorNews* 6.1, pp. 87–89 (cit. on p. 52).

Khrenov, B. A. (2002). “Design and development of space experiments KLYPVE and TUS for study of UHECR”. In: *Nuclear Physics B Proceedings Supplements* 113.1, pp. 115–122 (cit. on p. 67).

Khrenov, B. A., Garipov, G. K., Kaznacheeva, M. A., et al. (2020). “An extensive-air-shower-like event registered with the TUS orbital detector”. In: *Journal of Cosmology and Astroparticle Physics* 2020.3, 033, p. 033. arXiv: `1907.06028 [astro-ph.HE]` (cit. on p. 67).

Kikwaya, J. B., Campbell-Brown, M., and Brown, P. G. (2011). “Bulk density of small meteoroids”. In: *Astronomy and Astrophysics* 530, A113, A113 (cit. on p. 132).

King, Ashley J., Daly, Luke, Rowe, James, et al. (2022). “The Winchcombe meteorite, a unique and pristine witness from the outer solar system”. In: *Science Advances* 8.46, eabq3925, eabq3925 (cit. on p. 52).

Kleine, T., Budde, G., Burkhardt, C., et al. (2020). “The Non-carbonaceous-Carbonaceous Meteorite Dichotomy”. In: *Space Science Reviews* 216.4, 55, p. 55 (cit. on p. 46).

Klimov, P. A., Panasyuk, M. I., Khrenov, B. A., et al. (2017). “The TUS Detector of Extreme Energy Cosmic Rays on Board the Lomonosov Satellite”. In: *Space Science Reviews* 212.3-4, pp. 1687–1703. arXiv: `1706.04976 [astro-ph.IM]` (cit. on p. 66).

Klimov, Pavel, Battisti, Matteo, Belov, Alexander, et al. (2022). “Status of the K-EUSO Orbital Detector of Ultra-High Energy Cosmic Rays”. In: *Universe* 8.2, p. 88. arXiv: `2201.12766 [astro-ph.IM]` (cit. on p. 67).

Kohout, TomáÅ. ¡, Haloda, Jakub, Halodová, Patricie, et al. (2017). “Annama H chondrite—Mineralogy, physical properties, cosmic ray exposure, and parent body history”. In: *Meteorit. Planet. Sci.* 52.8, pp. 1525–1541. arXiv: `1710.07687 [astro-ph.EP]` (cit. on p. 52).

Kornoš, Leonard, Koukal, Jakub, Piffl, Roman, and Tóth, Juraj (2014). “EDMOND Meteor Database”. In: *Proceedings of the International Meteor Conference, Poznan, Poland, 22-25 August 2013*. Ed. by M. Gyssens, P. Roggemans, and P. Zoladek, pp. 23–25 (cit. on pp. 190, 191, 193, 194).

Korochantseva, E. V., Verchovsky, A. B., Lorenz, C. A., Buikin, A. I., and Korochantsev, A. V. (2019). “The Ozerki Meteorite: Petrology and the First Data on Noble Gases and Nitrogen Released by Stepwise Combustion and Crushing Methods”. In: *82nd Annual Meeting of The Meteoritical Society*. Vol. 82. LPI Contributions, 6458, p. 6458 (cit. on p. 52).

Koschny, D., Drolshagen, E., Drolshagen, S., et al. (2017). “Flux densities of meteoroids derived from optical double-station observations”. In: *Planetary and Space Science* 143, pp. 230–237 (cit. on pp. 202, 203).

Koschny, Detlef and Zender, Joe (1998). “Comparing Meteor Number Fluxes from Ground-Based and Airplane-Based Video Observations”. In: *Earth Moon and Planets* 82, pp. 209–220 (cit. on p. 68).

Kresak, L. and Kresakova, M. (1976). “A Note on Meteor and Micrometeoroid Orbits Determined from Rough Velocity Data”. In: *Bulletin of the Astronomical Institutes of Czechoslovakia* 27, p. 106 (cit. on pp. 207, 208).

Krot, A. N., Keil, K., Scott, E. R. D., Goodrich, C. A., and Weisberg, M. K. (2014). “Classification of Meteorites and Their Genetic Relationships”. In: *Meteorites and Cosmochemical Processes*. Ed. by Andrew M. Davis. Vol. 1, pp. 1–63 (cit. on p. 39).

Landsman, W. B. (1993). “The IDL Astronomy User’s Library”. In: *Astronomical Data Analysis Software and Systems II*. Ed. by R. J. Hanisch, R. J. V. Brissenden, and J. Barnes. Vol. 52. Astronomical Society of the Pacific Conference Series, p. 246 (cit. on p. 81).

Lauretta, D. S., Balram-Knutson, S. S., Beshore, E., et al. (2017). “OSIRIS-REx: Sample Return from Asteroid (101955) Bennu”. In: *Space Science Reviews* 212.1-2, pp. 925–984. arXiv: `1702.06981 [astro-ph.EP]` (cit. on p. 14).

Le Pichon, Alexis, Ceranna, Lars, Pilger, Christoph, et al. (2013). “The 2013 Russian fireball largest ever detected by CTBTO infrasound sensors”. In: *Geophysical Research Letters* 40.14, pp. 3732–3737 (cit. on p. 35).

Levenberg, K. (1944). “A method for the solution of certain non-linear problems in least squares”. In: *Quarterly of applied mathematics* 2.2, pp. 164–168 (cit. on p. 81).

Levin, B. Yu (1956). “Physical theory of meteors and meteoroid substance in the solar system”. In: *AN SSSR, Moscow* (cit. on p. 119).

Leya, Ingo, Hirtz, Jason, and David, Jean-Christophe (2021). “Galactic Cosmic Rays, Cosmic-Ray Variations, and Cosmogenic Nuclides in Meteorites”. In: *The Astrophysical Journal* 910.2, 136, p. 136 (cit. on pp. 162, 163).

Lindblad, B. A., Neslušan, L., Porubčan, V., and Svoreň, J. (2003). “IAU Meteor Database of photographic orbits version 2003”. In: *Earth Moon and Planets* 93.4, pp. 249–260 (cit. on pp. 207, 208).

Lipschutz, Michael E. and Schultz, Ludolf (2007). "Meteorites". In: *Encyclopedia of the Solar System*. Ed. by L. A. Adams McFadden, P. R. Weissman, and T. V. Johnson, pp. 251–282 (cit. on p. 39).

Llorca, J., Trigo-Rodríguez, J. M., Ortiz, J. L., et al. (2005). "The Villalbeto de la Peña meteorite fall: I. Fireball energy, meteorite recovery, strewn field, and petrography". In: *Meteorit. Planet. Sci.* 40, p. 795 (cit. on p. 52).

Lovell, Alfred Charles Bernard (1954). *Meteor astronomy* (cit. on p. 206).

Lyytinen, E. and Gritsevich, M. (2016). "Implications of the atmospheric density profile in the processing of fireball observations". In: *Planetary and Space Science* 120, pp. 35–42 (cit. on p. 125).

MacPherson, G. J. (2014). "Calcium-Aluminum-Rich Inclusions in Chondritic Meteorites". In: *Meteorites and Cosmochemical Processes*. Ed. by Andrew M. Davis. Vol. 1, pp. 139–179 (cit. on p. 43).

MacPherson, G. J. and Boss, A. (2011). "Cosmochemistry Special Feature: Cosmochemical evidence for astrophysical processes during the formation of our solar system". In: *Proceedings of the National Academy of Science* 108.48, pp. 19152–19158 (cit. on p. 42).

Macrossan, MN (2007). "Scaling parameters for hypersonic flow: correlation of sphere drag data". In: (cit. on p. 124).

Mancuso, S., Taricco, C., Colombetti, P., et al. (2019). "Long-term heliomagnetic field variation based on cosmogenic ^{44}Ti in meteorites". In: *Nuovo Cimento C Geophysics Space Physics C* 42.1, 43, p. 43 (cit. on p. 158).

Marcelli, L., Arnone, E., Barghini, M., et al. (2022). "Observation of ELVES with Mini-EUSO telescope on board the International Space Station". In: *37th International Cosmic Ray Conference*, 367, p. 367. arXiv: `2112.08004 [astro-ph.HE]` (cit. on p. 71).

Markwardt, C. B. (2009). "Non-linear Least-squares Fitting in IDL with MPFIT". In: *Astronomical Data Analysis Software and Systems XVIII*. Ed. by D. A. Bohlender, D. Durand, and P. Dowler. Vol. 411. Astronomical Society of the Pacific Conference Series, p. 251. arXiv: `0902.2850 [astro-ph.IM]` (cit. on p. 81).

Marquardt, D. W. (1963). "An algorithm for least-squares estimation of nonlinear parameters". In: *Journal of the society for Industrial and Applied Mathematics* 11.2, pp. 431–441 (cit. on p. 81).

Masiero, Joseph R., Mainzer, A. K., Grav, T., et al. (2011). "Main Belt Asteroids with WISE/NEOWISE. I. Preliminary Albedos and Diameters". In: *The Astrophysical Journal* 741.2, 68, p. 68. arXiv: `1109.4096 [astro-ph.EP]` (cit. on pp. 9, 10).

McCord, Thomas B., Adams, John B., and Johnson, Torrence V. (1970). "Asteroid Vesta: Spectral Reflectivity and Compositional Implications". In: *Science* 168.3938, pp. 1445–1447 (cit. on p. 46).

McCord, Thomas B. and Sotin, Christophe (2005). "Ceres: Evolution and current state". In: *Journal of Geophysical Research (Planets)* 110.E5, E05009, E05009 (cit. on p. 6).

McCrosky, R. E., Posen, A., Schwartz, G., and Shao, C. Y. (1971). "Lost City Meteorite Its Recovery and a Comparison with Other Fireballs". In: *Journal of Geophysical Research* 76.17, pp. 4090–4108 (cit. on p. 52).

McMullan, Sarah, Vida, Denis, Devillepoix, Hadrien A. R., et al. (2023). “The Winchcombe Fireball – that Lucky Survivor”. In: *arXiv e-prints*, arXiv:2303.12126, arXiv:2303.12126. arXiv: `2303.12126 [astro-ph.EP]` (cit. on p. 52).

Meier, Matthias M. M., Gritsevich, Maria, Welten, Kees C., et al. (2020). “Orbit, Meteoroid Size and Cosmic History of the Osceola (L6) Meteorite”. In: *European Planetary Science Congress*, EPSC2020-730, EPSC2020–730 (cit. on p. 52).

Michel, Patrick, Benz, Willy, and Richardson, Derek C. (2003). “Disruption of fragmented parent bodies as the origin of asteroid families”. In: *Nature* 421.6923, pp. 608–611 (cit. on p. 17).

Michel, R., Dragovitsch, P., Cloth, P., Dagge, G., and Filges, D. (1991). “On the production of cosmogenic nuclides in meteoroids by galactic protons”. In: *Meteoritics* 26, pp. 221–242 (cit. on p. 158).

Michel, R. and Neumann, S. (1998). “Interpretation of cosmogenic nuclides in meteorites on the basis of accelerator experiments and physical model calculations”. In: *Proceedings of the Indian Academy of Science, Earth and Planetary Sciences* 107, pp. 441–457 (cit. on p. 163).

Miller, Steven, Haddock, Steven H. D., Straka, William, et al. (2021a). “First Detection of Bioluminescent Milky Seas by the VIIRS Day/Night Band: Maritime Continent”. In: *AGU Fall Meeting Abstracts*. Vol. 2021, A54B-08, A54B–08 (cit. on p. 70).

Miller, Steven D., Haddock, Steven H. D., Elvidge, Christopher D., and Lee, Thomas F. (2005). “Detection of a bioluminescent milky sea from space”. In: *Proceedings of the National Academy of Science* 102.40, pp. 14181–14184 (cit. on p. 70).

Miller, Steven D, Haddock, Steven HD, Straka III, William C, et al. (2021b). “Honing in on bioluminescent milky seas from space”. In: *Scientific Reports* 11.1, p. 15443 (cit. on p. 70).

Milley, E. P., Hildebrand, A. R., Brown, P. G., et al. (2010). “Pre-fall orbit of the Buzzard Coulee meteoroid”. In: *GeoCanada 2010* (cit. on p. 52).

Mittlefehldt, D. W. (2014). “Achondrites”. In: *Meteorites and Cosmochemical Processes*. Ed. by Andrew M. Davis. Vol. 1, pp. 235–266 (cit. on p. 44).

Miyamoto, H., Battisti, M., Belov, A. S., et al. (2019). “Space Debris Detection and Tracking with the Techniques of Cosmic Ray Physics”. In: *36th International Cosmic Ray Conference (ICRC2019)*. Vol. 36. International Cosmic Ray Conference, 253, p. 253. arXiv: `1909.05601 [astro-ph.IM]` (cit. on p. 172).

Moilanen, J., Gritsevich, M., and Lyytinen, E. (2021). “Determination of strewn fields for meteorite falls”. In: *Monthly Notices of the Royal Astronomical Society* 503.3, pp. 3337–3350 (cit. on pp. 31, 124).

Moorhead, Althea V., Blaauw, Rhiannon C., Moser, Danielle E., et al. (2017). “A two-population sporadic meteoroid bulk density distribution and its implications for environment models”. In: *Monthly Notices of the Royal Astronomical Society* 472.4, pp. 3833–3841 (cit. on pp. 132, 194).

Moorhead, Althea V. and Matney, Mark (2021). “The ratio of hazardous meteoroids to orbital debris in near-Earth space”. In: *Advances in Space Research* 67.1, pp. 384–392 (cit. on p. 26).

Moré, J. J (1978). “The Levenberg-Marquardt algorithm: implementation and theory”. In: *Numerical analysis*. Springer, pp. 105–116 (cit. on p. 81).

Moreno-Ibáñez, Manuel, Silber, Elizabeth A., Gritsevich, Maria, and Trigo-Rodríguez, Josep M. (2018). “Verification of the Flow Regimes Based on High-fidelity Observations of Bright Meteors”. In: *The Astrophysical Journal* 863.2, 174, p. 174. arXiv: `1807.04509 [astro-ph.EP]` (cit. on pp. 35, 124).

Moretti, P. F., Maras, A., and Folco, L. (2007). “Space weathering, reddening and gardening of asteroids: A complex problem”. In: *Advances in Space Research* 40.2, pp. 258–261 (cit. on p. 12).

Morrison, David, Chapman, Clark R., Steel, Duncan, and Binzel, Richard P. (2004). “Impacts and the public: communicating the nature of the impact hazard”. In: *Mitigation of Hazardous Comets and Asteroids*. Ed. by Michael J. S. Belton, Thomas H. Morgan, Nalin H. Samarasinha, and Donald K. Yeomans, p. 353 (cit. on p. 26).

Narula, S. C. and Wellington, J. F. (1982). “The minimum sum of absolute errors regression: A state of the art survey”. In: *International Statistical Review/Revue Internationale de Statistique*, pp. 317–326 (cit. on p. 90).

Nedelcu, Dan Alin, Birlan, Mirel, Turcu, Vlad, et al. (2018). “Meteorites Orbits Reconstruction by Optical Imaging (MOROI) Network”. In: *Romanian Astronomical Journal* 28.1, pp. 57–65 (cit. on p. 56).

Nesvorny, D. (2015). “Nesvorny HCM Asteroid Families V3.0”. In: *NASA Planetary Data System*, EAR-A-VARGBDET-5-NESVORNYFAM-V3.0, EAR–A–VARGBDET–5–NESVORNYFAM–V3.0 (cit. on pp. 16, 17).

Nesvorný, D., Morbidelli, A., Vokrouhlický, D., Bottke, W. F., and Brož, M. (2002). “The Flora Family: A Case of the Dynamically Dispersed Collisional Swarm?” In: *Icarus* 157.1, pp. 155–172 (cit. on p. 23).

Nesvorný, David, Bottke, William F., Levison, Harold F., and Dones, Luke (2003). “Recent Origin of the Solar System Dust Bands”. In: *The Astrophysical Journal* 591.1, pp. 486–497 (cit. on p. 23).

O’Brien, David P. and Greenberg, Richard (2003). “Steady-state size distributions for collisional populations:. analytical solution with size-dependent strength”. In: *Icarus* 164.2, pp. 334–345. arXiv: `1407.3307 [astro-ph.EP]` (cit. on p. 9).

Olmsted, D. (1834). “Observations of the meteors of November 13, 1833”. In: *American Journal of Science* 25, pp. 354–411 (cit. on p. 29).

Oort, J. H. (1950). “The structure of the cloud of comets surrounding the Solar System and a hypothesis concerning its origin”. In: *Bulletin of the Astronomical Institutes of the Netherlands* 11, pp. 91–110 (cit. on p. 20).

Öpik, E. (1940). “Meteors (Council report on the progress of astronomy)”. In: *Monthly Notices of the Royal Astronomical Society* 100, p. 315 (cit. on p. 206).

Opik, E. J. (1951). “Collision probability with the planets and the distribution of planetary matter”. In: *Proc. R. Irish Acad. Sect. A* 54, pp. 165–199 (cit. on p. 23).

Osteria, G., Scotti, V., and JEM-EUSO Collaboration (2019). “EUSO-SPB: In-flight performance”. In: *Nuclear Instruments and Methods in Physics Research A* 936, pp. 237–238 (cit. on p. 66).

Palotai, Csaba, Sankar, Ramanakumar, Free, Dwayne L., et al. (2019). “Analysis of the 2016 June 2 bolide event over Arizona”. In: *Monthly Notices of the Royal Astronomical Society* 487.2, pp. 2307–2318. arXiv: `1801.05072 [astro-ph.EP]` (cit. on p. 52).

Peña-Asensio, Eloy, Trigo-Rodríguez, Josep Maria, Gritsevich, Maria, and Rimola, Albert (2021). “Accurate 3D fireball trajectory and orbit calculation using the 3D-FIRETOC automatic Python code”. In: *Monthly Notices of the Royal Astronomical Society* 504.4, pp. 4829–4840. arXiv: `2103.13758 [astro-ph.EP]` (cit. on p. 124).

Pecina, P. and Ceplecha, Z. (1984). “Importance of atmospheric models for interpretation of photographic fireball data.” In: *Bulletin of the Astronomical Institutes of Czechoslovakia* 35, pp. 120–123 (cit. on p. 125).

Perna, D., Barucci, M. A., and Fulchignoni, M. (2013). “The near-Earth objects and their potential threat to our planet”. In: *The Astronomy and Astrophysics Review* 21, 65, p. 65 (cit. on p. 26).

Perryman, M. A. C., Lindegren, L., Kovalevsky, J., et al. (1997). “The HIPPARCOS Catalogue”. In: *Astronomy and Astrophysics* 323, pp. L49–L52 (cit. on pp. 84, 98).

Picone, J. M., Hedin, A. E., Drob, D. P., and Aikin, A. C. (2002). “NRLMSISE-00 empirical model of the atmosphere: Statistical comparisons and scientific issues”. In: *Journal of Geophysical Research (Space Physics)* 107.A12, 1468, p. 1468 (cit. on p. 124).

Piotrowski, Lech, Casolino, Marco, Arnone, Enrico, et al. (2022). “The search for nuclearites on-ground and in space”. In: *44th COSPAR Scientific Assembly. Held 16-24 July*. Vol. 44, p. 2998 (cit. on p. 72).

Piotrowski, Lech Wiktor, Małek, Katarzyna, Mankiewicz, Lech, et al. (2020). “Limits on the Flux of Nuclearites and Other Heavy Compact Objects from the Pi of the Sky Project”. In: *Physical Review Letters* 125.9, 091101, p. 091101 (cit. on p. 72).

Plebaniak, Z., Karczmarczyk, J., Marszał, W., et al. (2017). “HVPS system for * - EUSO detectors”. In: *35th International Cosmic Ray Conference (ICRC2017)*. Vol. 301. International Cosmic Ray Conference, 378, p. 378 (cit. on p. 74).

Plebaniak, Z., Przybylak, M., Barghini, D., et al. (2022). “Study of the calibration method using the stars measured by the EUSO-TA telescope”. In: *37th International Cosmic Ray Conference*, 240, p. 240. arXiv: `2112.09904 [astro-ph.IM]` (cit. on p. 66).

Poemma Collaboration, Olinto, A. V., Krizmanic, J., et al. (2021). “The POEMMA (Probe of Extreme Multi-Messenger Astrophysics) observatory”. In: *Journal of Cosmology and Astroparticle Physics* 2021.6, 007, p. 007 (cit. on p. 67).

Popova, O., Borovička, J., and Campbell-Brown, M. D. (2019). “Modelling the Entry of Meteoroids”. In: *Meteoroids: Sources of Meteors on Earth and Beyond*. Ed. by Galina O. Ryabova, David J. Asher, and Margaret J. Campbell-Brown, p. 9 (cit. on pp. 30, 32, 37).

Popova, Olga P., Jenniskens, Peter, Emel’yanenko, Vacheslav, et al. (2013). “Chelyabinsk Airburst, Damage Assessment, Meteorite Recovery, and Characterization”. In: *Science* 342.6162, pp. 1069–1073 (cit. on pp. 25, 52).

Pratesi, G., Moggi Cecchi, V., Greenwood, R. C., et al. (2021). “Cavezzo—The double face of a meteorite: Mineralogy, petrography, and geochemistry of a very unusual chondrite”. In: *Meteoritics and Planetary Science* 56.6, pp. 1125–1150 (cit. on pp. 155, 156).

Pravec, Petr and Harris, Alan W. (2000). “Fast and Slow Rotation of Asteroids”. In: *Icarus* 148.1, pp. 12–20 (cit. on p. 9).

Rabaza, O, Galadí-Enríquez, D, Estrella, A Espín, and Dols, F Aznar (2010). “All-sky brightness monitoring of light pollution with astronomical methods”. In: *Journal of environmental management* 91.6, pp. 1278–1287 (cit. on p. 55).

Reddy, Vishnu, Sanchez, Juan A., Bottke, William F., et al. (2016). “Physical Characterization of ∼2 M Diameter Near-Earth Asteroid 2015 TC25: A Possible Boulder from E-type Asteroid (44) Nysa”. In: *The Astronomical Journal* 152.6, 162, p. 162. arXiv: `1612.00113 [astro-ph.EP]` (cit. on p. 45).

Register, P. J., Mathias, D. L., and Wheeler, L. F. (2017). “Asteroid fragmentation approaches for modeling atmospheric energy deposition”. In: *Icarus* 284, pp. 157–166 (cit. on p. 131).

Revelle, D. O., Brown, P. G., and Spurný, P. (2004). “Entry dynamics and acoustics / infrasonic / seismic analysis for the Neuschwanstein meteorite fall”. In: *Meteorit. and Planet. Sci.* 39.10, pp. 1605–1626 (cit. on p. 52).

Rigby, Jane, Perrin, Marshall, McElwain, Michael, et al. (2022). “Characterization of JWST science performance from commissioning”. In: *arXiv e-prints*, arXiv:2207.05632, arXiv:2207.05632. arXiv: `2207.05632 [astro-ph.IM]` (cit. on p. 26).

Rivkin, A. S., Howell, E. S., Britt, D. T., et al. (1995). “3-μm Spectrophotometric Survey of M- and E-Class Asteroids”. In: *Icarus* 117.1, pp. 90–100 (cit. on p. 13).

Robertson, James B and Ayers, Wendell G (1968). *Photometry of an Iron Artificial Meteor Reentering at 11 Kilometers Per Second*. National Aeronautics and Space Administration (cit. on pp. 70, 202).

Rostoker, G. (1972). “Geomagnetic indices.” In: *Reviews of Geophysics and Space Physics* 10, pp. 935–950 (cit. on p. 125).

Rozenberg, G.V. (1966). *Twilight; A Study in Atmospheric Optics. With a Pref. by J.V. Dave. Authorized Translation From the Russian by Richard B. Rodman* (cit. on p. 97).

Rubincam, David Parry (2000). “Radiative Spin-up and Spin-down of Small Asteroids”. In: *Icarus* 148.1, pp. 2–11 (cit. on p. 24).

Ruiz-Hernandez, Oliver I., Sharakin, Sergei, Klimov, Pavel, and Martínez-Bravo, Oscar M. (2022). “Meteors observations by the orbital telescope TUS”. In: *Planetary and Space Science* 218, 105507, p. 105507 (cit. on pp. 67, 68).

Ryabova, Galina O., Asher, David J., and Campbell-Brown, Margaret J. (2019). *Meteoroids: Sources of Meteors on Earth and Beyond* (cit. on p. 27).

Sadovnichii, V. A., Panasyuk, M. I., Amelyushkin, A. M., et al. (2017). ““Lomonosov” Satellite—Space Observatory to Study Extreme Phenomena in Space”. In: *Space Science Reviews* 212.3-4, pp. 1705–1738 (cit. on p. 66).

Sansaturio, María Eugenia and Arratia, Oscar (2008). “Apophis: the Story Behind the Scenes”. In: *Earth Moon and Planets* 102.1-4, pp. 425–434 (cit. on p. 26).

Sansom, E. K., Bland, P. A., Towner, M. C., et al. (2020). “Murrili meteorite’s fall and recovery from Kati Thanda”. In: *arXiv e-prints*, arXiv:2006.07151, arXiv:2006.07151. arXiv: `2006.07151 [astro-ph.EP]` (cit. on p. 52).

Schiaparelli, Giovanni Virginio (1867). *Note E riflessioni intorno alla teoria astronomica delle stelle cadenti* (cit. on pp. 27, 29).

Schulte, Peter, Alegret, Laia, Arenillas, Ignacio, et al. (2010). “The Chicxulub Asteroid Impact and Mass Extinction at the Cretaceous-Paleogene Boundary”. In: *Science* 327.5970, p. 1214 (cit. on p. 24).

Scotti, V., Osteria, G., and JEM-EUSO Collaboration (2020). “The EUSO-SPB2 mission”. In: *Nuclear Instruments and Methods in Physics Research A* 958, 162164, p. 162164 (cit. on p. 66).

Sephton, Mark A. (2002). “Organic compounds in carbonaceous meteorites”. In: *Natural Product Reports* 19, pp. 292–311 (cit. on p. 43).

Shaddad, Muawia H., Jenniskens, Peter, Numan, Diyaa, et al. (2010). “The recovery of asteroid 2008 TC_3”. In: *Meteorit. Planet. Sci.* 45.1557, pp. 1557–1589 (cit. on p. 52).

Sharp, Zachary (2017). “Chapter 13 – Extraterrestrial Material”. In: *Principles of stable isotope geochemistry* (cit. on p. 41).

Shinozaki, K., Shinozaki, K., Bertaina, M., et al. (2019). “Estimation of the exposure for the air shower detection mode of EUSO-SPB1”. In: *36th International Cosmic Ray Conference (ICRC2019)*. Vol. 36. International Cosmic Ray Conference, 427, p. 427. arXiv: `1909.05713 [astro-ph.HE]` (cit. on p. 66).

Shinto, D., Iwami, Y., Fujioka, M., et al. (2022). “Solar Power Supply and Environmental Control System for DIMS Experiment”. In: *37th International Cosmic Ray Conference*, 502, p. 502 (cit. on p. 217).

Shober, Patrick M., Devillepoix, Hadrien A. R., Sansom, Eleanor K., et al. (2022). “Arpu Kuilpu: An H5 from the outer main belt”. In: *Meteoritics and Planetary Science* 57.6, pp. 1146–1157. arXiv: `2202.07185 [astro-ph.EP]` (cit. on p. 52).

Shrbený, Lukáš, Krzesińska, Agata M., Borovička, Jiří, et al. (2022). “Analysis of the daylight fireball of July 15, 2021, leading to a meteorite fall and find near Antonin, Poland, and a description of the recovered chondrite”. In: *Meteoritics and Planetary Science* 57.12, pp. 2108–2126 (cit. on p. 52).

Shukla, P. N., Shukla, A. D., Rai, V. K., et al. (2005). “The Dergaon (H5) chondrite: Fall, classification, petrological and chemical characteristics, cosmogenic effects, and noble gas records”. In: *Meteoritics and Planetary Science* 40, p. 627 (cit. on p. 162).

Sidhu, Jagjit, Mammen Abraham, Roshan, Covault, Corbin, and Starkman, Glenn (2019). “Macro detection using fluorescence detectors”. In: *Journal of Cosmology and Astroparticle Physics* 2019.2, 037, p. 037. arXiv: `1808.06978 [astro-ph.HE]` (cit. on pp. 219, 222).

Sidhu, Jagjit Singh and Starkman, Glenn (2019). “Macroscopic dark matter constraints from bolide camera networks”. In: *Physical Review D* 100.12, 123008, p. 123008 (cit. on pp. 72, 222).

Silber, Elizabeth A. and Brown, Peter G. (2014). “Optical observations of meteors generating infrasound-I: Acoustic signal identification and phenomenology”. In: *Journal of Atmospheric and Solar-Terrestrial Physics* 119, pp. 116–128. arXiv: `1407.6331 [physics.ao-ph]` (cit. on p. 35).

Simon, S. B., Grossman, L., Clayton, R. N., et al. (2004). “The fall, recovery, and classification of the Park Forest meteorite”. In: *Meteorit. Planet. Sci.* 39.4, pp. 625–634 (cit. on p. 52).

Smith, Jeffrey C., Morris, Robert L., Rumpf, Clemens, et al. (2021). “An automated bolide detection pipeline for GOES GLM”. In: *Icarus* 368, 114576, p. 114576. arXiv: `2106.09189 [astro-ph.EP]` (cit. on p. 69).

SonotaCo (2009). “A meteor shower catalog based on video observations in 2007-2008”. In: *WGN, Journal of the International Meteor Organization* 37.2, pp. 55–62 (cit. on p. 193).

Spurný, P., Bland, P. A., Shrbený, L., et al. (2011). “The Mason Gully Meteorite Fall in SW Australia: Fireball Trajectory and Orbit from Photographic Records”. In: *Meteorit. Planet. Sci. Suppl.* 74, 5101, p. 5101 (cit. on p. 52).

Spurný, P., Borovička, J., Haloda, J., Shrbeny, L., and Heinlein, D. (2016). “Two Very Precisely Instrumentally Documented Meteorite Falls: Zdar nad Sazavou and Stubenberg - Prediction and Reality”. In: *79th Annual Meeting of the Meteoritical Society*. Vol. 79, 6221, p. 6221 (cit. on p. 52).

Spurný, P., Borovička, J., Baumgarten, G., et al. (2017a). “Atmospheric trajectory and heliocentric orbit of the Ejby meteorite fall in Denmark on February 6, 2016”. In: *Planetary and Space Sciences* 143, pp. 192–198 (cit. on p. 52).

Spurný, P., Borovička, J., Mucke, H., and Svoreň, J. (2017b). “Discovery of a new branch of the Taurid meteoroid stream as a real source of potentially hazardous bodies”. In: *Astronomy and Astrophysics* 605, A68, A68. arXiv: `1705.08633 [astro-ph.EP]` (cit. on p. 28).

Spurný, Pavel (1994). “Recent fireballs photographed in central Europe”. In: *Planetary and Space Sciences* 42.2, pp. 157–162 (cit. on p. 52).

Spurný, Pavel, Bland, Philip A., Shrbený, Lukáå. ¡, et al. (2012). “The Bunburra Rockhole meteorite fall in SW Australia: fireball trajectory, luminosity, dynamics, orbit, and impact position from photographic and photoelectric records”. In: *Meteorit. Planet. Sci.* 47.2, pp. 163–185 (cit. on p. 52).

Spurný, Pavel, Borovička, Jiří, Kac, Javor, et al. (2010). “Analysis of instrumental observations of the Jesenice meteorite fall on April 9, 2009”. In: *Meteorit. Planet. Sci.* 45.8, pp. 1392–1407 (cit. on p. 52).

Spurný, Pavel, Borovička, Jiří, and Shrbený, LukáÅ. ¡ (2020). “The Žďár nad Sázavou meteorite fall: Fireball trajectory, photometry, dynamics, fragmentation, orbit, and meteorite recovery”. In: *Meteorit. Planet. Sci.* 55.2, pp. 376–401. arXiv: `1912.11784 [astro-ph.EP]` (cit. on p. 52).

Spurný, Pavel, Haloda, Jakub, Borovička, Jiří, Shrbený, Lukáš, and Halodová, Patricie (2014). “Reanalysis of the Benešov bolide and recovery of polymict breccia meteorites - old mystery solved after 20 years”. In: *Astronomy and Astrophysics* 570, A39, A39 (cit. on p. 52).

Spurný, Pavel, Heinlein, Dieter, and Oberst, Jürgen (2002). “The atmospheric trajectory and heliocentric orbit of the Neuschwanstein meteorite fall on April 6, 2002”. In: *Asteroids, Comets, and Meteors: ACM 2002*. Ed. by Barbara Warmbein. Vol. 500. ESA Special Publication, pp. 137–140 (cit. on p. 52).

Spurný, Pavel, Oberst, Jürgen, and Heinlein, Dieter (2003). “Photographic observations of Neuschwanstein, a second meteorite from the orbit of the Příbram chondrite”. In: *Nature* 423.6936, pp. 151–153 (cit. on p. 52).

Stern, S. Alan (2003). “The evolution of comets in the Oort cloud and Kuiper belt”. In: *Nature* 424.6949, pp. 639–642 (cit. on p. 20).

Stern, S. Alan and Weissman, Paul R. (2001). “Rapid collisional evolution of comets during the formation of the Oort cloud”. In: *Nature* 409.6820, pp. 589–591 (cit. on p. 20).

Sunshine, J. M., Connolly, H. C., McCoy, T. J., Bus, S. J., and La Croix, L. M. (2008). “Ancient Asteroids Enriched in Refractory Inclusions”. In: *Science* 320.5875, p. 514 (cit. on p. 14).

Sunshine, J. M. and Pieters, C. M. (1993). “Estimating modal abundances from the spectra of natural and laboratory pyroxene mixtures using the modified Gaussian model”. In: *Journal of Geophysical Research* 98.E5, pp. 9075–9087 (cit. on p. 12).

Tagliaferri, E., Spalding, R., Jacobs, C., Worden, S. P., and Erlich, A. (1994). “Detection of Meteoroid Impacts by Optical Sensors in Earth Orbit”. In: *Hazards Due to Comets and Asteroids*, p. 199 (cit. on p. 69).

Takahashi, Y. (1995). “Maximum-energy Auger Air Shower Satellite (MASS) for Observing Cosmic Rays in the Energy Region 10^{19-22} eV”. In: *International Cosmic Ray Conference*. Vol. 3. International Cosmic Ray Conference, p. 595 (cit. on p. 63).

Tapping, K. F. (2013). “The 10.7 cm solar radio flux ($F_{10.7}$)”. In: *Space Weather* 11.7, pp. 394–406 (cit. on p. 125).

Taricco, C., Bhandari, N., Cane, D., Colombetti, P., and Verma, N. (2006). “Galactic cosmic ray flux decline and periodicities in the interplanetary space during the last 3 centuries revealed by ^{44}Ti in meteorites”. In: *Journal of Geophysical Research* 111, A08102, A08102 (cit. on pp. 158, 160).

Taricco, C., Bhandari, N., Colombetti, P., and Verma, N. (2008). “Mid 19th century minimum of galactic cosmic ray flux inferred from ^{44}Ti in Allegan meteorite”. In: *Advances in Space Research* 41, pp. 275–279 (cit. on p. 158).

Taricco, C., Bhandari, N., Colombetti, P., et al. (2010). “Cosmogenic radioisotopes in the Almahata Sitta ureilite”. In: *Meteoritics and Planetary Science* 45.1743, pp. 1743–1750 (cit. on p. 162).

Taricco, C., Colombetti, P., Sinha, N., et al. (2019). “Cosmic ray effects in the iron meteorite Gebel Kamil and its asymmetric ablation”. In: *Astrophysics and Space Science* 364.5, 76, p. 76 (cit. on pp. 123, 158).

Taricco, C., Sinha, N., Bhandari, N., et al. (2016). “Early 18th century cosmic ray flux inferred from ^{44}Ti in Agen meteorite”. In: *Astrophysics and Space Science* 361, 338, p. 338 (cit. on p. 158).

Tholen, David James (1984). “Asteroid Taxonomy from Cluster Analysis of Photometry.” PhD thesis. University of Arizona (cit. on p. 12).

Tóth, Juraj, Svoreå, JáN., BorovičKa, Jiří, et al. (2015). “The Košice meteorite fall: Recovery and strewn field”. In: *Meteorit. Planet. Sci.* 50.5, pp. 853–863 (cit. on p. 52).

Assessment and Mitigation of Asteroid Impact Hazards (2017). Vol. 46 (cit. on p. 35).

Trigo-Rodríguez, Josep M., Borovička, Jiří, Spurný, Pavel, et al. (2006). “The Villalbeto de la Peña meteorite fall: II. Determination of atmospheric trajectory and orbit”. In: *Meteorit. Planet. Sci.* 41.4, pp. 505–517 (cit. on p. 52).

Trigo-Rodríguez, Josep M., Lyytinen, Esko, Gritsevich, Maria, et al. (2015). “Orbit and dynamic origin of the recently recovered Annama’s H5 chondrite”. In: *Monthly Notices of the Royal Astronomical Society* 449.2, pp. 2119–2127. arXiv: `1507.04342 [astro-ph.EP]` (cit. on p. 52).

Tsien, H.-S. (1946). “Superaerodynamics, mechanics of rarefied gases”. In: *Journal of the Aeronautical Sciences* 13.12, pp. 653–664 (cit. on p. 33).

Turner, D. G., Majaess, D. J., Lane, D. J., et al. (2010). “HDE 344787, the Polaris Analogue that is Even More Interesting Than Polaris”. In: *Odessa Astronomical Publications* 23, p. 125. arXiv: `1102.4848 [astro-ph.SR]` (cit. on p. 101).

Unsalan, Ozan, Jenniskens, Peter, Yin, Qing-Zhu, et al. (2019). “The Sariçiçek howardite fall in Turkey: Source crater of HED meteorites on Vesta and impact risk of Vestoids”. In: *Meteorit. Planet. Sci.* 54.5, pp. 953–1008 (cit. on pp. 48, 52).

Valsecchi, G. B., Jopek, T. J., and Froeschle, Cl. (1999). “Meteoroid stream identification: a new approach - I. Theory”. In: *Monthly Notices of the Royal Astronomical Society* 304.4, pp. 743–750 (cit. on p. 151).

Van Schmus, W. R. and Wood, J. A. (1967). “A chemical-petrologic classification for the chondritic meteorites”. In: *Geochimica et Cosmochimica Acta* 31.5, 747,IN7,755–754,IN10,765 (cit. on p. 44).

Vaubaillon, Jérémie, Neslušan, Luboš, Sekhar, Aswin, Rudawska, Regina, and Ryabova, Galina O. (2019). “From Parent Body to Meteor Shower: The Dynamics of Meteoroid Streams”. In: *Meteoroids: Sources of Meteors on Earth and Beyond*. Ed. by Galina O. Ryabova, David J. Asher, and Margaret J. Campbell-Brown, p. 161 (cit. on p. 30).

Verniani, Franco (1973). “An Analysis of the Physical Parameters of 5759 Faint Radio Meteors”. In: *Journal of Geophysical Research* 78.35, pp. 8429–8462 (cit. on pp. 202, 203).

Vida, Denis, Blaauw Erskine, Rhiannon C., Brown, Peter G., et al. (2022). “Computing optical meteor flux using global meteor network data”. In: *Monthly Notices of the Royal Astronomical Society* 515.2, pp. 2322–2339. arXiv: `2206.11365 [astro-ph.EP]` (cit. on pp. 68, 193).

Vida, Denis, Gural, Peter S., Brown, Peter G., Campbell-Brown, Margaret, and Wiegert, Paul (2020). “Estimating trajectories of meteors: an observational Monte Carlo approach - I. Theory”. In: *Monthly Notices of the Royal Astronomical Society* 491.2, pp. 2688–2705. arXiv: `1911.02979 [astro-ph.EP]` (cit. on pp. 109, 127).

Vida, Denis, Šegon, Damir, Gural, Peter S., et al. (2021a). “The Global Meteor Network - Methodology and first results”. In: *Monthly Notices of the Royal Astronomical Society* 506.4, pp. 5046–5074. arXiv: `2107.12335 [astro-ph.EP]` (cit. on p. 209).

Vida, Denis, Šegon, Damir, Šegon, Marko, et al. (2021b). “Novo Mesto meteorite fall - trajectory, orbit, and fragmentation analysis from optical observations”. In: *European Planetary Science Congress*, EPSC2021-139, EPSC2021–139 (cit. on p. 52).

Von Niessl, Gustav and Hoffmeister, C. (1925). “Katalog der Bestimmungsgrössen für 611 Bahnen Grosser Meteore”. In: *Denkschriften der Kaiserlichen Akademie der Wissenschaften Wien. Mathematisch-Naturwissenchaftliche Klasse* 100, pp. 1–70 (cit. on p. 205).

Walker, David E., Schwarz, Hugo E., and Bustos, Edison (2006). “Monitoring the night sky with the Cerro Tololo All-Sky camera for the TMT and LSST projects”. In: *Society of Photo-Optical Instrumentation Engineers (SPIE) Conference Series*. Ed. by Larry M. Stepp. Vol. 6267. Society of Photo-Optical Instrumentation Engineers (SPIE) Conference Series, 62672O, 62672O (cit. on p. 55).

Warner, Brian D., Harris, Alan W., and Pravec, Petr (2009). “The asteroid lightcurve database”. In: *Icarus* 202.1, pp. 134–146 (cit. on p. 9).

Watanabe, Sei-ichiro, Tsuda, Yuichi, Yoshikawa, Makoto, et al. (2017). “Hayabusa2 Mission Overview”. In: *Space Science Reviews* 208.1-4, pp. 3–16 (cit. on p. 14).

Weissman, P. R. (1996). “The Oort Cloud”. In: *Completing the Inventory of the Solar System*. Ed. by Terrence Rettig and Joseph M. Hahn. Vol. 107. Astronomical Society of the Pacific Conference Series, pp. 265–288 (cit. on p. 19).

Wells, D. C., Greisen, E. W., and Harten, R. H. (1981). “FITS - a Flexible Image Transport System”. In: *Astronomy and Astrophysics Supplement* 44, p. 363 (cit. on p. 61).

Welten, Kees C., Meier, Matthias M. M., Caffee, Marc W., et al. (2010). “Cosmogenic nuclides in Almahata Sitta ureilites: Cosmic-ray exposure age, preatmospheric mass, and bulk density of asteroid 2008 TC_3”. In: *Meteorit. Planet. Sci.* 45.1728, pp. 1728–1742 (cit. on p. 52).

Wenger, M., Ochsenbein, F., Egret, D., et al. (2000). “The SIMBAD astronomical database. The CDS reference database for astronomical objects”. In: *Astronomy and Astrophysics Supplement Series* 143, pp. 9–22 (cit. on p. 84).

Weryk, Robert J. and Brown, Peter G. (2013). “Simultaneous radar and video meteors—II: Photometry and ionisation”. In: *Planetary and Space Science* 81, pp. 32–47 (cit. on p. 203).

Wiegert, Paul A. (2014). “Hyperbolic meteors: Interstellar or generated locally via the gravitational slingshot effect?” In: *Icarus* 242, pp. 112–121. arXiv: `1404.2159 [astro-ph.EP]` (cit. on p. 206).

Wiencke, L., Olinto, A., and JEM-EUSO Collaboration (2017). “EUSO-SPB1 Mission and Science”. In: *35th International Cosmic Ray Conference (ICRC2017)*. Vol. 301. International Cosmic Ray Conference, 1097, p. 1097 (cit. on p. 66).

Wilson, G. and McCausland, P. (2012). “Canadian meteorites: A brief review”. In: *Can. J Earth Sci.* 50, pp. 4–13 (cit. on p. 52).

Witten, Edward (1984). “Cosmic separation of phases”. In: *Physical Review D* 30.2, pp. 272–285 (cit. on pp. 71, 217).

Yager, Robert J (2014). *Calculating Drag Coefficients for Spheres and Other Shapes Using C++*. Tech. rep. ARMY RESEARCH LAB ABERDEEN PROVING GROUND MD WEAPONS and MATERIALS RESEARCH … (cit. on p. 124).

Ye, Quanzhi and Jenniskens, Peter (2022). “Comets and meteor showers”. In: *arXiv e-prints*, arXiv:2209.10654, arXiv:2209.10654. arXiv: `2209.10654 [astro-ph.EP]` (cit. on p. 28).

Zamorano, Jaime, Nievas, Miguel, Sánchez de Miguel, Alejandro, et al. (2015). “Low-cost photometers and open source software for Light Pollution research”. In: *IAU General Assembly*. Vol. 29, 2254626, p. 2254626 (cit. on p. 55).

Zuluaga, Jorge I., Cuartas-Restrepo, Pablo A., Ospina, Jonathan, and Sucerquia, Mario (2019). “Can we predict the impact conditions of metre-sized meteoroids?” In: *Monthly Notices of the Royal Astronomical Society* 486.1, pp. L69–L73. arXiv: `1902.03980 [astro-ph.EP]` (cit. on p. 52).

Acknowledgements

First of all, I would like to acknowledge the constant support of my supervisors, Prof. Mario Edoardo Bertaina and Dr. Daniele Gardiol, for their wise guidance during the whole period of the PhD.

My deep thanks go to the Project Office of PRISMA (Dr. Sara Bertocco, Dr. Albino Carbognani, Dr. Matteo Di Carlo, Dr. Mario Di Martino, Dr. Carmelo Falco, Dr. Marco Morelli, Prof. Giovanni Pratesi, Dr. Walter Riva, Dr. Giovanna Maria Stirpe, Dr. Antonio Volpicelli, Dr. Tullia Carriero) for the close and fruitful collaboration during these years.

I acknowledge also the support of the entire JEM-EUSO and Mini-EUSO team and its individual members (Dr. Matteo Battisti, Dr. Francesca Bisconti, Dr. Marco Casolino, Dr. Laura Marcelli, Dr. Hiroko Miyamoto, Dr. Lech Wiktor Piotrowski, Dr. Giulia Romoli, and all the others).

I deeply thanks Dr. Mária Hajduková and Dr. Silvia Ďurišová for their kind hospitality and collaboration during my visiting period at the Astronomical Institute of the Slovak Academy of Sciences in Bratislava.

I also acknowledge the support and collaboration of the Cosmogeophysical research group (Prof. Enrico Arnone, Dr. Ilaria Bizzarri, Dr. Paolo Colombetti, Dr. Salvatore Mancuso, Prof. Carla Taricco).

Finally, I acknowledge the important work of Prof. Rossella Caruso and Dr. François Colas in the review of this manuscript.